

Journal of Machine Construction and Maintenance

no 2/2019



Journal of Machine Construction and Maintenance

Scientific quarterly of the ŁUKASIEWICZ Research Network – Institute for Sustainable Technologies

Information about articles printed in the Journal can be found in the following three renowned databases:

- BazTech
- EBSCO
- Index Copernicus
- TEMA

Articles are reviewed by more than 100 reviewers constantly cooperating with the Journal under the auspices of the Committee on Machine Building of the Polish Academy of Sciences. Reviewers are listed on the website of the Journal: www.jmcm.itee.radom.pl

EDITORIAL BOARD

Editor-in-chief – Prof. Adam MAZURKIEWICZ, tel. 48 364 39 03, adam.mazurkiewicz@itee.radom.pl

Deputy Editor – Dr. Andrzej MAJCHER, tel. 48 364 92 72, andrzej.majcher@itee.radom.pl

Secretary – Dr. Beata BELINA, tel. 48 364 92 98, beata.belina@itee.radom.pl

Issue coordinator – Mgr Anna RUSINOWSKA, tel. 48 364 93 40, anna.rusinowska@itee.radom.pl

Dr. Demófilo Maldoado CORTÉS	– Universidad de Monterrey (Mexico)
Prof. Gualtiero FANTONI	– University of Pisa (Italy)
Dr. Sergey FILLIPOV	– Fintech Policy (Belgium)
Prof. Bolesław KARWAT	– AGH University of Science and Technology (Poland)
Prof. Emmanuel KOUKIOS	– National Technical University of Athens (Greece)
Prof. Jose M. Gutierrez LOPEZ	– Aalborg University (Denmark)
Dr. Sangeeta KARMOKAR	– Auckland University of Technology (New Zealand)
Prof. Jens Myrup PEDERSEN	– Aalborg University (Denmark)

THEMATIC EDITORS:

Prof. Tomasz GIESKO	– mechatronic systems and optomechatronic measurement methods;
Dr. Joanna ŁABĘDZKA	– knowledge transformation systems and IT;
Dr. Andrzej MAJCHER	– control systems, metrology;
Dr. Anna KOWALIK-KLIMCZAK	– biotechnologies, ecology, operational fluids management;
Prof. Beata POTERAŁSKA	– innovations, technology transfer, foresight;
Prof. Jerzy SMOLIK	– surface engineering, hybrid technologies, materials test methods;
Prof. Andrzej ZBROWSKI	– design and construction of machines, operational and standardization tests

Address:

ul. K. Pułaskiego 6/10, 26-600 Radom

tel. 48 364 92 98, fax 48 364-47-60

e-mail: jmcm@itee.radom.pl

Journal co-funded by the Ministry of Science and Higher Education

ISSN 1232-9312

© Copyright by ŁUKASIEWICZ Research Network – Institute for Sustainable Technologies, Radom 2019

Editing: Bożena Mazur, Joanna Iwanowska

Edition: 250 copies

Journal of Machine Construction and Maintenance

QUARTERLY ISSN 1232-9312 2/2019 (113)

Published under the auspices of the Committee on Machine Building of the Polish Academy of Sciences



SCIENTIFIC BOARD

Prof. Janusz KOWAL
AGH University of Science and Technology (Poland) – Chairman

Prof. Jerzy BAJKOWSKI
Warsaw University of Technology (Poland)

Dr Bretislav BERANEK
European Vision Technologies, Ltd., Brno (Czech Republic)

Prof. Patrice BRAUN
Collaborative Research Network, Ballarat (Australia)

Prof. Ramón González CARVAJAL
Universidad de Sevilla (Spain)

Associate Professor Josef CERNOHORSKY
Technical University of Liberec (Czech Republic)

Dr Alexander CHULOK
Institute for Statistical Studies and Economics of
Knowledge, Moscow (Russia)

Prof. Pengyang DENG
Changchun Institute of Applied Chemistry Chinese
Academy of Sciences (China)

Dr Antonio José DIECK-ASSAD
President of the Universidad de Monterrey (Mexico)

Associate Professor Gualtiero FANTONI
University of Pisa (Italy)

Prof. Józef GAWLIK
Cracow University of Technology (Poland)

Prof. Aharon GEDANKEN
Bar-Ilan University, Ramat Gan (Israel)

Dr Susanne GIESECKE
Austrian Institute of Technology, Vienna (Austria)

Prof. Thomas GRAULE
EMPA Materials Science and Technology, Dübendorf (Switzerland)

Prof. Wojciech GUTOWSKI
Commonwealth Scientific and Industrial Research Organisation
(CSIRO) of Melbourne (Australia)

Dr Attila HAVAS
Institute of Economics, Hungarian Academy of Sciences,
Budapest (Hungary)

Dr. Sangeeta KARMOKAR
Auckland University of Technology (New Zealand)

Prof. Bolesław KARWAT
AGH University of Science and Technology, Krakow (Poland)

Prof. Jan KICIŃSKI
The Szewalski Institute Of Fluid-flow Machinery
Polish Academy of Sciences, Gdansk (Poland);
PAN corresponding member

Prof. Emmanuel KOUKIOS
National Technical University of Athens (Greece)

Prof. Piotr KULA
Lodz University of Technology (Poland)

Prof. Xiubing LIANG
National Innovation Institute of Defense Technology, Beijing (China)

Prof. Tadeusz ŁAGODA
Opole University of Technology (Poland)

Prof. Krzysztof MARCHELEK
West Pomeranian University of Technology, Szczecin (Poland)

Dr Tarja MERISTÖ
Laurea University of Applied Sciences, Vantaa (Finland)

Prof. Jens Myrup PEDERSEN
Aalborg University (Denmark)

Eng. Thomas ROESLER
Director Manufacturing Asia Pacific, Shanghai (China)

Prof. Krzysztof SANTAREK
Warsaw University of Technology (Poland)

Prof. Janusz SEMPRUCH
UTP University of Science and Technology, Bydgoszcz (Poland)

Prof. Jerzy SMOLIK
ŁUKASIEWICZ Research Network – Institute for Sustainable
Technologies, Radom (Poland)

Prof. Józef SZALA
UTP University of Science and Technology, Bydgoszcz (Poland)

Prof. Eugeniusz ŚWITOŃSKI
Silesian University of Technology, Gliwice (Poland)

Dr Kim Hua TAN
Nottingham University Business School (United Kingdom, China, Malaysia)

Prof. Sabrina VANTADORI
Università Degli Studi di Parma (Italy)

Prof. Ho-Don YAN
Feng Chia University (Taiwan)

Prof. Claudia ZACCAI
Università di Roma (Italy)

Prof. Wiesław ZWIERZYCKI
Poznan University of Technology (Poland)

CONTENTS

volume 113
december 2019
ISSN 1232-9312
pages 7–129

Mateusz KOWALSKI, Tadeusz ŁAGODA, Fabian ŻOK, Vladimir CHMELKO FATIGUE LIFE OF BUTT WELDMENTS MADE OF S1100QL STEEL Trwałość zmęczeniowa doczołowych złączy spawanych wykonanych ze stali S1100ql	7
Beata NIESTEROWICZ, Paweł DUNAJ, Krzysztof MARCHELEK MODAL ANALYSIS OF LOADER CRANE WITH VARIABLE CONFIGURATION Analiza modalna żurawia przeładunkowego o zmiennej konfiguracji	15
Marek WYLEŻOŁ TOPOLOGICAL OPTIMIZATION IN MECHANICAL CONSTRUCTIONS – AN EXAMPLE OF APPLICATION Optymalizacja topologiczna w konstrukcjach mechanicznych – przykład zastosowania	23
Vladimir ABRAMOV, Anna ABRAMOVA, Giancarlo CRAVOTTO, Roman NIKONOV, Vladimir SISTER, Adam MAZURKIEWICZ, Wojciech PIĄTKIEWICZ, Jerzy SMOLIK, Andrzej MAJCHER INDUSTRIAL APPLICATIONS OF HIGH-INTENSITY ULTRASOUND Przemysłowe zastosowania ultradźwięków o wysokiej intensywności	31
Łukasz MUCHA DEVELOPMENT WORKS ON APPLYING FORCE FEEDBACK IN ROBOT CONTROL SYSTEM Prace rozwojowe nad zastosowaniem siłowego sprzężenia zwrotnego w sterowaniu robotem	41
Andrzej MICHNIK, Jakub WOŁOSZYN, Mariusz SOBIECH, Grzegorz NOWAK REHABILITATION ROBOT FOR UPPER LIMBS Robot rehabilitacyjny kończyn górnych	49
Piotr TYCZYŃSKI, Zbigniew SIEMIĄTKOWSKI, Mirosław RUCKI DRILL BASE BODY FABRICATED WITH ADDITIVE MANUFACTURING TECHNOLOGY: STRUCTURE, STRENGHT AND RELIABILITY Korpus wiertła wykonany za pomocą technologii addytywnej: struktura, wytrzymałość i trwałość	59
Edwin GEVORKYAN, Mirosław RUCKI, Vladimir CHISHKALA, Maksim KISLITSA, Zbigniew SIEMIĄTKOWSKI, Dmitrij MOROZOW HOT PRESSING OF TUNGSTEN MONOCARBIDE NANOPOWDER MIXTURES BY ELECTROCONSOLIDATION METHOD Spiekanie mieszanek nanoproczków węglików wolframu metodą elektrokonsolidacji....	67

Dariusz OZIMINA, Monika MADEJ, Tomasz DESANIUK, Magdalena ŻÓŁTY, Andrzej KULCZYCKI	
EFFECTS OF A GRAPHENE-ENHANCED LUBRICANT ON THE PERFORMANCE OF A TRIBOSYSTEM	
Wpływ dodatku grafenu w olejach smarowych na właściwości systemów tribologicznych	75
Joanna KOWALCZYK, Monika MADEJ, Krystian MILEWSKI, Łukasz NOWAKOWSKI, Dariusz OZIMINA	
THE INFLUENCE OF CUTTING FLUID AND DIAMOND-LIKE CARBON COATING ON CUTTING TOOL WEAR	
Wpływ chłodziwa i powłoki diamentopodobnej na zużycie narzędzi skrawających	83
Robert SOŁTYSIAK, Agnieszka SOŁTYSIAK, Piotr WASILEWSKI	
DEVELOPMENT OF LASER CUTTING TECHNOLOGY WITH A HIGH QUALITY OF THE CUT SURFACE	
Opracowanie technologii cięcia laserowego o wysokiej jakości powierzchni	93
Michał KEKEZ, Tomasz DESANIUK, Jurek DUSZCZYK, Dariusz OZIMINA	
ON THE USE OF ACOUSTIC EMISSION TO ASSESS THE WEAR IN A TRIBOSYSTEM	
Ocena emisji akustycznej w procesie zużycia elementów systemu tribologicznego	99
Krzysztof STANKIEWICZ	
SMART MINING COMMUNICATION SYSTEMS	
Inteligentne górnicze systemy komunikacyjne	105
Jacek DŁUGOPOLSKI, Maria RICHERT	
NATURALLY PARALLEL MEASURING SYSTEM BASED ON FPGA HARDWARE	
Naturalnie równoległy system pomiarowy oparty na technologii FPGA.....	113
Mirosław NESKA	
REFRIGERATION SYSTEMS WITH ONE ADSORPTION BED	
Układy chłodnicze z pojedynczym złożem adsorpcyjnym.....	121

Mateusz KOWALSKI^a, Tadeusz ŁAGODA^{a,*},
Fabian ŻOK^b, Vladimír CHMELKO^c

^a Department of Mechanics and Machine Design, Opole University of Technology, Poland

^b As Company Nakonieczny Andrzej Werakso Bartłomiej, Opole, Poland

^c Faculty of Mechanical Engineering, Slovak University of Technology, Bratislava, Slovakia

* Corresponding author: T.Lagoda@po.edu.pl

FATIGUE LIFE OF BUTT WELDMENTS MADE OF S1100QL STEEL

© 2019 Mateusz Kowalski, Tadeusz Łagoda, Fabian Żok, Vladimír Chmelko

This is an open access article licensed under the Creative Commons Attribution International License (CC BY)



<https://creativecommons.org/licenses/by/4.0/>

Key words: welding, UHSS, fatigue, welding parameters.

Abstract: Fields of application for quenched and tempered advanced high-strength steels are mainly ground-moving, mining equipment, commercial vehicles, and truck cranes. One of the main aspects determining range of applicability for the high strength steels is the possibility to obtain welded joints with the given fatigue strength. Information about fatigue behaviour of the weld joints strongly increases the operational safety of the structures. Factors influencing mechanical properties of the joints can be related to the welding parameters, i.e. welding current, voltage, and interpass and preheat temperatures. Thermo-mechanical process (fusion welding) also causes the diversification of the microstructure in the weld and heat affected zones. Microstructure changes induce residual stress, influencing the fatigue behaviour of the weld joint. The main topic of the paper are results of the experimental fatigue tests performed for S1100QL butt welds produced with two different technological parameter setups. Technological parameters configurations were selected on the basis of experimental tests carried out for sheets with a thickness of 12 mm. The low and high welding parameters differed due to energy introduced into the system. The energy was controlled by current parameters and the preheating of joined elements. In both configurations, it was possible to make welded joints that meet regulatory requirements but differ in the level of introduced internal stresses and microstructural properties in heat affected zone sizes. The joints were additionally subjected to standard strength and microstructural tests.

Trwałość zmęczeniowa doczołowych złączy spawanych wykonanych ze stali S1100ql

Słowa kluczowe: spawanie, UHSS, zmęczenie, parametry spawania.

Streszczenie: Obszar zastosowania stali ulepszanych cieplnie to głównie maszyny służące do robót ziemnych, urządzenia górnicze, pojazdy użytkowe oraz żurawie samochodowe. Jednym z głównych aspektów określających zakres stosowalności stali wysoko wytrzymałych jest możliwość uzyskania połączeń spawanych o zadanej minimalnej wytrzymałości zmęczeniowej. Informacje na temat zjawisk zmęczeniowych zachodzących w złączach spawanych znacznie zwiększają bezpieczeństwo eksploatacyjne konstrukcji. Czynniki wpływające na właściwości mechaniczne złączy mogą być związane z parametrami spawania, tj. prądem spawania, napięciem, temperaturą międzysięgową i temperaturą wstępnego podgrzewania. Proces termomechaniczny, jakim jest spawanie łukiem elektrycznym, powoduje również zróżnicowanie mikrostruktury w samych spoinach i strefach wpływu ciepła. Zmiany mikrostruktury wywołują między innymi naprężenia szczątkowe wpływające na trwałość zmęczeniową złącza spawanego. Głównym tematem artykułu są wyniki eksperymentalnych testów zmęczeniowych wykonanych dla spoin doczołowych S1100QL wytworzonych przy użyciu dwóch różnych konfiguracji parametrów technologicznych. Połączenia zostały dodatkowo poddane standardowym testom wytrzymałościowym i mikrostrukturalnym. W artykule zaprezentowano również symulację propagacji wzrostu pęknięć zmęczeniowych.

Introduction

The development of the new mechanical engineering constructions requires specified criterions described by industrial and environmental standards. The combination of operational safety and mass reduction is one of the main trends in the optimization of mechanical structures [1, 2]. In the case of mechanical

design, those aims can be obtained by the application of ultra-high-strength steels. From the environmental point of view, carbon dioxide emissions generated by the metal industry are increasing year by year. There is a possibility for reducing air pollution and the use of natural resources by increasing material efficiency.

The higher strength of UHSS steel has an important influence on the mass of the automotive structures. Less material is required to sustain similar performance,

which can affect the reduction of CO₂ emissions directly related to energy consumption and lower fuel economy. The use of ultra-high-strength steel (UHSS) rather than conventional structural steel can probably influence and reduce emissions (Fig. 2).

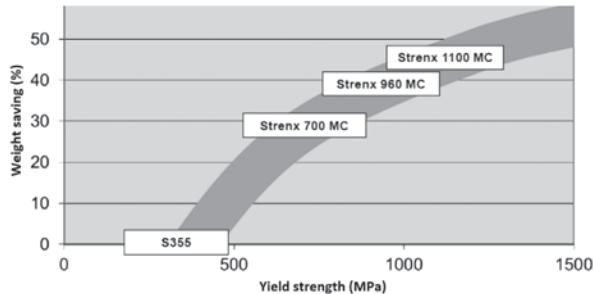


Fig. 1. Potential weight saving as a percentage when using UHSS structural steels compared to regular structural steel [3]

According to the definitions available in literature, steels with yield strength higher than 550MPa are described as UHSS, which is inconsistent with the definition of HSS steel (yield strength higher than 355 MPa and lower than 700 MPa).

Highly strength steels are a group of materials that have gained greater use in recent years. The number of papers published in journals is increasing in the past years. Hence, the most typical applications for UHSSs are booms, lifters, and vehicles of all kind.



Fig. 2. Comparison of cross-sections for standard steel and UHSS

The main difficulties resulting from UHSS use in structural and mechanical constructions are related to the description of the standards. Eurocode 3 standards (EC3) does not include information about designing structures using over 700 MPa yield strength steels. Other challenges are linked with the use of cold forming and welding technologies. The manufacturing process becomes more difficult when yield strength becomes higher. A higher overall strength of the material causes higher residual stress and a higher spring-back effect. Moreover, a larger possible bending radius is needed compared to the standard construction steel. Bending machines with a higher power have to be used [4]. Fusion welding technology of the UHSS also causes additional strength and technological problems. During cooling, quenched and tempered UHSSs have a tendency to cold- and hydrogen cracking. Welding itself also causes thermomechanical changes in the microstructure, which result in a softening phenomenon registered in the heat-

affected zone (HAZ). Lower strength zones influence weld strength performance and reduce the advantage of the UHSS. However, there are also steels that do not suffer from the softening of the HAZ as transformation induced plasticity and complex phase steels [5] and such steels have been adopted in the automotive industry and for mobile heavy equipment. Welding of UHSS is, however, not without its complications and welding processes for these steels need careful attention. For instance, their high susceptibility to cracking and Heat Affected Zone (HAZ). Research on mechanical properties is required to expand the scope of the application of UHSS. Factors influencing joint strength are directly related to the technical parameters of the welding process. The energy put into the weldments and preheating temperature can affect the overall strength and fatigue properties of the joints. The paper presents the results of the experimental fatigue tests performed for S1100 specimens subjected to cyclic tension-compression loading. Fatigue testing was performed for two groups of specimens described by welding parameters. Finite element stress analysis in the weldments is also presented.

1. Fatigue tests of the UHSS – recent research

SSAB's Weldox S1100 E steel transverse butt weldments were subjected to fatigue loading [6]. The results of experimental tests exhibited a decrease in mechanical properties related to the cutting technology (laser cutting compared to water cutting). Yield strength and ultimate tensile strength were lowered at the edge cuts by 12% and 25%, respectively, than manufacturer technical data descriptions. In the base material fatigue tests, S690 steel had higher fatigue strength compared to the S1100. This result was explained with the different surface roughness properties. In the fatigue tests of butt-welded joint, S1100 specimens obtained higher fatigue life compared to the S690 steel (Fig. 1). Cracks initiated in the area of the weld toe [6].

Studies on the low cycle fatigue (LCF) UHSS butt welds were presented in the paper [7]. Specimens of three steel grades S960QL, S960M, and S1100QL were subjected to constant and variable amplitude loadings. Variable loading was generated on the base of the crane truck data logging system. Specimens were welded with the MAG welding process and filler material with 890MPa yield strength. According to the research conclusions, welding quality had a meaningful influence on fatigue life. Moreover, differences in the fatigue life were exhibited in comparison to manual automatic welding.

The low cycle fatigue range of the UHSS welds was also described in [8]. Specimens made of S960QL steel were TIG welded. X96-IG filler material was used in the specimen preparation. Monotonic tensile tests were

conducted to identify mechanical properties. Residual stress was measured using X-ray diffraction. The fatigue lives of the welds were significantly lower than the base material (around 90%). The decrease was observed in high and low cycle fatigue regimes. Stress concentration factors were also determined via the Lawrence's method, Jawdokimov's method, and FEA.

Other works related to fatigue phenomena of UHSS welds can also be indicated in [9–11].

2. Material properties

Specimens were cut from 12 mm thick plates. Mechanical properties of the material were identified with standard testing methods: tension and Charpy tests. Mechanical properties and the chemical composition of the S1100 steel are presented in Tables 1 and 2.

Table 1. Mechanical properties of the s1100ql steel

Mechanical properties						
R_e , MPa	R_m , MPa	A, %	K_V , J (-40°C)	K_V , J (-60°C)	E, GPa	ν , -
1157	1384	10	46	33	200	0,3

where: R_e – yield strength, R_m – ultimate strength, A – elongation, K_V – impact resistance, E – Young modulus, ν – Poisson's ratio.

Table 2. Chemical composition of the s1100ql

Chemical composition of the S1100 steel												
C	Si	Mn	P	S	N	B	Cr	Cu	Mo	Nb	Ni	Ti
0.17	0.25	1.12	0.011	0.001	0.003	0.002	0.67	0.05	0.62	0.03	0.06	0.005

Table 3. Welding parameters

Parameter Description	Welding Parameters								
	Welding position	Layers	Pre-heat, °C	Filler Size, mm	Current, A	Voltage, V	Current type	Travel speed [cm/min]	Heat input [kJ/mm]
High	PA	A	120-150	2.5	100-120	24-26	DC/(+)	10-20	0.58-1.48
		B,C,D		3.2	150-170	27-28		15-20	0.97-1.52
Low	PA	A	120-150	2.5	60-80	22-23	DC/(+)	15-30	0.21-0.59
		B,C,D		3.2	80-100	23-24		30-50	0.18-0.38

Parameter settings were based on the experience and the limits of achieving joints meeting the requirements of technical supervision. Edges of the plates were prepared before welding. Parameters of the joint preparation design are presented in Figure 4.

The obtained joints were subjected to strength and metallographic tests to confirm the correctness of weldments mechanical properties. An exemplary microstructure of the joint is presented in Figure 5.

The microstructure of the S1110 alloy is characterized by a typical martensitic structure due to the change in the chemical composition and the production process. Inclusions of high-temperature carbides are visible. An example of the microstructure is presented in Figure 3.

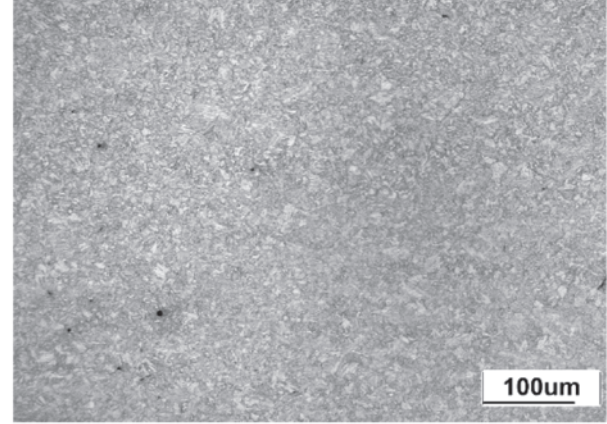


Fig. 3. Martensitic microstructure of the S1100 steel

Method 111 (MMA) was used in the welding of the specimens, and it is the most commonly used method for assembly work. It consists of striking the arc and melting the material with a hot-melted electrode. During the melting of the electrode, the cover is mixed with the connected material and provides a gas shield for the liquid weld pool and is the source of elements that enrich the composition of the weld. Weldments were made according to specifications of the technological parameters.

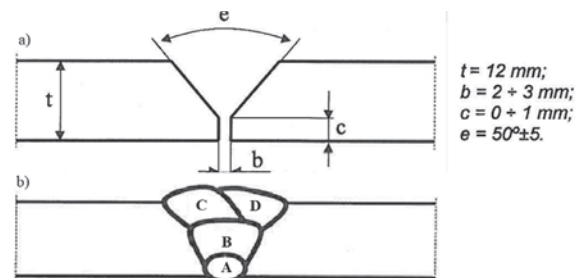


Fig. 4. Joint design: a – plate preparation, b – layers layout

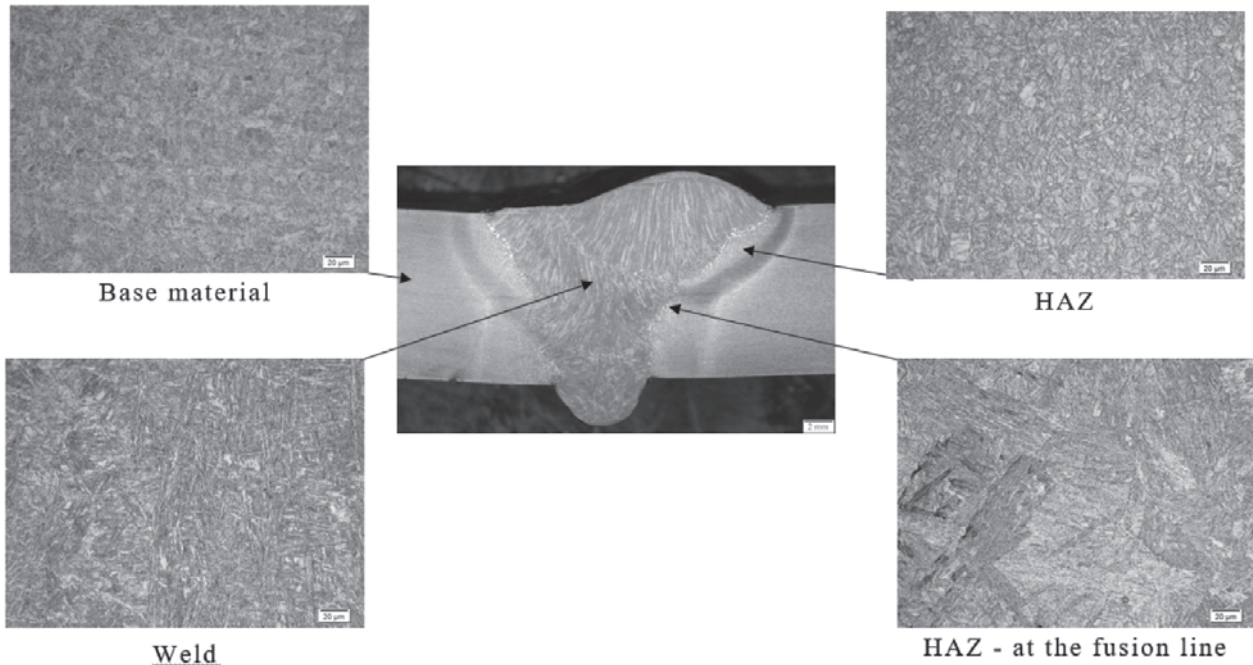


Fig. 5. Weld zones microstructure

The microstructure of the S1100QL base material consists of tempered martensite. The welds are dominated by fine-grained martensite, and the areas of the bainitic structure are also visible. Martensite fragmentation is higher closer to the weld face and in the areas of overlapping welds.

In the heat affected zone (HAZ), the area of grain growth near the martensite-bainitic fusion line can be distinguished. In the place of the influence of heat cycles of overlapping welds, the HAZ has a coarser character and the zone is wider. In this case, there is also a tendency to form structures with martensitic islands at the transition from the heat affected zone to the base material. Observed weld asymmetry results from welding technology (sequence of runs).

3. Fatigue tests

Fatigue tests were performed using a hydraulic testing machine equipped with force and displacements measurement systems. Specimens were subjected to the cyclic loading. The asymmetry coefficient for all of the performed tests was $R = -1$. Fatigue properties were obtained for welds and the base material. The shape and dimensions of the specimens are presented in Figure 6. In the case of the base material, the dimensions of the specimens were identical and did not contain weld geometry.

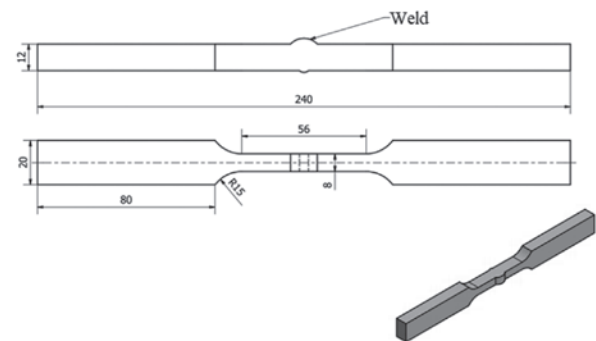


Fig. 6. Specimen shape and dimensions

Results of the fatigue tests were presented in the form of S-N Wöhler characteristics [12].

$$\sigma_a = A + m \log N_f \quad (1)$$

where: N_f – number of cycles, σ_a – nominal stress amplitude, A , m – coefficients of regression model.

Base material results are presented in Figure 7. Results of the fatigue testing performed for weldments are presented in Figure 8. Fatigue life obtained by the specimens is much lower compared to the base material. The influence of welding parameters on fatigue life of the samples is relatively small, and, at this step of the research, the phenomena require more testing. Due to the number of tested samples in combination with the relative repeatability of results falling within the standard spreading band equal to three for fatigue tests,

fatigue characteristics presented in Figures 7 and 8 were extended beyond the regions of the stress state, which were included in the research.

Initiation of the fatigue cracks was observed in the root side of the weldments. Example cracks are presented in Figure 9.

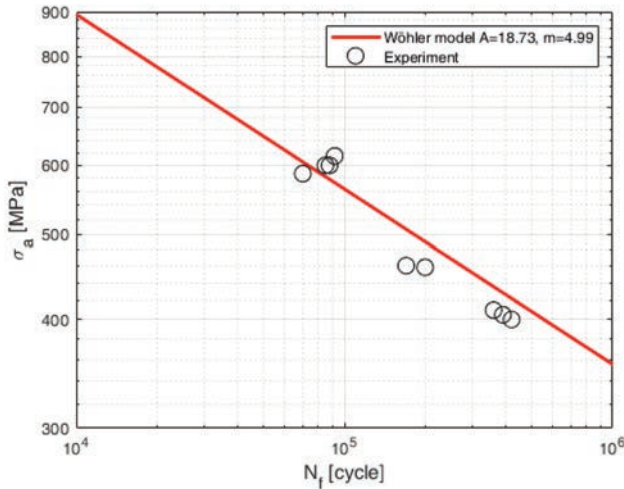


Fig. 7. Results of the fatigue tests of the base material

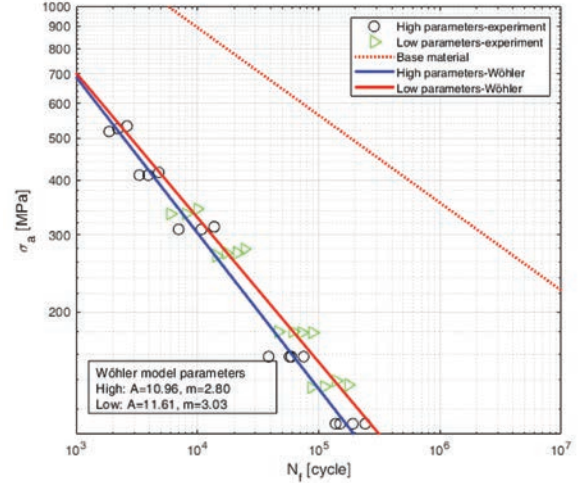


Fig. 8. Results of the fatigue tests of the welded specimens

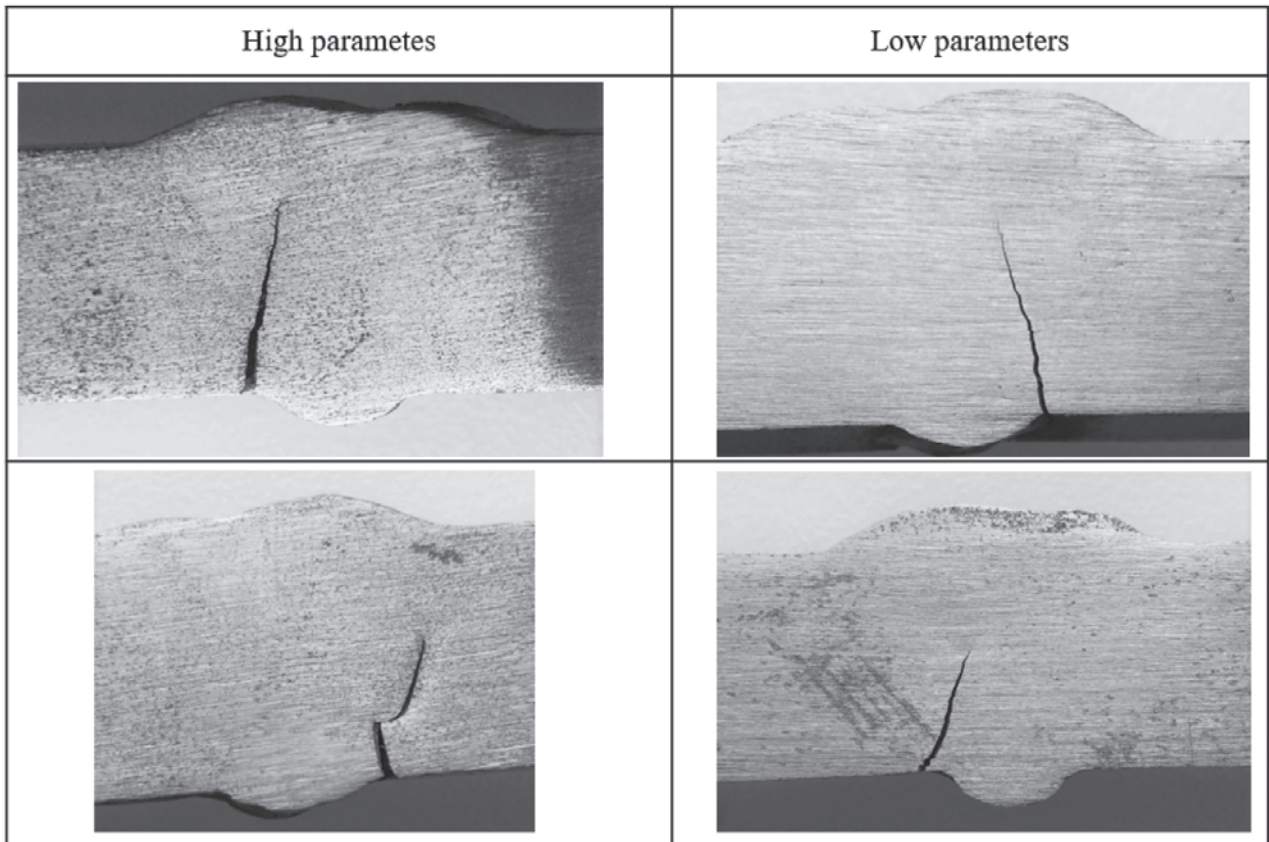


Fig. 9. Fatigue cracks in the specimens

4. Effective notch stress method

In the fatigue strength assessment by the effective notch stress (ENS), the stress value in the local profile of the weld is taken into calculations. In this method, the shape of the weld is replaced by the effective notch root radius (1 mm for structural steels with plate thickness

higher than 5 mm) [13]. In the presented research, the weld profile was created on the base of the microstructure observations. Maximum local stress values in the notch were obtained by FEA. The weld geometry model, mesh, and results are presented in Figures 10–11. The linear elastic material behaviour model was used in the analysis. Strength properties were defined in accordance with Table 1.

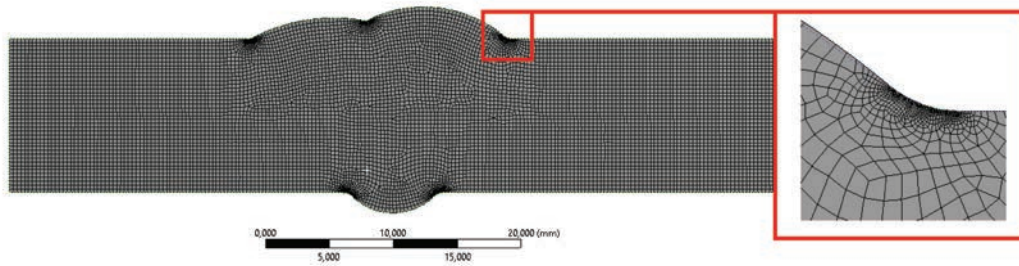


Fig. 10. FEM model of the weldment

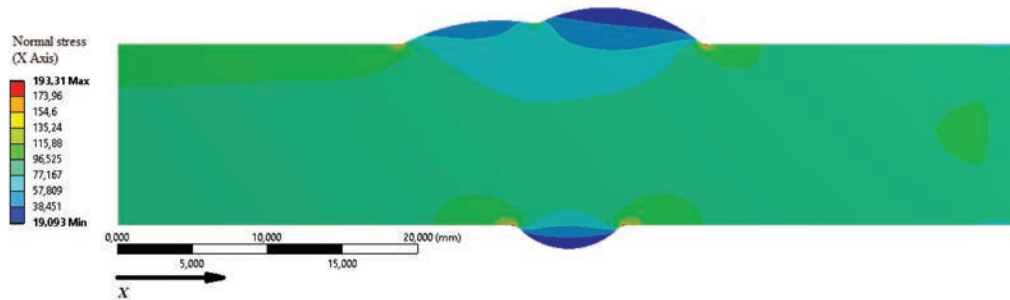


Fig. 11. Results of the calculations, normal stress distribution

The result from the calculations can be used to evaluate the fatigue life of weldments. Comparisons between fatigue lives calculated on the base ENS method and base material fatigue data are presented in Figure 12. The results of the calculations do not fit experimental data and cannot be used in design calculations.

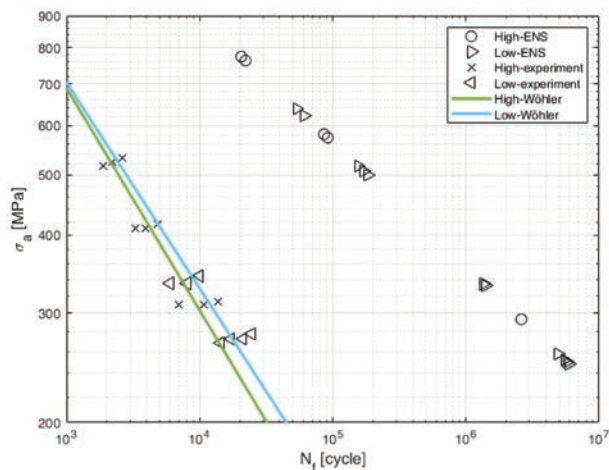


Fig. 12. Results of the ENS calculations and experimental data

Conclusions

The following conclusions and observations were made on the basis of the conducted research:

- Fatigue tests performed on two groups of specimens made of S1100QL steel showed relatively small differences in the obtained results for low and high welding parameters. The phenomena require further tests and investigations.
- Fatigue cracks propagated in all samples from the root of the weld (D weld run side – Figure 4), which may result from the asymmetrical weld.
- The fusion welding process decreases the fatigue life of the S1100 steel.
- Fatigue life obtained by means of ENS calculations does not correspond to the experimental characteristics of joints. In the case of the used joint configuration and load, the method cannot be used to assess fatigue life.
- The phenomenon of fatigue in welded joints from UHSS requires further research. From the perspective of the application of this type of materials in engineering constructions, it is reasonable to look for a computational algorithm that allows one to design the durability of connections in various load conditions.

References

1. Kowalski M.: Identification of fatigue and mechanical characteristics of explosively welded steel – titanium composite. *Frattura ed Integrità Strutturale*, 2017, 42, pp. 85–92, DOI: 10.3221/IGF-ESIS.42.10.
2. Łagoda T., Biłous P., Blacha Ł.: Investigation on the effect of geometric and structural notch on the fatigue notch factor in steel welded joints. *International Journal of Fatigue*, 2017, 101, pp. 224–231, DOI: 10.1016/j.ijfatigue.2016.09.006.
3. Mikkonen P., Björk T., Skriko ja Niko Tuominen T.: Ultralujien terästen ominaisuudet lopputuotteeseen osaavan suunnittelun ja valmistuksen avulla. *Hitsaus Trknikka*, 2017, 1, pp. 26–30.
4. Kujanpää V.: *Properties of joints produced by hybrid laser-arc welding*. In: Olsen F.O. (ed.): *Hybrid Laser-Arc Welding*. Woodhead Publishing, 2009, pp. 106–126.
5. Kah P., Pirinen M., Suoranta R., Martikainen J.: Welding of Ultra High Strength Steels. *Advanced Materials Research*, 2014, 849, pp. 357–365, DOI: 10.4028/www.scientific.net/AMR.849.357.
6. Pijpers R.J.M., Kolstein M.H., Romeijn A., Bijlaard F.S.K.: Fatigue experiments on very high strength steel base material and transverse butt welds. *Advanced Steel Construction*, 2009, 5(1), pp. 14–32.
7. Möller B., Wagener R., Hrabowski J., Ummehofer T., Melz T.: Fatigue Life of Welded High-strength Steels under Gaussian Loads. *Procedia Engineering*, 2015, 101, pp. 293–301, DOI: 10.1016/j.proeng.2015.02.035.
8. Goss C. Marecki P.: Fatigue Test Welded Joints Steel S960QL. *Materials Science Forum*, 2012, 726, pp. 93–99, DOI: 10.4028/www.scientific.net/MSF.726.93.
9. Hensel J., Nitschke-Pagel T., Tchoffo Ngoula D., Beier H.-Th., Deflor Tchuindjang D, Zerbst U.: Welding residual stresses as needed for the prediction of fatigue crack propagation and fatigue strength. *Engineering Fracture Mechanics*, 2018, 198, pp. 123–141, DOI: 10.1016/j.engfracmech.2017.10.024.
10. Nowacki J., Sajek A., Matkowski P.: The influence of welding heat input on the microstructure of joints of S1100QL steel in one-pass welding. *Archives of Civil and Mechanical Engineering*, 2016, 16, pp. 777–783, DOI: 10.1016/j.acme.2016.05.001.
11. Guo H., Wan J., Liu Y., Hao J.: Experimental study on fatigue performance of high strength steel welded joints. *Thin-Walled Structures*, 2018, 131, pp. 45–54, DOI: 10.1016/j.tws.2018.06.023.
12. Łagoda T.: *Lifetime Estimation of Welded Joints*. Springer, 2008.
13. Hobbacher A.F.: *Recommendations for Fatigue Design of Welded Joints and Components*. 2nd ed., Springer International Publishing, 2016.

This article appeared in its printed version in Journal of Machine Construction and Maintenance. The electronic version is published in DEStech Publications, Inc., Lancaster, PA, 2019, Proceedings of FUTURE ENGINEERING CONFERENCE.

Beata NIESTEROWICZ*, Paweł DUNAJ, Krzysztof MARCHELEK

Faculty of Mechanical Engineering and Mechatronics, West Pomeranian University of Technology Szczecin, Poland

* Corresponding author: beata.niesterowicz@zut.edu.pl

MODAL ANALYSIS OF LOADER CRANE WITH VARIABLE CONFIGURATION

© 2019 Beata Niesterowicz, Paweł Dunaj, Krzysztof Marchelek

This is an open access article licensed under the Creative Commons Attribution International License (CC BY)

<https://creativecommons.org/licenses/by/4.0/>**Key words:** modal analysis, loader crane, FEM analysis.

Abstract: Paper presents a method of simplifications used over numerical studies on dynamic properties of a hydraulic loader crane. Simplification concerns hydraulic actuators and allows for a significant reduction in the time of building model and calculations. Modal analysis of a loader crane using the finite element method, for both complex and simplified models, was carried out. The modal analysis computation times for both models were compared. Next, the results obtained on the basis of simplified model were compared with the results of experimental studies.

Analiza modalna żurawia przeładunkowego o zmiennej konfiguracji**Słowa kluczowe:** analiza modalna, żuraw przeładunkowy, analiza MES.

Streszczenie: W pracy przedstawiono metodę uproszczeń stosowanych w badaniach numerycznych nad właściwościami dynamicznymi żurawia hydraulicznego. Uproszczenie dotyczy siłowników hydraulicznych i pozwala na znaczne skrócenie czasu budowy i obliczeń modelu. Przeprowadzono analizę modalną żurawia za pomocą metody elementów skończonych zarówno dla pełnych, jak i uproszczonych modeli. Porównano czasy obliczeń analizy modalnej dla obu rodzajów modeli. Następnie porównano wyniki uzyskane na podstawie uproszczonego modelu z wynikami badań eksperymentalnych.

Introduction

Loader cranes are devices of wide application in various areas of transport. From the point of view of their structure, they can be classified as manipulators. The growing demand and simultaneously increasing functional requirements have led to constant improvement of their construction. As a result, they have become more complex and sophisticated. In the case of such structures, accurate prediction of problems related to time varying loads at the design stage is of significant importance.

One of the methods to predict the dynamic behaviour of such structures is the finite element method. However, the fact that dynamic properties of loader cranes change with their configuration, a new model for each configuration should be constructed. For models of such complexity, it is ineffective in terms

of calculations time. Therefore, modelling methods that allow a significant reduction of model order while maintaining the high accuracy are sought.

In this paper, a simplified model of a loader crane hydraulic actuator is proposed. Modal analysis of a loader crane using the finite element method using full and simplified actuator models was carried out. All analyses were conducted in Midas NFX. This was the basis for the influence of simplifications comparing accuracy and model order. In the first part, analysis of a simple model of loader crane with only two rotational joints was conducted. The computational times for the structure with the actuator modelled in a classical way and for the structure with the substitution in place of actuator model were compared. Based on these results, it was concluded that used simplifications has a negligible effect on the results. Therefore, in the second part of the work, a model of crane was built that consisted of six translational joints. For this structure, all of the actuators

were modelled in a simplified way. The obtained results were then compared with the results of experimental studies.

1. Research problem

Loader cranes are a very popular subject of scientific research in many aspects. In paper [1], the authors compiled a lot of works related to the study of the dynamics and control of cranes. They specified three types of these mechanisms: gantry, rotary, and boom cranes. Truck cranes generally consist of booms with a rotary basis. The other mentioned aspect is the way of modelling their load; it could be modelled as a lumped mass or a distributed mass. The difference in both approaches in terms of mathematics is presented in paper [1].

While modelling a truck crane, all subsystems influencing its operation should be considered. Paper [2] presents a universal mathematical model that considers complex interaction between the elements of dynamic system. There were specified five main subsystems that determine the truck loader working conditions: supporting structure, base surface, basic machine (basis), loader crane construction, and actuating elements. The identification of the elastic support system has been presented in [3]. That consisted in the determination of spring constants replacing the flexible carrier system. The values of these elastic constants were determined based on the solution of the problem of optimization and experimental modal analysis. The other works present the issue of interactions between mechanical and hydraulic system of loader crane [4] or interaction with operator [5] and the environment [6, 7].

Loader cranes, during operation, are exposed to very high loads related to dynamic forces. These forces of various origins could cause a loss of stability or a decrease in accuracy at the end-point. The former was studied both in terms of structural [8,9] and dynamic stability [10, 11]. The other research on dynamic properties of loader cranes concerned tip over stability of mobile boom cranes [12]. The latter could be caused by stopping the movement of flexible manipulator that makes residual vibrations occur. Numerical and experimental studies on vibration control of single link flexible manipulators with payloads were presented in [13].

Although there are many works addressed to issue of loader cranes, dynamic analysis of structure is one of the most valuable. There are papers which consider analytical modelling of dynamic properties such as mode shapes and natural frequencies. The most popular method of numerical modelling of dynamic properties is the finite element method. Free vibration analysis of truck cranes and studies on changes in the frequency of vibration for different radii of the crane and its load

were presented in [14]. Paper [15] presents the results of numerical and experimental analysis of mode shapes and eigenvalues of the telescopic platform with 5 booms.

There are papers which present the results of experimental modal analyses of cranes. In [16], the authors received eigenvalues and mode shapes of a full-scale crane, and in [17] for smaller, laboratory one. Due to multiple flexible links, there are many translational contacts, which change in various configurations, so creating a full model of crane is very time consuming and it take a long time to solve. Authors in paper [18] present an efficient model by using the assumed modes method with consistent kinematics and suggest that using a low-order dynamic model is sufficient.

The description of the variable-configuration loader crane dynamic properties can be represented by a set of models corresponding to the distinguished configuration options associated with the characteristic points of the workspace. There can be a significant number of such distinguished variants; therefore, the dynamic model of the crane should be simplified as much as possible to reduce the building and computational time.

In the presented paper, a method of loader crane model reduction by replacing hydraulic actuators by substitute elements is presented. This simplification enables shortening both the time of building the model and solving. Calculations were carried out on Hiab XS 111 HI DUO, which was presented in Fig. 1.

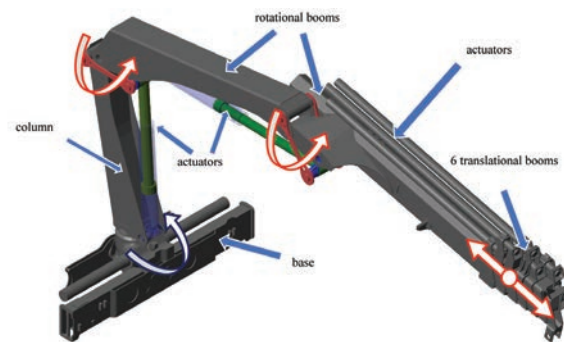


Fig. 1. Hiab XS 111 HI DUO structure

2. Modelling hydraulic actuators with FEM

The finite element method is the most common approach of modelling dynamic properties of loader cranes. It assumes the replacement of all solid parts and liquids with adequate finite elements. Structural elements like booms or columns can be modelled relatively easily using solid or beam finite elements. However, due to phenomena occurring in hydraulic oil, modelling hydraulic cylinders is a rather problematic task.

Loader cranes usually contain several hydraulic cylinders that control the movement of its individual components. In the conventional modelling approach,

the geometry of hydraulic cylinder (including hydraulic oil located in it) should be divided into a deliberate mesh of finite elements with appropriate properties and parameter values. Such an approach results in the necessity of building an actuator model with a significant number of degrees of freedom; moreover, each change in configuration, forces model re-discretization.

Therefore, a simplified model of the actuator was proposed, which does not require re-discretization but only changes in the values of the parameters that describe it. Simplifications consist in replacing the actuator model with an equivalent stiffness ROD

element and inertia elements, which depend on the actuator configuration. The concept of model simplifications is presented in Fig. 2.

The area of fixing the cylinder and piston to the construction was modelled with rigid elements, while the rod element and the mass element were stretched over their whole length. The rigid elements have been fixed in the way to allow the arms to rotate, while the parameters of the mass elements were based on the weight distribution related to the mutual configuration of individual hydraulic cylinder elements.

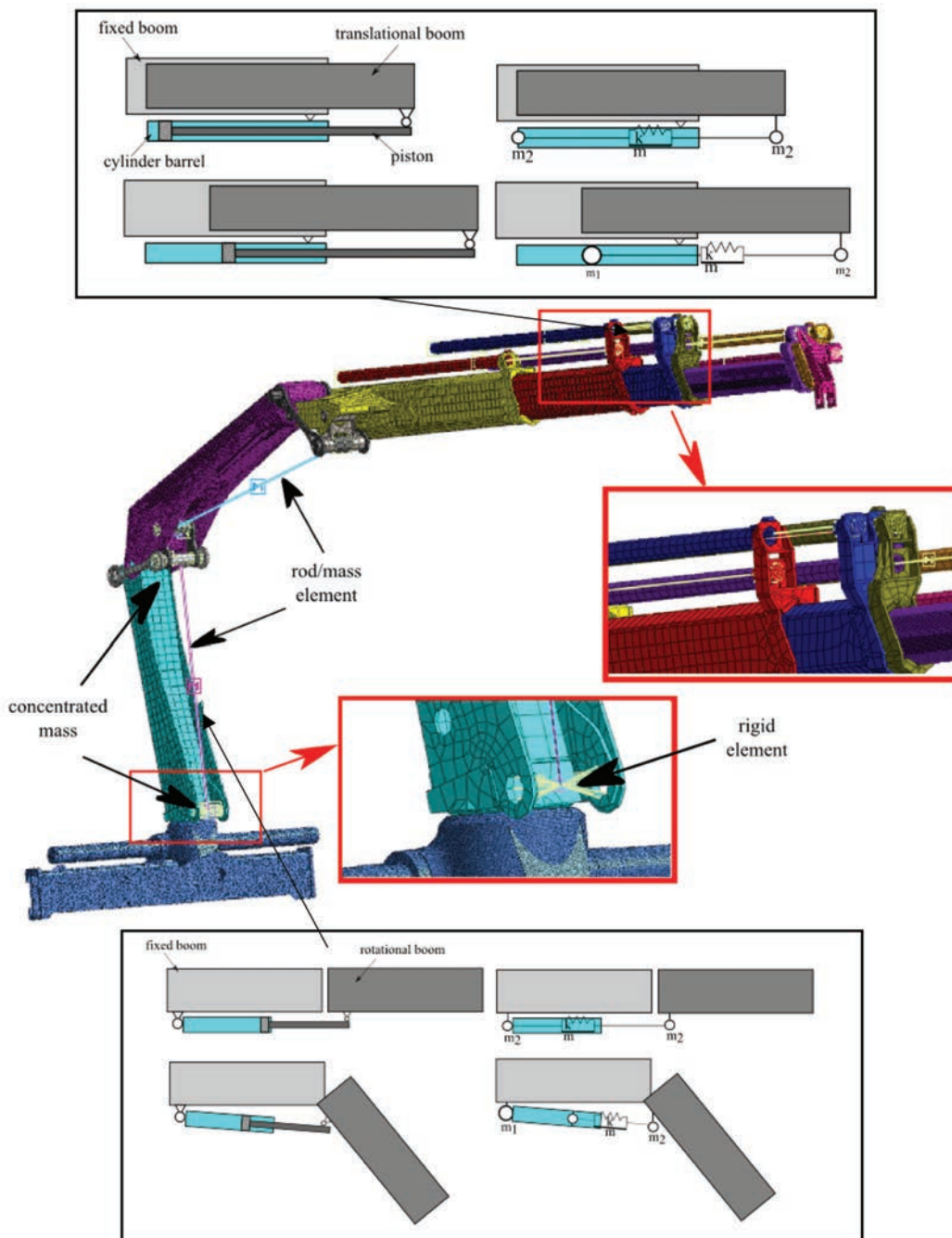


Fig. 2. The idea of actuator model simplifications

To determine the equivalent stiffness of the ROD element, the main factors affecting the stiffness of a hydraulic cylinder like the stiffness of the hydraulic oil k_o , the piston rod k_R , and cylinder k_C were considered. Due to the fact that, in the analysed crane structure, hoses were not flexible, its stiffness was omitted. Therefore, the equivalent stiffness the k of the ROD elements can be expressed as follows:

$$\frac{1}{k} = \frac{1}{k_o} + \frac{1}{k_R} + \frac{1}{k_C} \quad (1)$$

where: k_o – stiffness of the hydraulic oil; k_R – stiffness of the piston; k_C – stiffness of the cylinder.

According to the literature [19], the stiffness of the hydraulic oil contained in the cylinder (5) is composed of the stiffness of the oil in the chamber from the side of the piston and in the chamber from the side of the head, and it can be expressed as follows:

$$k_o = B \left(\frac{A_1}{V_1 + V_{L1}} + \frac{A_2}{V_2 + V_{L2}} \right) \quad (2)$$

where B – elastic modulus of the oil, $A_{1,2}$ – the effective area the head chamber (1) and the rod chamber (2); $V_{1,2}$ – the effective volumes, $V_{L1,L2}$ – fluid line volumes.

The basic parameter of hydraulic oil is its elastic modulus B described by Equation (3). For the most commonly used hydraulic fluids and at a normal temperature (around 20°C), the elastic modulus B is close to the value of $B_1 = 1500$ MPa [20]. However, it is important that the value of this parameter depends on its properties (e.g., aeration) and working conditions. Its value decreases with the increase of the temperature $a_{\Delta t}$, and in the case of air admixture in oil, but slightly increases with the pressure increase $a_{\Delta p}$, and it can be expressed as follows:

$$\frac{1}{B} = \frac{1}{B_1(1 + a_{\Delta p} + a_{\Delta t})} + \frac{\varepsilon}{P} \quad (3)$$

where: ε – is an oil aeration coefficient and P is the absolute pressure increased by pressure changes in chambers.

The stiffness of the piston rod results from the fact that it is a cylindrical bar, so its axial rigidity can be calculated from following formula:

$$k_R = \frac{EA_R}{L_R} \quad (4)$$

where: E – Young's modulus of piston rod material, A_r , L_r – cross-sectional area and length of a piston rod respectively. The stiffness of a cylinder is understood

as both the stiffness associated with its extension and deformation, and it can be expressed as follows:

$$k_c = \frac{E_B A_c}{2L_c} \cdot \frac{1}{\lambda_c + \nu_b} \quad (5)$$

where: E – Young's modulus for the cylinder barrel, A_c , L_c – cross-sectional area and length of the cylinder barrel, respectively, γ_c – expansion coefficient, ν_b – is the Poisson ratio for cylinder barrel.

In order to pre-check the correctness of the suggested simplification, computational analyses were carried out for a simple three-boom model with two actuators (Fig. 3).

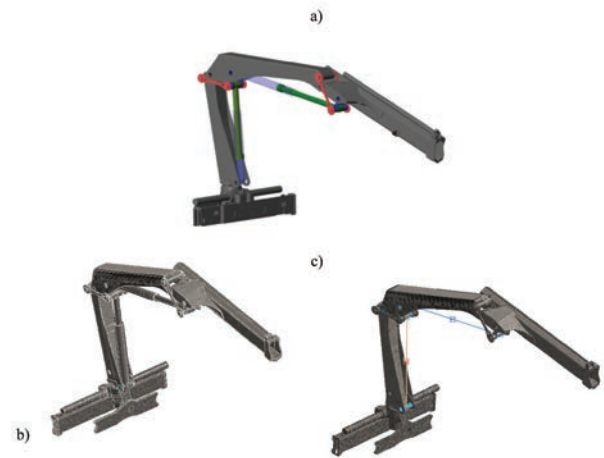


Fig. 3. Geometry (a) and discretized model of a simple tree-boom, b) full model, c) simplified model

The tests were carried out for two variants. In one of them, the actuators were modelled using the classical approach. In the second, the actuators were replaced by presented substitute elements, choosing the values of their parameters, respectively. For such prepared models, a modal analysis was carried out, which resulted in the natural frequency of the crane for both variants. The values of the first five frequencies are presented in Table 1.

Table 1. Natural frequencies comparison between full and simplified model

Full FEM model	Simplified FEM model	Relative error
5.8 Hz	5.4 Hz	6%
7.9 Hz	8.2 Hz	4%
19.7 Hz	19.3 Hz	2%
20.8 Hz	21.8 Hz	4%
47.0 Hz	45.7 Hz	3%

Differences between the obtained eigenvalues for both variants differ by no more than 6%. Therefore, it can be concluded that applying the suggested simplification is justified.

Therefore, in this convention, a model was created for the entire crane, and then the obtained results were compared with the results from experimental research. For entire crane, there were conducted analyses in two configurations. In both configurations, two rotational booms were in the same angle, but in the first configuration, designated ‘min’, all translational booms were retracted, and, in the second – ‘max’ configuration – chosen booms were partially extracted (Fig. 4). Incomplete booms extraction was caused by the space limitations during experimental research.

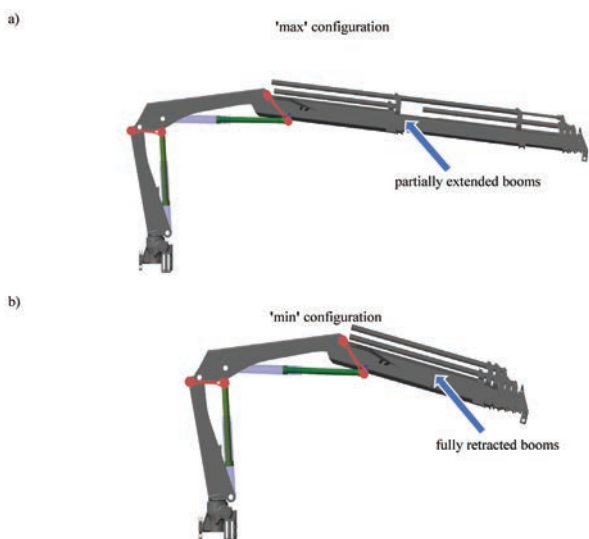


Fig. 4. Research object configurations: a) extracted ‘max’ and b) retracted ‘min’

4. Model Validation

To validate developed model, an experimental modal analysis in form of impact test was conducted for analysed variants. The experimental setup is presented schematically in the Fig. 5. Excitation was realized using a modal hammer with a 1.5 kg head mass. To obtain spatial mode shapes, the structure was excited at the end of the telescopic boom in three orthogonal directions. The response of the structure was measured using PCB 393A03 accelerometers, due to their high sensitivity level and accurate signal representation at the low frequency range. The experiment was performed using Siemens Testlab software and Scadas III hardware and included data processing, monitoring power, spectral density, and coherence functions. The detailed procedure was presented in [16].

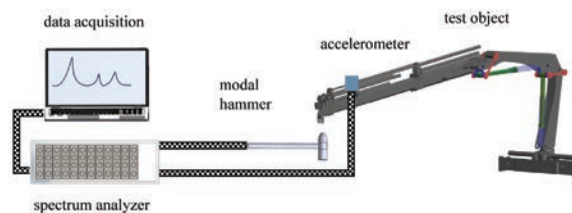


Fig. 5. Experimental setup

On the basis of determined frequency response functions, the modal model was built using a Polymax algorithm. The estimation process was supported by the stabilization diagram interpretation. Obtained values of natural frequencies are presented and compared by δ ratio with FEM model results in Table 2.

Table 2. Comparison of natural frequencies obtained from model and experiment for both variants

Mode number	Variant „max”			Variant „min”		
	Experiment	FEM analysis	δ	Experiment	FEM analysis	δ
1	0.92 Hz	0,87 Hz	4%	1.93 Hz	1.98 Hz	3%
2	1,41 Hz	1,34 Hz	7%	3.09 Hz	3.42 Hz	11%
3	4.87 Hz	5.21 Hz	1%	7.11 Hz	6.97 Hz	2%
4	7.26 Hz	7,20 Hz	1%	9.58 Hz	9.97 Hz	4%
5	13,67 Hz	14,26 Hz	4%	13.29 Hz	12.66 Hz	5%

$$\delta = \frac{|f_{iFEM} - f_{iEXP}|}{f_{iEXP}} \cdot 100\% \quad (6)$$

where f_{iFEM} is sequent frequency from FEM analysis, and f_{iEXP} is sequent frequency from experimental research. Comparisons of the first mode shapes are presented in Fig. 6.

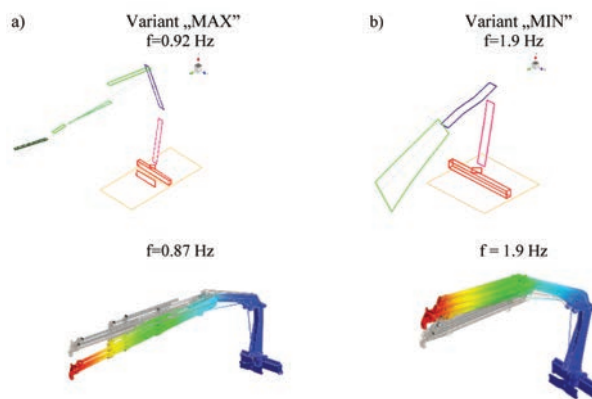


Fig. 6. Comparison of first mode shapes for both variants: a) “MAX” variant, b) “MIN” variant

Conclusions

The dynamics of loader cranes can be represented by a set of configurable models. In the classical FEM method, for each configuration, re-discretization is required. The presented method of modelling allows conducting analyses in various configurations on the same mesh. The use of simplified elements in place of hydraulic cylinders allows one to shorten the time of the model building, as well as reduce its dimensionality and thus the time of calculations. Searching for such simplifications in the case of reconfigurable structures, for which a new model needs to be built for each configuration, is particularly reasonable. Owing to the shortening of the calculation time, it is possible to perform a computational analysis of a larger number of configurations in order to obtain the most complete description of the dynamic properties of the considered crane. Based on the results presented in the paper, it can be concluded that, despite the simplifications used, a high model compliance with the experimental results was obtained. The greatest difference in frequency values between experimental and numerical one is 7%, and the mean value of disagreement is 4%. However, it should be taken into account that a very important step is an appropriate selection of the equivalent parameters of the mass and stiffness elements of an actuator.

References

1. Abdel-Rahman E.M., Nayfeh A.H., Masoud Z.N.: Dynamics and control of cranes: Review. *Journal of Vibration and Control*, 2003, 9(7), pp. 863–908.
2. Lagerev I.A., Lagerev A.V.: Universal Mathematical Model of a Hydraulic Loader Crane. *IOP Conference Series: Earth and Environmental Science*, 2018, 194, 032015.
3. Cekus, D.: The identification of the elastic support system of the laboratory truck crane. *Machine Dynamics Research*, 2014, 38(2), pp. 5–15.
4. Pawełko P., Szymczak B.: Simulation of interactions between mechanical and hydraulic system of loader crane. *Modelowanie Inżynierskie*, 2016, 29(60), pp. 58–66 [in Polish].
5. Herbin P., Pajor M.: *ExoArm 7-DOF (Interactive 7-DOF Motion Controller of the Operator Arm) Master Device for Control of Loading Crane*. In: Hamrol A., Cizak O., Legutko S., Jurczyk M. (eds): *Advances in Manufacturing. Lecture Notes in Mechanical Engineering*. Springer, Cham, 2018. pp. 439–449.
6. Miądlicki K., Pajor M., Saków M.: Ground Plane Estimation from Sparse LIDAR Data for Loader Crane Sensor Fusion System. In: *22nd International Conference on Methods and Models in Automation and Robotics (MMAR), Międzyzdroje (Poland), 28–31 August 2017*. IEEE, 2017.
7. Miądlicki K., Pajor M., Saków M.: Real-time Ground Filtration Method for a Loader Crane Environment Monitoring System Using Sparse LIDAR Data. In: *International Conference on INnovations in Intelligent SysTems and Applications (INISTA), Gdynia (Poland), 3–5 July 2017*. IEEE, 2017.
8. Kłosiński J., Janusz J.: Control of Operational Motions of a Mobile Crane under a Threat of Loss of Stability. *Solid State Phenomena*, 2009, 144, pp. 77–82.
9. Kacalak W., Budniak Z., Majewski M.: Crane stability assessment method in the operating cycle. *Transport Problems*, 2017, 12(4), pp. 141–151.
10. Towarek Z.: The dynamic stability of a crane standing on soil during the rotation of the boom. *International Journal of Mechanical Sciences*, 1998, 40(6), pp. 557–574.
11. Sochacki W.: The dynamic stability of a laboratory model of a truck crane. *ThinWalled Structures*, 2007, 45, pp. 927–930.
12. Rauch A., Singhose W., Fujioka D., Jones T.: Tip-over stability analysis of mobile boom cranes with swinging payloads. ASME. *Journal of Dynamic Systems, Measurement and Control. Transactions of the ASME*, 2013, 135(3), 031008–031008-6.
13. Malgaca L., Yavuz S., Akdag M., Karagülle H.: Residual vibration control of a single-link flexible curved manipulator. *Simulation Modelling Practice and Theory*, 2016, 67, pp. 155–170.
14. Geisler T.: Free vibration analysis of a crane support system of a DST-0285 truck crane considering changes in the system load configuration. *MATEC Web of Conferences*, 2018, 157, 03005.
15. Yucel A., Arpacı A.: Analytical and experimental vibration analysis of telescopic platforms. *Journal of Theoretical and Applied Mechanics*, 2016, 54(1), pp. 41–52.
16. Chodźko M., Dunaj P.: Experimental investigation on dynamic properties of loader crane. *Machine Dynamics Research*, 2016, 40(2), pp. 145–154.
17. Sochacki W.: An experimental modal analysis of the laboratory truck crane model. *PAMM*, 2004, 4(1), pp. 416–417.
18. Linjama M., Virvalo T.: Low-order dynamic model for flexible hydraulic cranes. *Proceedings of the Institution of Mechanical Engineers, Part I: Journal of Systems and Control Engineering*, 1999, 213(1), pp. 11–22.

19. Feng H., Du Q., Huang Y., Chi Y.: Modelling Study on Stiffness Characteristics of Hydraulic Cylinder under Multi-Factors. *Journal of Mechanical Engineering*, 2017, 63(7–8), pp. 447–456.
20. Koralewski J.: Influence of viscosity and compressibility of aerated oil on determination of volume losses in variable displacement piston

pump. *Napędy i sterowanie*, 2013, 11, pp. 118–132 [in Polish].

This article appeared in its printed version in *Journal of Machine Construction and Maintenance*. The electronic version is published in DEStech Publications, Inc., Lancaster, PA, 2019, Proceedings of FUTURE ENGINEERING CONFERENCE.

Marek WYLEŻOŁ*

Faculty of Mechanical Engineering, Silesian University of Technology, Gliwice, Poland

*Corresponding author: marek.wylezol@polsl.pl

TOPOLOGICAL OPTIMIZATION IN MECHANICAL CONSTRUCTIONS – AN EXAMPLE OF APPLICATION

© 2019 Marek Wyleżoł

Topological optimization in mechanical constructions – an example of application

<https://creativecommons.org/licenses/by/4.0/>**Key words:** topological optimization, virtual modelling, constructing.**Abstract:** The article will refer to an example of topological optimization applied to a typical constructional form of an exemplary technical object.

Topological optimization, in this case, is to reduce the mass of the element by removing the material that is not necessary to fulfil its objective function, resulting from specific design requirements and accepted criteria. The object form resulting from topological optimization is usually theoretical and presents only the optimal distribution of material in the design space. The development of the target construction form requires further modelling activities.

The presented topological optimization process was made using the Altair Inspire [1] system. While, the CATIA v5 [6] system was used for further modelling. Target constructions will be made taking into account two manufacturing technologies: (1) cutting from sheet metal, bending, and welding, and (2) generative technology (DMLS) [8]. All obtained functional models of the same object will be compared in terms of strength characteristics and the obtained weight loss.

Optymalizacja topologiczna w konstrukcjach mechanicznych – przykład zastosowania

Słowa kluczowe: optymalizacja topologiczna, modelowanie wirtualne, konstruowanie.**Streszczenie:** Tematyka poruszona w artykule dotyczy opisu przykładu zastosowania optymalizacji topologicznej w odniesieniu do konwencjonalnej postaci konstrukcyjnej przykładowego obiektu technicznego.

Optymalizacja topologiczna – w rozpatrywanym przypadku – ma za zadanie zmniejszenie masy elementu poprzez automatyczne usunięcie tworzywa, które nie jest niezbędne do spełnienia jego funkcji celu, wynikającej z określonych wymagań projektowych i przyjętych kryteriów. Postać obiektu, będąca wynikiem zastosowania optymalizacji topologicznej, zwykle ma charakter teoretyczny i przedstawia jedynie optymalną dystrybucję tworzywa w przestrzeni projektowej. Opracowanie docelowej postaci konstrukcyjnej wymaga dalszych działań modelowych.

W artykule przedstawiono przykładowy proces optymalizacji topologicznej z użyciem systemu Altair Inspire [1]. Pozostałe prace modelowe wykonano z użyciem systemu klasy CAx – CATIA [6]. Podczas opracowania konstrukcji docelowej (już zoptymalizowanej) przedstawiono różne postaci konstrukcyjne z uwzględnieniem technologii ich wykonania. Pierwszy model wirtualny zaprezentowano jako wynik operacji wycinania z arkusza blachy, gięcia i spawania. Natomiast postać konstrukcyjna drugiego modelu wirtualnego jest dostosowana do wytworzenia z użyciem technologii generatywnej (technologia SLS) [8].

Opracowane modele tego samego obiektu porównano pod względem cech wytrzymałościowych oraz uzyskanego ubytku masy.

Introduction

Many mechanical objects have constructions of a conventional nature, which is often the result of their subordination to standard production technologies (and the construction [7] is the basis for the creation

of a given technical object). This approach often results in simplifying the construction (e.g., through the widespread use of generally available blanks) or its complete subordination to a given technological process. Such proceedings are often subordinated to economic conditions, i.e. the cost of producing a given

element cannot exceed a given price limit on which the profitability of production depends.

The author, using a fairly simple example, wants to show how a slightly altered approach to the design-manufacturing process can result in considerable savings in the use of the material, which is derived from the adopted method of construction, based on topological optimization [2, 4, 11], taking into account the weight minimization criterion and the use of two different technologies (one standard second advanced).

The above-described object (and precisely its virtual model) will be a typical technical holder, produced by machining and welding as standard.

It should also be mentioned that the author's area of interest is not the development of theoretical methods of optimization [3] from the mathematical point of view, but their applicability [9, 11]. The article concerns a simulation studies only (without producing of the target handles). The final verification testing of the optimized handles should be after their production on the test bench strength tests.

1. Topological optimization

The basis for further consideration in this article will be the realization of the construction process using topological optimization. Topological optimization is a type of mathematical method, which is a method based on finite elements. Thus, it is always realized with the use of computer-aided using specialized software. Its main purpose is to obtain the optimal distribution of the material forming the volume of the constructed object (and also its constructional form) so that, at the given boundary conditions and for the given load, its target form is optimal due to the adopted criteria. Thus, the goal of this procedure is to maximize the fulfilment of the objective function of a given technical object (e.g., the reduction of mass with unimpaired strength in relation to the initial model). In other words, topological optimization ensures an increase in the durability and safety of a given construction while reducing its mass.

A certain disadvantage of the algorithms implementing the optimization process is the creation of a topological form of optimized objects that are purely theoretical. Therefore, obtaining the correct construction and technological form requires further actions in order to give a real constructional form (usually realized by 3D modelling).

It should also be mentioned that topological optimization differs from other optimization methods used during construction. An example can be a topographic optimization, where only the placement and oversizing of predetermined structural elements is optimized (e.g., the number and location of reinforcing

ribs at their given shape, depending on load forces and boundary conditions).

2. Model of a technical holder as an example of technical object

The object that will be optimized in terms of topology will be a typical technical holder. This holder was originally made of three sheet metal elements and a piece of pipe (Fig. 1).

All components of the holder are connected by welding technology. For further consideration, it was assumed that the holder was made of austenitic stainless steel 0H18N9 (by other markings X5CrNi18-10, DIN 1.4301, AISI 304). Its computational weight is 700.5 g.

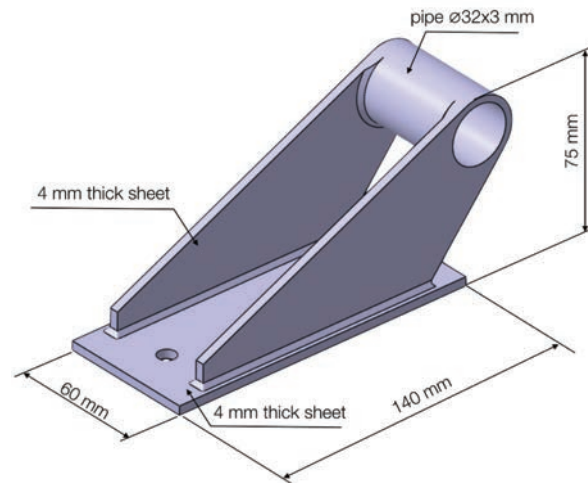


Fig. 1. Form and overall dimensions of the holder model

3. Software implementation of topological optimization

The holder model was virtually fixed rigidly with two sets of M8 bolts with washers. The bushing of the holder was laden with a static force of 1000 N (red arrows in Fig. 2), spread over the middle of its inner surface (load direction according to Fig. 2). All of the bushing and fragments of the model around the fastening bolt holes are left as non-optimization zones (grey colour in Fig. 2). The remaining part of the model is the “construction space”, which is subject to changes in the form as a result of the applied optimization (in Figure 2 shown as a brown colour).

As an optimization criterion, weight minimization was assumed, while maintaining a safety factor of 1.5 and maintaining a minimum wall thickness of 4 mm. All computational and optimization activities are performed using the Altair Inspire 2018 system [1].

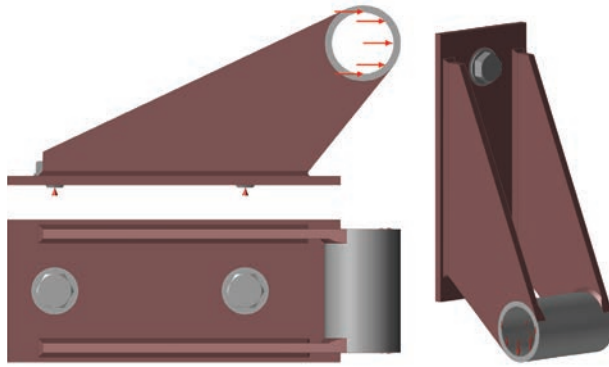


Fig. 2. Boundary conditions and load of the holder model

To maintain the correct reference point, the input model of the holder was subjected to a strength analysis (reduced stresses were taken into account, according to the von Mises hypothesis), according to these boundary conditions and the load. The results of this analysis (colour maps and scales of stress and displacements) are shown in Figure 3. As can be seen, the strength of the loaded holder is not large (the stress scale refers to the strength limit of the used material). This indicates, among other things, a large material allowance that causes an increase of mass and material use.

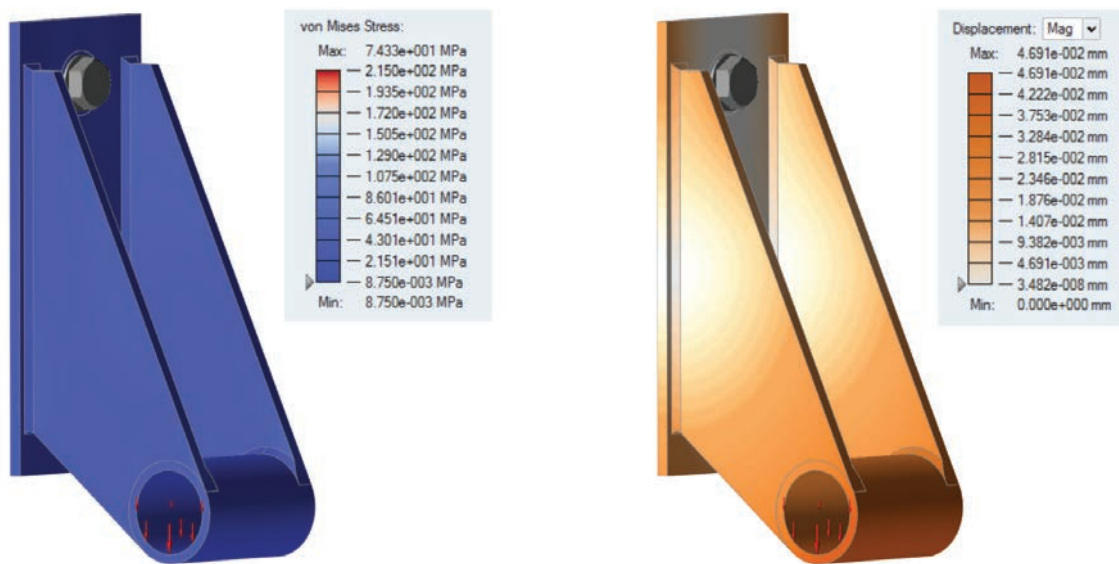


Fig. 3. Stress and displacements maps of the input model

Thus, the input model of the holder was subjected to topological optimization according to these guidelines. The result of this process is the theoretical form of the holder model (Fig. 4).

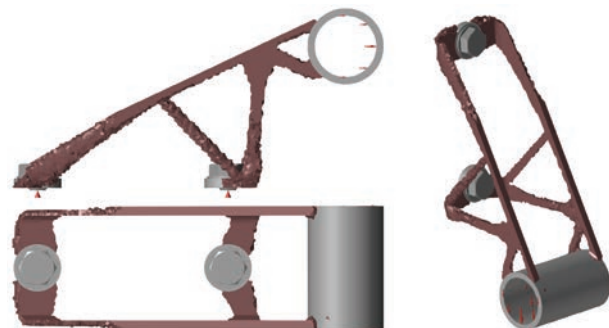


Fig. 4. Theoretical form of the optimized holder model

The obtained theoretical holder model was subjected to a strength analysis, according to identical boundary conditions and loads.

The results of this analysis (colour maps and scales of stresses, displacements and safety factor are visible in Figure 5, and the outline of the input holder model has been preserved in the background). We observe the increase in stresses and displacements, but the safety factor at a level of 1.8 has been preserved. However, there was a significant decrease in the mass of the holder. The computational mass is 211 g, which is a weight reduction of 30.12%.

As already mentioned, the models obtained as a direct result of the optimization process are only theoretical (although nowadays technologically feasible, for example, with the use of print 3D technologies [5, 10]); therefore, further modelling activities should refer to obtaining a constructional form but including production technology.

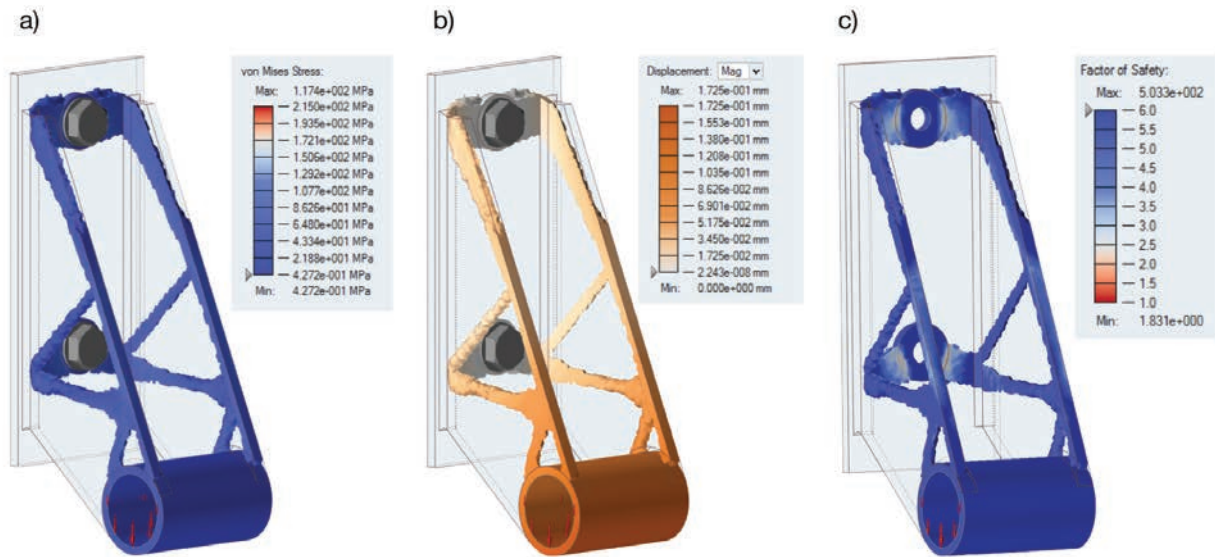


Fig. 5. Stress (a), displacements (b), and safety factor (c): Maps of the theoretical holder model after optimization (bolts view removed in “c” figure)

The next chapter will describe two different design forms for the holder model.

4. Construction models

The theoretical 3D model was used as the basis for the implementation of two models with designs adapted to make a real holder using two different technologies: conventional technology (sheet-metal working and welding) and generative technology – DMLS (Direct Metal Laser Sintering, i.e. selective sintering of metal powders) [10].

4.1. Sheet Metal Model

The sheet metal model (Fig. 6) was made of the same material as the input model, i.e. steel 0H18N9. The construction of the holder has been divided into two parts: a bracket made of 4 mm sheet metal and a bushing made of a pipe $\text{Ø}32 \times 3$ mm (the length of the pipe was slightly lengthened to obtain space for an additional fillet weld). The profile of the bracket has been applied to the sheet metal and then cut using cutting technology, e.g., water jet. Then, with the use of, e.g., press brakes, the bracket has been properly bent. The connection to the bushing was made using welding technology.

The virtual model was made using the Generative Sheet Metal Design module of the CATIA v5 system. The holder model was made in accordance with the all principles of sheet bending (the bending radius was considered, and the layout of the model was verified on a flat sheet of metal).

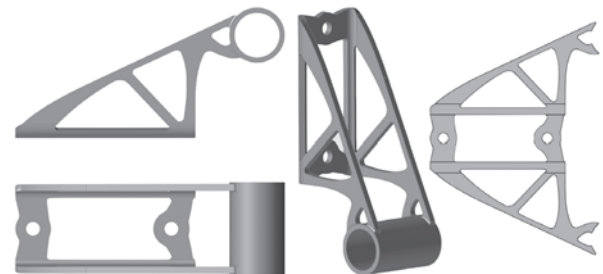


Fig. 6. Form of the sheet metal holder and pattern of the bracket (without the bushing)

4.2. 3D Printed Model

During the modelling of the holder designed to be made using DMLS generative technology, small form changes were made. They concerned mainly the decommissioning sharp edges (characteristic of the sheet metal cutting process).

There is a slightly changed geometric form of the holder base, which does not need to be an integral part of the whole (as in the case of sheet metal cutting and bending). Between the base and the both side walls, rounding with larger radii have been added, which significantly reduced the stresses in these places (Fig. 7).

3D print using DMLS technology must be done on a specific machine and using a specific material. Therefore, the EOSINT M270 printer was selected and the EOS StainlessSteel GP1 material [8]. EOS StainlessSteel GP1 material is supplied in the form of a steel powder. Its chemical composition corresponds to the standards of the USA 17-4 and 1.4542 X5CrNiCuNb16-4, and tensile strength (R_m) is 590 MPa.

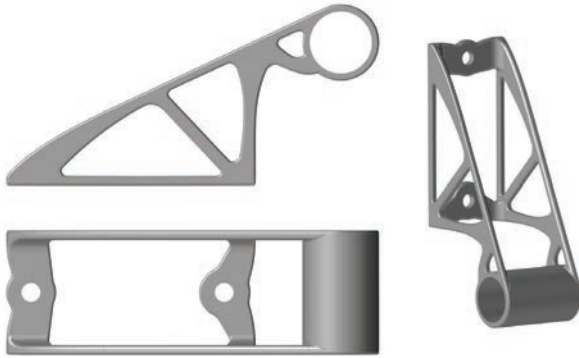


Fig. 7. Form of the 3D printed holder model

This type of steel is characterized by good mechanical properties and especially excellent ductility, which is widely used in many different fields of technology.

Importing the STL file theoretical holder model to the CATIA v5 system was done using the Digitized Shape Editor module. Other model activities were implemented using the Part Design module (the use of the solid modelling module was sufficient).

4.3. Comparison of Structural and Strength Characteristics of the Received Optimized Models

The strength properties of the models of the two holders are shown in Figures 8 and 9. As can be seen, the “printed” model is slightly more strenuous (increase in the maximum von Mises stress by 17 MPa and an increase in elastic deformation by 0.002 mm – Tab. 1). However, these values are so small that they can be omitted from the overall comparison. The more so that

the assumed safety factor in both cases is greater than the assumed 1.5 (high maximum values apply to areas not optimized – Fig. 8 and 9).

Both design models have a slightly higher mass compared to the theoretical model. This involves, among other things, the necessity of smoothing along the edge of the holder and the adaptation of the both models to the production technology. In the context of the sheet metal holder model, it comes with additional bending of the base bracket, elongation of the bushing and the addition of a weld. For the 3D printed handle model, the change of material is the most important change among others.

However, the weight difference between the two holder models is 20.77 g (weight reduction of 6.8%), in favour of the 3D printed model. This is already a noticeable value, especially if the number of such holders mounted on the exemplary technical object was significant.

Table 1. Mechanical parameters of the virtual models

	Mass [g]	Percentage of input mass [%]	Von Mises Stress [MPa]	Displacements [mm]
Input model	700.50	100	74.33	0.047
Optimized theoretical model	211	30.12	117.40	0.172
Optimized sheet metal model	300.58	42.90	128.80	0.135
Optimized 3D printed model	279.88	39.96	145.80	0.157

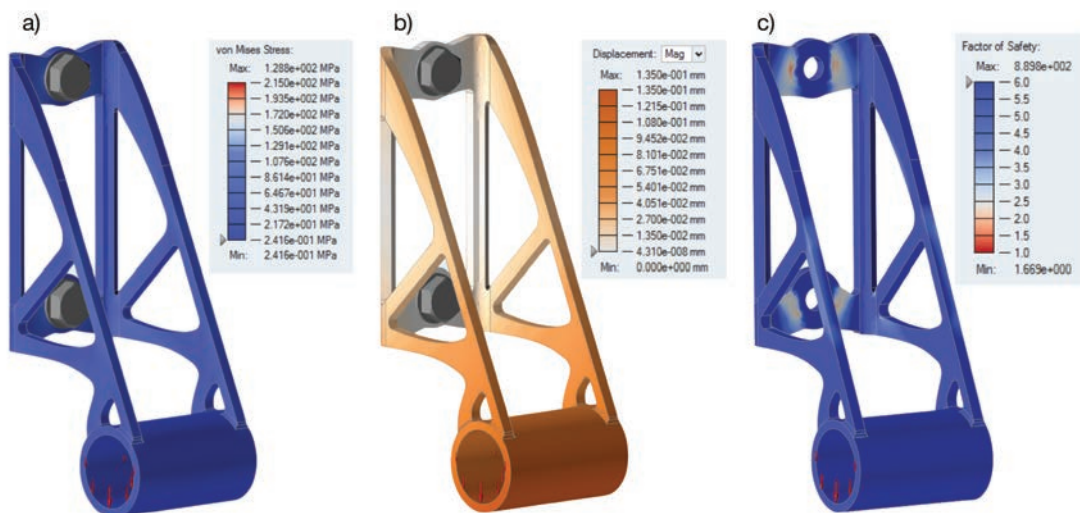


Fig. 8. Stress (a), displacements (b), and safety factor (c): Maps of the sheet-metal holder model

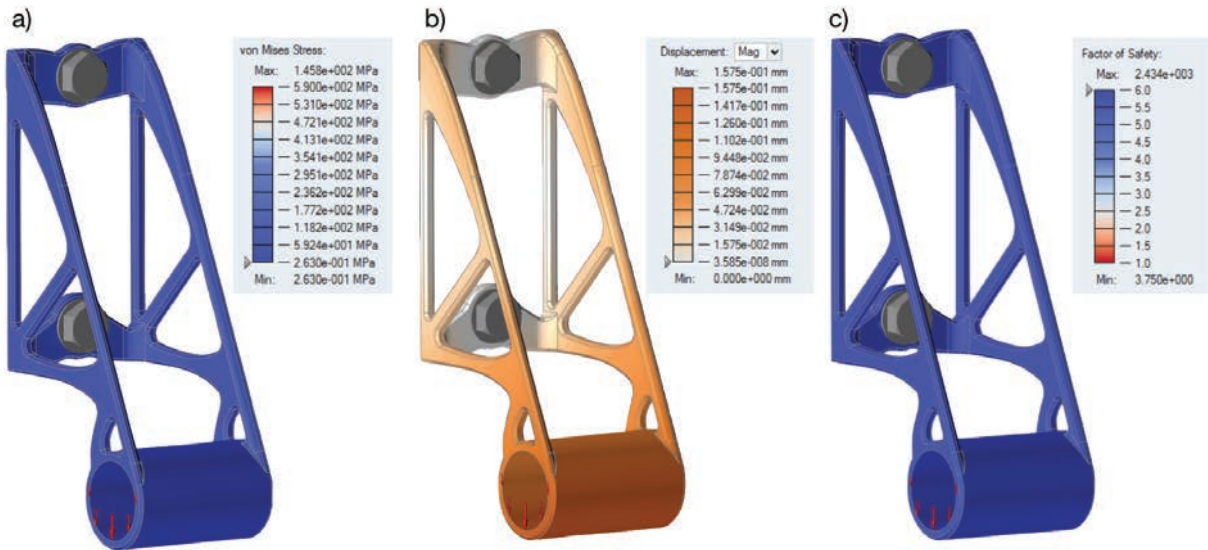


Fig. 9. Stress (a), displacements (b), and safety factor (c): Maps of the 3D printed model

The geometric forms of both optimized holder models are very similar to each other. For the end user, this can be even unnoticeable. However, the technologies of their production are extremely different. The first used technology can be called traditional, but the second one (generative 3D printing) is already a quite modern technology.

The choice of one of the above proposed technologies should be dependent on factors other than the minimization of the weight criteria.

In the case of a mass production need of such holders, it will undoubtedly be cheaper to manufacture the holders made of sheet metal. In relation to the input holder model, there will be a significant reduction in weight (weight reduction of 57.10%).

However, if the criterion of mass minimization (weight reduction of 60.04% – Tab. 1) is the most important for the constructor and the production is of unitary or low-serial character, the application of modern DMLS technology may be justified.

Of course, the used example of a holder as a technical object is quite simple as to the design, but also as to the manner of the load. In the case of multidirectional load (even static), the form of such a handle after topological optimization may take non-technological forms, taking into account conventional technologies. Then the only way out would be to use generative technology (3D printing).

Technological problems associated with the production of many objects with complex forms, which are the result of topological optimization were the main reason for inhibiting the progress in the construction of many objects that have preserved conventional forms.

Summary and conclusions

- Topological optimization should be already used at the beginning of the construction process as a method to assist the constructor in the selection of design features of technical objects.
- The resulting theoretical virtual model as a result of topological optimization should be the input to the further construction process and should be treated as the boundary condition of the final design form.
- When selecting optimization criteria, the problem should be analysed very carefully, especially in terms of boundary conditions and loads, because topological optimization leads to constructional forms tailored only to the adopted conditions.
- The design criterion adopted for topological optimization may be different from the criterion (criteria) adopted in further proceedings, e.g., the implementation of the manufacturing process.
- Generative manufacturing is generally suitable for the manufacture of any design form obtained as 3D model (virtual model), but the actual limitations may be the cost of production and the dimensions of the target object.
- Confirmation of the theoretical results obtained from virtual models should take place with the use of experimental studies conducted on the handles produced using the two mentioned technologies.

References

1. Altair: *Solid thinking*. [Online]. 2019. [Accessed 06 April 2019]. Available from: <http://www.solidthinking.com>

2. Bendsoe M.P.: *Optimization of Structural Topology, Shape and Material*. Berlin: Springer-Verlag, 1995.
3. Bendsoe M.P. Sigmund O.: *Topology optimization: theory, methods and applications*. Berlin: Springer-Verlag, 2003.
4. Chen J.: Shape optimization with topological changes and parametric control. *International Journal for Numerical Methods in Engineering*, 2007, 71(3), pp. 313–346.
5. Chlebus E.: *Innowacyjne technologie rapid prototyping – rapid tooling w rozwoju produktu*. Wrocław: Oficyna Wydawnicza Politechniki Wrocławskiej, 2003.
6. Dassault Systemes: *CATIA v5*. [Online]. 2019. [Accessed 06 April 2019]. Available from: <https://www.3ds.com/products-services/catia/products/v5/portfolio>
7. Dietrych J.: *System i konstrukcja*. Warszawa: WNT, 1985.
8. Drukarki3D: *Material data sheet – EOS-StainlessSteel-GP1*. [Online]. 2009. [Accessed 08 April 2019]. Available from: <https://drukarki3d.pl/wp-content/uploads/2015/09/karta-materialowa-EOS-StainlessSteel-GP1-ENG.pdf>
9. Patyk R., Kułakowska A.: Topologiczna optymalizacja konstrukcji na przykładzie widłaka wału przegubowego. *Autobusy. Technika, eksploatacja, systemy transportowe*, 2012, 13(5), pp. 380–386.
10. Siemiński P., Budzik G.: *Techniki przyrostowe. Druk 3D. Drukarki 3D*. Warszawa: Wyd. OWPW, 2015.
11. Tarnowski W.: *Optymalizacja i polioptymalizacja w technice*. Koszalin: Wydawnictwo Uczelniane Politechniki Koszalińskiej, 2011.

This article appeared in its printed version in Journal of Machine Construction and Maintenance. The electronic version is published in DESTech Publications, Inc., Lancaster, PA, 2019, Proceedings of FUTURE ENGINEERING CONFERENCE.

Vladimir ABRAMOV^{a*}, Anna ABRAMOVA^a, Giancarlo CRAVOTTO^b, Roman NIKONOV^a,
Vladimir SISTER^c, Adam MAZURKIEWICZ^d, Wojciech PIĄTKIEWICZ^d, Jerzy SMOLIK^d, Andrzej MAJCHER^d

^a Institute of General and Inorganic Chemistry, Russian Academy of Sciences, Russia

^b Department of Drug Science and Technology, University of Turin, Turin, Italy and Sechenov First Moscow State Medical University, Moscow, Russia

^c Moscow Polytechnic University, Russia

^d Łukasiewicz Research Network – Institute for Sustainable Technologies, Radom, Poland

* Corresponding author: novita@mail.ru

INDUSTRIAL APPLICATIONS OF HIGH-INTENSITY ULTRASOUND

© 2019 Vladimir Abramov, Anna Abramova, Giancarlo Cravotto, Roman Nikonov, Vladimir Sister, Adam Mazurkiewicz, Wojciech Piątkiewicz, Jerzy Smolik, Andrzej Majcher

This is an open access article licensed under the Creative Commons Attribution International License (CC BY)



<https://creativecommons.org/licenses/by/4.0/>

Key words: ultrasonic equipment, molten metal, enhanced oil recovery, waste water, antibacterial nanomaterials.

Abstract: In the last two decades, an increasing interest of academy and industry in the development of enabling technologies for process intensification has been paid. The main bottle neck for scientists and engineers to apply non-conventional technologies at industrial levels, such as high-intensity ultrasound, is the scaling up. Power ultrasound is proving to be a front-runner and offers a wide range of profitable applications. Although most examples reported by patents and scientific literature are not yet an industrial reality, few applications are recognised as the best available techniques for big scale production. Eloquent examples are reviewed in this article.

Przemysłowe zastosowania ultradźwięków o wysokiej intensywności

Słowa kluczowe: urządzenia ultradźwiękowe, stopiony metal, ulepszony odzysk oleju, ścieki, antybakteryjne nanomateriały.

Streszczenie: W ciągu ostatnich dwóch dekad wzrosło zainteresowanie środowiska naukowego i przemysłowego rozwojem technologii wspomagających intensyfikację procesów. Główną przeszkodą dla naukowców i inżynierów do stosowania niekonwencjonalnych technologii na poziomie przemysłowym, takich jak ultradźwięki o wysokiej intensywności, jest zwiększanie skali. Ultradźwięki oferują szeroką gamę dochodowych zastosowań i okazują się być dobrym rozwiązaniem. Pomimo że większość zastosowań zgłaszanych w formie patentów lub przedstawianych w literaturze naukowej nie istnieje w rzeczywistości przemysłowej, niektóre z nich uznawane są za najlepsze dostępne techniki dla produkcji na dużą skalę. Konkretnie przykłady zostały omówione w artykule.

Introduction

The course of any physicochemical process in a given system is determined by temperature, pressure, their changing rates, and the speed of relative movement of particular parts of the system. The kinetics of any chemical conversion can be affected by varying these parameters in the search for optimal conditions to enhance the reaction rate. This also occurs in materials manufacturing science and biological processes affecting the metabolism of micro- and macro-organisms.

Innovative technologies, such as lasers, plasma, electromagnetic fields, and high-energy particle fluxes, appreciably widen the range of means to control

physicochemical processes. Compared to natural processes and standard technologies, they may substantially affect heat and mass transfer and common parameters (temperature, pressure, speed of convective flows in liquids and structural imperfection movement in solids). The use of the latest scientific advances in the processes of physicochemical transformations could appreciably contribute to the development of efficient technologies of industrial interest. In this regard, one of the most emerging technologies is high-intensity ultrasound, because it is environmentally friendly and effective in a wide range of processes [1]. Power ultrasound is already exploited by the industry and several other uses have a real chance to be applied on a large scale.

1. Technical issues in the design of industrial ultrasonic equipment

The design of *ad hoc* tailored high-intensity ultrasound reactors and a rational scaling up of lab scale facilities is not a trivial task. The construction of new generators with the development of complex oscillatory systems and the design of suitable geometries for an efficient transmission of ultrasonic waves are now a matter of extensive research. The extent of this development largely determines the efficiency of high-intensity ultrasound applications in industrial processes in view of the electrical energy required. The transducers, power supply systems, radiators, and various systems for the measurement and control of acoustic parameters are part of such installations. Typically ultrasonic units include at least five blocks, namely, an electric ultrasonic generator, an electroacoustic transducer, a waveguide system, a technological load, and a control system.

Magnetostrictive and piezoelectric effects are the two phenomena exploited by electroacoustical transducers to generate ultrasonic waves. Depending on the type of the electroacoustic transducer, magnetic or electric fields induce elastic strains in electromechanically active materials. Magnetostriction is typical for ferromagnetics and ferrites. Magnetostriction is a change in the linear and volumetric dimensions of metallic bars made of specific alloy as a result of the interaction of an external magnetic field. Although only moderately efficient, these transducers are extremely robust and reliable enabling harsh working conditions. Currently, piezoceramic transducers are the most widely used in ultrasonic technologies. The piezoelectric effect consists in strain imposed on the transducer material by external electric fields. When the piezoceramic transducer operates under optimal conditions, its electroacoustical efficiency ranges from 90 to 98%.

Aiming to achieve a high level of efficiency, the ultrasonic units have to address the following two conditions [2, 3]:

1. The system should operate at or in the vicinity of its electric and mechanical resonance (the frequency of the electric current generated by the ultrasonic generator should match the frequency of the natural resonance of the electroacoustic transducer and the waveguide system).
2. There must be effective transmission of the vibrations through the contact area between the transducer and the waveguide system.

Experimental search of the optimal waveguide dimensions is complicated and time consuming. Nevertheless, aiming to simplify and speed up the procedure to get the best waveguide parameters, besides experimental work, a computational modelling

of these parameters can be performed. Modelling of resonance frequencies and waveguides geometry can be calculated by means of the finite-element method (i.e. by the commercially available COMSOL Multiphysics) [4]. This is a powerful interactive environment for modelling and calculating data that is based on partial differential equations (PDE) by the finite-element method. This software package expands the standard models which use one differential equation (application mode) and Multiphysics® Models for calculating inter-related physical phenomena. This method of calculation enables one to find the optimum shape and structure while avoiding the construction of test parts. This significantly accelerates the design of ultrasound devices and the selection of optimal processing modes.

2. Ultrasonic Action on Molten and Solidifying Metal

Ultrasonic action on molten and solidifying metal is one of the most technologically advanced ultrasonic technologies in the industry. Vibrational treatment leads to solid non-metallic and gaseous impurities removal from liquid metal and to structure refinement of the ingot in shape casting. The effect of ultrasound on the alloy structure can be summarized as follows [2, 3, 5–7]:

- Reduction of the grain size;
- Formation of equiaxed grains;
- Variation of phase distribution in terms of relative amounts, structure refinement, and mutual geometry;
- Improvement of material homogeneity; and,
- Uniformity improvement of the distribution of non-metallic inclusions.

Thus, ultrasonic treatment of molten and solidifying metals improves their mechanical properties of strength and plasticity. Ultrasonic treatment was industrially used for such metals as Al and Mg. Figure 1 shows a specific device for ultrasonic treatment of molten aluminium.

The insertion of high-power ultrasonic vibrations into molten metal leads to cavitation and acoustic streaming. Cavitation involves the formation, growth, pulsating and collapsing of tiny discontinuities or bubbles in the melted material. The discontinuities result from the tensile stress generated by the sound wave during the tensioning phase. The compression rate of this unsteady state can be so high that their collapse generates a hydraulic shock wave. The bubble is initiated and moves in liquid simultaneously with many other bubbles spaced by less than one wavelength and forming a cavitation region. The average bubble collapse pressures of $\sim 10^4$ MPa vary for low-melting metals within one order of magnitude. Besides cavitation, the propagation of high intensity ultrasonic wave involves the initiation of steady state acoustic streaming in the liquid.



Fig. 1. Ultrasonic treatment of molten aluminium

Ultrasonic refining of metal melts is intended for effective removal of solid non-metallic and gaseous impurities from liquid metal. This method might be recommended for the refining of light metal alloys (Al, Mg), where material defects, due to solid and gaseous impurities, must be minimised. As depicted in Figure 2, the efficiency of ultrasonic degassing is higher in comparison with melt treatment by the additions of chlorine salts and evacuation [3].

The concentration of hydrogen in aluminium alloys is reduced by ultrasound by the factor 2–3 in comparison to the untreated metal. For example, the concentration of hydrogen in the melt of grade A19 alloy is normally 0.45–0.75 cm³/100 g of metal at a temperature 720°C. Ultrasonic treatment reduces the gas concentration level

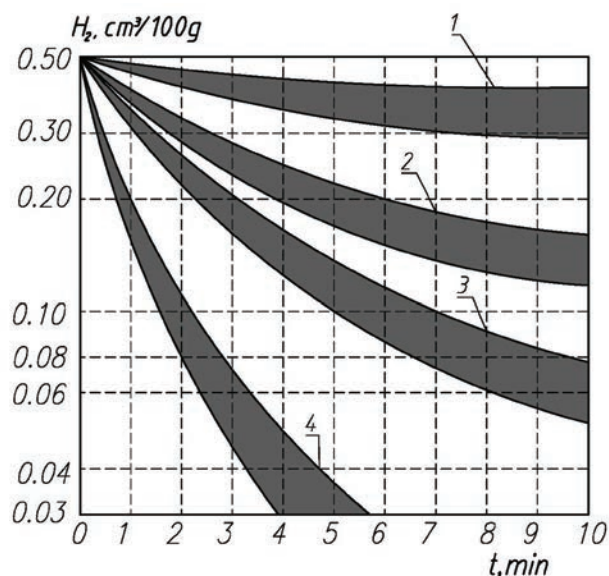


Fig. 2. Degassing kinetics for grade A19 aluminium alloy: 1 – zinc chloride process, 2 – vacuum degassing, 3 – ultrasonic degassing, 4 – ultrasonic + vacuum degassing

to 0.1 cm³/100 g. Similar results were obtained during the degassing of other aluminium and magnesium alloys (grade AMg6, A14, MA8, etc.). Ultrasonic refining improves mechanical properties (characteristics of strength and plasticity, fracture toughness, and fatigue properties) of as-cast and as-worked product. It enables one to increase the characteristics of the strength and plasticity of alloys by 15–30%.

The introduction of vibrations into solidifying metal results in refining of its structures and an increase of the chemical homogeneity of the produced ingot or casting and also provides a non-dendritic structure. In solidifying metal (melt and two-phase liquid-solid zone), cavitation and acoustic streaming might produce crystal nucleation and the dispersion of growing crystals.

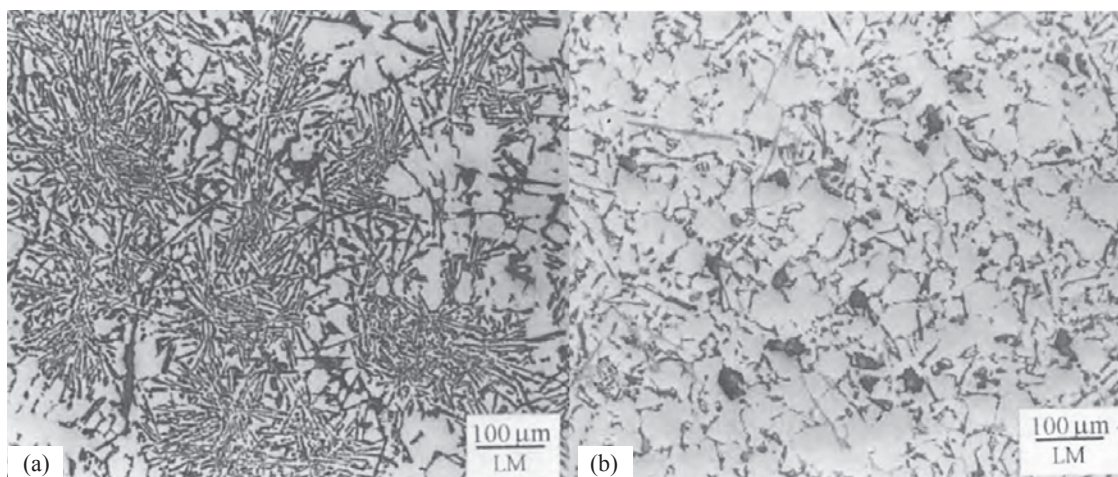


Fig. 3. Microstructure of AlSi13 alloys solidified conventionally: (a) and with ultrasonic treatment (b)

For example, in hypereutectic AlSi13 specimens prepared with the aid of convectional casting, the primary silicon crystals as hexagonal plates joined together at the centre into star-shaped particles, as they appear in cross section. The ultrasonic treatment may refine the silicon crystals providing a homogeneous cross-section. Most of the silicon plates were disconnected and broken during the ultrasonic treatment, forming spheroid crystals. This may be observed in Figure 3. Typically, ultrasonic treatment results in a plasticity increase of a factor of 1.3 to 1.6.

3. Ultrasonic technology for enhanced oil recovery and transportation of highly viscous oil

Another example of an industrial scale application of high power ultrasound is to enhance oil recovery. Generally, the efficiency of oil recovery from wells is less than 40% with a strong effort in the search of new enabling technologies [8]. Existing processes for enhanced oil recovery (EOR) are high-energy and labour consuming and often environmentally unfriendly [9, 10]. Thus, there is great interest in the development of more efficient technologies. Over the last few years, the use of physical EOR techniques have been reported, especially those based on ultrasonic treatment [11–15]. We have developed an ultrasound-assisted method that operates in the wellbore perforation zone with the simultaneous creation of a zone of lower pressure. The methodology is particularly useful for older wells which are in the later stages of reduced yields.

Ultrasonic treatment is one of the most promising alternative methods for affecting a fluid both under well conditions and on the surface. Laboratory and field tests have shown that acoustical oscillations initiate a variety of chemical and physical processes in oil bearing formations. Under well conditions, ultrasonic treatment can lead to such effects as increase of fluid penetration into capillaries due to the sonocapillary effect, an increase

of fluid mobility, and the detachment of paraffinic and other deposits from the rock [14]. Under well and surface conditions, ultrasound can lead to viscosity reduction [16, 17]. In high viscosity oil conglomerates, the molecules are bonded to each other by intermolecular forces. The goal of ultrasonic treatment is to destroy these bonds and to bring the properties of the oil closer to what they would have been if no conglomerates were present. To study the potential of ultrasonic treatment, we have carried out the following:

- Studies of the effect of ultrasonic – hydrodynamic treatment (UHT) and chemical agents on the rheological characteristics of oil; and,
- Studies of the effect of ultrasonic treatment on the rheological properties and heavy oil production under well conditions.

Fluid from one field of Samara region (Russia) was used to investigate the effect of UHT and chemical agents on the rheological characteristics of extremely viscous oil. The fluid had the following characteristics: the density was 0.953 g/m^3 , the effective viscosity at 20°C was $1014 \text{ mPa}\cdot\text{s}$, and the freezing point was 17°C . The fluid contained 64.05% oil, 28.6% resins, and 6.1% asphaltenes. To study the effect of UHT on crude oil and petroleum products, an experimental setup was assembled. The setup made it possible to vary the pressure at the inlet of the reactor. The maximum inlet pressure was 50 MPa, and the maximum capacity of the setup was 1200 L/h. Figure 4a shows the scheme of the UHT experimental setup. The setup consisted of a pump, a working section (reactor), a tank for the untreated oil, a receiving tank, an electric heater, an emergency discharge tank, control and stop valves, and instrumentation (pressure gages, a compound pressure and vacuum gage and thermocouples). A hydrodynamic emitter is inserted in the working chamber, as depicted in Fig. 4b. The operation of the emitter is based on the generation of oscillations in a liquid media, when the jet from the nozzle interacts with a barrier of a certain shape and size. The perturbations caused by the obstacle affect the jet base, causing auto-oscillations. In the experimental setup, we used an annular slotted nozzle, which was formed by two conical surfaces. The barrier had the

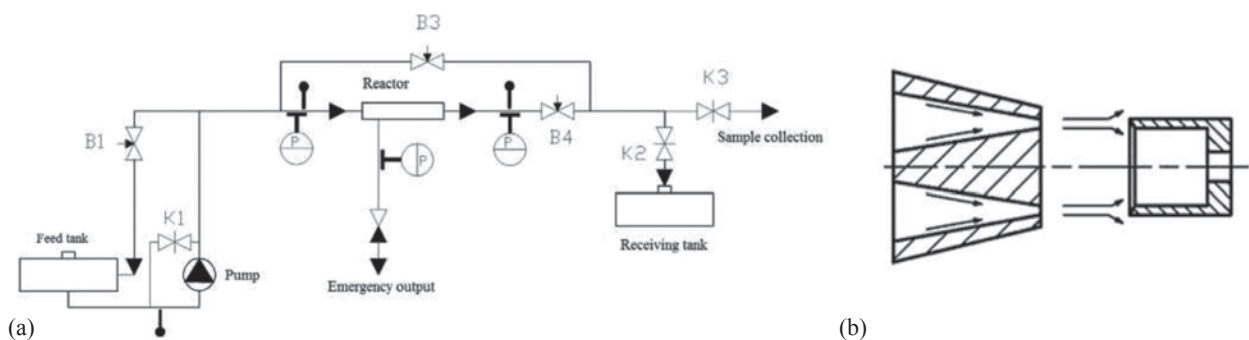


Fig. 4. a) Schematic of the experimental setup for ultrasonic – hydrodynamic oil treatment; b) Schematic of the hydrodynamic emitter in the setup for UHT

shape of a hollow cylinder, dissected along the elements. Thus, the barrier consisted of cantilever plates, arranged circumferentially. The frequencies of the oscillations, caused by that emitter, were in the range of 15–35 kHz. The electric heater in the setup was used to maintain constant temperature of the treated oil.

Experiments have shown that the use of UHT is a promising acoustic method for decreasing the viscosity of oil after its recovery. Such treatment makes it possible to reduce oil viscosity by more than 30%. In addition, treatment in the designed setup allows a chemical agent to be effectively introduced into the oil. The introduction of a chemical agent during UHT lead to a synergistic effect and cause a further reduction in viscosity, compared to the viscosity of oil after UHT only.

Aiming to study the effect of ultrasound on the rheological properties of oil under well conditions, an ultrasonic tool was placed into the perforation zone of the well. The tool was attached to the tubing and was powered with a suitable cable, attached to the outer surface of the tubing using cable bands. An ultrasonic generator was installed near the wellhead on the surface to power the downhole tool. The output power of the ultrasonic generator was 9 kW and 5 kW at the ultrasonic downhole tool. The scheme of the whole equipment set up is shown in Fig. 5.

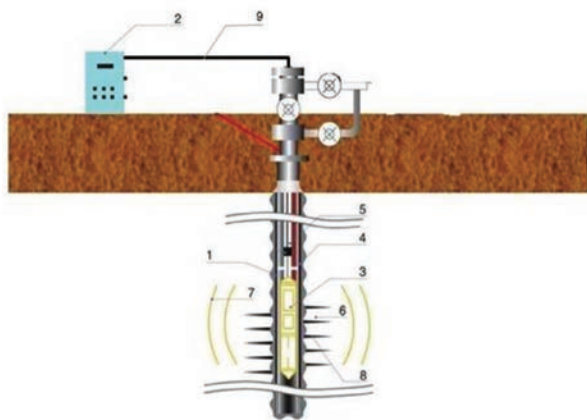


Fig. 5. Arrangement of ultrasonic equipment in the well:
 1 – anchor, 2 – ultrasonic generator, 3 – downhole tool (102 mm), 4 – casing, 5 – tubing, 6 – reservoir, 7 – area of acoustic impact, 8 – perforation zone, 9 – cable

4. Experimental set up in oil well

Experiments were carried out in the producing well No. 4620 at the Demkinskoe oil field (Russia). The well had the following characteristics: 168 mm production casing, C1bb formation, perforated interval depth 1309.3–1312 m, fluid production before treatment was 1.82 m³/day, oil production before treatment was 1.51 tons/day, bottom hole pressure (on average during the last month before treatment) was 25.6 atm, temperature was

23°C, water cut was 10.3%, formation pressure was 49 atm, and the production coefficient was 0.071. The outer diameter of the downhole tool was 102 mm, and its length was 700 mm. The downhole tool contained three annular magnetostrictive transducers that generated an ultrasonic field at a frequency of 19 kHz.

Ultrasonic treatment by a downhole tool located directly in the perforation zone leads to a decrease of the viscosity of oil and simultaneously to an increase in oil production. Both effects were demonstrated during field experiments: a viscosity reduction by 16% 4 h after treatment was observed, and oil production was simultaneously increase by 26.5%. As a result, the velocity of oil rise from the well increased. Consequently, the oil, which is supplied to the pipeline near the well, was 10°C hotter and the aggregated viscosity change was based on two factors: the change of the rheological properties of oil due to ultrasonic treatment and the higher temperature. Besides the increase production rate in the well, ultrasonic treatment performed inside the well can facilitate the pipeline transportation of heavy oil.

For the treatment of horizontal wells a sonochemical approach [12] should be used when a combination of acoustical and chemical treatment is used. In this case, ultrasonic treatment not only contributes to the cleaning of the perforation zone and increasing the mobility of oil, but also to the penetration of the reagent into the formation and acceleration of the chemical reaction in the porous media of the formation. In order to carry out effective treatment of horizontal wells, specially designed equipment has been developed. Any technology of EOR for horizontal wells should be based upon the following guidelines:

- The formation intervals, i.e. those which need treatment, should be based on geophysical studies.
- In order to achieve synergistic effects, the reagents need to be injected directly into the zone of acoustic treatment.
- The treatment should be selective in that only the problematic zones should be treated, and this decreases the overall treatment time.

Taking into account the mentioned above, ground and downhole equipment for sonochemical EOR of horizontal wells has been developed [12]. The ground equipment includes an upgraded ultrasonic generator involving a unit for processing the information obtained regarding pressure and temperature in the borehole, and this information is obtained from a downhole tool. The ultrasonic generator is matched to the ultrasonic downhole tool and easily adapts to changes in the technological load by controlling the voltage and the current which goes to the downhole tool. The ultrasonic generator can work in a pulse mode and can modulate the power. The operating frequency is 15–30 kHz, and the output power is 10 kW. During the operation of the generator, the following parameters can be monitored on the display: voltage, current, work/pause, and frequency.

The downhole equipment includes a sonotrode, a system for injection of chemicals, and a probe for acquiring geophysical data (temperature, pressure, flow). In order to use this equipment in horizontal wells, the equipment complex must include a special signal cores to control the parameters of the process. The cable is an armoured polymeric tube, and the copper cores are nested within it. The cross section of the cable is represented in Fig. 6. The diameter of the hydraulic channel is 15 mm. Power up to 5 kW can be delivered through the cable. The cable can be also used for moving the ultrasonic downhole tool through the horizontal area of the well during the treatment. Apart from the injection of reagents directly to the zone of the acoustical treatment, the cable can also be used to wash and clean the horizontal area of the well with technological fluid prior to and after the treatment. The armour surrounding the cable protects it from external damage.



Fig. 6. Cross-section of the cable with hydraulic channel and power and signal cores

It has the required breaking strength and torsional stiffness to be wound onto a drum on a geophysical truck. Photographs of the wireline truck constructed specially for sonochemical treatment of horizontal wells in the transport (a) and working (b) position are presented in Fig. 7.



Fig. 7. Photograph of the wireline truck for sonochemical treatment of horizontal wells in working position

During the treatment of wells, it is necessary to continuously process the data in order to choose the appropriate treatment modes and to adjust them during the operation. Complex geophysical downhole tools, which are used during the treatment, measure the following parameters: pressure, temperature, flow of the fluid, and magnetic location of the couplings. A special cable with a hydraulic channel for the injection of technological fluids was developed. The cable includes electrical cores to power the ultrasonic equipment (1.5 mm diameter) and the geophysical probe (0.4 mm diameter).

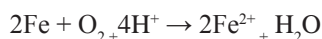
To select the optimal design of the sonotrode, various waveguide systems were designed, modelled, manufactured, and tested. The best results were achieved when sonotrodes emitted from the sidewall were used. The operating frequency of the sonotrode used for sonochemical treatments of wells was 20 kHz.

Our preliminary work on the sonochemical treatment of horizontal wells is not sufficient to provide a full statistical analysis. However, the results obtained to date allow us to take an optimistic view on the potential of this technology. Thus far, we have treated 3 horizontal wells in sandstone reservoirs in Western Siberia. The time of ultrasonic treatment of 1 m of the formation after injection of the reagent was 15 min. Before and after sonochemical treatment of the well, geophysical studies of the well were carried out. Based on the information received, the zones for sonochemical treatment were determined. The treated area was 200-300 m long. As a result of sonochemical treatment, the production of fluid and production of oil from all three treated wells grew. On average, the production of fluid increased from 51 to 72 tons per day, and the production of oil increased from 23 to 33 tons per day.

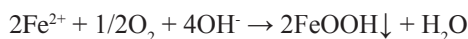
5. Combined acoustical – chemical method for purification and disinfection of wastewater

Another application of high-power ultrasound, which has a big potential for use in industry, is the activation of reagents, used for wastewater treatment. Contaminated water from industrial sources can contain a range of pollutants, including heavy metals and oil, the latter often in the form of an emulsion. One general treatment adopted for such wastewater is coagulation, which involves the addition of aluminium salts, such as $AlCl_3$ or $Al_2(SO_4)_3$, that generate aluminium hydroxide flocs. The coagulation process can also be initiated through the electrochemical generation of Al_3^+ or Fe_3^+ ions. These flocs absorb pollutants, which are concentrated in the material, which settles out and can be separated from the water [18]. Coagulation and electrocoagulation can also be used to break oil/water emulsions [19–21].

A valuable but so far relatively unexploited method for water remediation is the use of galvanochemistry for the generation of particles capable of removing metal ions and oil contaminants from wastewater [22]. The method is based on the use of two inexpensive bulk materials, i.e. iron and coke. Iron metal is corroded in the presence of coke which acts as the other part of the electrochemical cell due to their difference in standard electrode potential. The elements undergo intermittent contact during mechanical mixing and during this process iron becomes the anode and oxidises without the requirement for the application of an electric current (carbon is the cathode).



Fe^{2+} is then oxidized further and ions of Fe^{3+} are formed the majority of which is magnetic.



There is no specific instrumentation required, and yet the technology is almost unknown outside of Russia; although, it presents a huge potential for both industrial wastewater treatment and hazardous waste remediation because of its effectiveness and low cost. The use of power ultrasound in various fields and has been widely studied [23]. It has been proven to provide process intensification in water purification through both its effect on heterogeneous systems and sonochemical reactions. The particle size of the iron oxide crystals (most of which is magnetite Fe_3O_4) generated in the galvano-reactor is around $8.5 \mu\text{m}$, but subsequent ultrasonic treatment of these particles reduces the size to $5 \mu\text{m}$. It is important to note that only the suspension of magnetite emerging from the galvano-reactor is sonicated in a flow system prior to the cleaning process in a separate reactor. This allows more intensive treatment of a concentrated suspension rather than treating the whole volume of the polluted water. In this way, power ultrasound can significantly increase the effectiveness of the treatment and expand its use to include the removal of oil pollution. Results are presented in Figure 8. Based on the methodology described above, a mobile system was constructed – see Fig. 9.

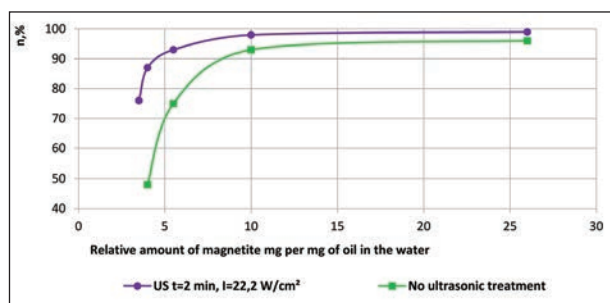


Fig. 8. Dependence of the degree of water purification (g) from the relative concentrations of magnetite and petroleum products in the contaminated water



Fig. 9. Mobile complex of ultrasonically assisted galvano-coagulation wastewater treatment. Placement of equipment inside the container

6. Ultrasonic-assisted production of antibacterial nanomaterials and textiles coating

Many efforts have been made for the application of ultrasound for the coating of various materials and fabrics with nanoparticles, in particular, textiles. The industrial potential of this application is tremendous [24]. Below, we have briefly described the procedure we have studied [25]. A method for the production of antibacterial ZnO nanoparticles has been developed. The technique combines the simultaneous treatment with ultrasonic waves and an electric current flow. By using high-power ultrasound, a cavitation zone is created between two zinc electrodes with the generation of a spatial electrical discharge in water. This discharge leads to the depletion of the electrodes and the formation of ZnO nanoparticles, which demonstrate antibacterial properties. At the end of this reaction, the suspension of ZnO nanoparticles is transported to a specially developed ultrasonic reactor in which the nanoparticles are deposited on the textile. The nanoparticles are embedded into the fibres by the cavitation jets, which are formed by asymmetrically collapsing bubbles in the presence of a solid surface and are directed towards the surface of textile at very high velocities. A SEM image of the treated fabric is shown in Figure 10. Fabrics coated with ZnO nanoparticles by using the developed method showed good antibacterial activity against *E. coli*.

We have tested the antibacterial activity against *E. coli* of the two sets of fabrics. Figure 11 shows the results of these tests. It is clearly visible that the antibacterial activity of the textile coated by the sonoplasma particles against *E. coli* is higher than the fabric coated with industrial NP's. This might be explained as the result of the small ZnO NPS obtained by the sonoplasma synthesis. We have repeatedly shown

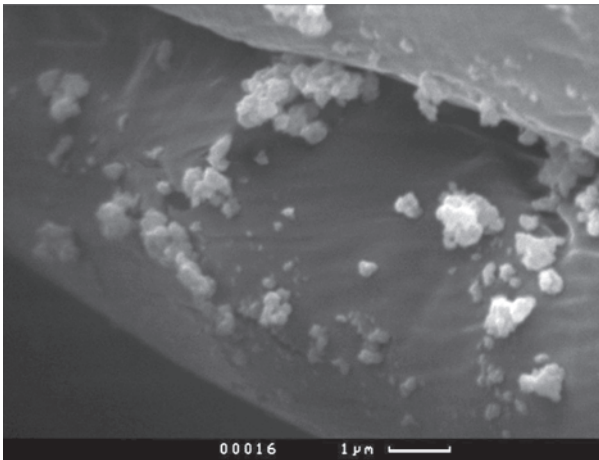


Fig. 10. SEM image of coated textile fibres. The scale bar is 1mm

that the biocidal effect is size dependent and particles with smaller size have a stronger bactericidal effect. The suspension continuously exposed to an ultrasonic field prevents the formation of particles agglomerates.

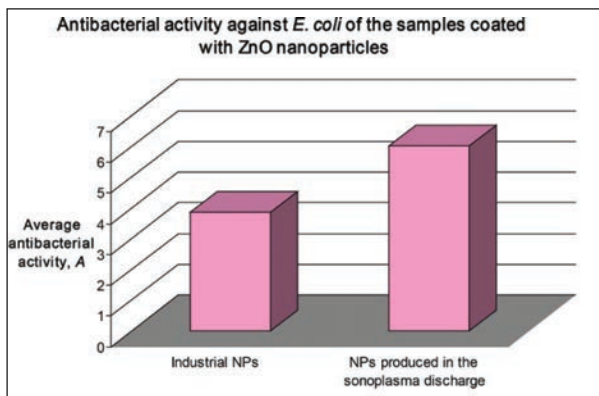


Fig. 11. Antibacterial activity against *E. coli* of ZnO nanoparticles coated fabric

Conclusions

Studies on fundamental phenomena related to high-power ultrasound propagation in liquids and solids paved the way for development of important applications of ultrasonic technologies. Ultrasonication can significantly influence heat and mass transfer in several chemical processes, modify the structure and properties of solids, and thereby interfere with interactions. This article reports a number of relevant industrial applications of ultrasound in which remarkable process intensification was documented. In general, ultrasound-assisted processes are faster, environmentally friendly, energy saving, and provide high quality products and new materials. We have shown that ultrasonic technologies can be successfully used in foundries, the oil industry, the production of bactericidal materials, and environmental protection. In spite of these relevant

achievements, ultrasonic technology still remains unexploited and the industrial potential underestimated.

References

- Cravotto G., Cintas P.: Power ultrasound in organic synthesis: moving cavitation chemistry from academia to innovative and large-scale applications. *Chem. Soc. Rev.*, 2006, 35(2), pp. 180–196.
- Abramov O.V.: *Ultrasound in Liquid and Solid Metals*. Boca Raton, FL: CRC Press, 1994.
- Dobatkin V.I., Eskin G.I.: *Vozdeystvie Moschnogo Ultrazvuka na Mezhfaznuyu Poverhnost Metallov (The Effect of High-Intensity Ultrasound on the Phase Interface in Metals)*. Moscow: Nauka, 1986 [in Russian].
- Norrie D.H., Vries G.: *An introduction to Finite Element Analysis*. New York: Academic Press, 1988.
- Abramov V., Abramov O.V., Bulgakov V., Sommer F.: Solidification of aluminium alloys under irradiation using water-cooled resonator. *Materials Letters*, 1998, 37, pp. 27–34.
- Abramov V., Abramov O.V., Straumal B.B., Gust W.: Hypereutectic Al-Si based alloys with a thixotropic microstructure produced by ultrasonic treatment. *Materials & Design*, 1997, 18(4–6), pp. 323–326.
- Sommer F., Abramov O.V., Orlov D., Abramov V.O.: Properties of Al-Pb base alloys applying electromagnetic forces and ultrasonic vibration during casing. *Materials Letters*, 1995, 23(1–3), pp. 17–20.
- Abramova A.V., Abramov V.O., Kuleshov S.P., Timashev E.O.: *Analysis of the modern methods for enhanced oil recovery*. In: U.Ch. Sharma, S. Kumar, R. Prasad, J.N. Govil (eds.): *Energy Science and Technology*. USA: Studium Press LLC, 2015, pp. 118–148.
- Stepanova G.S.: *Gas and Water–Gas Methods of Influence on Oil Reservoirs*. Moscow: Gazoil Press Publisher, 2006.
- Kryaev D.Y.: *Theory and Practice of the Use of EOR Methods*. Moscow, 2013.
- Abramov V.O., Abramova A.V., Bayazitov V.M., Altunina L.K., Gerasin A., Pashin D.S., Mason T.J.: Sonochemical approaches to enhanced oil recovery. *Ultrasonics Sonochemistry*, 2015, 25, pp. 76–81.
- Abramov V.O., Abramova A.V., Bayazitov V.M., Marnosov A.V., Kuleshov S.P., Gerasin A.S.: Selective ultrasonic treatment of perforation zones in horizontal oil wells for water cut reduction. *Appl. Acoust.*, 2016, 103, pp. 214–220.
- Abramova A., Abramov V., Bayazitov V., Gerasin A., Pashin D.: Ultrasonic technology for enhanced oil recovery. *Engineering*, 2014, 6, pp. 177–184.

14. Mohsin M., Meribout M.: An extended model for ultrasonic-based enhanced oil recovery with experimental validation. *Ultrasonics Sonochemistry*, 2015, 23, pp. 413–423.
15. Abramov V.O., Mullakaev M.S., Abramova A.V., Esipov I.B., Mason T.J.: Ultrasonic technology for enhanced oil recovery from failing oil wells and the equipment for its implementation. *Ultrasonics Sonochemistry*, 2013, 20, pp. 1289–1295.
16. Hamidi H., Mohammadian E., Junin R., Rafati R., Azdarpour A., Junid M., Savory M.: The effect of ultrasonic waves on oil viscosity. *Pet. Sci. Technol.*, 2014, 32(19), pp. 2387–2395.
17. Abramov V.O., Abramova A.V., Bayazitov V.M., Mullakaev M.S., Marnosov A.V., Ildiyakov A.V.: Acoustic and sonochemical methods for altering the viscosity of oil during recovery and pipeline transportation. *Ultrasonics Sonochemistry*, 2017, 35, pp. 389–396.
18. Fu F., Wang Q.: Removal of heavy metal ions from wastewaters: a review. *J. Environ. Mgmt.*, 2011, 92(3), pp. 407–418.
19. Biswas N., Lazarescu G.: Removal of oil from emulsions using electrocoagulation. *Int. J. Environ. Studies*, 1991, 38(1), pp. 65–75.
20. Canizares P., Martinez F., Jimenez C., Saez C., Rodrigo M.A.: Coagulation and electrocoagulation of oil-in-water emulsions. *J. Hazard. Mater.*, 2008, 151(1), pp. 44–51.
21. Emamjomeh M.M., Sivakumar M.: Review of pollutants removed by electrocoagulation and electrocoagulation/flotation processes. *J. Environ. Mgmt.*, 2009, 90(5), pp. 1663–1667.
22. Gogate P.R., Sutkar V.S., Pandit A.B.: Sonochemical reactors: important design and scale up considerations with a special emphasis on heterogeneous systems. *Chem. Eng. Process.*, 2011, 166, pp. 1066–1082.
23. Abramov V.O., Abramova A.V., Keremetin P.P., Mullakaev M.S., Vexler G.B., Timothy J., Mason T.J.: Ultrasonically improved galvanochemical technology for the remediation of industrial wastewater. *Ultrasonics Sonochemistry*, 2014, 21, pp. 812–818.
24. Petkova P., Hoyoa J., Perelshtein I., Tzanov T.: Durable antimicrobial cotton textiles coated sonochemically with ZnO nanoparticles embedded in an in-situ enzymatically generated bioadhesive. *Carbohydrate Polymers*, 2018, 189, pp. 198–203.
25. Abramova A., Gedanken A., Popov V., Mason T.J., Joyce E.M., Beddow J., Perelshtein I., Bayazitov V.: A sonochemical technology for coating of textiles with antibacterial nanoparticles and equipment for its implementation. *Materials Letters*, 2013, 96, pp. 121–124.

This article appeared in its printed version in Journal of Machine Construction and Maintenance. The electronic version is published in DEStech Publications, Inc., Lancaster, PA, 2019, Proceedings of FUTURE ENGINEERING CONFERENCE.

Łukasz MUCHA^{a, *}

^a Professor Zbigniew Religa Foundation of Cardiac Surgery Development, Zabrze, Poland

* Corresponding author: lukasz.mucha.polsl@gmail.com

DEVELOPMENT WORKS ON APPLYING FORCE FEEDBACK IN ROBOT CONTROL SYSTEM

© 2019 Łukasz Mucha

This is an open access article licensed under the Creative Commons Attribution International License (CC BY)

 <https://creativecommons.org/licenses/by/4.0/>

Key words: RobinHand, haptic, force feedback.

Abstract: The article presents the design stages, the principles of operation, and the tests of the force that is exerted on the operator. It also includes the developed a laboratory stand for testing the force interactions, concepts and ways of implementing the transfer of tactile stimuli, subsequent variants of the developed devices with the short description of them, the project of the operator-surgeon stand that is based on the assumption that the method of control of this device is compatible with the natural work of the surgeon, and the project of control console that is used to manipulate the surgical robot. This paper presents the actual state of the work and further possible directions of the development of the human-machine interface which is developed within the project LIDER VIII.

Prace rozwojowe nad zastosowaniem siłowego sprzężenia zwrotnego w sterowaniu robotem

Słowa kluczowe: RobinHand, haptyczny, siłowe sprzężenie zwrotne.

Streszczenie: W pracy przedstawiono etapy projektowania, zasadę działania oraz badania statyczne siły wywieranej na operatora przez opracowane urządzenie sterujące RobinHand do manipulacji robotem chirurgicznym. Zaprezentowano opracowane stanowiska badawcze umożliwiające badanie zadajników ruchu. W pracy opisano koncepcję oraz sposoby realizacji przekazywania bodźców dotykowych z rzeczywistych urządzeń lub wirtualnej rzeczywistości użytkownikowi. Przedstawiono poszczególne warianty rozwojowe opracowanych urządzeń oraz krótki opis ich konstrukcji. Praca przedstawia stan aktualny oraz dalszy kierunek rozwoju interfejsu człowiek–maszyna rozwijanego w ramach projektu LIDER VIII. Przedstawiono koncepcję stanowiska operatora-chirurga opartą na założeniu, że sposób sterowania jest zgodny z naturalną pracą chirurga. Zaprezentowano projekt zintegrowanej jednostki centralnej – konsoli sterującej umożliwiającej manipulację robotem chirurgicznym.

Introduction

Nowadays, due to the growing demand of patients and doctors for less traumatic surgical methods, the idea of the operations performed by robots (telemanipulators) has appeared. Medical robotic systems can make surgical and rehabilitation interventions more efficient, accurate, accessible, and reliable. Thanks to that, the load of healthcare systems will be reduced. The need to introduce surgical robots to the operating rooms is caused by the current long waiting times for operations and the decreased group of specialists. The application of the robots not only increases the quality of operations, but also shortens the time of the procedure by using the advantages of the tools that are used during this operation. Medical robotic instruments are connected with instrumentations, imaging, and the verification of

the tool position in real time. A schematic diagram of surgery using surgical robots is shown in Fig. 1. On the one hand, there is a surgeon with the control console. On the other hand, there is the patient and the telemanipulator. The control console is equipped with special interfaces, which is a motion controller, to manipulate the robot. The surgeon's knowledge about the current position of the tool is needed for real time controlling. It is possible, thanks to the laparoscopic camera connected to the console monitor screen on which the operator observes the operating area. Based on the currently displayed image, the surgeon decides about the location of the laparoscopic tool inside the patient's abdominal cavity. Thanks to this solution, the surgeon can comfortably carry out surgery in a sitting position. This significantly increases his work comfort [1–5].

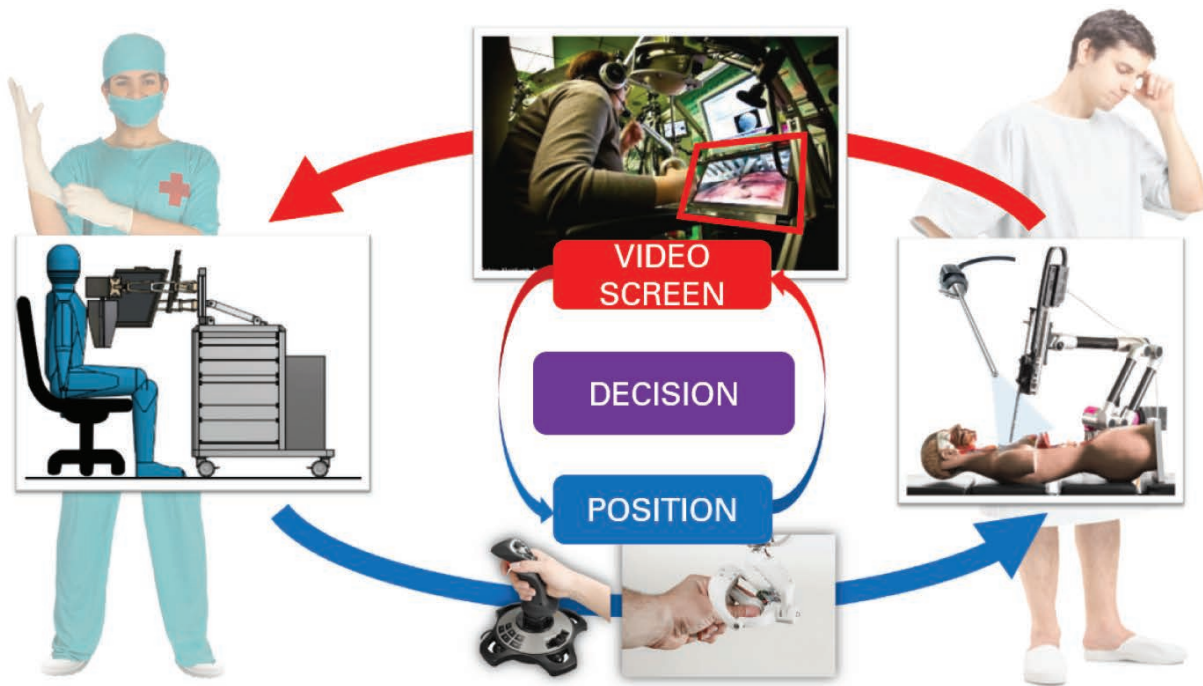


Fig. 1. A diagram of surgery with using surgical robots

1. The idea of control

Unlike operations using a robot, during operations performed manually the surgeon loses the sense of touch, which he uses to subjectively determine with what force the tool, held in his hand, affects to the organs. Currently, research works about the possibility of providing to the surgeon the additional information gathered from the operating area are being conducted. One of the concepts is the possibility of placing a special sleeve on the surgeon's forearm. Its main task is to exert an appropriate stimulus with the information about the contact of the tool with the object. The concept of this solution has been described by the author in the following works [1, 6–9].

The control system with the force feedback is the one of the most popular methods of controlling the telemanipulators (Fig. 2). The idea of such control procedure includes the following stages:

1. The operator observes the current position of the tool on the monitor screen and at the same time he changes the position of his hand in which he holds the end part of the motion controller.
2. Motion controller is equipped with a measuring system (encoders) that allows identification of the current position of the surgeon's hand in the space.
3. The control signal from the motion controller is transmitted to the telemanipulator, which

changes the orientation of his arm by using the servomechanism.

4. Along with the movement of the telemanipulator, the position of the tool also changes, and the manipulation of additional degrees of freedom of the tool and opening or closing the effector jaws are performed.
5. The surgical instrument may be equipped with the additional sensors that allow one to measure the force value. The force measurement can be also done on the robot arm.
6. The force value is transmitted to the motion controller.
7. The motion controller contains of some motors that allow the generation of the force with a given value and direction, which exerts an influence on the operator's hand and fingers.
8. The operator, thanks to the sensory receptors found in the skin of the hand, is able to recognize with what force and in what direction the contact with the organ occurred. Based on the visual observation and sensible forces, the surgeon makes further decisions about manual operations.

The implementation of the force feedback control includes: visual observation of the operating area, repeating the end part of the laparoscopic tool movements of the surgeon's hands, and also exerting a force vector that affects the hand holding the gripping part of the motion controller.

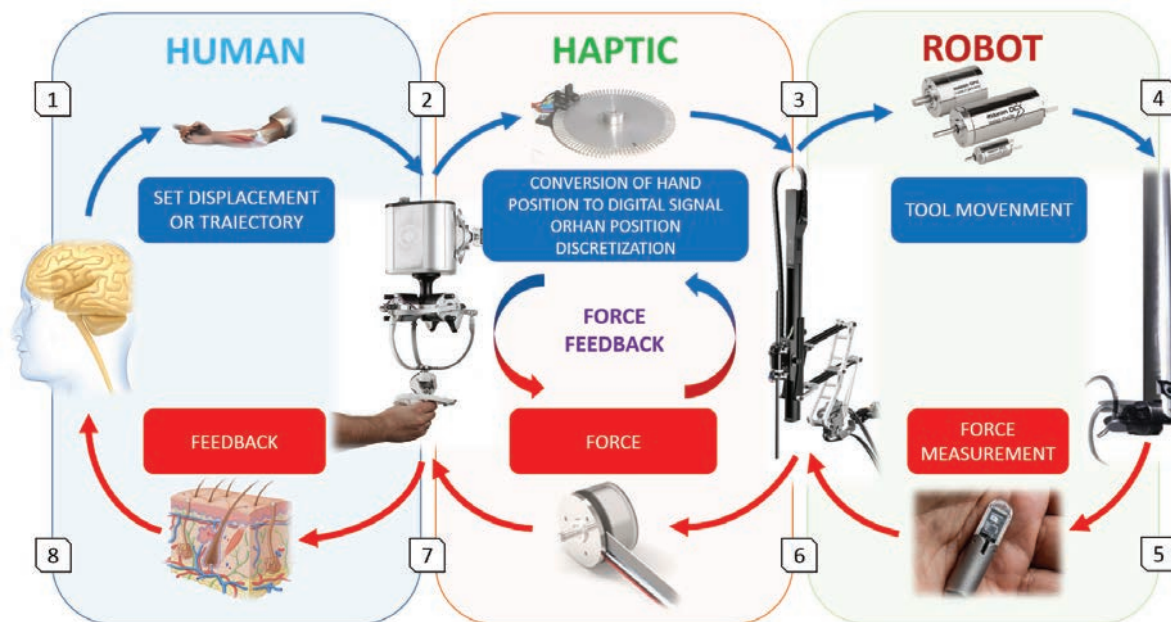


Fig. 2. The idea of control with force feedback

The particular control interfaces (motion controller) vary in kinematics and work parameters. They were discussed with more details in the author's works [6-8]. Together with the development of Polish medical robotics and the first industrial implementation of Robin Heart PVA robot in the Foundation for Cardiac Surgery Development (FRK), a tool and motion controller (with the force feedback) dedicated to the Robin Heart robot were developed. The measurement of the force that is necessary for the implementation of the force feedback can be carried out in the following several ways [11-14]:

- By measuring the power parameters of drive motors (e.g., currents) for particular degrees of freedom of the tool and the robot;
- By placing force sensors in the place where the tool is connected to the robot's arm;
- By fixing the sensors on the laparoscopic tube;
- By measuring the force in the drive rods; and,
- Through the measurement of the force in the effector of the tool.

2. Completed works

Due to the specification of the tool work (maintaining a constant transition point through the skin layers) and the distance between the actuator of the instrument and the fixed point, the displacement in the Z axis under the project INCITE (Intelligent Catheters in Advanced Systems for Interventions) that is coordinated by the Dutch company Phillips with the cooperation with a team of physicists and engineers from Hungarian Academy of Sciences (EK MFA, 3D Silicon), the Robin Heart robot with the special micro sensor 3D was developed. The laparoscopic tool (grasper) has been integrated with two force sensors in the effector of the instrument. A view of the end part of the tool with the located sensors is shown in Fig. 3. The first of them (SA) enables one to measure the clenching force of the effector's jaw, the other one (SB), which is located in the frontal part of the instrument, enables the measurement of force in X, Y, and Z axes.

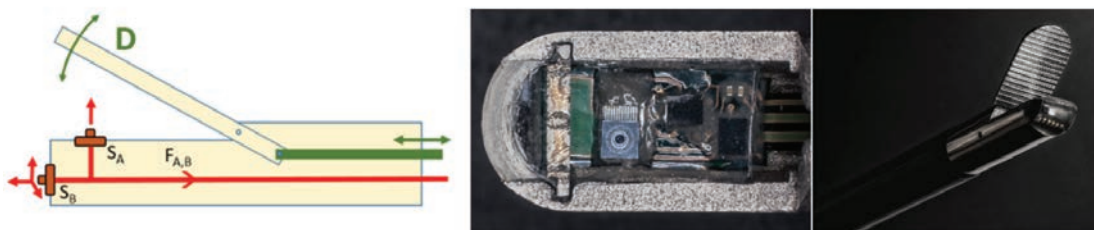


Fig. 3. INCITE tool equipped with force sensors [11]

A tool equipped with force sensors is mounted on the Robin Heart PVA robot arm. The robot is controlled through a console equipped with a motion controller with the force feedback.

The three prototype versions (H, F, and L of the motion controller RobinHand) were designed taking into account the delta type parallel kinematic structure.

In the last version (RobinHand L), the gripping part which the operator holds in the hand during the manipulation of the motion controller has been improved. Now it is possible to perform the 7 degrees of freedom (7DOF). The degrees of freedom (ABC) that are used to control the tool/robot with additional articulated parts and the degree of freedom D that performs the opening and closing of the jaws of the instrument are carried out by the gripping part of the motion controller. The ergonomics of the gripping part have also been improved. Currently, it is adjusted to the

operator's hands. The lines passing through the centres of the articulation elements intersect at exactly one point, between the operator's fingers. The force feedback is performed in the directions X, Y, and Z and in the jaw clamp D. Thanks to this solution, the manipulation of the motion controller became more intuitive. The construction of such complex shapes required the use of the latest technologies, manufacturing – 3D printing, as well as the connection of individual components (metal-plastic, metal-composite). Thanks to the use of rapid prototyping technology (3D printing with FDM method, used material: PCABS), it was possible to minimize the mass of the subassembly that was manipulated by the operator. This solution also allowed a shorter time for implementation of subsequent prototype versions. The minimum value of the force exerted on the user/surgeon was determined by using a test stand with one degree of freedom (Fig. 4).



Fig. 4. Measuring stand for verification of force impacts on the operator

The user moved the gripping part in the range of 110 degrees. The gripping part that is used by the operator was connected in its upper part with the motor (1), and the six-element force sensor NANO 25 from ATI Industrial Automation Company was placed at the operator's hand. This sensor recorded the current force exerted by the drive on the user. The position and the current in the motor were also recorded during the experiment. The operator notices the resistance of the arm movement, which he manipulated then he pressed the button under his foot. Tests were carried out on a group of 10 people during the Surgical Workshops organized by FRK. The exemplary results obtained from measurements for left and right movement and two braking strategies are shown in Figure 5. During the left-hand movement, the braking current grew dynamically as a function of the square difference between the actual and the set position. During the right-hand movement, the braking current increased

linearly in the displacement function. The braking current was 500, 800, and 1500 mA, respectively. Figure 5 shows the results from a single measurement. The indication of reaching the breaking point is marked with red circles.

Thanks to the use of rapid prototyping methods, the several conceptual models for mechanisms that implement the force feedback for displacements in X, Y, and Z axes were made. The laboratory stand to research different types of motors for haptic purposes was also developed. The tests with direct mechanism (the arm of the motion controller mounted on the motor shaft) and indirect mechanism (with using the transmission) were conducted. The tests were carried out including different types of drive systems, i.e. belts, and toothed and friction gears.

Various types of belts were used for the tests, i.e. metallic, plastic, and a combination of metallic and plastic materials.

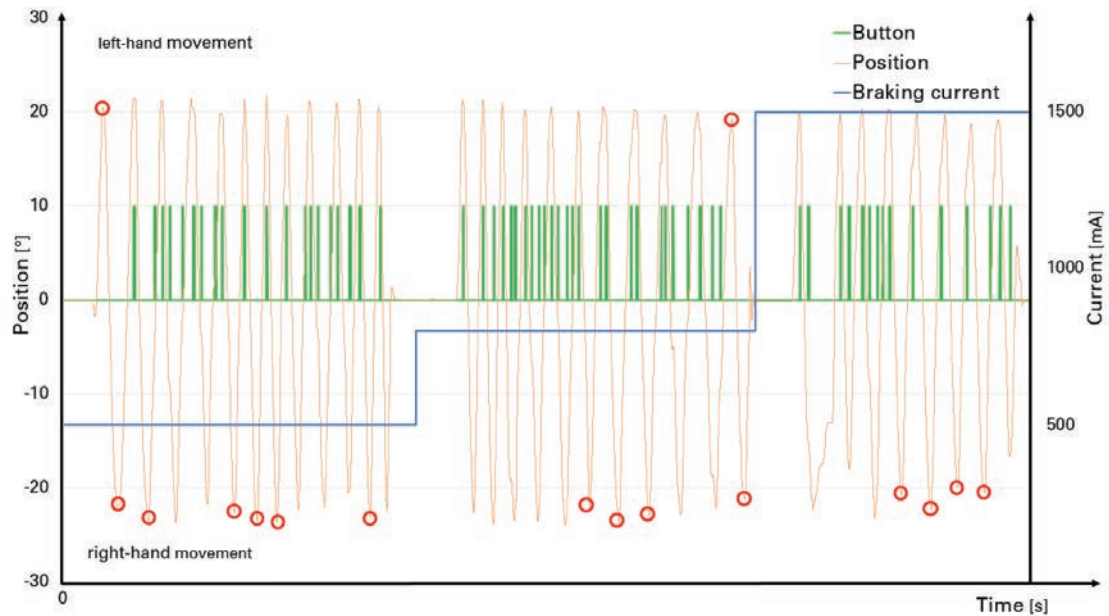


Fig. 5. Exemplary results from an experiment of subjective sensation of braking

The motors and measuring systems from Maxon, Faulhaber, Wobit, Rainshaw, Kubler, and Nanotec were used during the research works. Figure 6 presents the prototypes of selected variants of the transmission in the arms of the motion controller. Reproducibility tests of performed movements (the impact of the material and braid of the cable to the slip) were carried out at the stand with indirect mechanisms. Values derived from encoders located on the active and passive shaft of the drive mechanism were used. The motor DC Maxon 32691 and MOK40-5000-1224-BZ-K from Wobit were used to

drive the active shaft. For the purpose of determining the possible slip of the cable on the active pulley, a 24-hour tests research under the loading of 0.5N, 1N, and 3 N were conducted.

Based on the conducted analyses, it is possible to conclude that the highest repeatability of the performed movements and minimal wear of the cable was observed for the mechanism with a cable made of plastic that is placed in guide grooves located on the drive wheel. The number of cable braids for the drive wheel was in range from 2 to 8.

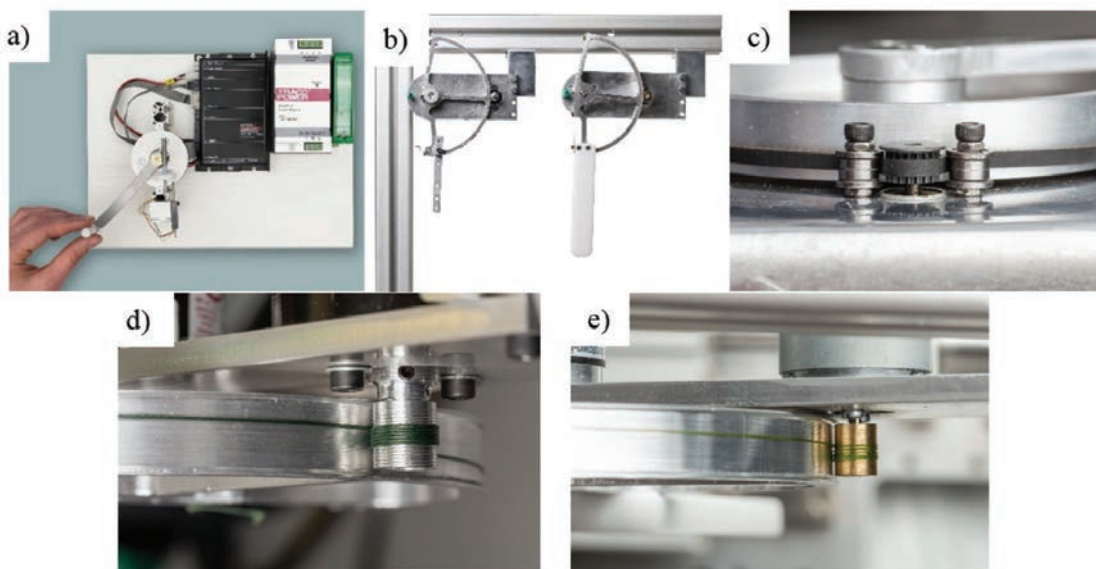


Fig. 6. Prototypes for variants of transmission: a) with direct drive mechanism, b) with using indirect mechanisms, c) mechanism with toothed belts, d), e) with using a belt drive that are braided on the drive drum

For the purpose of implementations of the force feedback in the end part of the motion controller, the various test variants of the part that is held by the operator were made using various mechanisms were made, e.g., belt drives or gear drives (Fig. 7). The tests were for two concepts: with one movable finger (index finger, Fig. 7a), and two fingers (index finger and thumb) working in parallel (Figs. 7b and c) are performed.

The prototype motion controller called RobinHand L was integrated with the control console and the Robin Heart Tele robot (Fig. 8).

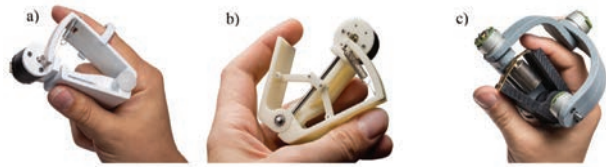


Fig. 7. Concepts of the gripping part: a) one-sided mechanism, b) parallel jaws system with a belt drive, c) with a gear train



Fig. 8. Robin Heart Tele robot with a control console equipped with motion controller with force feedback

Conclusions

Based on the preliminary research, a minimum value of the force that must affect the operator so that it can be felt on the hand during manipulation has been determined. The conducted experiment shows that much more accurate indications were obtained for the braking currents whose value increased in a dynamic way. For the current which changes in dynamic way, the minimum breaking current that the test group was able to indicate (100% of correct indications) was equal 1.5 A. Due to the limitations of the manufacturer that recommends to not exceed the value 4.3 A, it was decided to use an additional gearbox in the drive of the motion controller. This gear allowed the generation of the forces with the much higher values (without increasing the braking currents). Based on the carried out experiments, it can be concluded that the belt transmission was characterized by minimal resistance to movement and quiet operation. Taking into account the fatigue tests, the best results were obtained for gears with a cable made from plastic that is braided five times on the driving drum. On the driven wheel, the cable from one side is fixed and on the

other hand it is tensioned with a spring. To perform the opening-closing action of the jaws of the instrument, the two-finger mechanism that works in parallel during the gripping is the most convenient solution for the operator. A belt drive was also used for this solution. As a part of further work, it is planned to use a belt drive instead the direct mechanisms.

Acknowledgement

This work was done in the frame of the project LIDER/32/0175/L-8/16/NCBR/2017.

References

1. Nawrat Z.: *Robot chirurgiczny Robin Heart: Projekty, prototypy, badania, perspektywy* [Postdoctoral thesis]. Medical University of Silesia in Katowice, 2011 [in Polish].
2. Xin H., Zelek J.S., Carnahan H.: Laparoscopic surgery, perceptual limitations and force: A review. *First Canadian Student Conference on Biomedical*

- Computing, Kingston, Ontario, Canada, March 2006*. Proceedings, 2006, 144, pp. 1435–1451.
3. Nawrat Z., Kostka P., Lis K., Rohr K., Mucha Ł., Lehrich K., Sadowski W., Małota Z.: Interfejs operatora robota chirurgicznego – oryginalne rozwiązanie sprzężenia informacyjnego i decyzyjnego. *Medical Robotics Reports*, 2013, 2, pp. 12–21 [in Polish].
 4. Podsekowski L.: *Roboty medyczne – budowa i zastosowanie*. Warszawa: WNT, 2010 [in Polish].
 5. Lis K., Lehrich K., Mucha Ł.: Robin Heart PortVisionAble – idea, design and preliminary testing results. *Proceedings of the 10th International Workshop on Robot Motion and Control*, 2015, pp. 176–181.
 6. Mucha Ł., Nawrat Z., Lis K., Lehrich K., Kostka P., Sadowski W., Krawczyk D., Kroczeck P., Małota Z., Nawrat Z.: Postępy budowy specjalnych interfejsów operatora robota chirurgicznego Robin Heart. *Medical Robotics Reports*, 2015, 4, pp. 49–55 [in Polish].
 7. Lis K., Mucha Ł., Lehrich K., Nawrat Z.: *RobinHand Haptic Device*. In: Konstantinova J., Wurdemann H., Shafti A., Shiva A., Althoefer K. (eds): *Soft and Stiffness-controllable Robotics Solutions for Minimally Invasive Surgery: The STIFF-FLOP Approach*. River Publishers, 2018, pp. 289–305.
 8. Mucha Ł.: Interfejs użytkownika robota – przegląd urządzeń zadawania ruchu systemów sterowania telemanipulatorów. *Medical Robotics Reports*, 2015, 4, pp. 39–48 [in Polish].
 9. Mucha Ł., Lis K., Rohr K., Nawrat Z.: *Manipulator of a medical device with auxiliary motor and encoder*. Patent USA: 9393688. Current Assignee: Professor Zbigniew Religa Foundation of Cardiac Surgery Development, 2016.
 10. Mucha Ł., Nawrat Z., Lis K., Lehrich K., Rohr K., Fürjes P., Dücső C.: Force feedback control system dedicated for Robin Heart Pelikan. *Acta Bio-Optica et Informatica. Inżynieria Biomedyczna*, 2016, 22(3), pp. 146–153.
 11. Nawrat Z., Rohr K., Fürjes P., Mucha Ł., Lis K., Radó J., Dücső C., Földesy P., Sadowski W., Krawczyk D., Kroczeck P., Szébenyi G., Soós P., Małota Z.: Force Feedback Control System Dedicated for Robin Heart Surgical Robot. *Procedia Engineering*, 2016, 168, pp. 185–188.
 12. Lee D.H., Kim U., Gulrez T., Yoon W.J., Hannaford B., Choi H.R.: A Laparoscopic Grasping Tool With Force Sensing Capability. *IEEE/ASME Transactions on Mechatronics*, 2016, 21(1), pp. 130–141.
 13. Kim U., Lee D., Yoon W.J., Hannaford B., Choi H.R.: Force Sensor Integrated Surgical Forceps for Minimally Invasive Robotic Surgery. *IEEE Transactions on Robotics*, 2016, 31(5), pp. 1214–1224.
 14. Seibold U., Kuebler B., Hirzinger G.: *Prototypic Force Feedback Instrument for Minimally Invasive Robotic Surgery*. In: Bozovic V. (ed.): *Medical Robotics*. InTech Publishers, 2008, pp. 377–399.
- This article appeared in its printed version in Journal of Machine Construction and Maintenance. The electronic version is published in DEStech Publications, Inc., Lancaster, PA, 2019, Proceedings of FUTURE ENGINEERING CONFERENCE.

Andrzej MICHNIK*, Jakub WOŁOSZYN, Mariusz SOBIECH, Grzegorz NOWAK

Łukasiewicz Research Network – Institute of Medical Technology and Equipment ITAM, Zabrze, Poland

*Corresponding author: andrzejm@itam.zabrze.pl

REHABILITATION ROBOT FOR UPPER LIMBS

© 2019 Andrzej Michnik, Jakub Wołoszyn, Mariusz Sobiech, Grzegorz Nowak

This is an open access article licensed under the Creative Commons Attribution International License (CC BY)

 <https://creativecommons.org/licenses/by/4.0/>

Key words: rehabilitation, upper limb, robot, control system, force feedback.

Abstract: In an aging society, injuries and diseases are the causes of the dysfunction of motor structures. Recovering the required efficiency of the motor structures, in addition to immediate medical help, usually requires a tedious and long-term rehabilitation process. In the classic approach, rehabilitation is conducted and carried out by a rehabilitator, whose work consists in selecting appropriate types of exercises to limit dysfunction and then physical work, consisting in performing the appropriate exercises with a rehabilitated limb. This paper presents the process of creating a rehabilitation robot at the Institute of Technology and Medical Equipment in Zabrze, which, in the future, can relieve the physiotherapist from performing physical work, while providing a diagnostic tool, thanks to data obtained from robot sensors. An objective and rapid estimation of the patient's limb abilities can be valuable information that can be used to assess the progress of rehabilitation. Information about the progress of rehabilitation along with an attractive training scenario, in the form of 3D games, can be an important factor motivating the patient to long-term and laborious rehabilitation exercises.

Robot rehabilitacyjny kończyn górnych

Słowa kluczowe: rehabilitacja, kończyna górna, robot, system sterowania, siłowe sprzężenie zwrotne.

Streszczenie: Starzejące się społeczeństwo, doznane urazy, przebyte choroby są źródłem dysfunkcji narządów ruchu. Odzyskanie wymaganej sprawności narządów ruchu, oprócz doraźnej pomocy medycznej, zazwyczaj wymaga żmudnego i długotrwałego procesu rehabilitacji. W klasycznym podejściu, rehabilitację prowadzi i realizuje rehabilitant, którego praca polega na dobraniu odpowiednich do dysfunkcji typów ćwiczeń, a następnie pracy fizycznej, polegającej na wykonywaniu odpowiednich ćwiczeń rehabilitowaną kończyną. Niniejsza praca prezentuje proces powstawania robota rehabilitacyjnego w Instytucie Techniki i Aparatury Medycznej w Zabrzu, który w przyszłości może odciążyć rehabilitanta od wykonywania fizycznej pracy, jednocześnie dając mu narzędzie diagnostyczne dzięki danym uzyskanym z czujników robota. Obiektywna i szybka ocena możliwości kończyny pacjenta może być cenną informacją, którą będzie można wykorzystać do oceny postępów rehabilitacji. Informacja o postępach rehabilitacji wraz z atrakcyjnym scenariuszem treningowym w postaci gier 3D może stanowić istotny czynnik motywujący pacjenta do długoczasowych i żmudnych ćwiczeń rehabilitacyjnych.

Introduction

Physiotherapy is a major part of the treatment process of motor dysfunctions of the limbs as a result of past diseases or injuries. The large number of patients in need of rehabilitation is due to several different reasons. The main reasons include the fact that the society is

aging and civilization diseases caused by unhealthy lifestyles and road traffic accidents. Impairment of the locomotor system hinders the performance of vital functions, causes pain, and makes the patients unable to work [1, 2].

Physiotherapeutic training implemented sufficiently fast following the occurrence of the dysfunction is

a prerequisite for the recovery of lost ability as much as possible. Limited access to rehabilitation often results in long waiting times. As a consequence, subsequent procedures are less effective than might be expected [3].

Rehabilitation is likely to become more accessible due to the use of robotic devices supporting this process. Physiotherapists currently use devices that relieve them from the burden of performing exhausting exercises with the patient. Owing to the costs, popular devices mainly perform simple movements in single joints. Examples of simple devices for the rehabilitation of single joints include the following: for the fingers and wrist joint – Kinetec 8080, elbow joint – Artromot-E, and shoulder joint – Kinetec Centura Shoulder CPM [4]. There are also devices for spatial training. The main instance of such a device is the robot called ARMin, developed at the Zurich Polytechnic. In its first version, six degrees of freedom were applied, four of which were driven while two were passive. ARMin had a kinematic scheme allowing it to work from the shoulder joint to the forearm. In the next version, two degrees of freedom of movement for the forearm and wrist were added [5]. The design of the ARMin robot, Version III, was commercialized under the name of Armeo Power by HOCOMA and is currently a reference example of a commercial rehabilitation robot as shown in Fig. 1. The robot makes it possible to perform spatial rehabilitation training with feedback.



Fig. 1. A photo of the rehabilitation robot Armeo Power



Fig. 2. A photo of the rehabilitation robot Harmony

Other interesting designs of fixed exoskeleton rehabilitation robots include Harmony, an example of a robot developed at the University of Texas at Austin, USA. The robot is unique in that shoulder anatomy is mapped by the kinematic scheme of the robot arm and exercises can be performed simultaneously with two limbs [6] as shown in the photo in Fig. 2.

The physiotherapist's tool of the future that will make their work easier and will improve access to rehabilitation for the patients will be a robot that could repeat with the patient set patterns reflecting spatial movements without the need to involve the physiotherapist's muscles [7, 8]. Depending on the type of training, a physiotherapist's task would boil down to choosing a workout scenario and programming the essential parameters of the workout performed by the robot. In addition to relieving the physiotherapist from physical work and achieving a high repeatability of set parameters, sensor elements of the robot also make it possible to obtain precise information on flexion angles in the joints and the patient's muscle strength. Hence, the robot can also become a diagnostic tool to facilitate the evaluation of the patient's condition and rehabilitation progress, which is likely to increase motivation for further exercise. Another important factor that can increase the motivation for strenuous and exhausting exercises may be to offer the patient rehabilitation in the form of games in which the robot will play the role of human-machine interface with feedback.

In this paper, we would like to present the method of work on the design of the upper limb rehabilitation robot ARM-100 with seven degrees of freedom. The major part of the design was completed in 2010. We would also like to describe the on-going work on the construction of the ARM200 robot, where ITAM is the major subcontractor for project no. POIR.01.02.00-00-0014/17 for the company Technomex in Gliwice, within the framework of the competition InnoNeuroPharm announced by NCBiR. However, with regard to the ARM200 robot, due to the current lack of patent applications, detailed information will not be provided. The work will focus mainly on the components of the control system of the rehabilitation robot.

1. Key assumptions of the control system

The key assumption of the design of the ARM-100 rehabilitation robot was that the robot should take the form of a mechatronic exoskeleton operating one of the upper limbs. The exoskeleton was to be connected to the patient's seat, where the patient would perform exercises in a sitting position. An assumption was also made that the mechanical design and control system of the robot would allow the exoskeleton to be reconfigured to either the right or left upper limb. Another assumption was that the patient could have both passive and active training.

In the basic scenario, after attaching the patient's limb to the robot's arm, the physiotherapist moves the limb in the limb tracking mode. At this stage, the control system remembers the movement trajectory that is being entered. At the second stage of the training, the robot replays the stored trajectory for the set number of times. In order to implement this scenario, a versatile control system had to be developed, which would make it possible to build a robot with any number of nodes and would provide support for the required number of sensors. The control of the robot was divided into autonomous nodes controlling its individual drives. Another key assumption was to link the force sensor to a suitable drive so that the force exerted by the drive on the limb could be measured in the direction of the drive force, e.g., the drive responsible for the flexion of the elbow in Fig. 3 cooperates with the force sensor placed on the underside of the forearm holder and measures the force in the Y-axis. A node in the adopted control system is understood as a system doing a simple movement in relation to one axis for a selected joint. The control system divided into nodes allows for autonomous control of a selected drive. This solution makes it easier to control the forces exerted by the limb both in the case of passive and active movement (replaying and setting movement). What needed to be solved was also the issue of proper placement of force sensors on individual structural elements of the robot to obtain the required sensitivity and selectivity of force measurement.

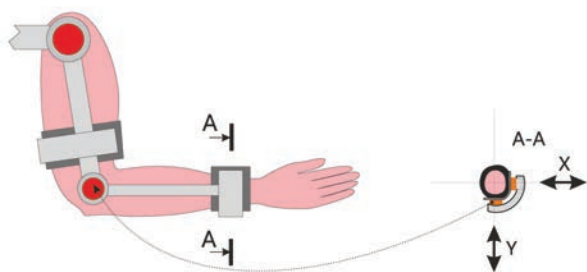


Fig. 3. The general idea behind the control of a rehabilitation robot; presentation of the connection between the drive and the correct pressure sensor

2. The control system of the robot

The control system of the rehabilitation robot consists of three main elements: modules of measurement and performance nodes, the communication module, and a PC with control software, Fig. 4. In the presented diagram, the node modules are placed on the robot's arm elements. This reduces the number of wires running through the moving parts of the robot's arm between the sensors and the node module.

In the control system of ARM-100, the time of complete information exchange between the PC program and all control nodes was set to 100 ms. The

communication module and the PC are connected with a USB interface. The RS-485 bus and a simple method of sequential information exchange are used to connect the control system nodes – Master asks, Slave answers. In each data exchange cycle, the PC program sends new operating parameters to the measurement and performance modules, which include information about the operating mode of the node and its operating parameters. In response, the node modules send information about operating parameters, such as angular positions, velocities, temperatures, and feed currents.

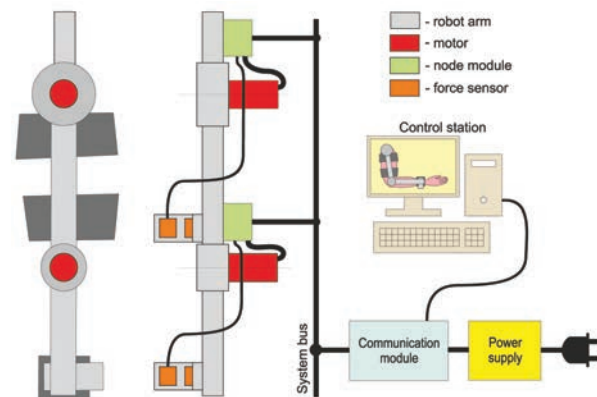


Fig. 4. The structure of the robot control system

A PC with control software makes it possible to remember the trajectory of the movement of the rehabilitated limb in the form of a training program as well as makes it possible to replay the remembered training program by adequately controlling the measurement and performance nodes. During the training session, the system operator starts the trajectory recording in the program. After the training trajectory input is complete, the operator initiates the trajectory replay. The program plays the role of a multi-channel movement recorder. Each of the remembered trajectories can be saved on a disk to compare rehabilitation progress later on.

The communication module is also used for disconnecting the power supply to the robot drives in an emergency. Emergency power supply disconnection results in immediate activation of the brakes in robot drives that may potentially cause hazard. The brakes are also activated in the event of power failure. The disconnection of the power supply for the brakes is operated by an independent control line. As a result, robot drives will definitely be stopped as soon as the emergency button is pressed.

3. The construction of the node

As part of the ARM-100 design, a dedicated node module was developed, which allowed the functions to be adjusted, the required sensors to be integrated, and

the drive to be operated in a single electronic package. Commercial drive controllers were not purchased. The Slave module makes it possible to control a BLDC motor with Hall sensors. Hall sensors installed inside the motor enable correct phase commutation at low revolutions. In addition, the Slave module calculates the relative rotational position and rotational velocity of the drive based on changes in signals from Hall sensors. The core of the Slave module in the ARM-100 robot is the 8-bit microcontroller PIC18F4431, dedicated to BLDC motors. Two force measurement channels, motor current measurement, and temperature sensors are connected to the microcontroller's analog-to-digital converter. The Slave module design diagram shown in Figure 5 presents the components of a node, where the letter M stands for

a three-phase BLDC motor which works with the brake: a temperature sensor and Hall sensors on the one hand and the gear behind which the absolute position sensor is placed on the other. The figure also demonstrates the schematically placed force sensor which is mounted between the robot arm and the patient. This makes it possible to use modes in which the robot arm follows the patient's arm based on pressure to achieve zero force. The information from the force sensor can also be used to stop the workout and thus protect the patient's limb from excessive load in the event of, e.g., spasmodic muscle contraction. It is also possible to use the force sensor to set the load by adjusting the appropriate insensitivity threshold. After the threshold is passed, the controller will enable the movement.

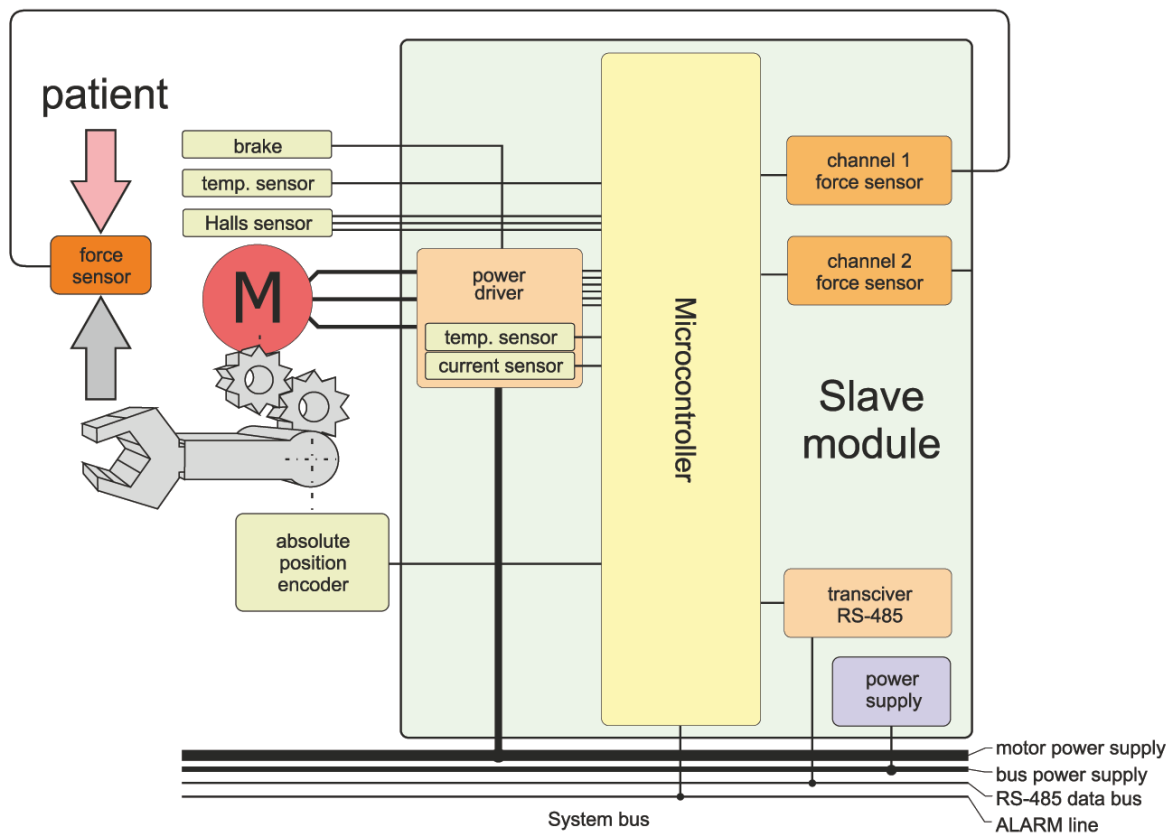


Fig. 5. The diagram of the measurement and performance node

During system startup or after starting the zero position procedure, the Slave module reads the absolute position from the external angular position sensor in the form of a magnetic sensor working with the magnet. The absolute position sensor is another element developed for the design. Figure 6 shows a photograph of the control system node, i.e. the Slave module, together with a connected BLDC motor, force sensor, and absolute angular position sensor.

BLDC drives with MAXON MOTOR planetary gearheads were used to develop the ARM-100 robot. In the current development of the ARM-200 robot, one of the major changes is the replacement of planetary gearheads with harmonic gears, which are more compact in size, with virtually no backlash and no additional bearing required. Moreover, 8-bit microcontrollers were replaced with 32-bit microcontrollers with an ARM Cortex-M4 core. 32-bit controllers make it possible to

perform a much larger number of operations between successive cycles of queries in the control system.

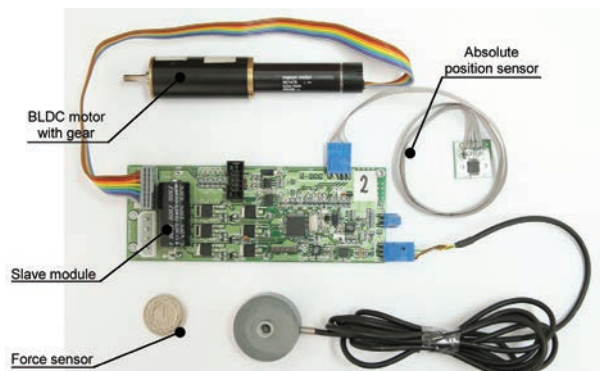


Fig. 6. A photo of the elements of the measurement and performance node

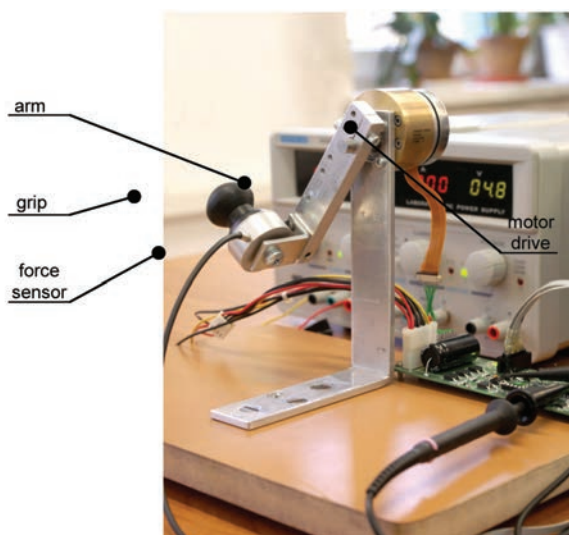


Fig. 7. A photo of the test stand for testing single-engine operation control algorithms

After assembling the electronics of the Slave module, a simple test stand was constructed to enable verification of the controller's operation, performance tests, and the improvement of drive control algorithms in different modes of operation. An important element of the work on the test stand was also the initial selection of coefficients for regulators stabilizing velocity and position. The stand shown in Fig. 7 consisted of a single Slave module working with a BLDC motor and a force sensor on the arm. A grip was mounted on the other side of the force sensor to allow hand contact with the sensor.

A second test stand, demonstrated in Fig. 8, was then built to test the end part of the robot's arm with three degrees of freedom. The second test stand made it possible to test the operation of the control system with two connected robot nodes. In this configuration, the Slave modules provide each other with amplified signals

from force sensors F1 and F2, which makes it possible to bend and rotate the hand with the sum and difference of the signals from the force sensors. Figure 9 shows a diagram of how the nodes operate in such a case. An additional third motor located at the top performs independent abduction and adduction movements in the wrist joint.

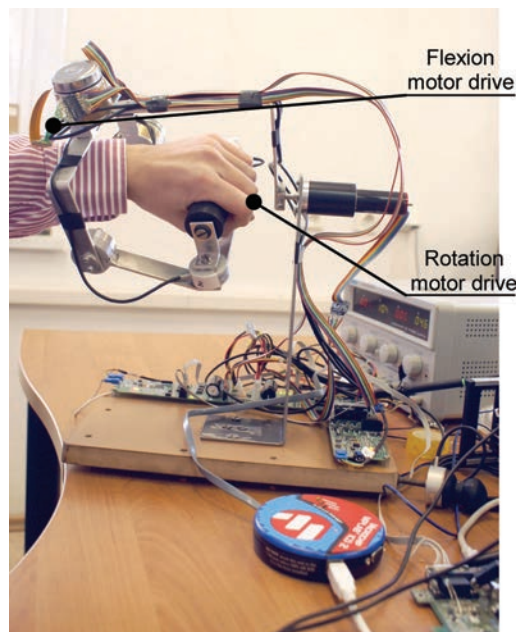


Fig. 8. A photo of the test stand for testing three-engine operation control algorithms

The built-in software of the Slave modules is the same for all nodes; however, the required parameters can be configured individually using the PC application. In this way, the gain of the measuring channel and the insensitivity zone can be set in order to limit the influence of the hysteresis of the sensor system in movement tracking modes based on the indications of force sensors. Individual configuration of PI regulators and other parameters, due to differences in the motors, gears, and sensors used, is also required. The configuration parameters are transferred during the initialization of the workout after the connection with the PC control program is made.

Each node is capable of operation in force-support mode or position stabilization mode. The force-support mode is mainly used for programming the rehabilitation trajectory, but it also allows for active training by adjusting the insensitivity threshold of the force measurement path. The position stabilization mode enables passive training, in which the robot replays the previously saved rehabilitation movement by moving the robot arm to the next previously saved points. Sending a new position frequently enough results in a smooth movement that maps the movement entered by the physiotherapist.

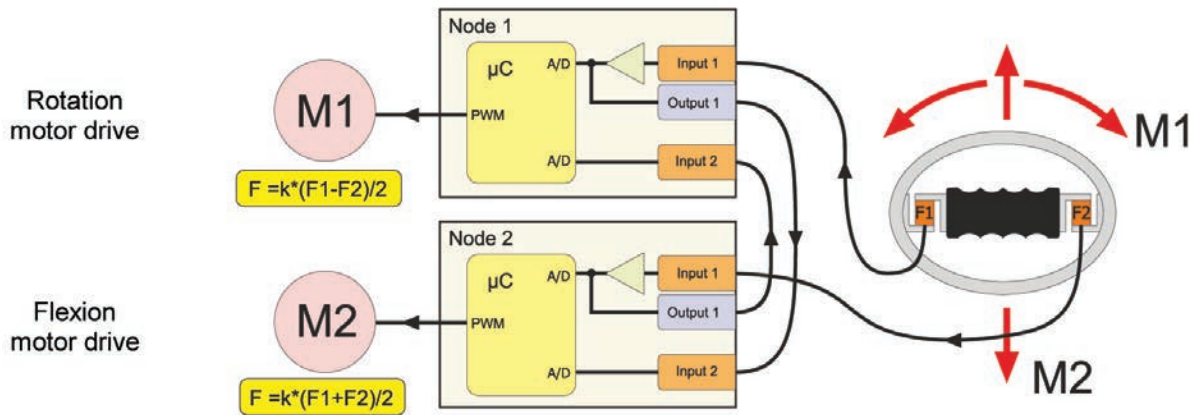


Fig. 9. A diagram of pairing nodes with the hand grip as an example

A simplified operating algorithm of the measurement and performance module in the force support mode is shown in Fig. 10. Two PI regulators are the core elements of this system. The first regulator stabilizes the rotation velocity of the drive, and the velocity is directly proportional to the applied force. The second regulator is intended to stabilize the position. As a consequence, the range of movement in a given node is limited. The direction of force is switched by the position regulator between two states: the position change to the angular

position MAX or to MIN. However, a given element is displaced only if appropriate force is applied which exceeds the set insensitivity threshold of the force measurement path. The displacement velocity is directly proportional to the applied force above the insensitivity threshold – subject to the permitted range of motion. The position controller automatically reduces the velocity to zero when the moving element reaches the limits of the movement range of a given part.

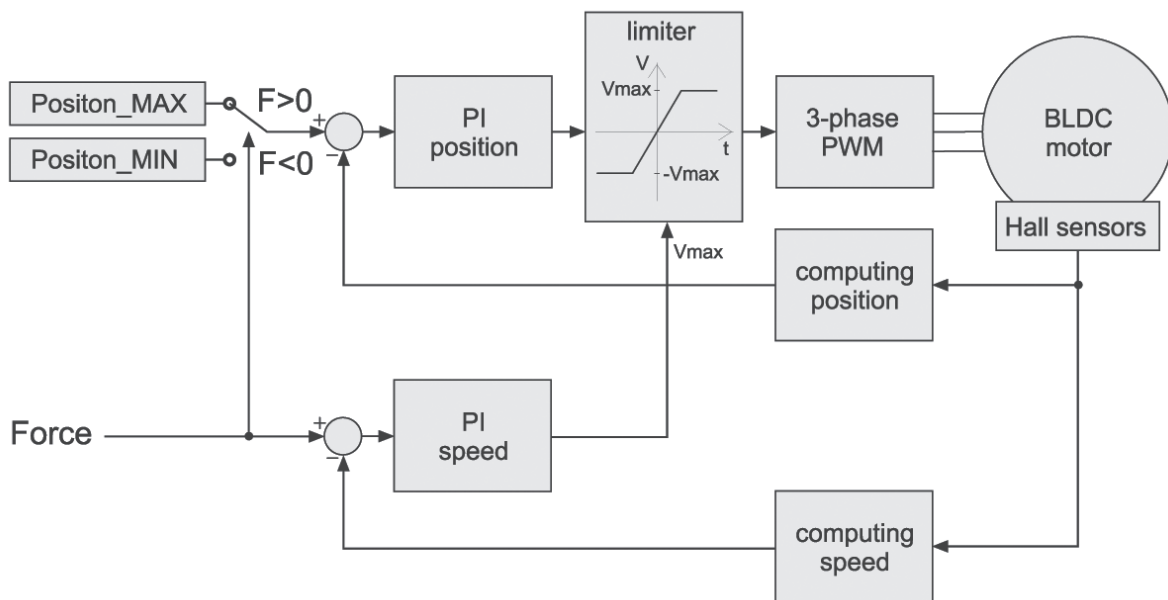


Fig. 10. A simplified block diagram of the force-support algorithm

4. Structure of the communication module

The communication module (Master module) mediates in communication between the computer application, which controls the workout and the performance modules. The communication module is responsible for receiving the data packet from the computer application via a USB interface, then for

distributing and sending sequentially the commands contained in it to individual Slave modules using the RS-485 bus, waiting for the answers of the Slave modules, and then sending the collected information to the control application via the USB interface. During the experiments, a significant impact of the access time of about 20 ms to the USB bus was observed. In order to limit the impact of this delay, commands and answers

sent via the USB interface were grouped into single packets as demonstrated in Fig. 11. In the current ARM-200 robot design, the Ethernet 100 MB interface, which is free from the above-mentioned disadvantage, is used to communicate with the computer.

An additional function of the communication module is to disconnect the power supply from the robot drives when one of the two emergency stop switches is pressed by means of relays built into the communication module shown in Fig. 12.

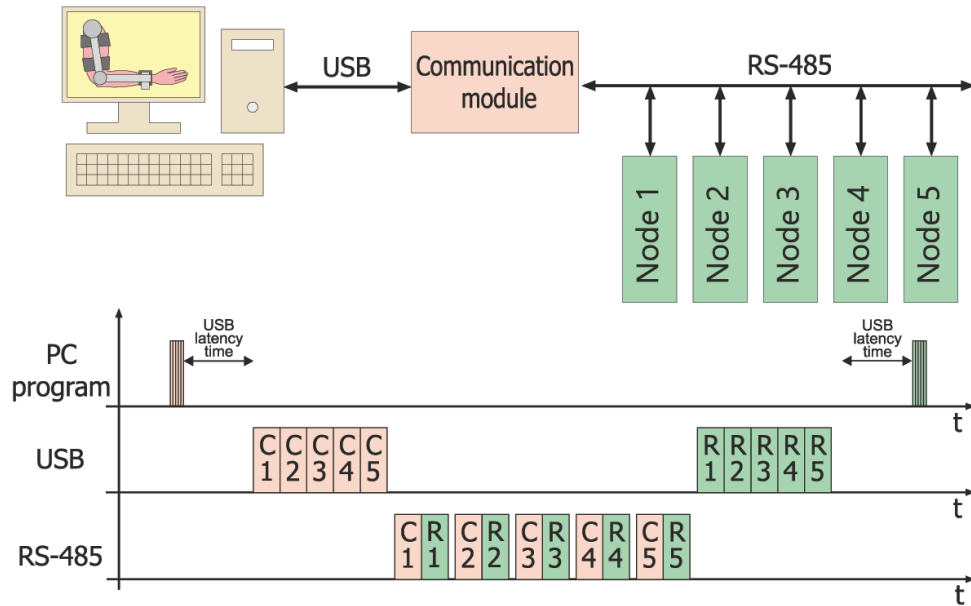


Fig. 11. A photo of the elements of the communication module

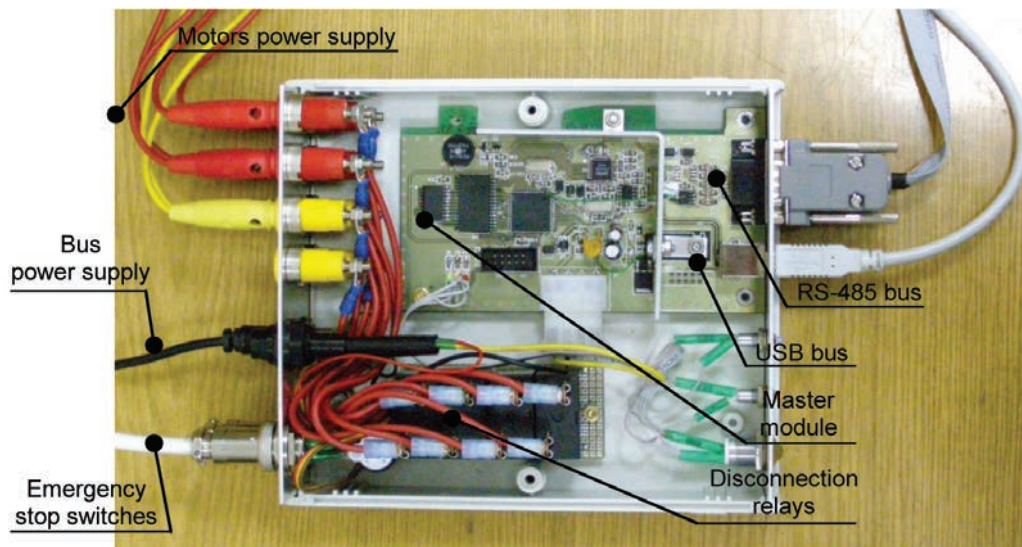


Fig. 12. A photo of the elements of the communication module

5. Computer application

The main element of the control system of the robot is a training control application installed on a PC. The application makes it possible to configure the parameters of performance nodes, present the status of individual performance nodes, and give commands. In the basic scenario, the movement trajectory learning mode can be

started by pressing the RECORD button. After entering the trajectory, the trajectory playback mode can be started with the set number of repetitions by pressing the PLAY button. The trajectory is replayed back and forth from the first to the last sample and then from the last to the first sample. As shown in Fig. 13, the application window makes it possible to monitor the parameters of the robot. This is a test application used to evaluate the operating parameters of the device.

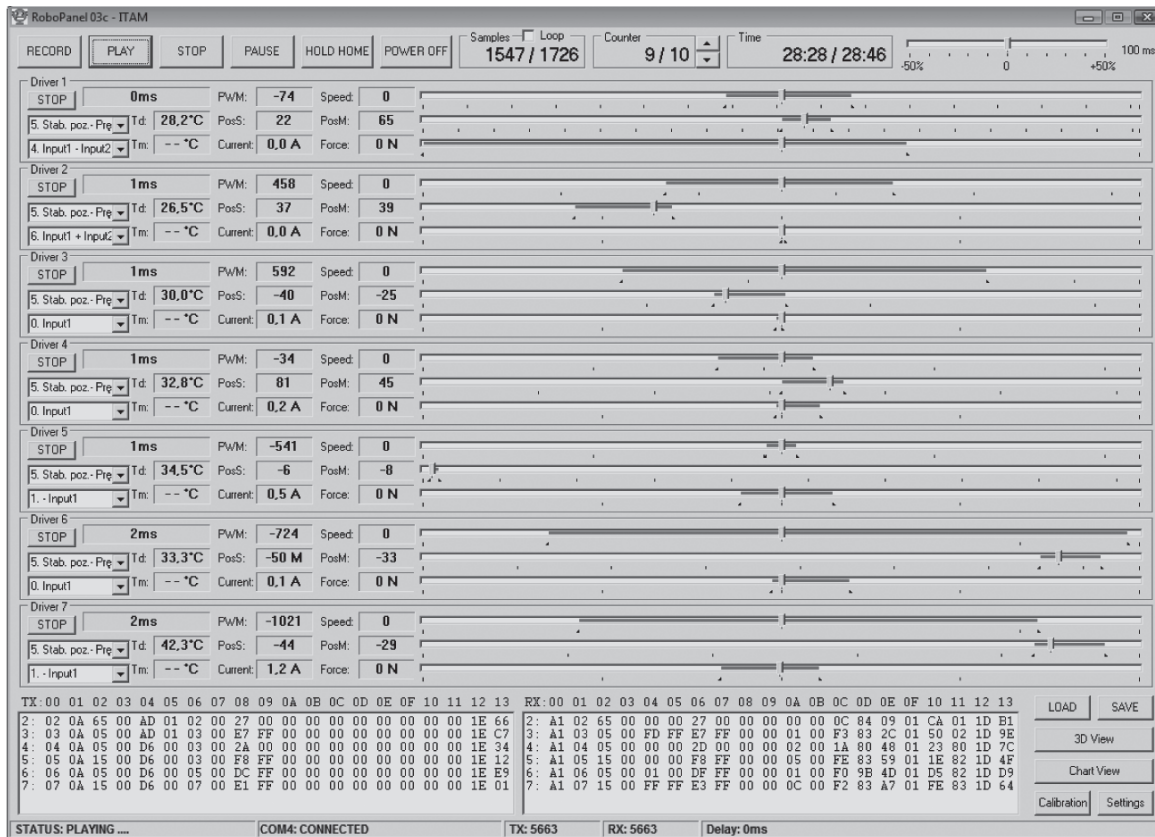


Fig. 13. The main window of the application controlling the ARM-100 rehabilitation robot

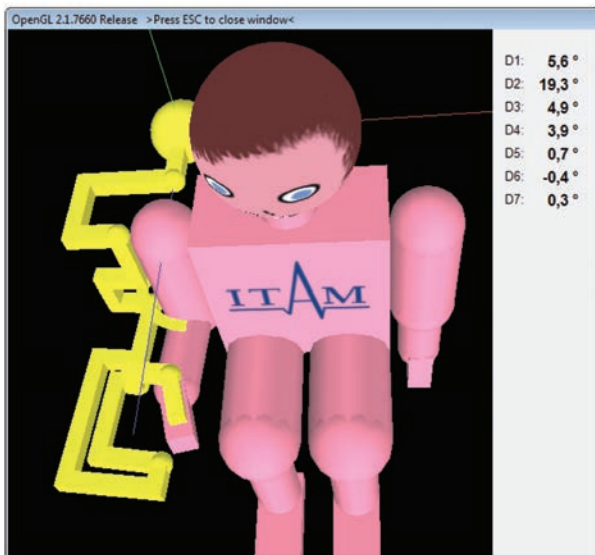


Fig. 14. 3D visualization windows of the ARM-100 robot: without the patient's visualization and with the patient

In order to better evaluate the robot's performance, a visualization of the robot's components has also been developed (Fig. 14) by means of the OpenGL standard function [9,10], with the use of appropriately modified

basic objects, such as a sphere, a cuboid, and a cylinder. The obtained information on rotations in individual physical nodes of the robot was used to animate the virtual robot in the application window in real time. The computer application of the current design of the ARM-200 robot will be equipped with simple 3D games to make the rehabilitation process more attractive, and, in addition, the games will be an important factor stimulating the regeneration of the patient's nervous system.

6. A prototype of the arm-100 robot

The end result of the project was the construction of a prototype of a rehabilitation robot with seven degrees of freedom (Fig. 15), containing the control system that has been described above. The design is based on drives from the Swiss company MAXON MOTOR, consisting of BLDC motors and planetary or cylindrical gearheads. In the current design of the ARM-200 robot, planetary gearheads have been replaced with harmonic gears in several nodes, which make it possible to significantly reduce the size of drive elements as well as to eliminate additional bearings and backlash in gears.



Fig. 15. A photo of the prototype of the ARM-100 robot

Summary

This work presents the stages of building a prototype of the ARM100 rehabilitation robot from the vantage point of the control system, without focusing on the mechanical challenges of the design. The aim of the paper is to present the path from a simple idea behind a single node of a control system to a working prototype. Current work on the new design of the ARM200 robot shows new hardware capabilities that enable the completion of tasks with greater accuracy, capabilities, and safety. An example can be power transistors, which at present are in the same housing, have ten times lower conductivity resistance. This translates into a significant reduction in the power lost in drive controllers. Another instance of a technological leap forward between the prototype of the ARM100 robot and the present version is the available microcontrollers. The previously used 8-bit microcontroller processed data with a 10 MHz clock, while the currently selected microcontroller is a 32-bit device with a 240 MHz clock. Moreover, the new microcontroller has a number of internal structures to carry out hardware tasks in order to relieve the processor. The paper is also aimed to inspire other engineers to build low-level solutions, such as drive controllers or 3D visualization using simple OpenGL functions.

References

1. Zambaty A. (ed.): *Kinezyterapia*. Kraków: Wydawnictwo „Kasper”, 2002.
2. Kwolek A., Drużbicki M., Przysada G.: *Zasady rehabilitacji szpitalnej chorych po udarze mózgu. Postępy Rehabilitacji*, 2004, 18(3), pp. 7–9.
3. Najwyższa Izba Kontroli: *Realizacja Zadań Narodowego Funduszu Zdrowia w 2017 Roku*. Nr ewid. 156/2018/P/18/055/KZD, 2018.
4. Blauth W.: *The CPM therapy with motorized exercise devices*. München: Urban&Vogel, 1992.
5. Nef T., Riener R.: Three-dimensional multi-degree-of-freedom arm therapy robot (ARMin). In: Dietz V., Nef T., Rymer W.Z. (eds): *Neurorehabilitation technology*. London: Springer; 2012, pp. 141–57.
6. Bongsu K., Ashish D.: An upper-body rehabilitation exoskeleton Harmony with an anatomical shoulder mechanism: Design, modeling, control, and performance evaluation. *The International Journal of Robotics Research*, 2017, 36(4), pp. 414–435.
7. Michnik R., Jurkojć J., Rak Z., Mężyk A., Paszenda Z., Rycerski W., Janota J., Brandt J.: Kinematic analysis of complex therapeutic movements of the upper limb. *Information Technologies in Biomedicine*, 2008, 47, pp. 551–558.
8. Michnik R., Jurkojć J., Rak Z., Mężyk A., Paszenda Z., Rycerski W., Janota J., Brandt J.: Analiza kinematyki ruchów kończyny górnej podczas wykonywania ćwiczeń rehabilitacyjnych metodą PNF. *Modelowanie Inżynierskie*, 2008, 36, pp. 243–248.
9. Matulewski J.: *C++Builder 2006–222 gotowe rozwiązania*. Gliwice: Wyd. Helion, 2006, pp. 391–423.
10. Hawkins K., Astle D.: *OpenGL. Programowanie gier*. Gliwice: Wyd. Helion, 2003.

This article appeared in its printed version in *Journal of Machine Construction and Maintenance*. The electronic version is published in DEStech Publications, Inc., Lancaster, PA, 2019, Proceedings of FUTURE ENGINEERING CONFERENCE.

Piotr TYCZYŃSKI^a, Zbigniew SIEMIĄTKOWSKI^{b,*}, Mirosław RUCKI^b

^a Mapal Narzędzia Precyzyjne Sp. z o.o., Poznań, Poland

^b Faculty of Mechanical Engineering, Kazimierz Pułaski University of Technology and Humanities in Radom, Poland

* Corresponding author: z.siemiatkowski@uthrad.pl

DRILL BASE BODY FABRICATED WITH ADDITIVE MANUFACTURING TECHNOLOGY: STRUCTURE, STRENGTH AND RELIABILITY

© 2019 Piotr Tyczyński, Zbigniew Siemiątkowski, Mirosław Ruck

This is an open access article licensed under the Creative Commons Attribution International License (CC BY)

 <https://creativecommons.org/licenses/by/4.0/>

Key words: additive manufacturing, selective laser melting, porosity, drilling, drill body design, coolant ducts.

Abstract: The paper presents an investigation of results on an additive manufactured drill base body. Due to the technological and strength limitations, conventional drills with inner coolant ducts may not be smaller than 13 mm diameter. The novel idea was to keep the strength of small diameter drills making spiral coolant ducts. Drills were fabricated using a 3D laser printer to obtain the designed geometry in a way not affecting its stiffness and strength. The tensile strength of samples was between $R_m = 1287$ and 1603 MPa, and microhardness of drills was between 606 and 627 HV5. The sintered material revealed a very small porosity rate (below 1%) and very few discontinuities. Thus, it was demonstrated that the 3D laser printing enabled the production of advantageous drill base bodies.

Korpus wiertła wykonany za pomocą technologii addytywnej: struktura, wytrzymałość i trwałość

Słowa kluczowe: technologie addytywne, technologia selektywnego topienia laserowego, porowatość, wiercenie, konstrukcja korpusu wiertła, kanały chłodzące.

Streszczenie: W artykule przedstawiono wyniki badań korpusu wiertła wykonanego za pomocą technologii addytywnej. Ze względu na ograniczenia technologiczne i wytrzymałościowe tradycyjne wiertła z wewnętrznymi kanałami nie mogą mieć średnic mniejszych niż 13 mm. Zaprojektowano nowatorskie wiertła o mniejszych średnicach ze spiralnymi kanałami wewnętrznymi, które w mniejszym stopniu obniżają wytrzymałość korpusu. Wykonano je za pomocą laserowej drukarki 3D, gdyż uzyskanie takiego kształtu technologią tradycyjną jest bardzo utrudnione. Wytrzymałość próbek uzyskano w granicach od $R_m = 1287$ do 1603 MPa, a mikrotwardość pomiędzy 606 a 627 HV5. Uzyskany materiał wykazywał bardzo małą porowatość poniżej 1% i bardzo niewiele nieciągłości struktury. W ten sposób wykazano, że laserowy druk 3D daje możliwość wykonania korpusów wiertel o wysokiej wytrzymałości.

Introduction

Additive Manufacturing (AM) technologies are opening new opportunities in terms of the production paradigm and manufacturing possibilities [1]. Commonly known as “three-dimensional (3D) printing,” it is a recently invented computer dependent technology that has proven its success as an option for production of parts in a wide application range [2]. These are often highly complexity items, which could be very difficult or even impossible to be manufactured by other processes [3]. The absence of waste material, like chips resulting from machining, is also a great AM advantage in terms

of saving energy, material, tooling, and man power. It is considered more environmental friendly even though, for most AM processes, 3D printers use more energy than that of comparable conventional processes at process or machine levels [4]. In particular, selective laser melting demonstrated its enormous potential on generating functional structures and complex geometries through layer-by-layer fabrication [5].

“Rapid tooling” describes the additive manufacturing of tools, tool inserts, gauges, and moulds. The additive manufacturing of tool inserts is older than those of final products and was introduced in the early 1990s [6]. In the last decade, some companies started to deliver machine tools with replaceable inserts fixed in the holders

produced using the additive manufacturing processes [7]. Within the space of the laser printer, tool geometries can be created unhindered by machine clamps, tools, and production means [8].

The present study is dedicated to a drill base body made out of Maraging Steel 1.2709 fabricated with selective laser melting (SLM) technology [9]. This method can be described as a rapid manufacturing process and consists of the consolidation of various materials with a laser beam [10]. Several methods were proposed to monitor and in-process control the quality of the produced details, e.g., image data analysis that enabled the detection of structural defects [11].

Recent research provided interesting results on the general microstructure and mechanical properties of maraging steel after the SLM process and post heat treatment [12]. Other teams examined its tensile, fracture, and fatigue strength [13], microstructural evolution, nano-precipitation behaviour, and mechanical properties [14] as well as the influence of scan length on the properties of the thin-walled components [15]. In the present study, the strength and microstructure of the drill base body was examined in order to demonstrate that SLM technology is advantageous in the fabrication of these specific tools.

1. AM design of drill body

In the case of higher requirements for productivity and quality, through-tool metalworking fluids (MWF) systems are applied [16]. Tool holders with integrated extension arms are used, which are widely available from major drilling tool suppliers. When a through-MWF tool is connected to a properly equipped tool holder, the fluid flows through the tool's internal channels and out of the tool's nozzles. Drills with coolant ducts are capable of pressing the coolant directly into the cutting position [17]. The required flow rate is assured by high MWF pressure up to 250 bar and by the optimized cross-section of the internal channel [18]. However, larger cross-sections of coolant ducts lead to a decrease in the wall thickness, which makes the tool fragile. Additionally, the base body is weakened by the openings for the screws or other elements holding the inserts. Until recently, these drills were only offered in diameters of 13 mm or larger, because central coolant supply channels with Y-shaped outlets substantially reduced their strength [19].

Several models of the cooling lubricant flow were proposed, which is very important for understanding and providing sufficient cooling, and to help optimizing the arrangements of the internal coolant channels [20]. Normally, the friction in the helical channel is greater than that for straight duct [16]. Nevertheless, the flow inside helical drill coolant channel has been demonstrated to have a small dependence on angular velocity [21]. Moreover, the helical ducts placed along the flutes in the drill bodies fabricated with 3D printing technology did

not weaken the drill core. Figure 1 presents a view of the SLM produced drill body and its tomography.

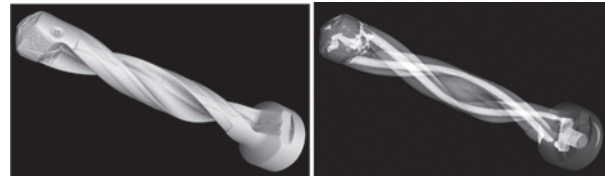


Fig. 1. Helical coolant ducts inside the drill base body

Layer-by-layer AM technology enables one to keep the coolant ducts diameters large enough for proper coolant flow, despite the small diameters of the drill itself. Moreover, the intersection of the coolant channel can be designed in any shape, e.g., the triangle shown in Fig. 2, which is absolutely unachievable in conventional technologies. In this way, it is possible to produce the insert drills with diameters as small as 8 mm, while keeping them strong.

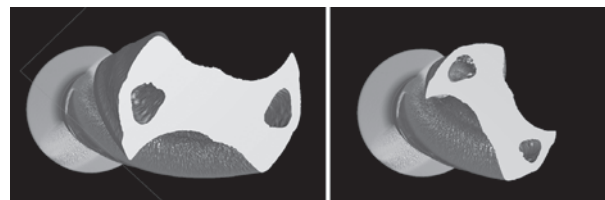


Fig. 2. Two intersections of the drill base body demonstrate a semi-triangle shape of the coolant ducts

The strength of the produced samples was calculated using the Finite Element Method (FEM). The analysis proved that the inner stresses in the drill base body fabricated in AM technology are ca. 50% smaller than that in the conventionally made ones. Figure 3 presents an example where inner stresses of the 3D-printed drill base body with triangle channels reach 820 MPa, while the ones for conventional steel drill base body of similar dimensions shown in Fig. 4 are as large as 1688.3 MPa [9].

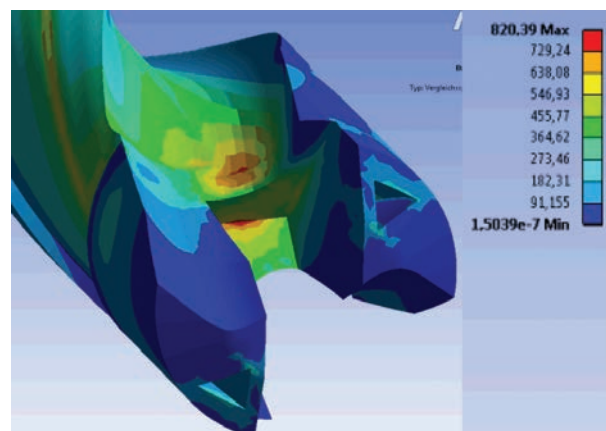


Fig. 3. Example of FEM analysis of the inner stresses in the 3D-printed drill base body [9]

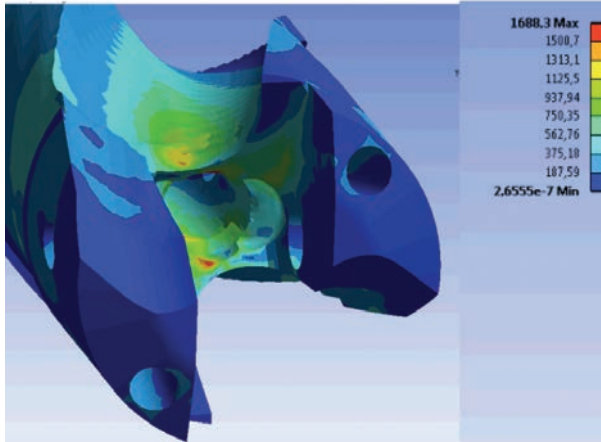


Fig. 4. Example of FEM analysis of the inner stresses in the conventionally fabricated drill base body [9]

2. Experimental conditions

The structure of the drill body was examined in order to determine its homogeneity and porosity, as well as microhardness. These features are very important for the drill's performance.

An Olympus BX51M microscope was used for metallographic analysis. The device enabled us to obtain the images in different lights, namely, white light, direct or reflected light, and polarized light, as well as in the interference contrast. The steady, stable, and shadeless exposition of the sample surface was ensured by a Koehler lighting system with smooth

regulation in the entire range. The surfaces exposed to the measurement were etched with 1% Nital. A camera adapter enabled capturing images and helped to perform acquisition, archiving, and morphometric measurements. Olympus Stream Essentials software was used in order to assess the porosity, i.e. percentage of the pores in the material structure. In Figure 5, a cross-section of the analysed drill body is shown with Points 1, 2, and 3 indicating where the porosity was measured. Figures 6a, b, and c present the images of its structure in the respective Points 1, 2, and 3. Red stains represent pores.

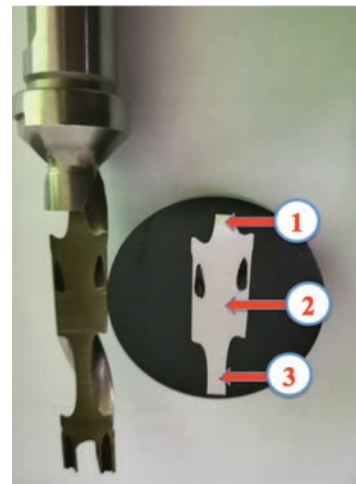


Fig. 5. The examined drill body prepared for porosity and microhardness measurements

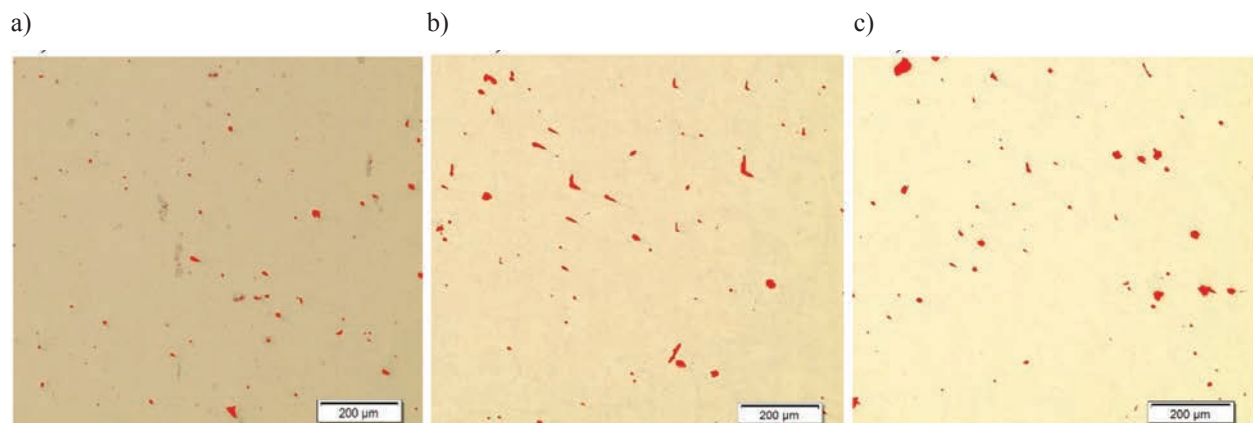


Fig. 6. Images of the drill body structure in the respective points

The hardness of the drill body fabricated with the SLM method was measured with a Qness Q250MS type device. The device is designed for the measurement of Brinell hardness according to the standard DIN EN ISO 6506, Vickers hardness (DIN EN ISO 6506), Rockwell hardness (DIN EN ISO 6508), and Koop microhardness (DIN EN ISO 4545). In the current research, the

methods HV5 and HV0.5 were applied. The former measurement was made in the points specified in Fig. 5, while the latter was repeated 50 times through the entire cross-section of the drill body. The distances between the points of HV0.5 microhardness were ca. 0.2 mm, as seen in Fig. 7.

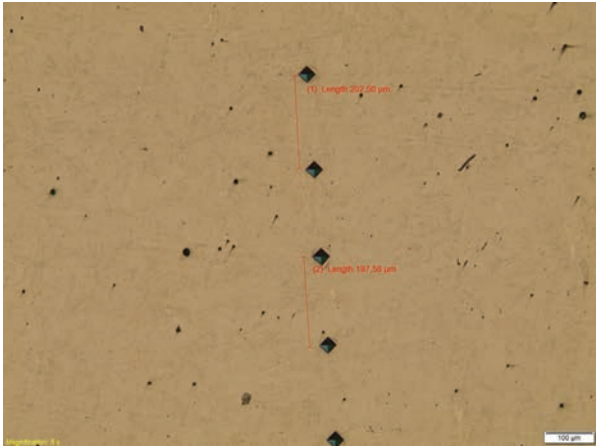


Fig. 7. HV0.5 microhardness measurement

Standard tensile testing was performed with an Instron 3382 device, according to the procedure described in PN-EN ISO 6892-1:2016-09. The 3382 Floor Model Universal Testing System has capacity up to 100 kN and maximum speed 500 mm/min. The force range is 100:1, i.e. using the load cell to 1.0% of its capacity causes no loss of accuracy. The Instron 3382 ensures the load accuracy at the level of 0.5% of the indicated load.

Moreover, fatigue tests were carried out in the laboratory of Rzeszow University of Technology, in accordance with the standard ASTM E466-15. The INSTRON 8801 device was used for the tests at room temperature. The samples underwent the sinusoidal alternating load with frequency of $f = 3$ Hz in conditions of one-sided tensile testing, where the tensions did not change their direction. The cycle asymmetry factor was $\sigma_{\min}/\sigma_{\max} = 0.05$. The maximal stress $\sigma_{\max} = 250$ MPa caused the destruction of the sample after 111,361 cycles, while at $\sigma_{\max} = 210$ MPa, the sample did not break even after 300,000 of cycles. Thus, it can be assumed that for the number of cycles $N_g > 300,000$, the expected fatigue strength of steel 1.2709 details made with SLM technology, in the one-sided tensile conditions, is between 210–250 MPa.

3. Results and discussion

3.1. Microstructure

The porosity of material at Points 1, 2, and 3 were calculated from the microstructure images shown in Figs. 6a, b and c, respectively. The pores percentage calculated by a Stream Essentials program was 0.35% for the Point 1, 0.87% for the Point 2 and 0.74% for the Point 3. As it is seen in Fig. 5, Point 1 with smaller percentage of pores is situated close to the drill holder. The rest of drill body reveals twice as many pores as the area represented by Point 1.

Apart from percentage, the influence of the pores on the drill performance is determined by their shapes and dimensions. Figure 8 presents the examples of pore analysis, where two pores of dimensions $37 \times 38 \mu\text{m}$ and $29 \times 39 \mu\text{m}$ are seen on the typical structure of the material with distinguishable curved melt pool lines. The latter correspond to the locally melted and rapidly solidified regions exposed to scanning laser irradiation [22]. In some cases, the pores had a more irregular shape as seen in Fig. 9, where the pores are slot-like along the melt pool lines. Here, the length of an area with pores forming a discontinuity chain is ca. 220 μm .

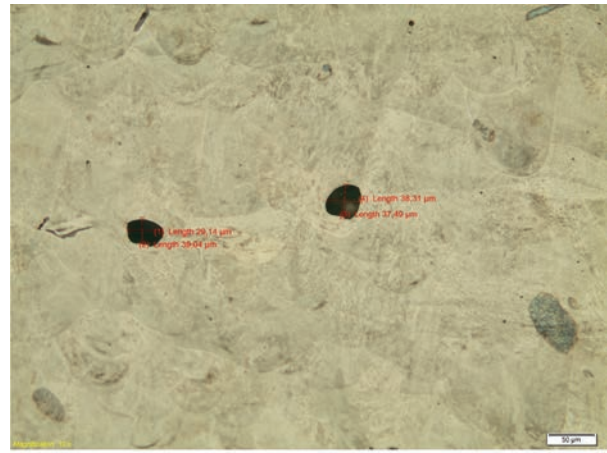


Fig. 8. Photomicrograph of the drill body intersection with semi-round pores

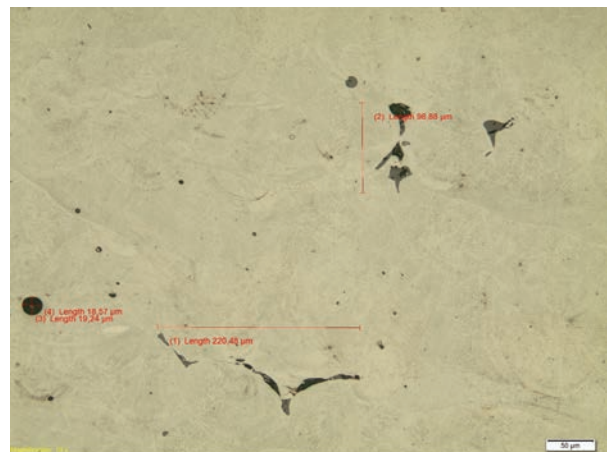


Fig. 9. Photomicrograph of the drill body intersection with pores formed along the melt pool lines

The globular pores were found throughout the entire surface of the analysed intersection. It was noted that they appeared more densely around the holes and close to the edges. The maximal dimension of a pore of this kind was 40 μm . Irregular shaped pores formed along the melt pool lines appeared rarely, and their length was typically below 220 μm .

In addition, the microstructure of edges should be mentioned. Especially in the case of the coolant ducts, the surface microstructure can heavily influence the thermal conditions of drilling process. Figure 10 illustrates how the surface of inner channels is formed.

Asperities made of melted material like dripstones stretch from the surface of coolant ducts. Their height, as seen in the photomicrographs, is ca. 140–180 μm , but some over 0.4 mm can be found. These are undesirable, since they may increase the coolant flow resistance.

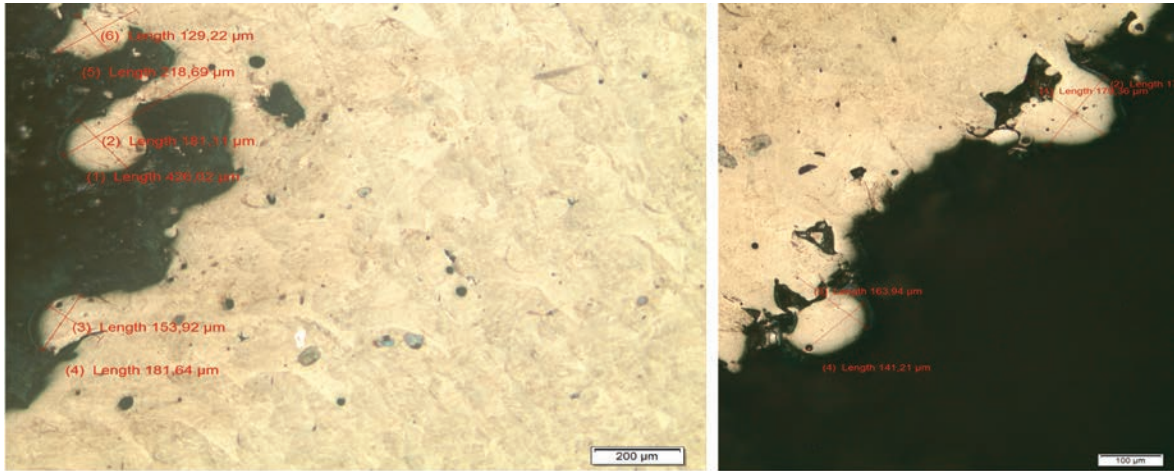


Fig. 10. Photomicrographs of the drill body coolant channels edges

3.2. Microhardness

Results of HV5 measurements are presented in Table 1.

Table 1. Microhardness at the points specified in Fig. 5

Point No.	Value	Method	Lens
1	627	HV5	20×
2	606	HV5	20×
3	619	HV5	20×

The results of microhardness measurement did not vary substantially in the measurement points and did not reveal any trend toward the drill holder or in the opposite direction. Its mean value was 617.3, and its range was $R = 21$, which is ca. 3% of the measured value.

Measurements in 50 subsequent points confirmed the high uniformity of hardness in the entire drill body. The results are presented graphically in Fig. 11.

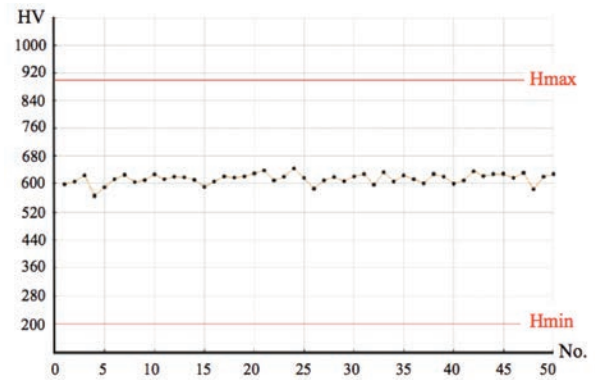


Fig. 11. Microhardness HV0.5 measured at the points specified in Fig. 7

Statistically, the measurement results revealed a very small standard deviation of $s = 15.1$ and a range of $R = 79$. The mean value was 614.3 HV0.5. The steady distribution of the hardness implies the uniformity of the drill body structure and suggests its strength [23, 24].

3.3. Strength of the material

Strain-stress curves for 5 samples of nominal diameter $d_0 = 6.0$ mm and gage length $l_0 = 25$ mm are shown in Fig. 10.

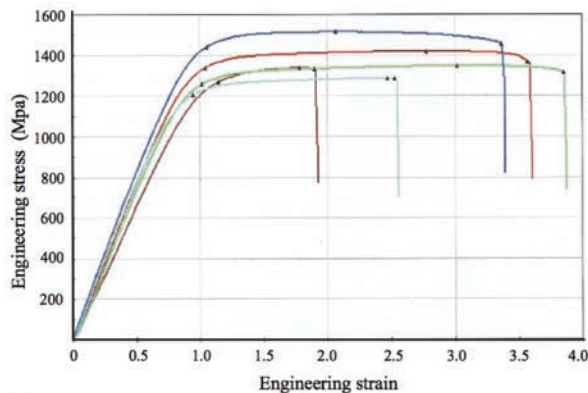


Fig. 12. Example of the strain-stress curves for maraging steel

The samples presented in Fig. 12 revealed a tensile strength between $R_m = 1290$ and 1520 MPa. However, a larger number of tested samples provided a much wider span of R_m values from 1287 up to 1603 MPa with a range of $R = 316$ MPa and a standard deviation of 97 MPa. The variations can be caused by the SLM production technology itself, because the layer-by-layer melting process generated a differentiated microstructure that remained layered despite the application of additional procedures. In the tested series, no correlation was noted between the microstructures and the strength, which may become the objective of further research.

Conclusions

The presented work demonstrated how additive technology could be applied in the production of a drill base body. The novel idea was to achieve spiral coolant ducts along the flutes without weakening the drill core. The research was aimed at assessing the strength and structure of the maraging steel drill bodies produced out of powder with SLM additive technology. The following conclusions can be made:

- 1) Standard strength and fatigue tests proved the good characteristics of the material, even though the tensile strength R_m varied to a high degree for different samples.
- 2) The microstructure of the drill body revealed uniform porosity with a little higher pore percentage at the edges, and smaller percentage of pores close to the drill holder. Occasionally, larger pores in form of slots along the melt pool lines appeared.
- 3) Microhardness HV0.5 measured on the entire length of the drill body proved the highly uniform properties of the detail.

Some problem with the application of the SLM technology for drill base body with inner coolant ducts was posed by the structure of the surface of the channels. High asperities may significantly increase the flow

resistance, which may worsen the cooling conditions of the drilling process. However, the merit from spiral coolant ducts is much more important, because they enable one to fabricate drills of much smaller diameters than that with straight ducts made using conventional technologies. The SLM production of drill base bodies, however, seemed to be limited to ca. 8 mm diameter. Thinner drills did not ensure the required strength.

From the practical perspective, the study demonstrated good properties of the 3D printed maraging steel drill base bodies. They may successfully replace the traditional drills with inner coolant ducts produced with other technologies.

No clear correlation between the microstructure and the strength was noted, so the issue should be addressed in future research.

Acknowledgement

The research was made in the frames of project “New generation of the hydraulic cylinder FBW made with application of Additive Manufacturing and machining technology at low temperatures (cryogenics),” Activity 1.2 of Sector Programs B+R, POIR 2014-2020, project No. POIR.01.02.00-00-0010/15.

References

1. Attaran M.: The rise of 3-D printing: The advantages of additive manufacturing over traditional manufacturing. *Business Horizons*, 2017, 60(5), pp. 677–688, DOI: 10.1016/j.bushor.2017.05.011.
2. DebRoy T., Wei H.L., Zuback J.S., Mukherjee T., Elmer J.W., Milewski J.O., Beese A.M., Wilson-Heid A., De A., Zhang W.: Additive manufacturing of metallic components – Process, structure and properties. *Progress in Materials Science*, 2018, 92, pp. 112–224, DOI: 10.1016/j.pmatsci.2017.10.001.
3. Umaras E., Tsuzuki M.S.G.: Additive Manufacturing – Considerations on Geometric Accuracy and Factors of Influence. *IFAC PapersOnLine*, 2017, 50(1), pp. 14940–14945, DOI: 10.1016/j.ifacol.2017.08.2545.
4. Rejeski D., Zhao F., Huang Y.: Research needs and recommendations on environmental implications of additive manufacturing. *Additive Manufacturing*, 2018, 19, pp. 21–28, DOI: 10.1016/j.addma.2017.10.019.
5. Zhang J., Tai W.G., Wang H., Kumar A.S., Lu W.F., Fuh J.Y.H.: Magnetic abrasive polishing of additively manufactured 316L stainless steel parts. *Euspen's 18th International Conference & Exhibition 4-8 June 2018, Venice (Italy)*. Proceedings, pp. 401–402.

6. Gebhardt A., Hötter J.S.: *Additive Manufacturing*. Munich: Hanser Publishers, 2016.
7. Sandvik Coromant: *Main website*. Online.. 2017. Accessed 30 December 2017. Available from: www.sandvik.coromant.com
8. Mapal: *Main website*. Online. 2017. Accessed 30 December 2017.. Available from: www.mapal.com
9. Tyczyński P., Siemiątkowski Z., Rucki M.: Analysis of the drill base body fabricated with Additive Manufacturing technology. *Euspen's 18th International Conference & Exhibition 4–8 June 2018, Venice (Italy)*. Proceedings, pp. 287–288.
10. Xue L.: *Laser Consolidation – A Rapid Manufacturing Process for Making Net-Shape Functional Components*. In: Lawrence J. (ed.): *Advances in Laser Materials Processing: Technology, Research and Applications*, 2nd edition, London: Woodhead Publishing, 2018, pp. 461–505.
11. Grasso M., Caltanissetta F., Petrò S., Colosimo B.M.: In-situ Monitoring of Geometric Accuracy in Laser Powder Bed Fusion processes. *Euspen's 18th International Conference & Exhibition 4–8 June 2018, Venice (Italy)*. Proceedings, pp. 293–294.
12. Mutua J., Nakata Sh., Onda T., Chen Zh.Ch.: Optimization of selective laser melting parameters and influence of post heat treatment on microstructure and mechanical properties of maraging steel. *Materials & Design*, 2018, 139, pp. 486–497, DOI: 10.1016/j.matdes.2017.11.042.
13. Suryawanshi J., Prashanth K.G., Ramamurty U.: Tensile, fracture, and fatigue crack growth properties of a 3D printed maraging steel through selective laser melting. *Journal of Alloys and Compounds*, 2017, 725, pp. 355–364, DOI: 10.1016/j.jallcom.2017.07.177.
14. Tan Ch., Zhou K., Ma W., Zhang P., Kuang T.: Microstructural evolution, nanoprecipitation behavior and mechanical properties of selective laser melted high-performance grade 300 maraging steel. *Materials & Design*, 2017, 134, pp. 23–34, DOI: 10.1016/j.matdes.2017.08.026.
15. Li Zh., Xu R., Zhang Zh., Kucukkoc I.: The influence of scan length on fabricating thin-walled components in selective laser melting. *International Journal of Machine Tools and Manufacture*, 2018, 126, pp. 1–12, DOI: 10.1016/j.ijmachtools.2017.11.012.
16. Astakhov V.P.: *Drills: Science and Technology of Advanced Operations*. Boca Raton: CRC Press, 2014.
17. Tschätsch H.: *Applied Machining Technology*. Heidelberg – London: Springer, 2009.
18. Heisel U., Stortchak M., Eisseler R.: *Optimization of Deep Hole Drilling Processes with Smallest Drilling Diameters*. In: Inasaki I. (ed.): *Initiatives of Precision Engineering at the Beginning of a Millennium*. New York: Kluwer Academic Publishers, 2002, pp. 157–163.
19. Hendrixson S.: *Additive Manufacturing Makes Subtractive Cutting Tools*. [Online]. 2015. Accessed 9 July 2018.. Available from: <https://www.additivemanufacturing.media/articles/additive-manufacturing-makes-subtractive-cutting-tools>
20. Schnabel D., Özkay E., Biermann D., Eberhard P.: Modeling the motion of the cooling lubricant in drilling processes using the finite volume and the smoothed particle hydrodynamics methods. *Computer Methods in Applied Mechanics and Engineering*, 2018, 329, pp. 369–395, DOI: 10.1016/j.cma.2017.09.015.
21. Johns A.S., Hewson R.W., Merson E., Summers J.L., Thompson H.M.: *Internal twist drill coolant channel modelling using computational fluid dynamics*. In: Oñate E., Oliver J., Huerta A. (eds.): *Proceedings of 6th European Conference on Computational Fluid Dynamics (ECFD)*, 2014, II, pp. 1114–1122.
22. Takata N., Nishida R., Suzuki A., Kobashi M., Kato M.: Crystallographic Features of Microstructure in Maraging Steel Fabricated by Selective Laser Melting. *Metals*, 2018, 8, pp. 440–450, DOI: 10.3390/met8060440.
23. Umamoto M., Liu Z.G., Tsuchiya K., Sugimoto S., Bepari M.M.A.: Relationship between hardness and tensile properties in various single structured steels. *Materials Science and Technology*, 2001, 17(5), pp. 505–511, DOI: 10.1179/026708301101510339.
24. Zhang P., Li S.X., Zhang Z.F.: General relationship between strength and hardness. *Materials Science and Engineering: A*, 2011, 529(25), pp. 62–73, DOI: 10.1016/j.msea.2011.08.061.

This article appeared in its printed version in Journal of Machine Construction and Maintenance. The electronic version is published in DEStech Publications, Inc., Lancaster, PA, 2019, Proceedings of FUTURE ENGINEERING CONFERENCE.

Edwin GEVORKYAN^a, Mirosław RUCKI^{b, *}, Vladimir CHISHKALA^c, Maksim KISLITSA^a,
Zbigniew SIEMIĄTKOWSKI^b, Dmitrij MOROZOW^b

^a Ukrainian State University of Railway Transport, Kharkov, Ukraine

^b Faculty of Mechanical Engineering, Kazimierz Pulaski University of Technology and Humanities in Radom, Poland

^c V.N. Karazin Kharkiv National University, Kharkov, Ukraine

* Corresponding author: m.rucki@uthrad.pl

HOT PRESSING OF TUNGSTEN MONOCARBIDE NANOPOWDER MIXTURES BY ELECTROCONSOLIDATION METHOD

© 2019 Edwin Gevorkyan, Mirosław Rucki, Vladimir Chishkala, Maksim Kislitsa, Zbigniew Siemiątkowski, Dmitrij Morozow

This is an open access article licensed under the Creative Commons Attribution International License (CC BY)

 <https://creativecommons.org/licenses/by/4.0/>

Key words: nanopowders, electroconsolidation, compaction, hot pressing, nanostructure.

Abstract: The paper presents theoretical and experimental results in the field of the manufacturing of cemented tungsten carbide materials. The important issue of avoiding any additional substances like plasticizers was challenged in order to reach the maximal possible density of sintered material while keeping its purity. To solve the problem, the electroconsolidation method of hot pressing supported by direct current was applied. The respective apparatus was constructed that enabled WC nanopowders to be sintered under pressure and high temperature during a very short time of ca. 3 minutes. In the experiments, because of the short heating time, grain size of the sintered bulk WC increased insignificantly, in general, remaining smaller than 1 μm . Similarly, sintering under hot pressing with direct current, a mixture of 3% by weight Y_2O_3 stabilized ZrO_2 and 50% by weight WC, produced a fine structure with a uniformly distributed WC grains. The applied electric field led to the formation of a temperature gradient around the pores, with a favourable impact on the compaction of large pores and an increase in the final density of the bulk material. The experimental research confirmed that the main mechanism of the densification of nanodispersed powders of tungsten monocarbide was a locally inhomogeneous diffusion-viscous flow with intergranular slipping.

Spiekanie mieszanek nanoproszków węglików wolframu metodą elektrokonsolidacji

Słowa kluczowe: nanoproszki, elektrokonsolidacja, kompaktacja, spiekanie, nanostruktura.

Streszczenie: W artykule przedstawiono rozważania teoretyczne i wyniki badań eksperymentalnych dotyczących wyrobów z węglików wolframu uzyskiwanych metodą spiekania. Podjęto próbę rozwiązania jednego z problemów, jakim jest obecność substancji uplastyczniających, która wspomagając proces spiekania jednocześnie utrudnia uzyskanie maksymalnej gęstości gotowego materiału. W celu rozwiązania tego zagadnienia zastosowano metodę elektrokonsolidacji, polegającą na spiekaniu wspomaganym przepływem prądu elektrycznego. Skonstruowana aparatura umożliwia spiekanie proszków węglika wolframu w bardzo krótkim czasie rzędu 3 minut. W badaniach eksperymentalnych wykazano, że krótki czas oddziaływania wysokiej temperatury na wzrost ziaren w strukturze spieku jest nieznaczny i rozmiary ziaren pozostają na poziomie 1 μm . Podobnie mieszanka 3% masy Y_2O_3 stabilizowanego ZrO_2 z 50% masy WC umożliwiła uzyskanie spieku o strukturze zawierającej równomiernie rozłożone ziarna węglika wolframu. Zastosowanie prądu elektrycznego powoduje wytworzenie gradientu temperatury wokół porów, korzystnie wpływając na proces kompaktacji i zwiększając wynikową gęstość spieku. Wyniki eksperymentów potwierdziły główne założenia stosowane w opisie teoretycznym kompaktacji nanodispersyjnych proszków węglika wolframu.

Introduction

Nanostructure science and technology is a multidisciplinary field of research that includes bulk nanostructured materials [1]. Many materials, like polymers, by virtue of their structural features are

always nanostructural systems [2]. The nanostructured ceramic materials are not a new development, because the very nature of the minerals taking part in the porcelain formation has resulted in features of the dimensions below 100 nm, which is considered “nanoscale” [3]. Recently, nanostructured materials found their

applications in many advanced technologies, such as thermomechanics, aerospace, nuclear power plants, and biomedicine [4]. In traditional engineering and manufacturing processes, nanostructure applications are especially found in the form of nanoceramic and nanocomposite coatings [5] or thin films [6].

Numerous researches have shown that nanostructured ceramics have unique properties and performance characteristics in comparison with coarse-grained analogues [7–10]. It has an increased crack resistance (toughness), strength, and toughness, and potentially allows the parameters of the “ceramic steel” [11] to be reached. Functional nanoceramics (piezoelectric, ferroelectric, dielectric, superconducting, etc.) significantly improve the electro-physical and magnetic properties.

In the cemented tungsten carbide materials, to obtain a unique combination of exceptional properties, a cobalt matrix is traditionally used as a bond, and a non-hazardous iron-based alloy binder phase was proposed [12]. Among manufacturing methods of nanostructured ceramics, spark plasma sintering (SPS) technology is reported to be very successful and promising [13–14]. As a modification, high pressure pulsed electric current activated equipment with a large volume chamber was proposed, reportedly capable of reaching high pressures up to 6 GPa and temperatures up to 1800°C [15]. Chuvildeev et al. published a paper stating that, when using the SPS method with direct current, they were able to obtain samples of high-density nanostructured tungsten carbide with high hardness and improved fracture toughness [16]. It was demonstrated that the increase in the sintering time up to 2 hours ensured the increased density of the nanostructured WC pieces, and a temperature increase from 1300° up to 1400°C increased their microhardness [17].

The challenging task of developing competitive manufacturing technologies for products for various purposes made out of nanostructured ceramics is very relevant. One of the propositions supported by the experimental researches is presented below.

1. Theoretical background

Technologically, the most important operation in the process of manufacturing products out of nanopowders is the formation of compacts of the required form and quality. Both single-phase nanopowders and multiphase compositions (often highly complex) have metastability of the structural-phase state, a developed unit surface, and, as a result, a high surface activity, and agglomeration ability. As a rule, they are characterized by poor mouldability and compressibility due to the specificity of their physical and chemical properties. In particular, high interparticle and near-wall friction

caused by a high unit surface area, agglomeration, and a significant amount of absorbed impurities should be mentioned. Therefore, it is technologically difficult to ensure uniform density distribution in compacted nanopowders even in a simple form, and thus to preserve the nanostructure in the compacts in proper form during the sintering process. In other words, it is difficult to create conditions for inhibiting the growth of grains (preventing recrystallization) and for sintering high-quality nanoceramic products with specified functional parameters. It is also important to keep the chemical purity and the required phase composition of finished products.

In this respect, the issue of obtaining compacts with a uniform distribution of density in products of relatively complex shapes without the use of any plasticizers is relevant. The plasticizers should be avoided, because they are potential sources of impurities and additional porosity in the sintered samples. In this way, the internal stresses, delaminations, and cracks are minimized and, thus, the embryos of such macro-defects are eliminated during the sintering of compacts. One of these methods ensuring the production of products from nanopowders with a minimal and uniform distribution of defects is the method of hot pressing supported by direct current, which is called *electroconsolidation* [18]. In the present work, the process of hot pressing under direct current through a billet of nanopowders of tungsten monocarbide WC underwent investigation.

Materials based on tungsten carbide are most often used as wear-resistance for dragging and cutting tools. The composition of these materials includes a cobalt binder that binds the WC grains and allows the material to be compacted at relatively low temperatures. However, the cobalt bond reduces the hardness of the material, which is a parameter that largely determines the future wear resistance. It was demonstrated that the cutting inserts made out of pure WC have ca. 8–10 times higher wear resistance compared to WC-Co plates when cutting the steel X12M [9, 19]. Products made out of pure WC powders are often obtained by hot pressing and hot isostatic pressing [20]. The pressing temperature is usually 200–500°C above the sintering temperature of the WC-Co powder mixture, and as a result, materials with increased brittleness are obtained. To increase the toughness of the WC powder, some tungsten, carbon, carbides, and nitrides are added. The most effective methods for compacting hard-to-weld materials are methods of compacting with heating by electric current, such as SPS (Spark Plasma Sintering) and FAST (Field Activated Sintering Technique), which have been developed recently [21]. In these methods, a pulsating electric current is applied together with an external pressure (up to 100 MPa), which allows sintering at different heating rates. The sintering cycle is very short, usually 1–5 min, which ensures only a slight increase in grain growth. The explanation was proposed that,

during sintering, electric discharges could occur under electric current in the zones of interparticle contacts, which caused the formation of plasma, and lead to the cleaning and activation of the surface of the sintered powders [22]. Previous studies indicated that purification of the surface of the powder particles led to the formation of pure grain boundaries [23]. For example, when sintering Al powders, which have an inhomogeneous layer of Al_2O_3 on the surface about 5 nm thick, this layer was removed by an electric field, and the powder was compacted to full density [24].

The applied electric field leads to the formation of a temperature gradient around the pores with a favourable impact on the compaction of large pores. In the intermediate stages of sintering, a charge gradient is formed in the pore region of different sizes. The electrical resistance increases as the concentration of equipolar lines increases, as was illustrated by Raychenko [25] in Figure 1 (left). The corresponding increased heating in contact points between grains, caused by the electrical current, is illustrated in the Fig. 1 (right).

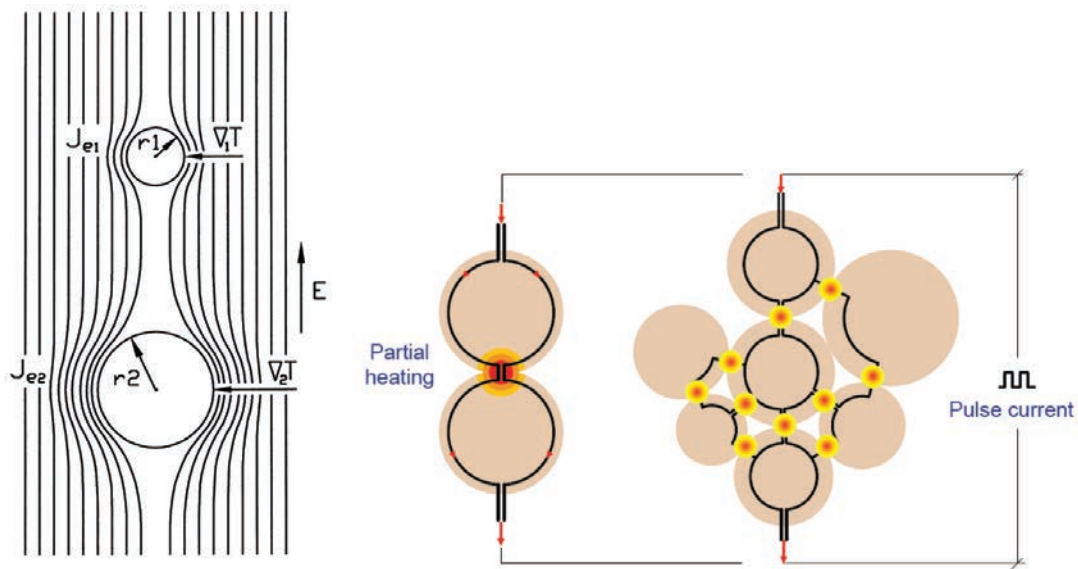


Fig. 1. Schemes of the electric field density in the temperature gradient in the work of large and small pores (left) [25] and partial heating in the contact zones between grains (right)

Source: left [25], right Authors.

The electric current density is higher in the region of large pores. This creates a temperature gradient, so the temperature is higher in the region of large pores. Raychenko obtained the following equation for calculating the temperature gradient ΔT near the pore [25]:

$$\Delta T \approx \frac{1}{R} \sqrt{\frac{\rho_0}{2C_M} \cdot \frac{T_0 E_0 \Delta \tau}{n}} \quad (1)$$

where R is the radius of the pore, ρ_0 is the electrical resistivity, C_M is the heat capacity, T_0 is the initial temperature, E_0 is the electric field strength, $\Delta \tau$ is the time of action of the electric field, and n is the number of electrical pulses.

The temperature gradient around the pores leads to the formation of the vacancy gradient ΔC_v . More vacancies are formed in the region of large pores [25]. The flow of vacancies J , can be represented in the following form:

$$J = D_v \left(\frac{k_T}{T} \Delta T - \Delta C_v \right) \quad (2)$$

where D_v is the diffusion coefficient of vacancies, and k_T is the coefficient of thermal diffusion.

According to Equation (2), vacancies diffuse from large pores to smaller ones, which leads to a reduction in the size of large pores. This process is the opposite of the process of vacancies diffusion under conditions of conventional furnace sintering, when the large pores grow due to small pores. In this case, the coalescence of the pores decelerates.

When hot pressing is performed under electric heating conditions (electroconsolidation), the compaction takes place during a short holding time, which prevents grain growth [26–27]. For example, SnO_2 powder was sintered to a density of 93% at 890°C for 10 minutes. At the same time, this powder

was compacted in ordinary furnace sintering at a temperature of 1000°C for 3 hours only to a density of 61% [27]. When electrosintering the TiN nanopowder, the total density was reached at a temperature of 1200°C and the obtained grain size was an order of magnitude lower than that obtained at traditional sintering at 1400°C [28]. The absence of a bundle during electrosintering made it possible to eliminate the process of cold pressing and stripping of the bundle. This stage took up to 30% of the cost of production by the powder metallurgy method [27]. Sintering of ceramics without additives by electric current made it possible to fabricate high-density ceramic, to increase significantly the wear resistance of the material, and to obtain high mechanical properties because of the direct binding of grains. High-density materials with a fine microstructure were obtained at relatively low temperatures and a short sintering time.

2. Experimental apparatus

To fabricate high-density products, a device for hot vacuum pressing with direct electric current was designed and manufactured. Figure 2 presents its overview (left) and scheme (right) with a description of the main units.

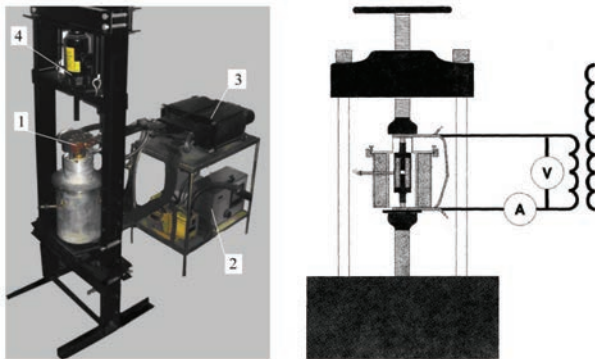


Fig. 2. Hot pressing machine: overall view (left) and scheme (right): 1 – hot vacuum pressing chamber, 2 – power supply unit, 3 – transformer TBK-75 with water-cooled current leads, 4 – hydraulic press HLR-12

Source: Authors.

With the developed apparatus, WC powder was sintered to a density of 99%. The obtained samples were of 20 mm diameter and 5 mm thickness. During the process, pressure was regulated manually and controlled with a special manometer. The initial powder was tungsten monocarbide obtained by the plasma-chemical method with the trade mark Tizit produced by the Austrian company Bergbau-und Hutten-GmbH Nfg as shown in Figure 3.

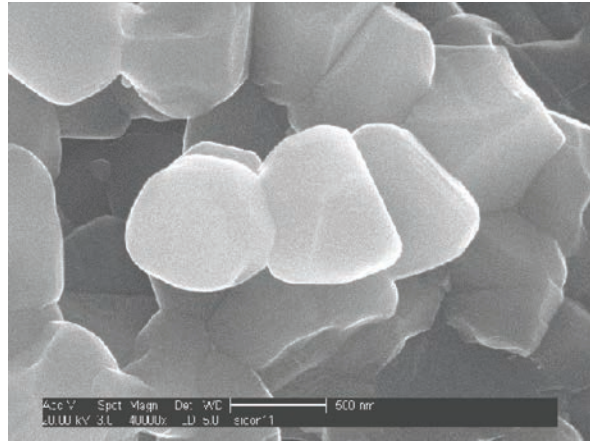


Fig. 3. Photomicrograph of pure WC initial powder

Source: Authors.

The specific surface area of the pure WC powder was 7 m²/g, and the apparent density was 1.22 g/cm³, with a particle size distribution of 60% – 40 nm, 30%–70.1% – 100 nm. According to the manufacturer of the powder, the abovementioned measurements were made with a CILAS HR850 granulometer. The content of tungsten monocarbide was 99.95%, and specific gravity was $\gamma = 15.63$ g/cm³. Pre-tableted tungsten carbide powder was sintered to the limit for the graphite MPG-7 at a pressure of about 50 MPa and a temperature above 1200°C. Therefore, the maximum pressure in the mould reached ca. 45 MPa. The shrinkage cessation temperature was 1700°C. Figure 4 presents the thermogram of the sintering procedure.

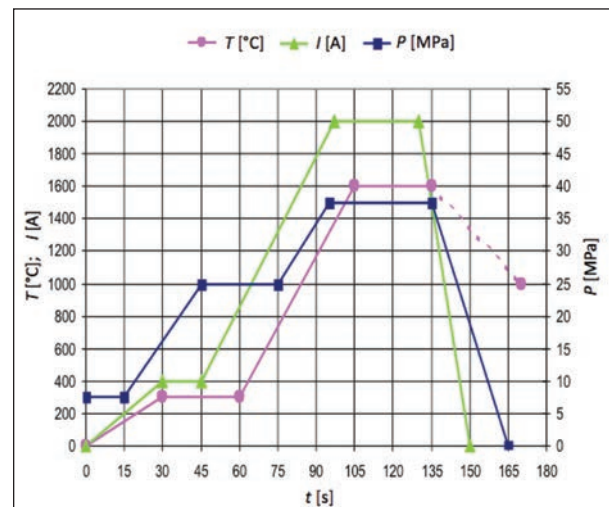


Fig. 4. Thermogram of sintering process under pressure and direct current

Source: Authors.

The density of the samples after grinding the surfaces were determined by hydrostatic weighing. The chips on their surface, like the powder form, were examined using a scanning electron microscope

JSM-840. The obtained material showed a high hardness $HV = 24.3$ GPa and $K_{Ic} = 6.1$ MPa·m^{1/2}. The grain size in the obtained samples was between 250 and 420 nm.

3. Results and discussion

Measurements of ρ density, hardness of HRA, tensile strength at bending (σ_{bd}), and grain size d_{av} of the samples obtained for different P and T were reported previously [24]. Table 1 presents the results for three samples sintered at $T = 1700^\circ\text{C}$ and $P = 40$ MPa during different time spans t . The dependence of grain size on the processing time is clear and unequivocal: When t was increased from 5 up to 10 min, grain sizes grew three times larger. Simultaneously, hardness HV and fracture toughness K_{Ic} decreased significantly, even below the values obtained after 2 minutes of a sintering process.

Table 1. Some physical and mechanical characteristics of the samples produced at $T = 1700^\circ\text{C}$ and $P = 40$ MPa

t [min]	ρ [g/cm ³]	HV [GPa]	K_{Ic} [MPa·m ^{1/2}]	d_{av} [nm]
2	96.2	23.0	5.5	350
5	99.0	24.3	6.1	400
10	99.0	21.0	4.5	1,200

The data presented in [24] and in the Table 1, as well as the structure observed with the electron microscope led to the conclusion that the process of high-temperature sintering under pressure should last 3–5 minutes. Under these conditions, the sintered WC grain size increased insignificantly, in general, remaining smaller than 1 μm , and the obtained material performed favourable characteristics. There is practically no porosity in the sintered material, as can be seen in the Figure 5.

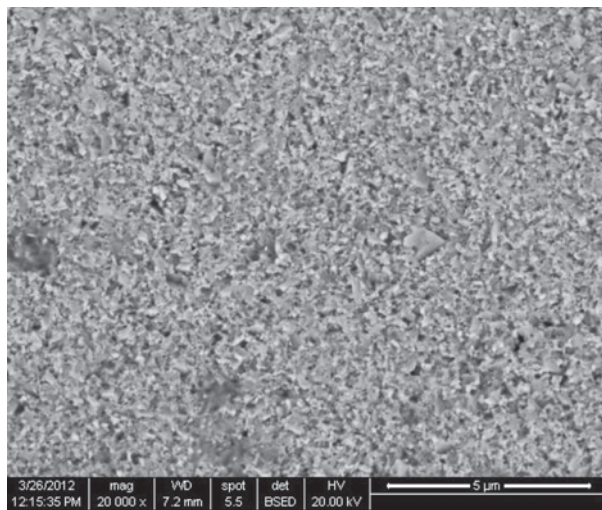


Fig. 5. Photomicrograph of pure WC structure sintered at $T = 1700^\circ\text{C}$ under pressure $P = 45$ MPa

Source: Authors.

That is why high values of $\sigma_{bd} = 720$ MPa were obtained. When WC the initial powders had a grain size between 2 μm and 5 μm , hot pressing at $T = 2500^\circ\text{C}$, during $t = 10$ min, under pressure $P = 12$ MPa, it produced a much smaller σ_{bd} value between 350 and 520 MPa. The examined nanostructured samples also exhibited a very high value of fracture toughness $K_{Ic} = 6.1$ MPa·m^{1/2} and a high HRA value, which is important for the ceramics applied in cutting tools.

The increase in the fracture toughness of the obtained materials made out of WC nanopowders in comparison with other reported values can be ascribed, first of all, to highly disperse grains and strong boundaries between them. The latter is predetermined by the short heat exposure time and not by the high sintering temperature. The method of hot pressing of nanopowders heated by direct current transmission accelerates the flow of vacancies on the pore surface [27]. However, a rapid decrease in porosity at the grain boundaries increases the mobility of the boundaries; therefore, the compaction due to grain deposition is a result of their sliding on the boundaries.

Interesting results are obtained by sintering nanopowder mixtures of tungsten monocarbide and partially stabilized yttria with zirconia. Some investigations were reported on the influence of WC particles on the microstructural and mechanical properties of 3mol% Y_2O_3 stabilized ZrO_2 matrix composites produced by hot pressing, where hard WC particles were added with various proportions up to 40 vol% [29]. In our research, during sintering under hot pressing with directly applied current, ZrO_2 stabilized with the addition of 3 wt% Y_2O_3 , which was mixed with WC powder in proportion of 50% by weight, forming a fine structure with uniformly distributed WC grains. Figure 6 presents the initial mixture of nanopowders, and Figure 7 shows the final nanostructured material obtained by hot pressing electroconsolidation at $T = 1450^\circ\text{C}$ and a pressure of 30 MPa, during the sintering time $t = 3$ min.

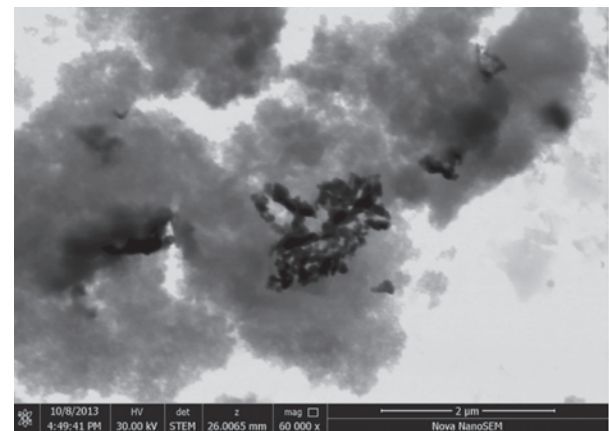


Fig. 6. The initial nanopowder mixture of 50 wt% WC and ZrO_2 stabilized with 3 wt% Y_2O_3

Source: Authors.

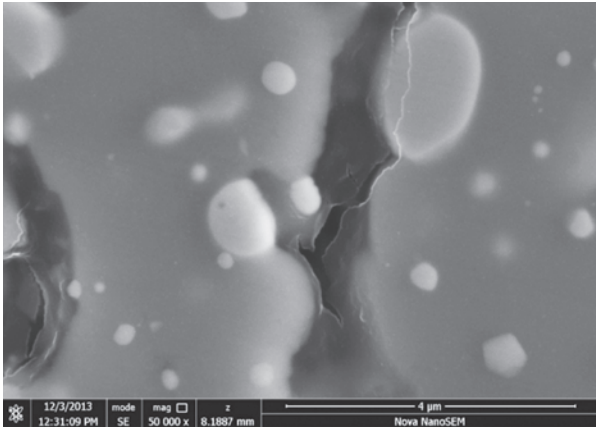


Fig. 7. The sintered nanostructure, obtained by hot pressing electroconsolidation at $T = 1450^{\circ}\text{C}$ and $P = 30\text{ MPa}$, sintering time 3 min

Source: Authors.

From the practical perspective, it is highly desirable to obtain better strength and toughness of the sintered material with less energy consumption. In the case of cutting tools inserts, their material and structure have an impact both on chip formation mechanisms [30] and on surface hardness [31]. The presented results demonstrated that the electroconsolidation method provided a nanostructural tungsten monocarbide compound of high properties with minimized energy losses. It can be assumed that the rapid decrease in porosity at the grain boundaries increases the mobility of the boundaries and improves the compaction of grains as a result of their sliding along the boundaries. In the initial stage of heating process, physical contact is formed between the particles and a branched boundary system, i.e. the free surface energy. That causes the system to become denser and to expand with the formation of boundaries, which subsequently releases excessive energy that plays the role of the driving force of the sintering process.

Conclusions

The presented researches on hot pressing electroconsolidation revealed improved physical and mechanical properties of the materials obtained from nanopowders of tungsten monocarbide WC in comparison with other reported ones. The following can be pointed out:

- The obtained properties are conditioned, first of all, by highly dispersed grains and strong boundaries between them, which is predetermined by short time and low sintering temperature.
- The method of hot pressing of nanopowders supported by direct current heating accelerates the flow of vacancies on the pore surface that resulted with higher density.

- As a consequence, better mechanical properties were obtained at lower energy consumption.

Acknowledgements

The research work reported here was made possible due to financial support by the Ministry of Science and Higher Education in Poland, research funds No. 3257/22/P on the subject “Modification of ceramic tool materials with ion implantation.”

References

1. Koch C.C. (ed.): *Nanostructured Materials: Processing, Properties, and Applications*. 2nd edition, Norwich, NY: William Andrew Inc., 2007.
2. Ciocoiu M.: *Materials Behavior: Research Methodology and Mathematical Models*. Waretown, NJ: Apple Academic Press Inc., 2018.
3. Cain M., Morell R.: Nanostructured ceramics: a review of their potential. *Applied Organometallic Chemistry*, 2001, 15, pp. 321–330.
4. Camargo N., Bellini O.J., Gemelli E., Tomiyama M.: Synthesis and characterization of nanostructured ceramics powders for biomedical applications. *Matéria (Rio J.)*, 2007, 12(4), pp. 574–582.
5. Makhlof A.S.H., Scharnweber D.: *Handbook of Nanoceramic and Nanocomposite Coatings and Materials*. Amsterdam: Elsevier-BH, 2015.
6. Guglya A., Kalchenko A., Solopikhina E., Vlasov V., Lyubchenko E.: Nanocrystalline Porous Thin Film VNx Hydrogen Absorbents: Method of Production, Structure and Properties. *Journal of Advances in Nanomaterials*, 2016, 1(1), pp. 1–10.
7. Andrievsky R.A., Glezer A.M.: Dimensional effects in nanocrystalline materials. 2. Mechanical and physical properties. *Fizika metallov i metallovedenie [Physics of Metals]*, 2000, 89(1), pp. 91–112 [in Russian].
8. Gleiter H.: Nanostructured materials: basic concepts and microstructure. *Acta Materialia*, 2000, 48(1), pp. 1–29.
9. Kodash V.Y., Gevorkian E.S.: Tungsten carbide cutting tool materials, 2003, United States Patent No. 6,617,271.
10. Gevorkian E.S., Gutsalenko Y.G., Chishkala V.A., Krishtal A.P.: Sintering of Al₂O₃ and WC powders activated by electric field. *Proceedings of 5th International Conference “Research and Development in Mechanical Industry” RaDMI*, Vrianska Banja, Serbia and Montenegro, September 2005, pp. 694–696.
11. Wessel J.K. (ed.): *The Handbook of Advanced Materials: Enabling New Designs*. Hoboken, NJ: Wiley-Interscience, 2004.

12. Pittari J.J., Murdoch H.A., Kilczewski S.M.: Sintering of tungsten carbide cermets with an iron-based ternary alloy binder: Processing and thermodynamic considerations. *International Journal of Refractory Metals and Hard Materials*, 2018, 76, pp. 1–11.
13. Gevorkian E., Lavrynenko S., Rucki M., Siemiątkowski Z., Kislitsa M.: Ceramic cutting tools out of nanostructured refractory compounds. *International Journal of Refractory Metals and Hard Materials*, 2017, 68, pp. 142–144.
14. Luo W., Liu Y., Luo Y., Wu M.: Fabrication and characterization of WC-AlCoCrCuFeNi high-entropy alloy composites by spark plasma sintering. *Journal of Alloys and Compounds*, 2018, 754, pp. 163–170.
15. Balima F., Bellin F., Michau D., Viraphong O., Poulon-Quintin A., Chung U.-Ch., Dourfaye A., Largeteau A.: High pressure pulsed electric current activated equipment (HP-SPS) for material processing. *Materials & Design*, 2018, 139, pp. 541–548.
16. Chuvil'deev V.N., Blagoveshchenskiy Yu.V., Nokhrin A.V., Boldin M.S., Sakharov N.V., Isaeva N.V., Shotin S.V., Belkin O.A., Popov A.A., Smirnova E.S., Lantsev E.A.: Spark plasma sintering of tungsten carbide nanopowders obtained through DC arc plasma synthesis. *Journal of Alloys and Compounds*, 2017, 708, pp. 547–561.
17. Sabzi M., Mousavi Anijdan S.H., Ghobeiti-Hasab M., Fatemi-Mehr M.: Sintering variables optimization, microstructural evolution and physical properties enhancement of nano-WC ceramics. *Journal of Alloys and Compounds*, 2018, 766, pp. 672–677.
18. German R.M.: *Consolidation Techniques*. In: Sarin V.K. (ed.): *Comprehensive Hard Materials*. Vol. 1, New York: Elsevier, 2014, pp. 237–263.
19. Liu Y., Wang Z., Sun Q.: Tribological behavior and wear mechanism of pure WC at wide range temperature from 25 to 800°C in vacuum and air environment. *International Journal of Refractory Metals and Hard Materials*, 2018, 71, pp. 160–166.
20. Eriksson M., Radwan M., Shen Zh.: Spark plasma sintering of WC, cemented carbide and functional graded materials. *International Journal of Refractory Metals and Hard Materials*, 2013, 36, pp. 31–37.
21. Quach D.V., Groza J.R., Zavaliangos A., Anselmi-Tamburini U.: *Fundamentals and applications of field/current assisted sintering*. In: Fang Zh.Z. (Ed.): *Sintering of Advanced Materials*. Cambridge: Woodhead Publishing Ltd., 2010, pp. 249–275e.
22. Schneider J.A., Groza J.R., Garcia M.: Surface Effects in Field-Assisted Sintering. *Journal of Materials Research*, 2001, 16(1), pp. 286–292.
23. Gevorkian E., Lavrynenko S., Rucki M.: Structure formation of hot pressed Al₂O₃ powders under the alternating electric current: experimental observations. *Advanced Materials Letters*, 2017, 8(10), pp. 945–949.
24. Gevorkyan E., Lavrynenko S., Rucki M., Siemiątkowski Z., Kislitsa M.: Preparation of nanostructured materials by electrical sintering. *Proceedings of the 7th International Conference on Mechanics and Materials in Design (M2D2017)*, Albufeira/Portugal June 2017. Editors J.F. Silva Gomes and S.A. Meguid, pp. 663–666.
25. Raychenko A.I.: *Fundamentals of the process of sintering powders by passing electric current*. Moskva: Metalurgia, 1987 [in Russian].
26. Scarlat O., Mihaiu S., Aldica G., Zaharescu M., Groza J.R.: Enhanced Properties of Tin(IV) Oxide Based Materials by Field-Activated Sintering. *Journal of the American Ceramic Society*, 2004, 86(6), pp. 893–897.
27. Groza J., Curtis J., Kramer M.: Field Assisted Sintering of Nanocrystalline Titanium Nitride. *Journal of the American Ceramic Society*, 2000, 83, pp. 1281–1283.
28. Gevorkyan E.S., Semchenko G.D., Kislitsa M.V., Chishkala V.A., Vovk S.R., Vovk R.V.: Synthesis by method of electro consolidation of SiC and WC, ZrO₂ nanocomposite materials with the high mechanical properties. *Physics*, 2017, 24, pp. 32–36.
29. Ünal N., Kern F., Öveçoğlu M.L., Gadow R.: Influence of WC particles on the microstructural and mechanical properties of 3mol% Y₂O₃ stabilized ZrO₂ matrix composites produced by hot pressing. *Journal of the European Ceramic Society*, 2011, 31(13), pp. 2267–2275.
30. Niu Zh., Jiao F., Cheng K.: An innovative investigation on chip formation mechanisms in micro-milling using natural diamond and tungsten carbide tools. *Journal of Manufacturing Processes*, 2018, 31, pp. 382–394.
31. Krolczyk G., Legutko S., Stoic A.: Influence of cutting parameters and conditions onto surface hardness of duplex stainless steel after turning process. *Tehnicki Vjesnik – Technical Gazette*, 2013, 20(6), pp. 1077–1080.

This article appeared in its printed version in Journal of Machine Construction and Maintenance. The electronic version is published in DEStech Publications, Inc., Lancaster, PA, 2019, Proceedings of FUTURE ENGINEERING CONFERENCE.

Dariusz OZIMINA^a, Monika MADEJ^a, Tomasz DESANIUK^{a,*}, Magdalena ŻÓŁTY^b, Andrzej KULCZYCKI^c

^a Faculty of Mechatronics and Mechanical Engineering, Kielce University of Technology, Poland

^b Oil and Gas Institute – National Research Institute, Cracow, Poland

^c Air Force Institute of Technology, Warsaw, Poland

* Corresponding author: desaniuk@gmail.com

EFFECTS OF A GRAPHENE-ENHANCED LUBRICANT ON THE PERFORMANCE OF A TRIBOSYSTEM

© 2019 Dariusz Ozimina, Monika Madej, Tomasz Desaniuk, Magdalena Żółty, Andrzej Kulczycki

This is an open access article licensed under the Creative Commons Attribution International License (CC BY)



<https://creativecommons.org/licenses/by/4.0/>

Key words: graphene, friction, wear, acoustic emission.

Abstract: The aim of the study was to determine how the presence of graphene in a lubricant (SN-500) affects the behaviour of a tribosystem. The tribological tests were conducted in lubricated, boundary lubricated, and dry sliding friction conditions using a tribometer with the pin and disc made of 100Cr6 steel. The pin and disc wear was monitored using the acoustic emission method. SpectraPLUS was employed to analyse the sampled signals written in the 16-bit linear pulse-code modulation format. Sound level measurements required applying an A-weighting filter and then 1/1 and 1/3 octave filters. The microstructural observations of the pin and disc that followed the tribological tests were performed using a scanning electron microscope. The surface texture of both specimens was measured with an optical profiler. Identification of the elements before and after tribological tests was performed using a scanning electron microscope equipped with an EDS X-ray microanalyser. The experimental data show that the most effective performance of the analysed tribosystem was observed in the presence of the graphene-enhanced lubricant.

Wpływ dodatku grafenu w olejach smarowych na właściwości systemów tribologicznych

Słowa kluczowe: olej bazowy, stal 100Cr6, grafen, zużycie, tarcie, pomiar dźwięku.

Streszczenie: Celem badania było porównanie wpływu grafenu w olejach smarowych na działanie systemów tribologicznych. Testy tribologiczne zostały zrealizowane na tribometrze TRB3 w ruchu ślizgowym w warunkach tarcia technicznie suchego, ze smarowaniem olejem SN-500 oraz z dodatkiem grafenem. Węzeł tarcia stanowiła próbka i przeciwpróbka wykonane ze stali 100Cr6. Dźwięk został zarejestrowany w standardzie Linear PCM 16-bit, a następnie poddany analizie w programie Spectra-Plus. Dla kolejnych chwil czasu wyznaczono wartości poziomu dźwięku, a także poziomy dźwięku w poszczególnych pasmach oktauwowych i 1/3-oktauwowych. Obserwacje struktury tarczy i kulki po testach tribologicznych wykonano mikroskopem skaningowym Phenom. Strukturę geometryczną powierzchni obu elementów zbadano za pomocą Profilometru optycznego Leica. W wyniku przeprowadzonych badań stwierdzono, że użycie środka smarowego wpłynęło na zmniejszenie zużycia badanych par tnących w systemach tribologicznych.

Introduction

The operation of the tribological system boils down to providing energy in the amount necessary to overcome the resistance caused by the phenomenon of friction. It is transformed into other forms of energy, i.e. thermal, electrical and mechanical, then accumulate and dissipate (Figure 1). The tribochemical reactions occurring under its influence have an important role in the transformation of the technological surface layer into an exploitation layer with new functional properties.

Graphene is a two-dimensional material consisting of carbon atoms that have been hybridized. It has very good optical, thermal, mechanical, and electrical properties. Therefore, it has been used in many areas of technology: electronics, power engineering, automation, medicine, and others. Graphene is an auxiliary substance as a component in organic photovoltaic cells and energy-accumulating materials [1]. It can potentially be used to reduce friction and wear between structural elements [2–6].

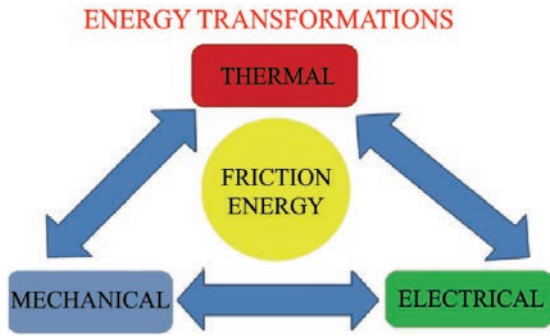


Fig. 1. Main forms of energy occurring during friction between the elements of a tribosystem

An important use of multilayer graphene is in systems operating in boundary friction conditions. Therefore, the influence of graphene addition in lubricating oils on the friction of steel elements was analysed [7–9].

This article compares the results of experimental research carried out during technically dry friction, boundary friction with the use of base oil SN-500 and SN-500 with the addition of graphene and the simultaneous identification of acoustic emission (AE), which was also used to identify the friction conditions.

1. Test materials

The material for the tests were discs made of 100Cr6 steel with a diameter of 42 mm and a height of 6 mm. The chemical composition of the tested discs is presented in Table 1.

Table 1. Chemical composition of steel 100Cr6

Element									
C	Si	Mn	P	S	Cr	Mo	Cu	Al	O
0.93–1.05	0.15–0.35	0.25–0.45	max. 0.025	max. 0.015	1.35–1.60	max. 0.10	max. 0.30	max. 0.050	max. 0.0015

The material used as a counter-sample in the friction junction were 100Cr6 steel balls with a diameter of 6 mm, loaded with a normal force of 10 N. The most important mechanical properties of 100Cr6 steel are shown in Table 2.

Table 2. Mechanical properties of steel 100Cr6

Material	Young's modulus E [GPa]	Tensile strength R_m [MPa]	Compressive Strength [MPa]	Hardness [Vickers]	Density [g/cm ³]
steel 100Cr6	243	520	454	210	7.83

Tribological tests were carried out on a tribometer Anton Paar TRB³ ball-on-disc type in sliding motion. A photograph of the friction junction is shown in Figure 2a.

The tribological tests were carried out with the technical and environmental parameters presented in Table 3. Resistance to motion was determined during Technically Dry Friction (TDF). The lubricant was SN-500 base oil under boundary friction conditions (BF) and SN-500 oil with an addition of graphene in the amount of 0.23 wt. %, designated as boundary friction with graphene (BFG). The chemical composition of the oil used is shown in Table 4.

Table 3. Technical and environmental parameters of test

Parameters	Units	Values
Load	N	10
Slide speed	m/s	0.07
Number of cycles	–	1000
Humidity	%	55 ± 5
Temperature	°C	25±1
Radius	mm	12.5

Table 4. Technical specifications of the sn-500 base oil [16]

Parameters	Units	Typical values
Density at 15°C	g/cm ³	0.886
Kinematic viscosity at 40°C	mm ² /s	min. 95
Kinematic viscosity at 100°C	mm ² /s	10.512.0
Viscosity index		90
Flow temperature	°C	9
Ignition temperature, o.c.	°C	220
Coke residue	%(m/m)	0.08
Incineration residue	%(m/m)	0.01
Acid number	mgKOH/g	0.05
External appearance 20+5°C		Transparent, free of suspended solids and sludges
Colour according to pattern		2.5
Oil/water emulsion separation time at 54°C	mg/kg	200
Oil/water emulsion separation time at 82°C	min.	30
Oxidation resistance – viscosity quotient at 40°C		1.5
Resistance to oxidation — coke growth	%(m/m)	1.1

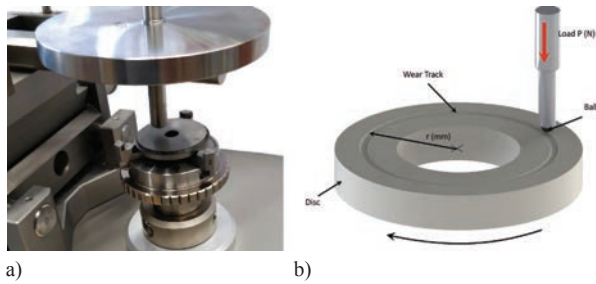


Fig. 2. a) photo of the Anton Paar TRB³ tribometer in the ball-on-disc configuration, b) view of ball-on-disc

$$L_{Aeq} = 10 \log \left(\frac{1}{N} \sum_{i=1}^N 10^{0.1L_{A,i}} \right) \quad (1)$$

where L_{Aeq} means the signal RMS level (corrected by A-weighting characteristic) in i -th second and $N = 10$ is the number of 1-second intervals in 10 seconds.

The sound was recorded with the OLYMPUS PCM RECORDER LS-P1 *linear PCM recorder*. Then, using SpectraPlus, the RMS (*Root Mean Square*) level was determined for 1-second sections of the signal corrected by A-weighting characteristics [17], expressed in full scale decibels (dBFS).

The A-weighting characteristic is used for measurements of industrial noise with low sound level. The next step was to determine the RMS signal levels for 10-second intervals of time, according to the following formula for equivalent sound level L_{Aeq} [13]:

2. Research methodology

The aim of the tests was to compare the influence of graphene in lubricating oils on the performance of tribological systems and to determine the surface morphology of the tested samples together with the evaluation of the connection between acoustic emission and the friction junction.

The next stage of the study was the assessment of surface damage after tribological tests. Figure 3 shows isometric images and primary profiles of surfaces before (Figure 3a) and after (Figures 3b, c, d) tribological tests.

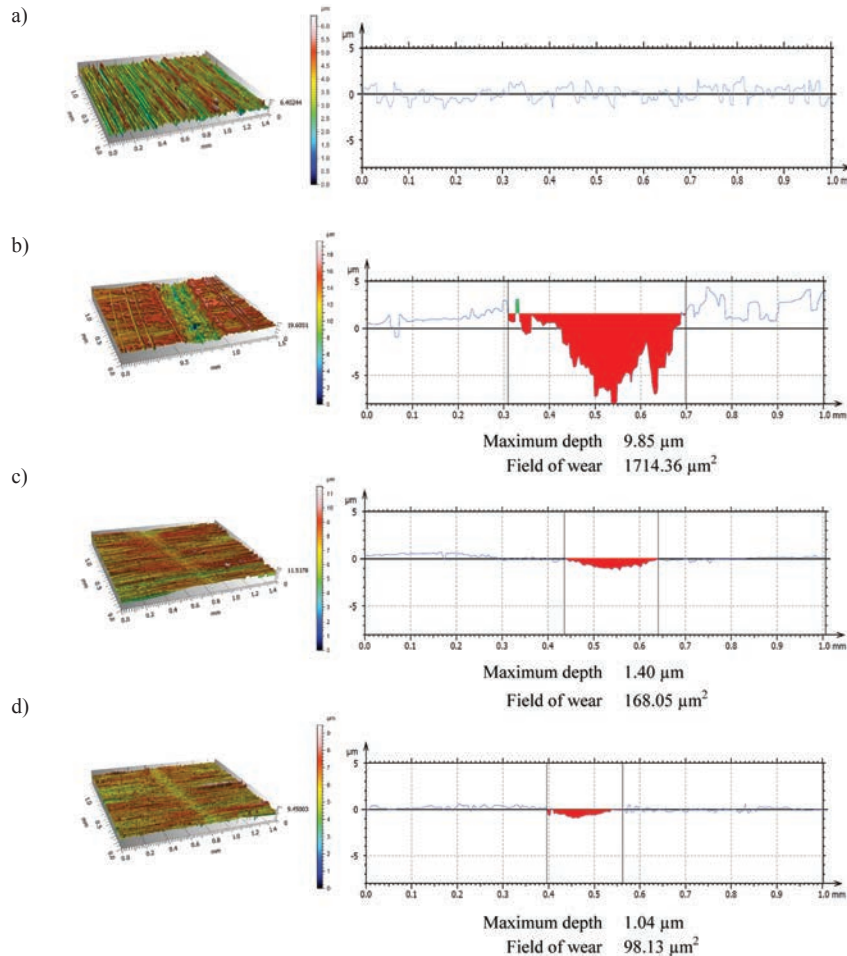


Fig. 3. The isometric image of the trace of wear and the wear profile in a cross-section: a) before friction, b) technically dry friction, c) BF, d) BFG

Three-dimensional images of the surface of the tested elements made it possible to analyse their shaping after tribological tests. Knowledge of the characteristics of surface topography is important for the assessment of its functional properties. By comparing the obtained isometric images and surface primary profiles (Figure 3), it was observed that the smallest wear track was formed after friction with lubrication with the base oil with graphene BFG (Figure 3d). Its maximum depth was 1.04

μm and its width was approximately 0.17 mm. After friction with BF base oil lubrication, the abrasion trace depth was 1.40 μm and the width was approx. 0.2 mm. The deepest (9.85 μm) and the widest (0.39 mm) abrasion traces were obtained after technically dry friction.

Using the Phenom XL scanning electron microscope with an EDS microanalyser, the elements forming the discs made of 100Cr6 steel were observed and identified.

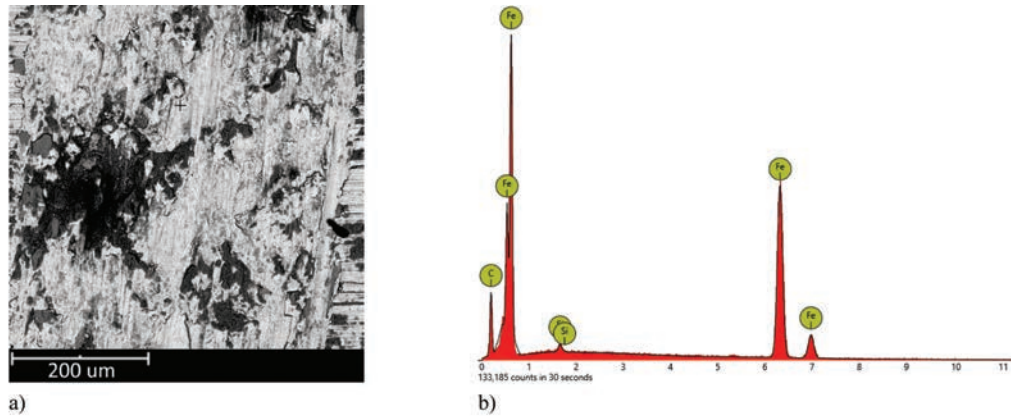


Fig. 4. SEM image: a) surface morphology, b) characteristic spectrum in a micro-area for a steel 100Cr6 after technically dry friction (TDF)

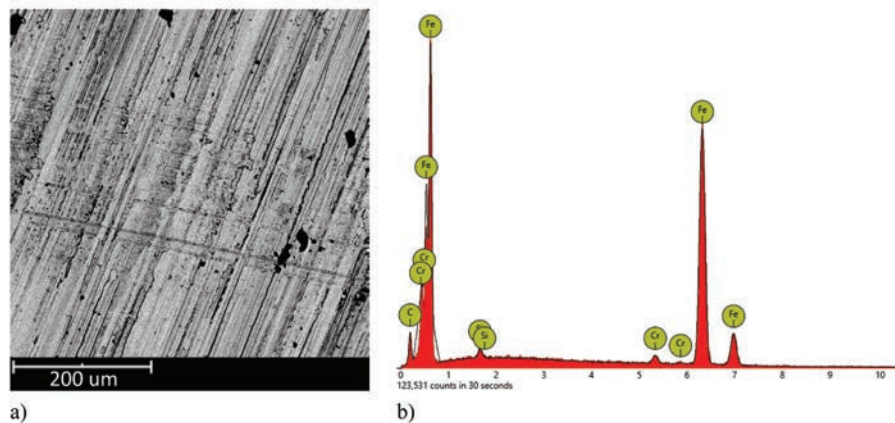


Fig. 5. SEM image: a) surface morphology, b) characteristic spectrum in a micro-area for a steel 100Cr6 after boundary friction (BF)

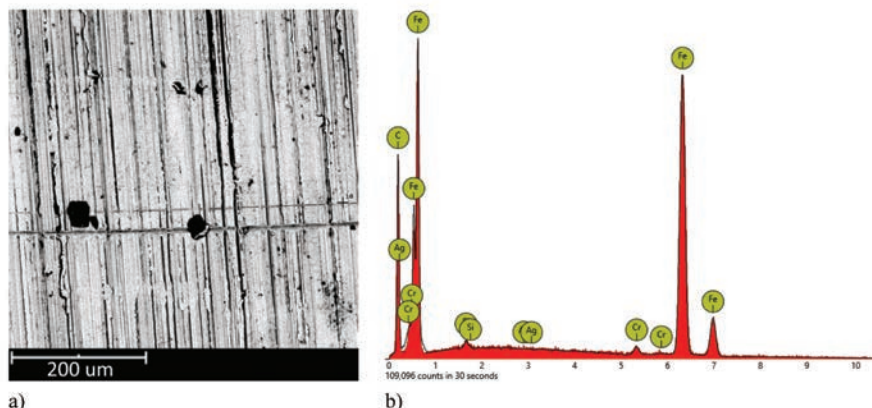


Fig. 6. SEM image: a) surface morphology, b) characteristic spectrum in a micro-area for a steel 100Cr6 after boundary friction with graphene (BFG)

The microstructure of the surface of the disc made of 100Cr6 steel (Figure 4) after BFG showed an iron content of 96.96% and a silicon content 0.81% by mass. The remaining 2.23% was carbon. After friction with base oil lubrication (Figure 5), the following elements were observed at the wear track: iron – 97.07%, chromium – 1.52%, silicon – 0.67%, and the rest was carbon 0.74%.

On the other hand, after friction with lubrication with base oil with graphene (Figure 6), the following elements

were observed: iron – 93.92%, chromium – 1.22%, silicon – 0.44%, and the rest was carbon 4.33%.

On the sample after lubrication with SN-500 base oil with graphene, the highest carbon content accumulated at the lowest point of the wear track. This can be caused by carbon deposits from the lubricant.

Figure 7 shows the level of acoustic emission, linear wear, and the friction coefficient after technically dry friction (TDF), with lubrication with base oil SN-500 (BF) and lubrication with oil SN-500 with graphene (BFG).

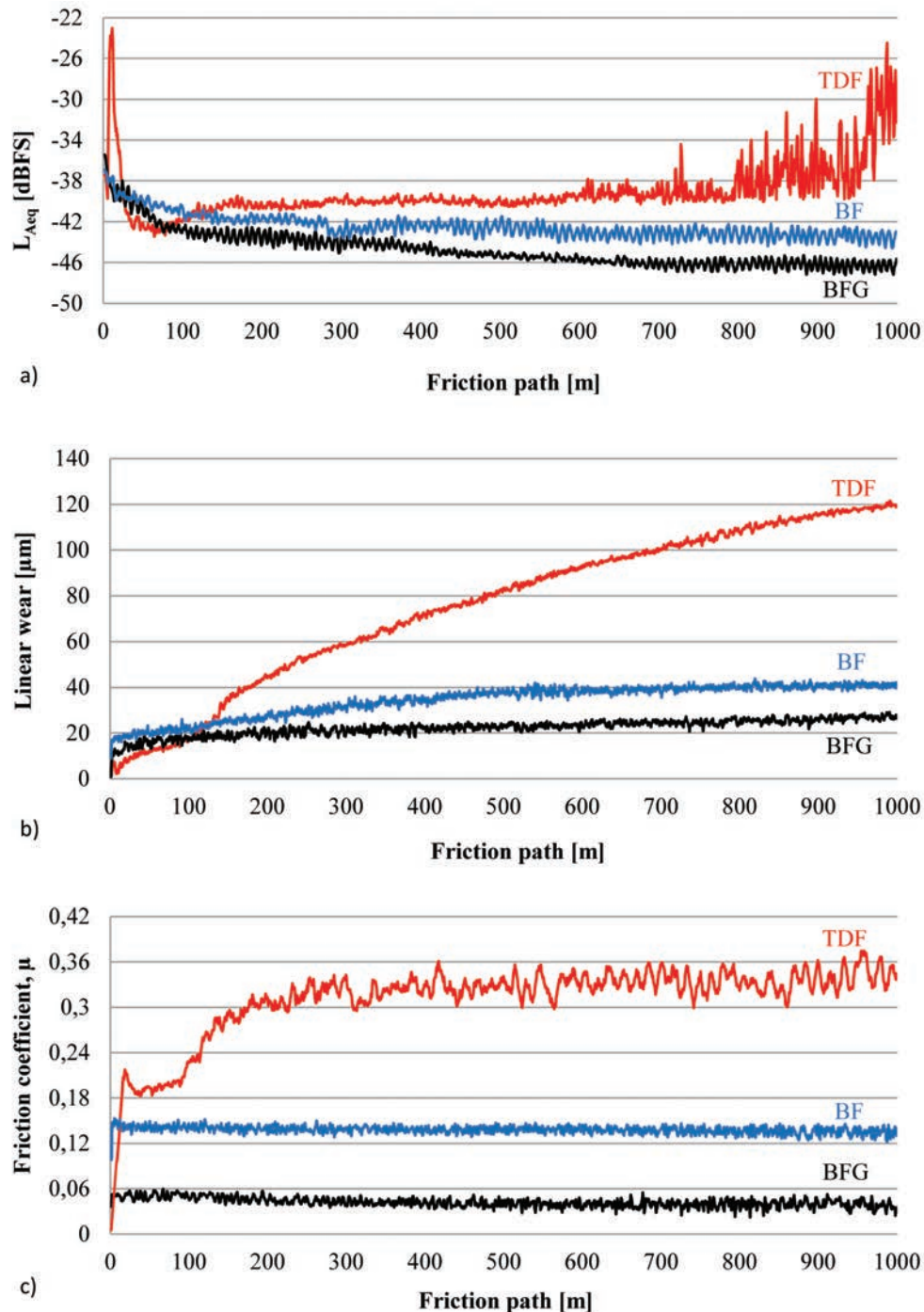


Fig. 7. Acoustic and tribological characteristics of the ball on disc tests: a) acoustic emission, b) linear wear, c) coefficient of friction

In the course of analysing the obtained characteristics (Figure 7), it was found that the phenomenon of sample running-in occurs at about 150 m of the wear truck. After a period of mutual running-in, the coefficient of friction stabilises as a result of oxidation and exposure to ambient humidity, which can be observed on Figure 7a by reading the acoustic emission level. At the end of the TDF test, at the friction length of 750 m, the destabilisation of frictional processes, characterised by a high-frequency cyclic emission, takes place.

Figure 8 shows graphs of average linear wear, the average coefficient of friction, the friction field, and the average sound level. These values were determined after the running-in of the abrasive elements (from approx. 200 m). Average linear wear and the average coefficient of friction were determined by averaging the obtained measurement data from the tribometer. The average sound level was obtained using the Formula [13], while the friction field was determined from the formula for the volume of wear during the rotary motion test, where r is- the friction radius (Table 3), and A is the surface area of the abrasion mark (Figure 3).

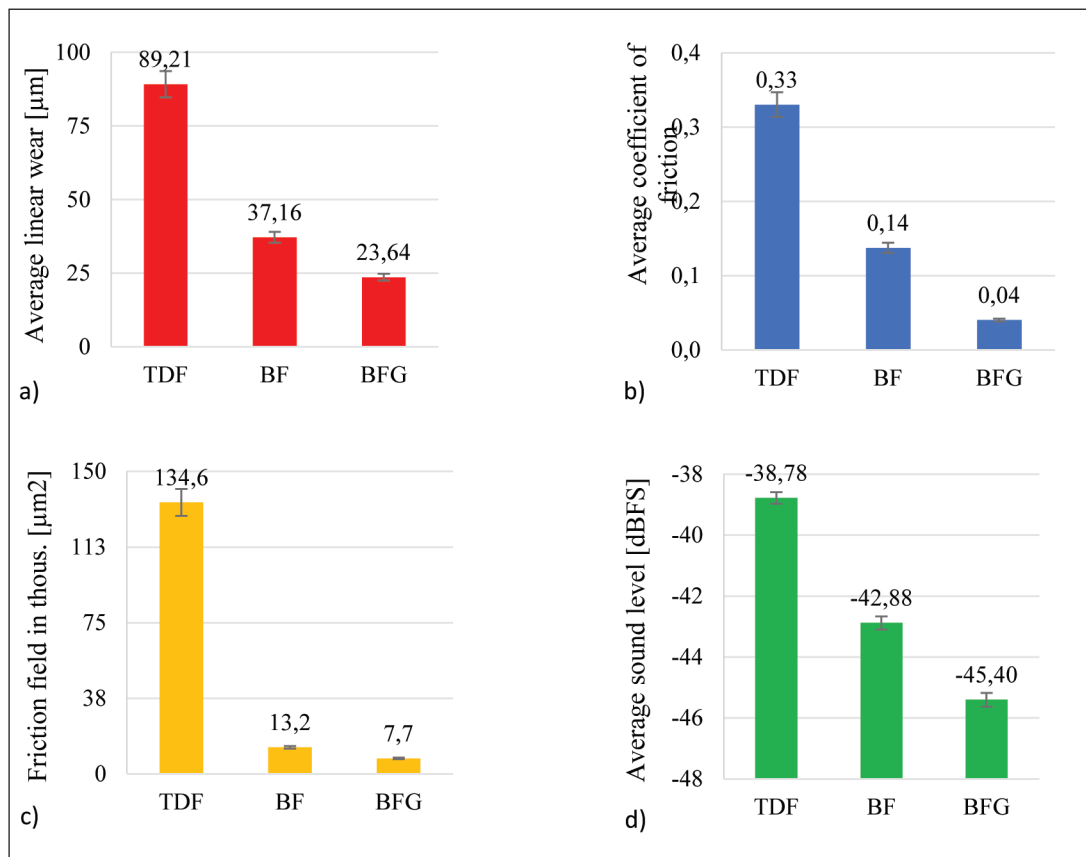


Fig. 8. Bar charts: a) average linear wear, b) average coefficient of friction, c) friction fields, d) medium sound level

When comparing the graphs presented in Figure 8, a correlation was observed that the lowest values of average linear wear, the average coefficient of friction, the friction field, and the average sound level were obtained after friction with lubrication with SN-500 oil with added graphene. The highest values of average linear wear, the average coefficient of friction, the friction field, and the average sound level were obtained after technically dry friction. In turn, the friction field, average sound level and linear wear for SN-500 base oil were about 50% higher than for SN-500 with graphene addition, and the coefficient of friction was as much as 2.5 times lower.

Conclusions

As a result of the conducted studies, it was found that the acoustic emission AE is closely related to the performance of the tribological system. On the basis of the recorded characteristics of AE, it was found that it is possible to monitor the course of phenomena and processes accompanying friction *in situ*.

The use of a lubricant with graphene significantly reduces the friction coefficient, the wear of rubbing elements and the intensity of changes in the acoustic emission of AE.

The results of the observed and studied surface shape (surface topography) indicate that the friction field on the friction junction elements after additive graphene into the lubricating oil is almost 50% of the friction field when using the base oil alone.

Application of lubricating oil with graphene ensures stable working conditions of the tested tribological system. Therefore, the influence of graphene as a modifying additive in lubricating oils on friction and wear of metal elements of tribological systems was investigated.

References

1. Gupta T.: *Carbon The Black, the Gray and the Transparent*. Switzerland: Cham, Springer Nature, Springer Intern. Publ. AG., 2018.
2. Bhowmick S., Yang Z., Banerji A., Alpas T.A.: Effect of Graphene Nanoplates Dispersed in Ethanol on Frictional Behaviour of Tool Steel Running Against Uncoated and DLC-Coated Tool Steel. *Tribology Letters*, 2019, 67, pp. 32–44.
3. Berman D., Erdemir A., Sumant A.V.: Graphene: a new emerging lubricant. *Mater. Today*, 2014, 17(1), pp. 31–42.
4. Lin J.S., Wang L.W., Chen G.H.: Modification of graphene platelets and their tribological properties as a lubricant additive. *Tribology Letters*, 2011, 41(1), pp. 209–215.
5. Berman D., Deshmukh S.A., Sankaranarayanan S.K.R.S., Erdemir A., Sumant A.V.: Extraordinary macroscale wear resistance of one atom thick graphene layer. *Adv. Funct. Mater.*, 2014, 24(42), pp. 6640–6646.
6. Peng Y., Wang Z., Zou K.: Friction and wear properties of different types of graphene nanosheets as effective solid lubricants. *Langmuir*, 2015, 31(28), pp. 7782–7791.
7. Mungse H.P., Kumar N., Khatri O.P.: Synthesis, dispersion and lubrication potential of basal plane functionalized alkylated graphene nanosheets. *RSC Adv.*, 2015, 5(32), pp. 25565–25571.
8. Fan X.Q., Xia Y.Q., Wang L.P., Li W.: Multilayer graphene as a lubricating additive in bentone grease. *Tribology Letters*, 2014, 55(3), pp. 455–464.
9. Ozimina D.: Metody oceny oddziaływań tribochemicznych dodatków przeciwтарыowych. *Metrologia i Systemy Pomiarowe*, 2000, 7(1), pp. 73–87 [in Polish].
10. Szczerek M.: *Metodologiczne problemy systematyzacji eksperymentalnych badań tribologicznych*. Radom: ITeE, 1997 [in Polish].
11. Totten G.E.: *Handbook of Lubrication and Tribology*. Boca Raton, London, New York: CRC Press Taylor & Francis Group, 2006.
12. Wiczorowski M.: *Wykorzystanie analizy topograficznej w pomiarach nierówności powierzchni*. Poznań: Wyd. Politechnika Poznańska, 2009 [in Polish].
13. ISO 9612:2009, Acoustics – Determination of occupational noise exposure – Engineering method.
14. Kajdas Cz., Kulczycki A., Ozimina D.: A new concept of the mechanism of tribocatalytic reactions induced by mechanical force. *Tribology International*, 2017, 107, pp. 144–151.
15. Rudnick L.R.: *Lubricant Additives: Chemistry and Applications*. Boca Raton, Londyn, New York: CRC Press Taylor & Francis Group, 2017.
16. Orlen Oil: *Datasheet of the base oil SN-500*. [Online]. 2019. [Accessed 30 April 2019]. Available from: [http://www.orlenoil.pl/PL/Nasza Oferta/Produkty/Strony/produkt.aspx?produkt=OLEJ-BAZOWY-SN-500.aspx](http://www.orlenoil.pl/PL/Nasza%20Oferta/Produkty/Strony/produkt.aspx?produkt=OLEJ-BAZOWY-SN-500.aspx)
17. Lindos Electronics: *Description of the characteristics used for sound measurements*. [Online]. 2019. [Accessed 30 April 2019]. Available from: [www.lindos.co.uk/cgi-bin/FlexiData.cgi?SO URCE=Articles&VIEW=full&id=2 – 06.2019](http://www.lindos.co.uk/cgi-bin/FlexiData.cgi?SO URCE=Articles&VIEW=full&id=2-06.2019)

This article appeared in its printed version in Journal of Machine Construction and Maintenance. The electronic version is published in DESTech Publications, Inc., Lancaster, PA, 2019, Proceedings of FUTURE ENGINEERING CONFERENCE.

Joanna KOWALCZYK^{a,*}, Monika MADEJ^a, Krystian MILEWSKI^b,
Łukasz NOWAKOWSKI^a, Dariusz OZIMINA^a

^a Faculty of mechatronics and Mechanical Engineering, Kielce University of Technology, Poland

^b Trzuskawica S.A., Nowiny, Poland

* Corresponding author: jkowalczyk@tu.kielce.pl

THE INFLUENCE OF CUTTING FLUID AND DIAMOND-LIKE CARBON COATING ON CUTTING TOOL WEAR

© 2019 Joanna Kowalczyk, Monika Madej, Krystian Milewski, Łukasz Nowakowski, Dariusz Ozimina

This is an open access article licensed under the Creative Commons Attribution International License (CC BY)



<https://creativecommons.org/licenses/by/4.0/>

Key words: diamond-like carbon coating (DLC), cutting tools wear, friction, turning.

Abstract: The aim of the research was to determine the effect of coolant on the wear of tools made of cemented carbides without a coating and with a diamond-like coating DLC type a-C:H and the quality of workpiece surface. The a-C:H coating was obtained by plasma-assisted chemical vapour deposition PACVD. Identification of the elements included in the cutting tool before and after turning was performed using a scanning electron microscope equipped with an EDS X-ray microanalyser. The face turning was carried out using a numerically controlled lathe. Turning were made without using cutting fluid (“dry”) and using a non-toxic cutting fluid containing zinc aspartate. After turning, the wear of cutting tools was measured using a stereoscopic inspection microscope, and the surface texture of the workpieces was examined with an optical profilometer. The research discussed in this article contributed to the development of production thanks to the comparison of materials used for cutting tools for metalworking, as well as in the search for more and more durable cutting tools for extending durability of cutting tools, improving the quality of treated surfaces and reducing machining costs. During the machining process with the cutting fluid aspartate, layers of zinc compounds were formed, which reduced the coefficient of friction and tool wear.

Wpływ chłodziwa i powłoki diamentopodobnej na zużycie narzędzi skrawających

Słowa kluczowe: powłoka diamentopodobna (DLC), zużycie narzędzi, tarcie, toczenie.

Streszczenie: W artykule przedstawiono realizację i wyniki badań, których celem było określenie wpływu chłodziwa na zużycie narzędzi z węglików spiekanych bez powłoki oraz narzędzi z węglików spiekanych z naniesioną powłoką diamentopodobną DLC typu a-C:H. Oceniono również jakość obrobionej powierzchni detalu. Powłokę a-C:H uzyskano techniką chemicznego osadzania z fazy gazowej wspomaganą plazmą PACVD. Identyfikację pierwiastków wchodzących w skład narzędzi przed i po toczeniu wykonano przy użyciu skaningowego mikroskopu elektronowego wyposażonego w mikroanalizator rentgenowski EDS. Toczenie poprzeczne przeprowadzono za pomocą tokarki sterowanej numerycznie. Wykonano toczenie poprzeczne bez użycia chłodziwa – „na sucho” oraz z zastosowaniem nietoksycznego chłodziwa zawierającego asparaginian cynku. Po toczeniu zmierzono zużycie narzędzi skrawających stereoskopowym mikroskopem inspekcyjnym, a teksturę powierzchni obrabianych przedmiotów zbadano profilometrem optycznym. Badania polegały na porównaniu materiałów stosowanych na narzędzia skrawające do obróbki metali, a także na poszukiwaniu coraz to wytrzymalszych, wpływających na przedłużenie trwałości narzędzi, poprawiających jakość obrabianych powierzchni oraz na zmniejszeniu kosztów obróbki. Podczas obróbki skrawaniem z użyciem chłodziwa zawierającego asparaginian cynku powstały warstwy związków cynku, które wpłynęły na zmniejszenie współczynnika tarcia oraz zużycia narzędzia.

Introduction

One of the most frequently used methods of forming products is machining [1], which consists in removing material with the use of cutting tools [1–3]. The method

is used in almost all production technologies [1]. During the machining process, tools are subjected to high loads arising during the chip formation process, as well as resistance to motion occurring between the tool and the workpiece. In addition, heat is generated during the

deformation of materials and friction, which can cause the tool and chips to overheat and partial overheating of the machined workpieces. The contact surfaces are usually clean and very chemically active; therefore, complex physico-chemical processes take place on them [1, 4, 5]. That is why tools should be made of hard and durable materials that reduce the adhesion of the cutting tool material to the workpiece material.

Carbides are a common material used to produce cutting tools [6, 7]. Cemented carbides are multiphase composite materials manufactured by powder metallurgy consisting of one or more hard phases and a metallic bonding phase [8]. They are characterized by exceptionally high hardness, wear resistance, and excellent strength [6]. One of the drawbacks is their brittleness [6, 7].

In order to improve the mechanical, physico-chemical and technological properties of cemented carbide elements, surface layers can be applied to them. In recent years, there has been a rapid development of research on thin diamond-like carbon coatings applied using chemical vapour deposition (CVD) and physical vapour deposition (PVD) methods. They are widely used in various branches of industry due to their excellent tribological properties (low friction, anti-wear properties), stability and corrosion resistance, high hardness and thermal stability [9–14].

Some coatings have self-lubricating properties and can be subjected to the process of dry machining without the use of cutting fluids. This method is used to avoid problems associated with the use of cutting fluids, such as environmental pollution when disposing of used, hazardous components in fluids used in machining. This form of machining is used in most cutting operations, such as turning or milling of steel, steel alloys and cast iron. Sreejith [15] examined the cutting parameters when machining a relatively soft 6061 aluminium alloy under various machining conditions. He conducted experiments on dry turning, turning with a minimum amount of cutting fluid, and with a large amount of cutting fluid. The results showed that, at high cutting speeds, a good quality of the surface can be achieved even in dry machining conditions. Diniz and Micaroni [16], on the other hand, conducted tests during dry turning and turning with the use of cutting fluids at variable cutting speeds, feed rates, and tool radii. The objective of their research was to determine the best parameter during dry machining. They found that it was necessary to increase the radius of the tool's cutting edge and reduce the cutting speed in order to obtain a good quality surface finish without excessive tool wear. They studied tool durability while improving the surface roughness of the workpiece and energy consumption. Although the use of cutting fluids can improve tool durability, dry machining results in lower energy consumption and better surface finish.

Scientists have developed many techniques to reduce or eliminate the use of cutting fluids. This can be achieved by improving the properties of the cutting tool

by, for example, applying a coating to it or developing new tool geometries. Advanced tool materials with a lower coefficient of friction, high hardness, good oxidation resistance, and high temperature resistance can significantly help in dry machining applications. This led to the introduction of advanced materials for the production of cutting tools such as regular boron nitride, cubic polycrystalline boron nitride, polycrystalline diamond, ceramic tools and others [17, 18].

Cutting fluids are also used to reduce tool wear and improve the surface quality of workpieces. They perform many directional functions, such as cooling, lubrication, a reduction in the friction coefficient, improvement in the surface condition, the transportation of chips from the machining zone, temporary protection of the product against corrosion, the extension of tool life, an improvement in the quality of manufactured products and the effectiveness of the machining process, a reduction in cutting force, and a reduction in workpiece deformation [19].

Mineral oil-based machining fluids are often used in machining operations. Statistics show that the costs of purchasing, preparing, maintaining, and removing cutting fluids account for a large share of the total production costs. In addition, global trends favour the environmental and health protection measures. They have contributed to scientific research towards safe/environmentally friendly production. Therefore, dry machining is becoming increasingly common, where the machining makes it possible to use a minimum amount of cutting fluids (Minimum Quantity Lubrication – MQL) as well as use non-toxic and biodegradable cutting fluids [18].

In this paper, the results of experimental studies carried out during dry turning and with a non-toxic cutting fluid containing zinc aspartate and tools made of carbide without and with a diamond-like carbon coating were compared.

1. Test materials

1.1. Tools and Workpiece

The following cemented carbide tools were used for facing: uncoated tools and tools with a a-C:H diamond-like carbon coating. The choice of these tools was dictated by the fact that carbide cutting tools are commonly used in machining. The chemical composition of SM25 cemented carbide is presented in Table 1.

Table 1. Composition of sm25 cemented carbide

Carbide/element	WC	TiC + TaC + NbC	Co
Share, %	69.5	21	9.5

Table 2. The characteristics of a-C:H coating

Microhardness, HV 0.025	Thickness, μm	Coefficient of friction	Coating process temperature, $^{\circ}\text{C}$	Coating operating temperature max., $^{\circ}\text{C}$	Colour
2000–4000	1.02	0.05–0.15	160–300	350	black

Table 3. Composition of C45 steel

Element	C	Mn	Si	P	S	Cu	Cr	Ni	Mo	W	V	Cu
Share, %	0.42–0.5	0.5–0.8	0.1–0.4	max 0.4	max 0.4	max 0.3	max 0.3	max 0.3	max 0.1	–	–	max 0.3

The a-C:H coating was obtained by plasma assisted chemical vapour deposition (PACVD). The PACVD process is a CVD process that is supported by glow discharge plasma. This method allows producing thin, hard surface layers, and layers with desired properties, e.g., protective, anticorrosive, and tribological [13]. Compared to CVD, the PACVD method is more effective in the initial phase of nucleation of the diamond structures. This process can produce a cleaner layer of high hardness, thermal conductivity, chemical inertia, as well as electrical and optical properties similar to diamond [20]. In the PACVD process, the pulsed glow discharge occurs at low pressure, resulting in higher internal energy, which allows the process temperature to be reduced from 300 $^{\circ}\text{C}$ to 700 $^{\circ}\text{C}$. The process parameters must be carefully selected to match the substrate and coating materials to achieve good adhesion. There are many ways to achieve this, e.g., by changing the composition and partial pressure of the gas, as well as the glow discharge parameters. These control variables ultimately determine stoichiometry, the ratio of sp³ to sp² bonds, the hardness of the layer, and the functional properties. When depositing ~1 $\mu\text{m}/\text{h}$, the PACVD layers have a dense column structure with a smooth surface that eliminates the need for final polishing [21].

The a-C:H coating has been applied to cemented carbide cutting tools. The properties of a diamond-like carbon coating are shown in Table 2.

The workpiece was a 38 mm diameter shaft made of C45 steel. It is unalloyed, quality steel for quenching and tempering, difficult-to-weld, and its chemical composition is presented in Table 3. C45 steel is used for medium duty machine and device components. Products made of this steel can be surface hardened to a hardness of 50–60 HRC.

1.2. Machining Fluid

An environmentally neutral cutting fluid based on DEMI demineralised water containing a biodegradable polymer – zinc aspartate was used in the tests. A 9% concentration of cutting fluid was used in the tests.

Table 4. Parameters of the demineralised water at 25 $^{\circ}\text{C}$

pH	Conductivity, mS/cm	Maximum resistivity, $\text{M}\Omega - \text{cm}$
5.0–7.2	$5.5 \cdot 10^{-5}$ (1.42 $\mu\text{S}/\text{cm}$)	18.2

Table 5. Properties of the cutting fluid containing zinc aspartate

Colour	Scent	pH	Density, g/cm^3	Water solubility
from orange to red	peculiar	9.2–9.7	1.20–1.25	soluble

This fluid contains, primarily the following:

- Alkanolamine borate – 60%.
- Biodegradable oligomer based on zinc poly (aspartic acid) (PASP) – 30%.
- Demineralised water.

The parameters of demineralised water are presented in Table 4.

Zinc poly-asparaginate are the basis for the biostability of the cutting fluid. The physical and chemical characteristics of the cutting fluid containing zinc aspartate are presented in Table 5.

2. Research methodology

The aim of the study was to compare uncoated cemented carbide cutting tools with cemented carbide cutting tools to which a a-C:H diamond-like carbon coating was applied.

2.1. Scanning Microscopy SEM/EDS

The elements forming the cutting tools made of cemented carbides with and without a-C:H coating were observed and identified with the use of a Phenom XL scanning electron microscope with an EDS microanalyser.

2.2. Turning Process

The turning process was performed on a CTX 310 ECO CNC lathe, located in the Conventional Machining Laboratory at the Kielce University of Technology. It is a DMG Gildemeister compact lathe controlled by the Sinumerika 810 system. Facing was performed both “dry” and with the use of a cutting fluid containing zinc aspartate. Table 6 presents the basic parameters of the turning process.

Table 6. Parameters of the turning process

Rotational speed, n, m/min	Turning diameter, d, mm	Cutting speed v_c , m/min.	Feed per revolution, f, mm/rev	Cutting depth, ap, mm
1,257–3,000	38–15.92	150	0.2	0.5
3,000	15.92–0	150–0	0.2	0.5

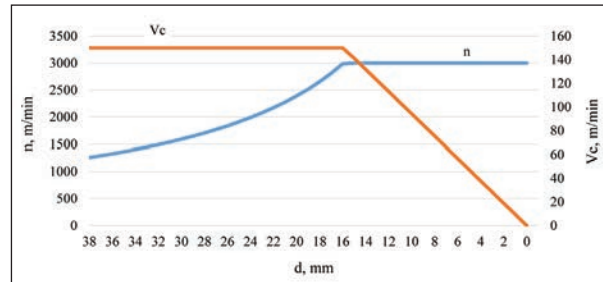


Fig. 1. Dependence of rotational speed and cutting speed on the turning diameter for cemented carbide tools without and with a-C: H coating

Facing was performed, during which 100 passages were made. After machining, the tool and the machined material were tested. The graph in Figure 1 shows the dependence of rotational speed and cutting speed on the turning diameter.

2.3. Geometric Structure of the Surface

The geometric structure of the surfaces of the elements after the turning process was analysed using a Leica DCM8 optical profilometer. In addition, an SX80 stereoscopic inspection microscope was used to observe the wear of the cutting tools after turning.

3. Results and discussions

3.1. Scanning Microscopy SEM/EDS

Figure 2 presents a photograph of the surface microstructure and an analysis of the chemical composition of the elements in the micro-area of the cemented carbide cutting tool.

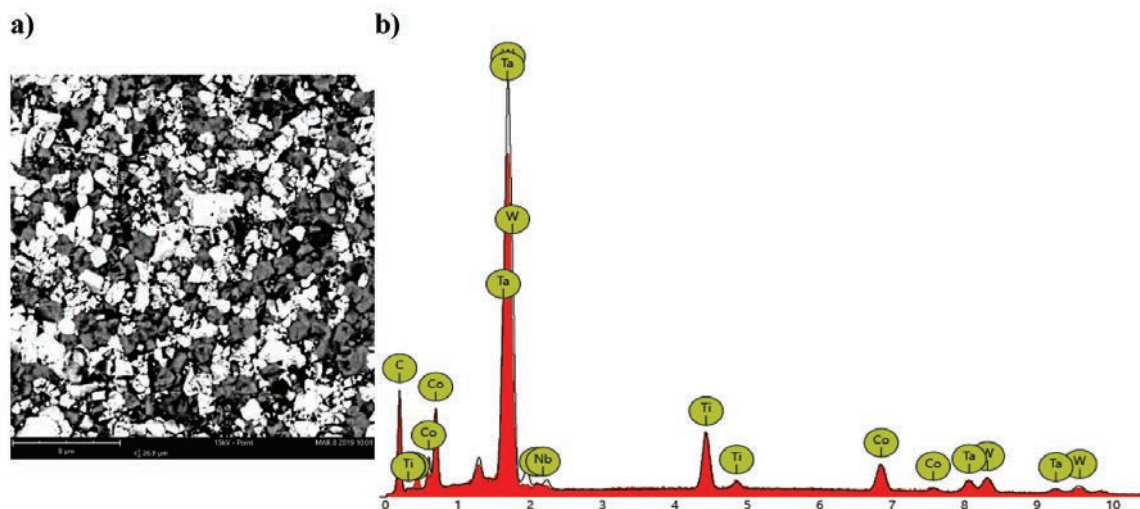


Fig. 2. SEM image: a) surface morphology, b) characteristic spectrum (EDS) in a micro-area for a cemented carbide insert

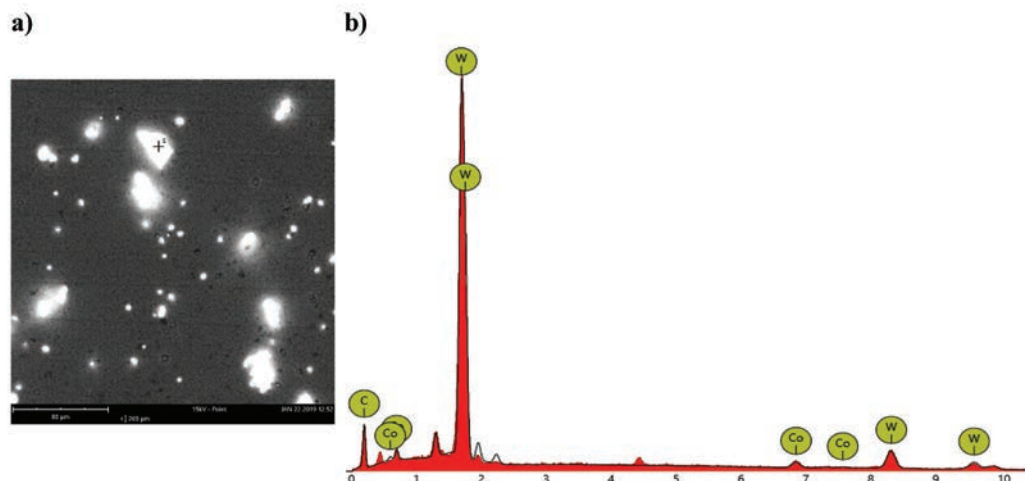


Fig. 3. SEM image: a) surface morphology, b) characteristic spectrum (EDS) in a micro-area for a diamond-coated cemented carbide insert

Figure 2a presents the microstructure of the cemented carbide tool surface. It has been observed that it has a rather heterogeneous surface with lighter and darker areas visible. The results of the point analysis of the chemical composition of the tool (Figure 2b) showed a tungsten mass content of 51.58%, tantalum – 32.02%, cobalt – 4.16%, titanium – 3.28, niobium – 0.38%, and the rest was carbon – 8.59%.

Figure 3 presents a photograph of the surface microstructure and an analysis of the composition of the elements in the micro-area of the cemented carbide cutting tool with coating a-C:H.

The microstructure of the a-C:H coating surface (Figure 3a) shows that the coating has a fairly homogeneous surface, although lighter areas are visible. 1.44% cobalt content was identified in these areas. Tungsten content was also recorded at the level of 92.54% of mass. The remaining 6.02% was carbon. In the analysed micro-area, no carcinogenic elements such as titanium, tantalum, or niobium were identified.

3.2. Geometric Structure of the Surface

Photographs of cutting tools were taken using a SX80 stereoscopic inspection microscope, and with the use of the inspection microscope software, measurements of average VB_B and maximum VB_{Bmax} widths of wear bands on the contact surface were taken according to PN-ISO 3685 [22]. Figure 4 summarises the obtained values of VB_B and VB_{Bmax} parameters.

The lowest mean value of the width of the band of abrasive wear on the contact surface (VB_B) was observed for uncoated cemented carbide tools, both in case of dry turning and with the use of a cutting fluid. In turn the smallest value of the maximum width of the band of abrasive wear on the contact surface (VB_{Bmax}) was

obtained after dry turning using cemented carbide tools with a-C:H coating (Figure 4b).

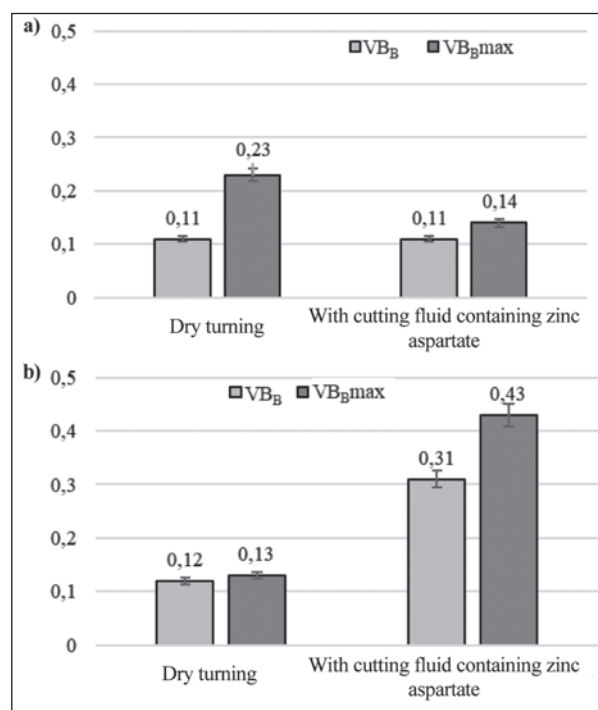


Fig. 4. Wear of the cutting tools made of cemented carbides after turning: a) without coating, b) with a-C:H coating

Comparing uncoated cemented carbide tools with a-C:H coated cemented carbide tools after dry turning, the tool diamond-like carbon coating was better. The VB_B value was slightly higher, and the VB_{Bmax} value was almost 50% lower. However, after turning using a cutting fluid, the consumption was about 3 times lower for uncoated cemented carbide tools than for those coated with a-C:H. A-C:H coated cemented carbide

tools are more effective in dry turning than turning with the use of a cutting fluid. This is due to the self-lubricating property of the diamond-like carbon coating. Such tools do not require lubrication and can be used for dry machining. Uncoated cemented carbide tools, on the other hand, work better when used with cutting fluids.

The use of a cutting fluid resulted in a reduction in the $VB_{B,max}$ value by about 1.6 times.

Topography and surface profiles of the workpieces after dry turning and with the use of zinc aspartate were observed in the place where the cutting speed was the highest (Figures 5–8).

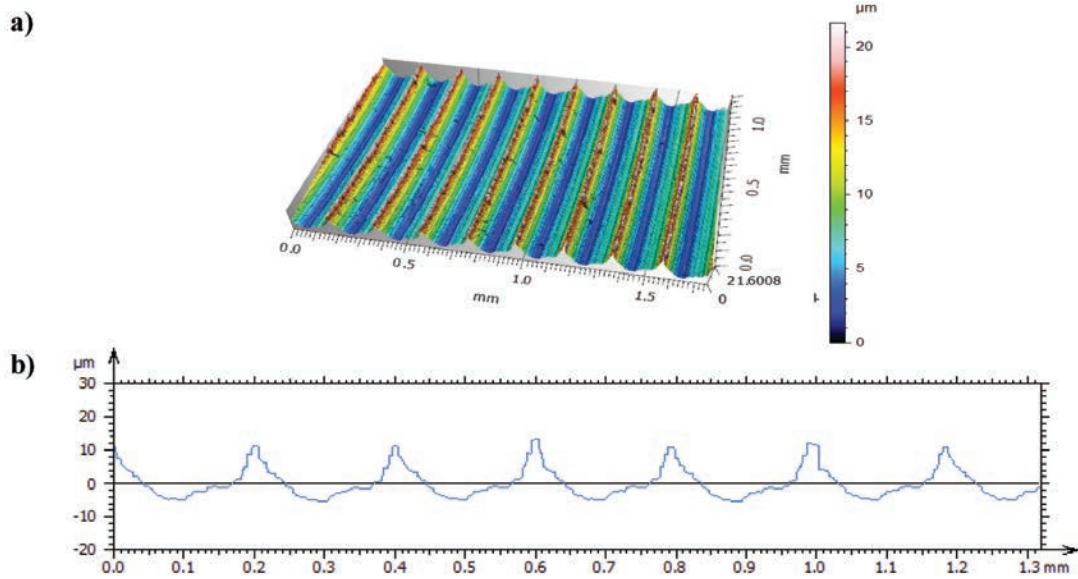


Fig. 5. Surface texture of the edge of the workpiece after dry turning with a cemented carbide cutting tool: a) isometric view, b) primary profile

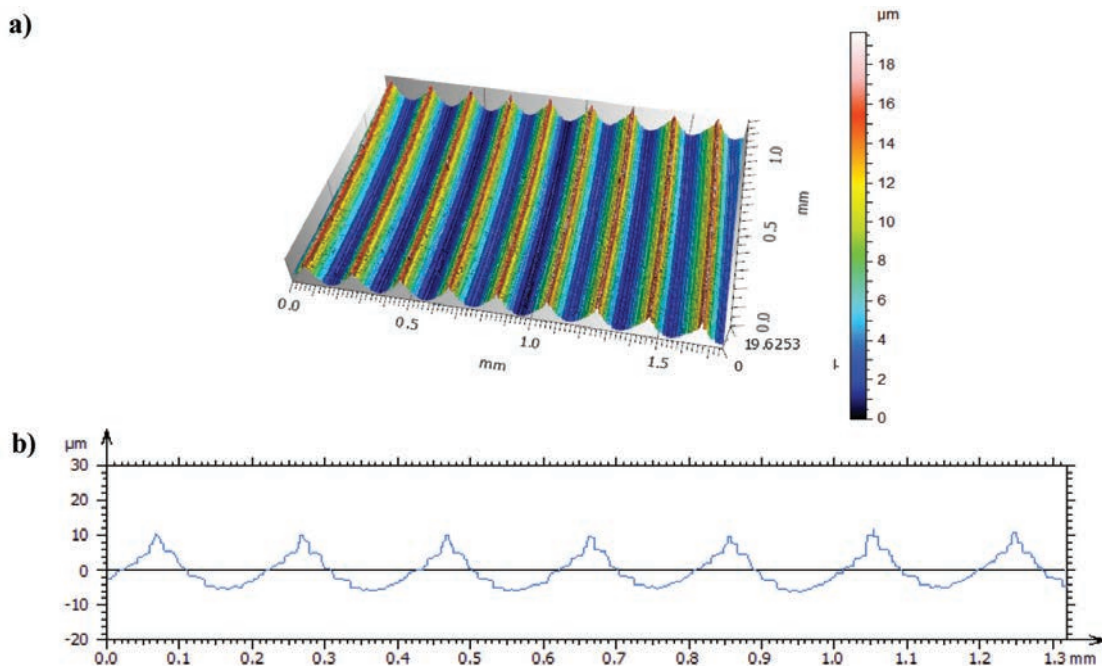


Fig. 6. Surface texture of the edge of the workpiece after dry turning with cemented carbide cutting tool with a-C:H coating: a) isometric view, b) primary profile

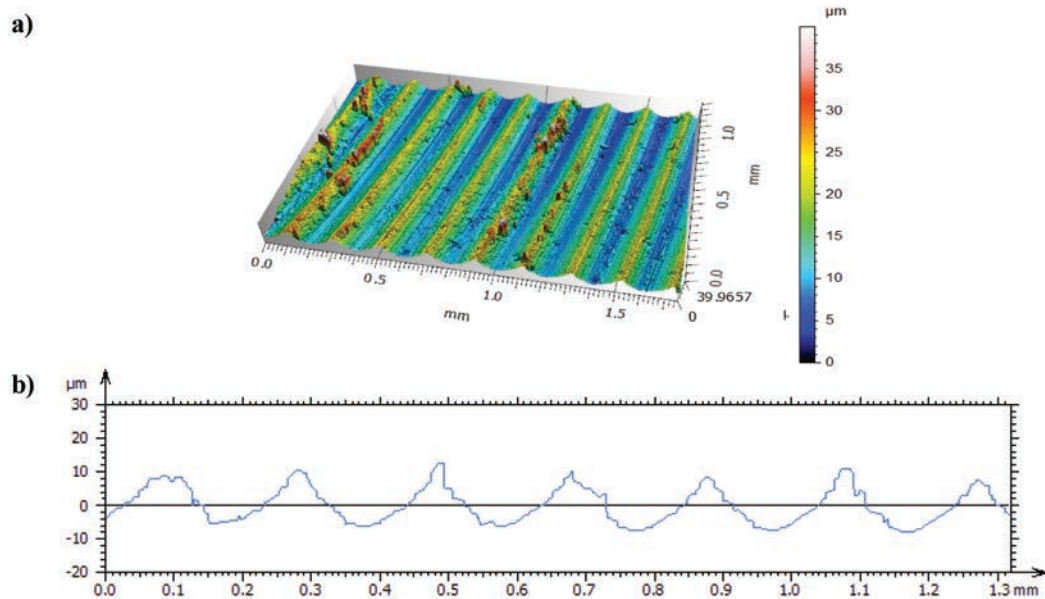


Fig. 7. Surface texture of the edge of the workpiece after turning with cutting fluid containing zinc aspartate with a cemented carbide cutting tool: a) isometric view, b) primary profile

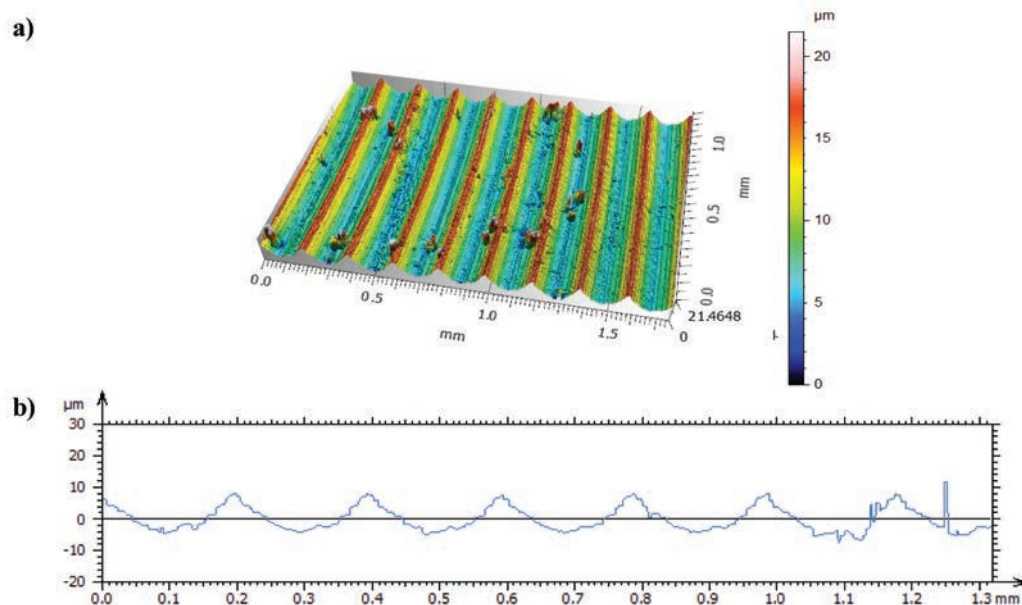


Fig. 8. Surface texture of the edge of the workpiece after turning with cutting fluid containing zinc aspartate with a cemented carbide with a-C:H coating cutting tool: a) isometric view, b) primary profile

The carried-out analyses indicate that the lowest elevations and the shallowest recesses were formed on the workpiece after turning using a-C:H coated cemented carbide cutting tools with a cutting fluid containing zinc aspartate. The parallel tool passages (feed rate: 0.2 mm per revolution) are clearly visible on all workpieces. After dry machining and machining

using a cutting fluid with an uncoated cemented carbide tool and after machining using a cutting fluid with an a-C:H coated cemented carbide tool, a few disturbances were observed. Peaks are clearly visible, and a few elevations could have been formed when the particles of the workpiece material transferred with the chip adhered to the workpiece.

Table 7 presents the parameters of the geometric structure of the surface of machined materials produced after dry turning and machining with a cutting fluid containing zinc aspartate.

When comparing the values of surface roughness parameters on the edge of the machined workpieces after the dry turning process and turning with a cutting fluid containing zinc aspartate, the following observations were made:

- The lowest values of Sa, Sq, Sp and Sz were observed for the cemented carbide tool with a-C:H coating after turning with a cutting fluid.
- The lowest Sv value was recorded for the cemented carbide tool after dry turning.
- The lowest Ssk and Sku values were observed for cemented carbide tools with a-C:H coating after dry turning.

Table 7. Surface texture parameters obtained for the discs after turning

Surface roughness parameters			“Dry” turning		With a cutting fluid	
			Made of cemented carbide	Made of cemented carbide with a-C:H coating	Made of cemented carbide	Made of cemented carbide with a-C:H coating
Sa	µm	Arithmetic mean of the height of the area	3.81	3.72	4.6	3.15
Sq	µm	Root mean square height of the surface	4.85	4.39	5.62	3.66
Sp	µm	Maximum height of the area peak	29.55	12.79	25.53	11.52
Sv	µm	Maximum height of the surface recess	8.25	6.84	14.44	9.95
Sz	µm	Maximum area height	37.79	19.63	39.97	21.46
Ssk	–	Surface asymmetry	1.46	0.60	0.75	0.66
Sku	–	Surface kurtosis	5.80	2.34	3.43	2.36

The amplitude parameters of Ssk and Sku are sensitive to characteristic elevations and recesses as well as defects. A positive value of the Ssk parameter indicates elevations with sharpened geometry. Whereas, the Sku parameter (kurtosis) is a measure of the smoothness of the distribution curve of ordinates, which is also called the coefficient of concentration. For the normal ordinates distribution, Sku = 3.

3.3. Scanning Microscopy SEM/EDS

Figures 9–10 present SEM images of traces of tool wear after machining with cutting fluids and a point analysis of the elemental composition.

On tools made of cemented carbides without and with a-C:H coating applied at selected points on the build-up after turning with a cutting fluid, in addition to

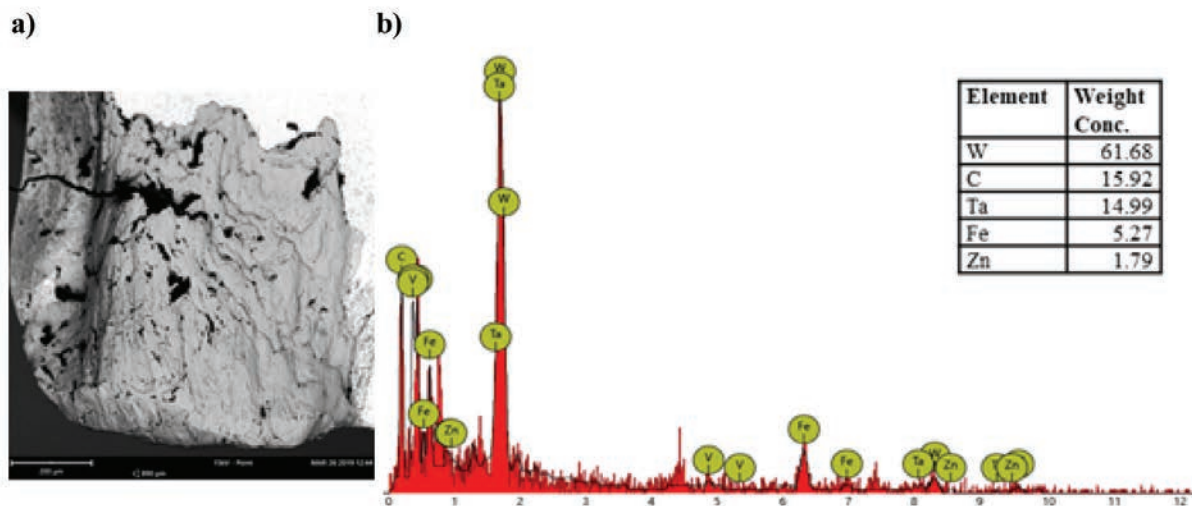


Fig. 9. ISEM analysis of the tool wear made of cemented carbides after turning with cutting fluid containing zinc aspartate: a) image of the wear track and b) X-ray energy spectrum

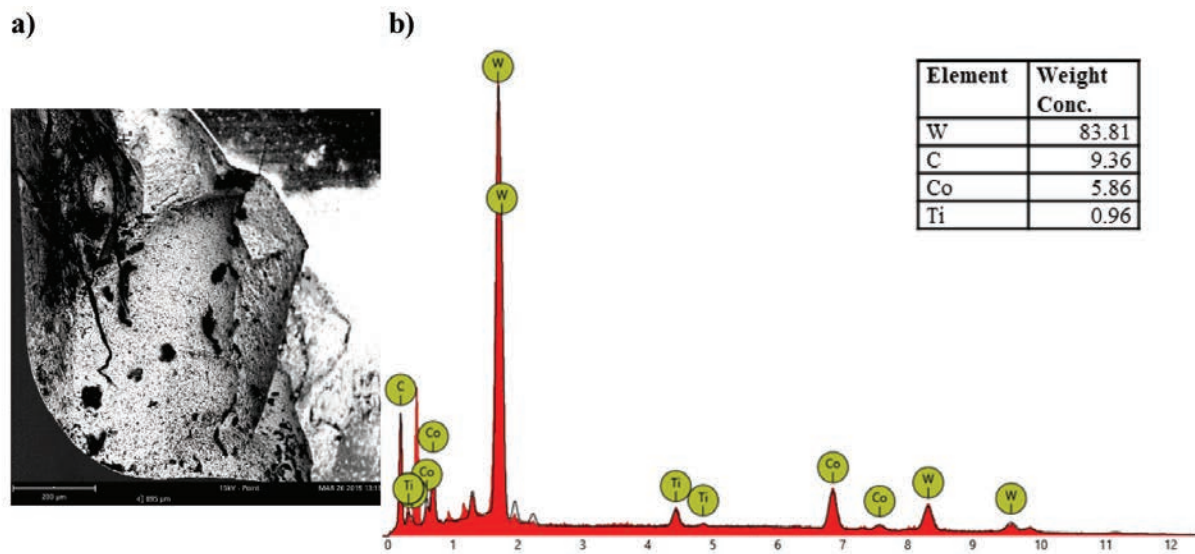


Fig. 10. SEM analysis of the tool wear made of cemented carbides with a-C:H coating after turning with cutting fluid containing zinc aspartate: a) image of the wear track and b) X-ray energy spectrum

the elements coming from the tool material, an additional element coming from the workpiece, i.e. iron, was observed. A local transfer of material from the workpiece occurred. Thus, adhesion of the tool material to the workpiece material and the process of their selective transfer took place. Iron from the workpiece was not identified on a-C:H coated cemented carbide tools. The presence of elements such as titanium and cobalt from the substrate, i.e. cemented carbide, was observed.

Moreover, after turning with uncoated cemented cutting tools with a cutting fluid containing zinc aspartate, the presence of zinc from the cutting fluid was also registered. This indicates that a layer of zinc compounds was formed there, reducing the coefficient of friction and the wear of the tool.

Conclusions

The tests carried out in this study are in line with current trends in the search for increasingly durable materials that will prolong use, ensure savings and eliminate downtime during production.

The lowest values of the width of the band of abrasive wear on the contact surface (VB_B) was obtained after facing using cemented carbide tools with a cutting fluid containing zinc aspartate as well as dry machining. On the other hand, the lowest value of the maximum width of the band of abrasive wear on the contact surface ($VB_{B,max}$) was obtained after dry turning with a-C:H coated cemented carbide tools. Thus, due to its self-lubricating properties, the a-C:H coating perfectly fulfils its anti-wear function during dry machining.

The best parameters of the geometric structure of the surface, i.e. the lowest elevations S_z and the shallowest recesses S_v , were characterized by the details after turning using an a-C:H coated cemented carbide tool with a cutting fluid.

After turning, build-up was formed on the tools. In the case of machining using an uncoated cemented carbide tool with a cutting fluid, a local transfer of material from the workpiece occurred and layers of zinc compounds were formed. These layers contributed to the reduction of the coefficient of friction and wear of the tool.

References

- Ozimina D., Kowalczyk J., Madej M.: The impact of biodegradable cutting fluid on the tribological properties of the friction pairs. *Tribologia*, 2016, 1, pp. 69–80.
- Sheikh-Ahmad J.Y.: *Machining of Polymer Composites*. USA: Springer, 2009.
- Olszak W.: *Obróbka skrawaniem*. Warszawa: WNT, 2009 [in Polish].
- Dolinšek S., Kopač J.: Mechanism and types of tool wear; particularities in advanced cutting materials. *Journal of Achievements in Materials and Manufacturing Engineering*, 2006, 19(1), pp. 11–18.
- Szczerek M.: *Metodologiczne problemy systematyzacji eksperymentalnych badań tribologicznych*, Radom: ITeE, 1997 [in Polish].
- Liu C., Lin N., He Y.H., Liu W.S., Ma Y.Z.: Influence of Micron WC Addition on the Microstructure

- and Mechanical Properties of Ultrafine WC–Co Cemented Carbides at the Elevated Temperature. *Journal of Superhard Materials*, 2018, 40(1), pp. 40–46.
7. Wirtz Ch., Dehmer A., Trauth D., Mattfeld P., Klocke F.: Analysis of the grinding wheel wear in dependency of the cemented carbide specification. *The International Journal of Advanced Manufacturing Technology*, 2018, 99, pp. 747–754.
 8. Lisovskii A. F., Gnatenko I.A.: On the Formation of Intercarbide and Interface Surfaces in WC–Co Cemented Carbides. *Journal of Superhard Materials*, 2018, 40(5), pp. 335–347.
 9. Madej M., Kowalczyk J., Ozimina D.: The tribological properties of DLC coatings lubricated with the biodegradable cutting fluid. *Tribologia*, 2014, 5, pp. 101–112.
 10. Folea M., Roman A., Lupulescu N.B.: An overview of DLC coatings on cutting tools performance. *Scientific papers. Academic journal of manufacturing engineering*, 2010, 8(3), pp. 30–36.
 11. Madej M., Marczevska-Boczkowska K., Ozimina D.: Effect of tungsten on the durability of diamond-like carbon coatings in the chemical industry. *Przemysł Chemiczny*, 2014, 93(4), pp. 505–505.
 12. Vengudusamy B., Grafl A., Preinfalk K.: Tribological properties of hydrogenated amorphous carbon under dry and lubricated conditions. *Diamond & Related Materials*, 2014, 41, pp. 53–64.
 13. Madej M.: *Properties of tribological systems with diamond-like carbon coatings*. Kielce: Ed. TU, 2013.
 14. Ozimina D.: *The exploitation of tribological systems. Tom I. The importance of scientific instrument in operation buildings*. M48. Kielce: Ed. TU, 2013.
 15. Sreejith P.: Machining of 6061 aluminium alloy with MQL, dry and flooded lubricant conditions. *Materials Letters*, 2008, 62, pp. 276–278.
 16. Diniz A.E. Micaroni R.: Cutting conditions for finish turning process aiming: the use of dry cutting. *International Journal of Machine Tools and Manufacture*, 2002, 42(8), pp. 899–904.
 17. Kustas F.M., Fehrehnbacher L.L., Komanduri R.: Nano coatings on cutting tools for dry machining. *CIRP Annals – Manufacturing Technology*, 1997, 46, pp. 39–42.
 18. Gupta K.: *Innovations in Manufacturing for Sustainability*. Switzerland: Springer, 2019.
 19. Smith G.T.: *Cutting tool technology. Industrial handbook*. London: Springer, 2008.
 20. Jethanandani R.: The Development and Application of Diamond Like Carbon Films. *The Journal of The Minerals, Metals & Materials Society (TMS)*, 1997, 49(2), pp. 63–65.
 21. Berns H., Theisen W.: *Ferrous Materials: Steel and Cast Iron*. Berlin: Springer, 2008.
 22. PN-ISO 3685: *Tool-life testing with single-point turning tools*.

This article appeared in its printed version in Journal of Machine Construction and Maintenance. The electronic version is published in DEStech Publications, Inc., Lancaster, PA, 2019, Proceedings of FUTURE ENGINEERING CONFERENCE.

Robert SOŁTYSIAK^{a,*}, Agnieszka SOŁTYSIAK^a, Piotr WASILEWSKI^b

^a UTP University of Science and Technology, Bydgoszcz, Poland

^b ZPHU TEMIROL Mirosław Łachacz, Olsztyn, Poland

* Corresponding author: robsol@utp.edu.pl

DEVELOPMENT OF LASER CUTTING TECHNOLOGY WITH HIGH QUALITY OF THE CUT SURFACE

© 2019 Robert Sołtysiak, Agnieszka Sołtysiak, Piotr Wasilewski

This is an open access article licensed under the Creative Commons Attribution International License (CC BY)



<https://creativecommons.org/licenses/by/4.0/>

Key words: laser cutting, surface accuracy, cutting technology.

Abstract: This paper describes the development of thermal cutting technology aimed at the achievement of the best possible quality class in order to obtain smooth, aesthetic edges. The technology has been developed for two different types of materials: S235JR steel grade and AW-5754 aluminium alloy. The main objective of the developed technology is to eliminate the additional mechanical treatment of the surface following the laser cutting and to allow the classification of the obtained surfaces (without additional measurements) to the appropriate quality class defined by the ISO 9013 standard.

Opracowanie technologii cięcia laserowego o wysokiej jakości powierzchni

Słowa kluczowe: cięcie laserowe, dokładność powierzchni, technologia cięcia.

Streszczenie: W artykule przedstawiono technologię cięcia termicznego opracowaną pod kątem osiągnięcia możliwie najlepszej klasy dokładności w celu otrzymania gładkich, estetycznych krawędzi. Technologię cięcia opracowano dla dwóch różnych rodzajów materiałów: stali S235JR oraz stopu aluminium AW-5754. Przeprowadzono wstępne testy cięcia i dobrano wartości parametrów mocy cięcia, odległości ogniska wiązki (focus) oraz ciśnienia gazu jako stałe dla danych grubości i rodzajów materiału. Zmianie poddawano prędkość cięcia, gdyż ten parametr ma decydujący wpływ na dokładność cięcia.

Po przeprowadzonych badaniach zauważono, że wraz ze wzrostem prędkości, dla danej grubości blachy, generalnie obserwuje się zmniejszenie wartości chropowatości Rz5. Jednak z drugiej strony w większości przypadków wzrost prędkości cięcia powoduje wzrost wielkości tolerancji prostopadłości powierzchni „u”.

Opracowano funkcje matematyczne, które umożliwiają dobór parametrów cięcia laserowego w zależności od rodzaju ciętego materiału, jak również od jego grubości. Zintegrowanie tych funkcji matematycznych z urządzeniem do cięcia laserowego może utworzyć zautomatyzowany system zapewniający wymierne korzyści prowadzące do otrzymania powtarzalnej technologii cięcia charakteryzującej się wysoką jakością powierzchni (odpowiadające ZAKRESOWI nr 1 zgodnie z normą ISO 9013) zarówno pod kątem prostopadłości powierzchni uzyskanej po cięciu „u”, jak i chropowatości powierzchni wyrażonej wartością „Rz5”.

Introduction

Laser technology was applied for the first time for cutting of steel sheets using a CO₂ laser. It took place in 1967 [1]. Thanks to advancements in the design of laser devices, laser cutting technology has become one of the basic technologies of cutting engineering materials [2]. CO₂ lasers have been used for a long time for laser cutting, but recently, fibre lasers have become more and more popular [3, 4].

Fibre optic lasers are characterized by a high quality laser beam. The BPP (Beam Parameter Product) value does not increase up to the cutting power value of 2 kW (i.e. the quality of the laser beam does not deteriorate). The BPP increases (the laser beam quality deteriorates) only when cutting with power greater than 2 kW [2].

Fibre-optic lasers emit waves of a relatively short length (e.g., their wavelength is tenth times shorter as compared to CO₂ lasers). Shorter wavelength improves the absorption coefficient of laser radiation. As a result,

it is possible to cut materials such as copper, nickel and its alloys, as well as composite materials such as Kevlar coated sheet metal [2].

Studies available in the professional literature concerning tests on surfaces obtained using various types of lasers demonstrate that the quality of the cut surface depends mainly on the roughness. In the study [5] on the surface quality after cutting with a Nd-YAG laser, it was shown that the surface roughness increases with the increase of the cutting speed.

It also depends on the frequency of the pulse as well as on its length. In other studies [6], the authors observed that the surface roughness after cutting with Slab type CO₂ gas lasers was sometimes increasing and sometimes was falling with the increase of the cutting power. Other researchers [7] determined optimal cutting parameters without roughness measurement.

However, the standard [8] clearly states that the mean height of the profile Rz5 and the value of the perpendicularity tolerance of the surface after cutting “u” are used to qualify the cutting quality. Authors of the paper [9] compared the quality of cutting with a CO₂ laser and a fibre laser based, among others, on the standard [8]. It was demonstrated that greater dimensional quality, better roughness, higher drag (n) quality, and perpendicularity or angularity tolerance (u) were obtained for cutting using a fibre laser.

This paper describes the development of thermal cutting technology aimed at the achievement of the best possible quality class in order to obtain smooth, aesthetic edges. The technology has been developed for two different types of materials: S235JR steel grade and AW-5754 aluminium alloy. The main objective of the developed technology is to eliminate the additional mechanical treatment of the surface following the laser cutting and to allow the classification of the obtained surfaces (without additional measurements) to the

appropriate quality class defined by the ISO 9013 standard.

1. Research object

High quality cutting technology has been developed for two different types of materials: S235JR steel grade and AW-5754 aluminium alloy. Initial cutting tests were carried out and the cutting power values, the laser beam focus, and gas pressure were selected. The main tests were carried out using these parameters as constant ones for a given thickness and type of material. The cutting speed was subject to change because this is the parameter [7] that is decisive as regards the cutting quality.

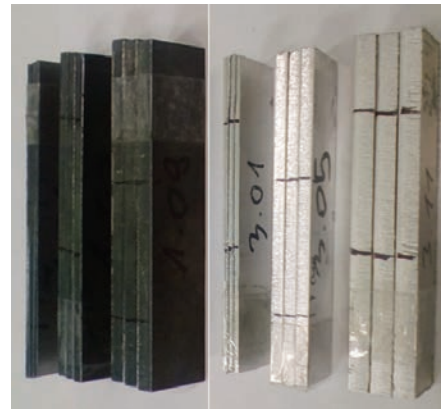


Fig. 1. A photograph of sets of samples prepared for testing

Eighteen samples of 100x20 mm and various thicknesses (2, 4 and 6 mm) were prepared for the main tests. Figure 1 shows photographs of sample packages. Cutting parameters for individual samples are summarized in Table 1.

Table 1. Specimen cutting parameters for the development of high quality cutting technology

	Sample number	Cutting speed mm/min	Sample number	Cutting speed mm/min	Sample number	Cutting speed mm/min
	Thickness 2 mm		Thickness 4 mm		Thickness 6 mm	
S235JR	Laser power = 1.2 kW Focus = 0.2 mm Pressure = 6.0 bar		Laser power = 2 kW Focus = -1.6 mm Pressure = 0.65 bar		Laser power = 2 kW Focus = -1.6 mm Pressure = 0.6 bar	
	1.01	v ₁ = 5000	1.05	v ₁ = 3000	1.09	v ₁ = 1800
	1.02	v ₂ = 6000	1.06	v ₂ = 3200	1.10	v ₂ = 2200
	1.03	v ₃ = 7000	1.07	v ₃ = 3400	1.11	v ₃ = 2600
	Laser power = 2 kW Focus = -1.5 mm Pressure = 10.0 bar		Laser power = 2 kW Focus = 3.0 mm Pressure = 15.0 bar		Laser power = 2 kW Focus = 5.5 mm Pressure = 15.0 bar	
	3.01	v ₁ = 6000	3.05	v ₁ = 2000	3.09	v ₁ = 840
3.02	v ₂ = 7000	3.06	v ₂ = 2500	3.10	v ₂ = 980	
3.03	v ₃ = 7500	3.07	v ₃ = 3000	3.11	v ₃ = 1120	

2. Measurement of surface quality after cutting operation

According to the [8] standard, the quality of surfaces after thermal cutting should be mainly defined by characteristic values, such as perpendicularity or angularity tolerance “u” and the mean height of the profile “Rz₅”. Those parameters were tested using a Mahr MarSurf GD 120 testing machine. A sample photograph of the conducted measurements is shown in Figure 2.

Measurements of the “u” parameter were performed three times in various places on the longer surface of the cut-out specimens. According to the [8] standard, the roughness was measured at a height of 1/3a as seen from the upper surface of the sheet metal. The measurements



Fig. 2. A sample photograph of the roughness measurement

were performed three times at different spacings. Table 2 presents the results of the measurements carried out.

Table 2. Results of „u” and „rz₅” measurements

	Thickness	2 mm			4 mm			6 mm		
S235JR	Sample number	1.01	1.02	1.03	1.05	1.06	1.07	1.09	1.10	1.11
	u ₁ , μm	0.014	0.037	0.114	0.096	0.091	0.058	0.073	0.086	0.086
	u ₂ , μm	0.029	0.034	0.109	0.095	0.105	0.059	0.073	0.092	0.098
	u ₃ , μm	0.023	0.036	0.158	0.098	0.093	0.056	0.046	0.092	0.088
	u _{sr} , μm	0.022	0.036	0.127	0.096	0.096	0.058	0.064	0.090	0.091
	Rz ₅₋₁	4.856	3.451	2.695	2.566	2.251	2.016	64.186	22.884	4.841
	Rz ₅₋₂	4.543	2.026	1.689	2.670	2.256	1.693	60.458	18.168	6.584
	Rz ₅₋₃	4.986	3.245	3.248	3.395	2.155	2.111	55.299	24.881	8.526
Rz _{sr}	4.795	2.907	2.544	2.877	2.221	1.940	59.981	21.977	6.650	
AW 5754	Sample number	3.01	3.02	3.03	3.05	3.06	3.07	3.09	3.10	3.11
	u ₁ , μm	0.014	0.037	0.114	0.096	0.091	0.058	0.073	0.086	0.086
	u ₂ , μm	0.039	0.034	0.109	0.095	0.105	0.059	0.073	0.093	0.098
	u ₃ , μm	0.033	0.036	0.158	0.098	0.093	0.056	0.046	0.093	0.088
	u _{sr} , μm	0.029	0.036	0.127	0.096	0.096	0.058	0.064	0.091	0.091
	Rz ₅₋₁	4.856	3.451	3.695	3.566	3.351	3.016	64.186	33.884	4.841
	Rz ₅₋₂	4.543	3.036	1.689	3.670	3.356	1.693	60.458	18.168	6.584
	Rz ₅₋₃	4.986	3.345	3.348	3.395	3.155	3.111	55.399	34.881	8.536
Rz _{sr}	4.795	3.277	2.911	3.544	3.287	2.607	60.014	28.977	6.654	

3. Scopes of cutting quality classification according to ISO 9013

Table 3 summarizes the limit values of “u” and “Rz₅” specified for SCOPE 1 depending on the thickness of the material subject to cutting. When developing high quality cutting technology, both the “u” perpendicularity tolerance and the average height of the profile (Rz₅) as well as the efficiency of the cutting process will be taken into account.

Table 3. “u” and “rz₅” tolerances for scope 1 determined in accordance with [8]

Scopes of perpendicularity or angularity tolerance „u”				Scopes of mean height of the profile „Rz ₅ ”			
Thickness a, mm	2	4	6	Thickness a, mm	2	4	6
SCOPE 1, μm	0.056	0.062	0.068	SCOPE 1, μm	11.20	12.40	13.60

4. Selection of high quality surface cutting technology

While selecting the cutting technology, the data obtained during the tests presented in Table 2 were analysed. Great emphasis was also put on the relatively high efficiency of the cutting process, trying to select the highest cutting speed while maintaining high quality falling within SCOPE 1 (according to Table 3) for both “u” and “Rz₅”. A graphic illustration of the results is shown in Figures 3 and 5 for S235JR steel grade and AW 5754 aluminium alloy, respectively. Vertical dashed lines in the presented graphs indicate the end of SCOPE 1 defined by the [8] standard. This scope, as shown in Table 3, depends on the thickness of the material being cut. The colours of the presented SCOPES marked by dotted vertical lines are consistent with the colours of the applied experimental points for a given material thickness.

For the analysis of the obtained test results, it was assumed that the relationship of “u” and “Rz₅” as a function of the cutting speed for a given material thickness is similar to a straight line. In all the analysed cases, the R² determination coefficient was higher than or equal to 0.75.

3.1. For S235JR Grade Steel

In the case of S235JR grade steel, for the thickness of 2 mm, when cutting at speeds approaching 7 000 mm/min., the “u” value above SCOPE 1 defined by the standard shall be obtained (Fig. 3a). Regarding the “Rz₅” value, for the thickness of 2 mm, all tested parameters fall into SCOPE 1 (Fig. 3b). It was observed that the roughness value defined by the “Rz₅” parameter decreases as the speed increases. However, increased speed for a thickness of 2 and 6 mm can cause deteriorated perpendicularity of the cut.

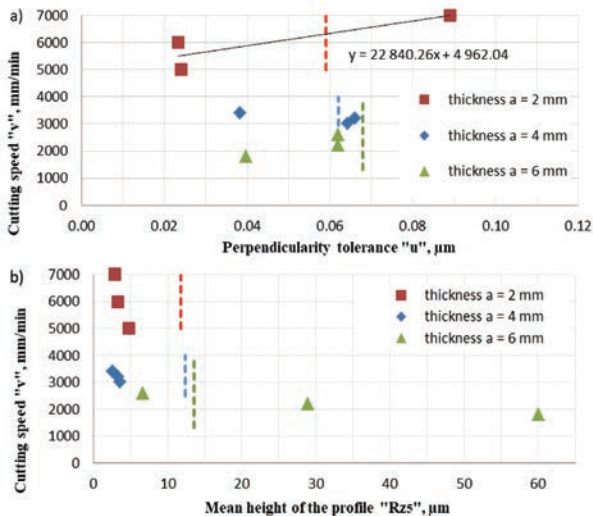


Fig. 3. Graphical representation of test results for S235JR steel grade

The parameters for the thickness of 2 and 6 mm were used to determine the function defining the parameters for the selection of the technology of cutting with high quality falling within SCOPE 1 of the [8] standard. For a thickness of 2 mm, the optimum cutting speed was chosen from the intersection of the regression line with the dotted line of SCOPE 1. This value amounted to 6310 mm/min. For cutting 6 mm thick sheet metal, the use of lower speeds (below 3500 mm/min) causes a significant deterioration of the surface roughness “Rz₅”. However, a reduction of the cutting speed improves the perpendicularity of the surface obtained after cutting. The use of the highest of the tested speeds for cutting 6 mm thick sheet metal results in achievement of the quality of the surface that qualifies it to SCOPE 1.

Figure 4 shows mathematical functions defining the selection of parameters by means of which cutting quality at the level of SCOPE 1 can be obtained. The functions, depending on the thickness of the material to be cut, allow the selection of the optimum laser power (P), cutting speed (v), and focus location (F).

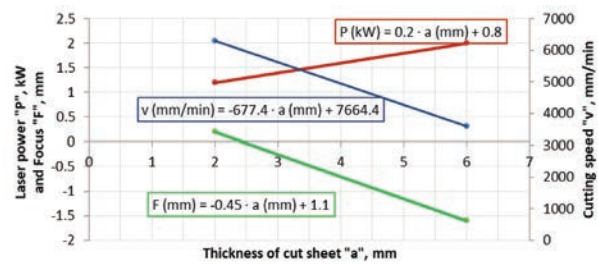


Fig. 4. Mathematical functions defining the selection of cutting parameters for S235JR steel grade

3.2. For AW 5754 aluminium alloy

Aluminium alloys are materials characterized by a relatively low laser beam energy absorption coefficient. This means that a relatively large portion of the laser beams are reflected from the surface of the aluminium sheet. Cutting of these materials requires higher laser power than in case of cutting, e.g., “black” sheet metal.

The parameters for the thicknesses of 2, 4, and 6 mm were used to determine the function defining the parameters for the selection of the technology of cutting with high quality falling within SCOPE 1 of the [8] standard. For a thickness of 2 mm, the optimum cutting speed was chosen from the intersection of the regression line with the dotted line of SCOPE 1 (Fig. 5a). This value amounted to about 6780 mm/min. For a thickness of 4 mm, the most optimum speed as regards to the surface quality after cutting was the highest tested speed of 3000 mm/min. In the case of cutting 6 mm thick aluminium alloy sheets, the use of the cutting speed up to about 870 mm/min will result in the qualification of perpendicular tolerance to SCOPE 1. However, at this speed, Rz₅ roughness will exceed SCOPE 1

(Fig. 5a). On the other hand, a cutting speed of above 1075 mm/min (Fig. 5b) will result in a cutting surface that can be qualified to SCOPE 1 in terms of the “Rz₅” roughness value. However, in that case, the perpendicularity tolerance “u” will be outside the SCOPE 1. Searching for a compromise in order to develop a high quality cutting technology, the mean value of those two specified speeds was used. However, cutting sheet metal plates made of the tested alloy with a thickness close to 6 mm may result in the non-qualification of the cutting surface in terms of “u” or “Rz₅” to SCOPE 1.

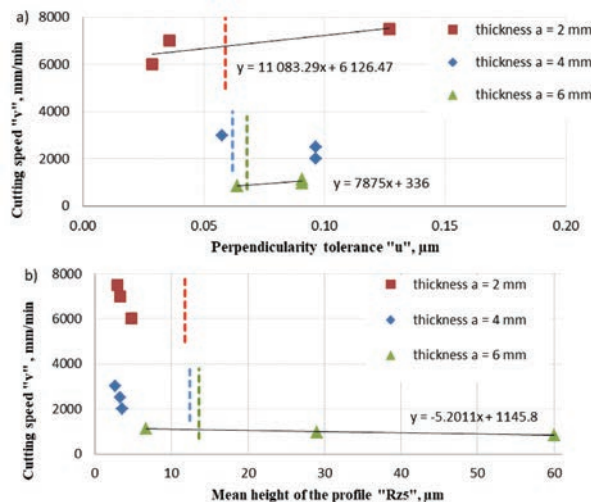


Fig. 5. Graphical representation of test results for AW 5754 aluminium alloy

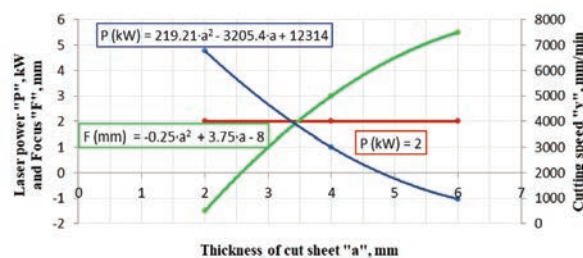


Fig. 6. Mathematical functions defining the selection of cutting parameters for AW 5754 aluminium alloy

Figure 6 shows mathematical functions which allow obtaining a high surface quality for a given material thickness and presents a graphical representation.

Summary

After the tests, it was noticed that, for a given sheet thickness, the “Rz₅” roughness value is generally reduced with the increase of the speed. On the other hand, in most cases, an increase in the cutting speed results in an increase in the “u” tolerance value. In order

to select the technology ensuring a high quality surface, it is worth determining which parameter – “u” or “Rz₅” – is more important when it comes to the quality of the surface after the cutting process.

This paper provides a method of developing a cutting technology that allows one to obtain high quality of cutting surfaces for two types of materials: S235JR and AW 5754. Within the framework of this study, mathematical functions have been developed that enable the selection of laser cutting parameters depending on the type of material being cut as well as its thickness. By integrating these mathematical functions with a laser cutting equipment, an automated system can be created that provides tangible benefits leading to development of a reproducible cutting technology characterized by high surface quality (corresponding to SCOPE 1 according to the [8] standard) both in terms of the perpendicularity of the surface after cutting “u” and surface roughness expressed by “Rz₅”.

References

- Houldcroft P.: Gas-jet laser cutting. *British Welding Journal*, 1967, p. 443.
- Klimpel A.: *Technologie laserowe. Spawanie, napawanie, stopowanie, obróbka cieplna i cięcie*. Gliwice: Wydawnictwo Politechniki Świętokrzyskiej, 2012.
- Mahrle A, Lütke M., Beyer E.: Fibre laser cutting: Beam absorption characteristics and gas-free remote cutting. *Proceedings of the Institution of Mechanical Engineers, Part C: Journal of Mechanical Engineering Science*, 2010, 224, pp. 1007–1018, DOI: 10.1243/09544062JMES1747.
- FIBER LASERS: *Fiber lasers: The state of the art*. [Online]. 2012. [Accessed 27 February 2018]. Available from: <https://www.laserfocusworld.com/articles/print/volume-48/issue-04/features/the-state-of-the-art.html>
- Sharma A. Yadava V.: Modelling and optimization of cut quality during pulsed Nd:YAG laser cutting of thin Al-alloy sheet for straight profile. *Optics & Laser Technology*, 2012, 44, pp. 159–168. DOI: 10.1016/j.optlastec.2011.06.012.
- Riveiro A, Quintero F., del Val J., Boutinguiza M., Comesaña R., Lusquinos F., Pou J.: Laser cutting using off-axial supersonic rectangular nozzles. *Precision Engineering*, 2018, 51, pp. 78–87. DOI: 10.1016/j.precisioneng.2017.07.013.
- Rodrigues G.C., Vanhove H., Duflou J.R.: Direct Diode Lasers for Industrial Laser Cutting: A Performance Comparison with Conventional Fiber and CO₂ Technologies. *Physics Procedia*, 2014, 56, pp. 901–908. DOI: 10.1016/j.phpro.2014.08.109.
- ISO 9013. *Thermal cutting – Classification of thermal cuts – Geometrical product specification and quality tolerances*.

9. Soltysiak R., Wasilewski P., Soltysiak A., et al.: The analysis of Fiber and CO₂ laser cutting accuracy. In: *9th International Conference on Manufacturing Science and Education, Sibiu (Romania), 5–7 June 2019*. MATEC Web of Conferences, 2019, (Prepared for printing).

This article appeared in its printed version in Journal of Machine Construction and Maintenance. The electronic version is published in DEStech Publications, Inc., Lancaster, PA, 2019, Proceedings of FUTURE ENGINEERING CONFERENCE.

Michał KEKEZ^{a,*}, Tomasz DESANIUK^a, Jurek DUSZCZYK^b, Dariusz OZIMINA^a

^a Faculty of Mechatronics and Mechanical Engineering, Kielce University of Technology, Poland

^b Delft University of Technology, Netherlands

*Corresponding author: m.kekez@tu.kielce.pl

ON THE USE OF ACOUSTIC EMISSION TO ASSESS THE WEAR IN A TRIBOSYSTEM

© 2019 Michał Kekez, Tomasz Desaniuk, Jurek Duszczyk, Dariusz Ozimina

This is an open access article licensed under the Creative Commons Attribution International License (CC BY)

 <https://creativecommons.org/licenses/by/4.0/>

Key words: tribosystem, DLC coating, sound, regression trees.

Abstract: The article focuses on the analysis of acoustic emission signals generated under dry sliding friction conditions. Two tests were conducted using a TRB³ tribometer with the disc made of 100Cr6 steel with a DLC coating, and pin made of corundum (Al₂O₃) and steel 100Cr6, respectively. Two tests with the disc without DLC coating were also carried out. The audio data written in the 16-bit linear pulse-code modulation (LPCM) format were analysed using the SpectraPLUS software. An A-weighting filter and 1/1 and 1/3-octave band filters were used for sound level measurements.

The analysis of the equivalent sound level calculated for 10-second time intervals was carried out. The highest A-weighted sound level occurred during the first 2 hours of the test with the disc having a DLC coating and pin made of 100Cr6 steel. At the end of this test, the sound level dropped by about 40 dB compared to the maximum. The lowest A-weighted sound level was recorded during the last 2 hours of the test with disc having a DLC coating and pin made of corundum.

The time-dependent variability of sound parameters was predicted using the regression tree and random forest models, which proved to be accurate and easy to follow.

Ocena emisji akustycznej w procesie zużycia elementów systemu tribologicznego

Słowa kluczowe: system tribologiczny, dźwięk, powłoka DLC, drzewa regresji.

Streszczenie: W pracy przedstawiono analizę dźwięku zarejestrowanego podczas tarcia technicznie suchego w ruchu ślizgowym. Dwa testy przeprowadzono na tribometrze TRB³ dla próbek wykonanych ze stali 100Cr6 z powłoką DLC i przeciwpróbek wykonanych odpowiednio z korundu (Al₂O₃) i stali 100Cr6. Przeprowadzono również dwa testy dla próbek bez powłoki DLC. Dźwięk został zarejestrowany w standardzie 16-bitowego liniowego PCM, a następnie poddany analizie w programie Spectra-Plus. Dla kolejnych chwil czasu wyznaczono wartości poziomu dźwięku A, a także poziomy dźwięku w wybranych pasmach oktauwowych i 1/3-oktauwowych.

Przeprowadzono analizę równoważnego poziomu dźwięku obliczonego dla 10-sekundowych odcinków czasu. Najwyższy poziom dźwięku A występował podczas pierwszych 2 godzin testu próbki z powłoką DLC i przeciwpróbki wykonanej ze stali 100Cr6. Pod koniec tego testu poziom dźwięku spadł o około 40 dB względem dotychczasowego maksimum. Najniższy poziom dźwięku A zanotowano podczas ostatnich 2 godzin testu, w którym próbka miała powłokę DLC, a przeciwpróbka była wykonana z korundu. Utworzono modele opisujące zmienność w czasie wybranych parametrów dźwięku, oddzielnie dla każdej próbki. Do utworzenia modeli zastosowano drzewa regresji oraz Random Forest. W pracy zamieszczono analizę dokładności i przejrzystości otrzymanych modeli.

Introduction

In tribological systems, energy required to overcome the resistance attributable to friction can be dissipated,

transformed, or accumulated [1]. One of the phenomena occurring during friction is acoustic emission. Vibration and noise generated during the stick-slip friction in an instrument panel was investigated in [2]. The effect of fluid film lubrication on the attenuation of noise and the

vibration of the gear mesh was discussed in [3]. The effect of grooves on the emission of 1–20 kHz sounds was analysed in [4]. The impact of windscreen waviness on the emission of the sound of the above-mentioned frequencies during wiper blades work was investigated in [5]. The influence of selected factors on the emission of sound caused by friction, as well as sound frequency analysis at various stages of tribotests was studied in [6]. This article presents original research and focuses on the analysis of sound generated under dry sliding friction conditions.

1. Materials and methodology

Tribological tests (Table 1) were performed on ball-on-disc tribometer (Figure 1). The balls with a diameter of 6 mm were made of 100Cr6 steel and aluminium (III) oxide – Al_2O_3 , while the rotating discs with a diameter of 42 mm and a height of 6 mm were made of 100Cr6 steel with or without a DLC coating. All tests were conducted under conditions of technically dry friction. The sliding distance was 1000 m.

Table 1. Parameters of tribological tests

Parameter	Unit	Value
Load	N	10
Sliding rate	m/s	0.07
Sliding distance	m	1000
Relative humidity	%	55 ± 5
Ambient temperature	$^{\circ}\text{C}$	25 ± 1

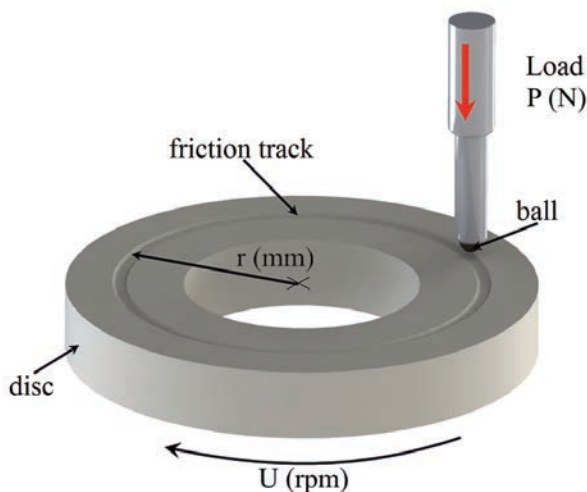


Fig. 1. Schematic of friction node used in tests

Tested material pairs are shown in Table 2, using the following notation: Test 1 for disc and a ball made of 100Cr6 steel, Test 2 for disc made of 100Cr6 steel and a ball made of Al_2O_3 , Test 3 for disc with a DLC coating and a ball made of Al_2O_3 , and Test 4 for disc with a DLC coating and a ball made of 100Cr6 steel. Material pairs were selected because they are widely used in maintenance technology.

Table 2. Materials used in tribological tests

Test	Disc	Ball
Test 1	100Cr6 steel	100Cr6 steel
Test 2	100Cr6 steel	Al_2O_3
Test 3	with DLC coating	Al_2O_3
Test 4	with DLC coating	100Cr6 steel

Properties of selected materials are shown in Table 3 (100Cr6 steel and Al_2O_3) and in Table 4 (DLC coating compared with diamond).

Table 3. Mechanical properties of 100Cr6 steel and Al_2O_3 [13, 14]

Material	Young's modulus E [GPa]	Tensile strength R_m [MPa]	Compressive Strength [MPa]	Hardness [Vickers]	Density [g/cm ³]
Steel 100Cr6	243	520	454	210	7.83
Al_2O_3	393	206–300	2070–2620	1365	3.987

Table 4. Mechanical properties of diamond and a-c:h-type dlc coating [15]

Material	Young's modulus E [GPa]	Form	Covalent bonds	Hardness [GPa]	Density [g/cm ³]
a-C:H	100–300	Films	Intermediate sp^3	10–30	~2.2
Diamond	1000	Bulk, films	100% sp^3	100	~3.5

During the tests, sound was registered by a Linear PCM Recorder Olympus LS-P1 in such a way that the analogue audio signal was sampled with 44100 Hz frequency and stored in digital 16-bit linear PCM (pulse-code modulation) format. Then, SpectraPlus SC software [7] applied A-weighting [12] to the recorded digital audio signal. Later, using the same software, the RMS (root mean square) level of the A-weighted signal was determined for each 1-second time period, and denoted by $L_{A,i}$. The obtained $L_{A,i}$ values were expressed

in decibels full-scale (dBFS) [8]. In the next step, the RMS level of the A-weighted audio signal for each 10-second time period, denoted by L_A and expressed in dBFS, was calculated using Equation (1) for equivalent sound level [9]:

$$L_A = 10 \log \left(\frac{1}{N} \sum_{i=1}^N 10^{0.1 L_{A,i}} \right) \quad (1)$$

where $L_{A,i}$ values come from 10 consecutive seconds, and N equals 10.

During selected tests, equivalent sound level A (A-weighted), as well as sound levels in each 1/3-octave bands, for 100-millisecond time periods were measured using a Class 1 digital sound level meter and analyser SVAN971.

2. Results and discussion

Figure 2 shows the course of the friction coefficient and linear wear as a function of sliding distance for tribological tests marked in Table 2 as Test 1 and Test 2. In both tests, the disc was made of 100Cr6 steel, and the ball was made of 100Cr6 steel and Al_2O_3 , respectively.

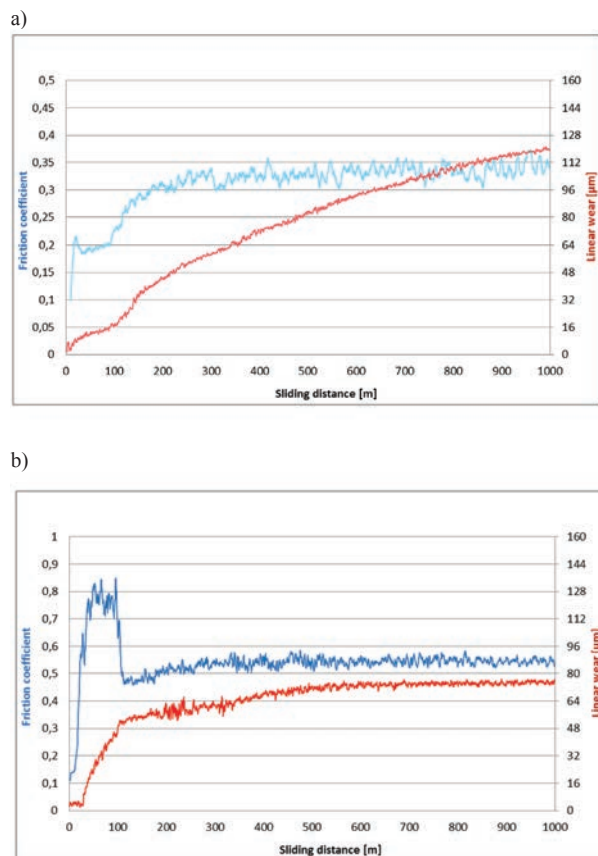


Fig. 2. The friction coefficient and linear wear in tribological tests: a) Test 1, b) Test 2

The results of Test 1 indicate that the friction coefficient reaches values below 0.25 during the first 100 meters, and then remains between 0.3 and 0.4. On the other hand, in Test 2, the friction coefficient reaches values exceeded 0.8 during the first 100 meters, and then decreased and maintained values between 0.45 and 0.6.

Figure 3 shows the course of the friction coefficient and linear wear as a function of sliding distance for tribological tests marked in Table 2 as Test 3 and Test 4. In both tests, the disc was coated with a diamond-like carbon coating (DLC), and the ball was made of Al_2O_3 and 100Cr6 steel, respectively. The friction coefficient for all of Test 3 was close to 0.1, while, in Test 4, it was about 0.35 for the first 300 meters and about 0.2 for the last 400 meters.

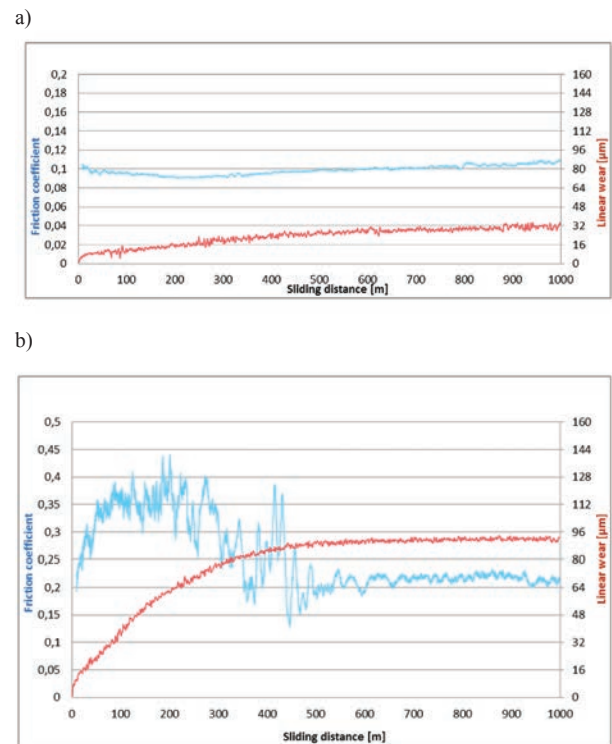


Fig. 3. The friction coefficient and linear wear in tribological tests: a) Test 3, b) Test 4

Figure 4 shows the surface texture of the disc formed during Test 2. In Figure 4b, the effects of the transport and deposition of material on the sides of friction path are visible. In all conducted tests, there is a correlation between friction coefficient and L_A values or high frequency sound emission. Figures 5 and 6 present L_A values as a function of sliding distance in tribological tests: Test 1, Test 2, Test 3, and Test 4.

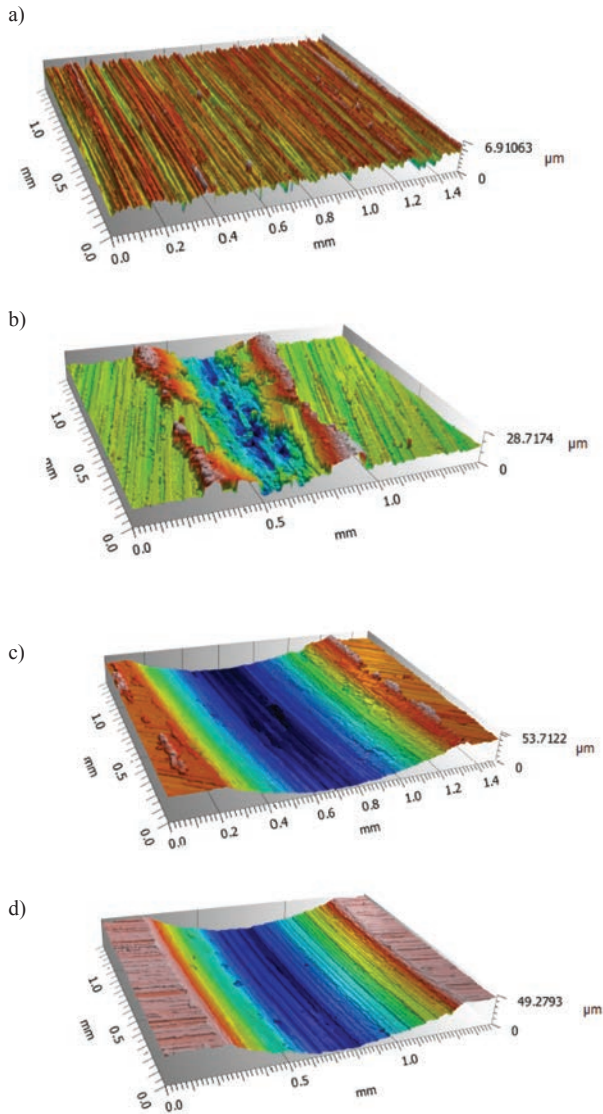


Fig. 4. Surface texture formed during Test 2: a) before friction, b) near the maximum of friction coefficient, c) at sliding distance of 300 m, d) at the end of the test

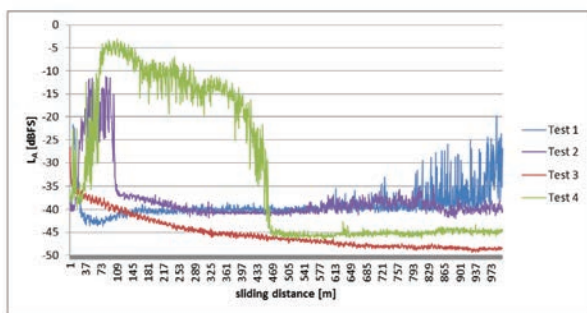


Fig. 5. L_A values during tribological tests from Table 2

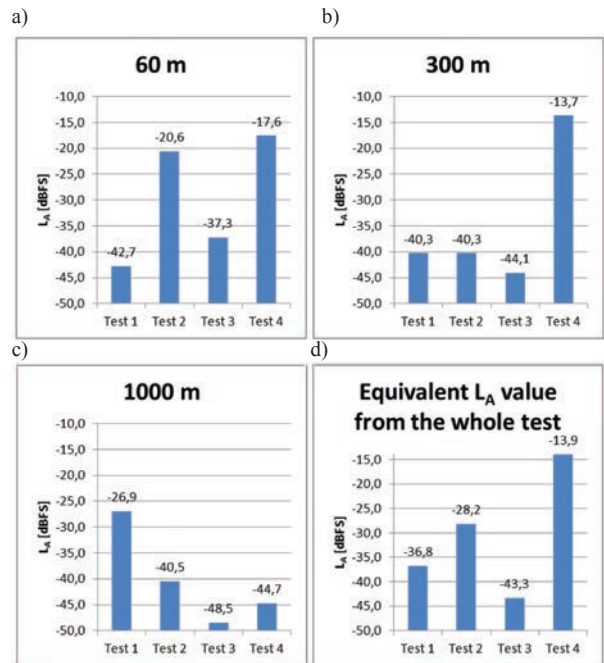


Fig. 6. L_A values during tribological tests from Table 2: a) at 60 m, b) at 300 m, c) at 1000 m of sliding distance, d) equivalent value for the whole test, calculated using Equation (1) not for $N = 10$, but $N = 15250$

The highest L_A values were at 60 m, 300 m, and these levels were reached throughout Test 4. However, at 1000 m of sliding distance, the L_A values are low in all tests except Test 1.

3. Model of sound level variability

The set of L_A values calculated by Equation (1) for 10-second time periods in Test 1 were used as the training dataset for the Random Forest algorithm [10] (random forest of regression trees) implemented in the Weka software package [11]. The obtained model (Figure 7) has very good accuracy on the training dataset

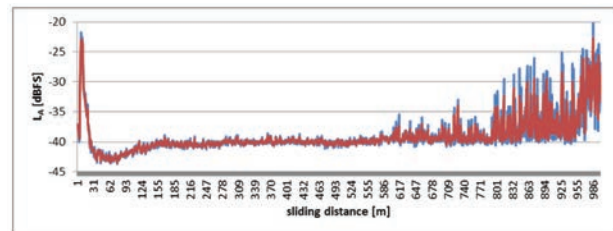


Fig. 7. L_A values during tribological Test 1: calculated from measurement (blue), and calculated by Random Forest model (red)

– root mean square error (RMSE) is 0.73 dB. However, accuracy is lower (RMSE equal to 1.94 dB) when tested by the 10-fold cross validation method. In this method, the whole dataset is divided into training (90% of data) and validation (10% of data) datasets, and the model is obtained. This process is repeated 10 times. Total accuracy is calculated as an average of accuracies of all 10 models on 10 respective validation datasets. The obtained Random Forest model of L_A variability can be used in practical technical applications.

The regression tree model of L_A variability, obtained using Weka and the same training dataset as for Random Forest, has slightly better accuracy (RMSE equal to 1.85 dB) when tested by 10-fold cross validation.

Conclusions

The emission of sound depends on phenomena and processes occurring in the friction node, which depends on the material pair used in dry sliding friction conditions. The highest L_A values were observed during the first 2 hours of Test 4 (the tribosystem consisting of DLC and 100Cr6 steel). The lowest L_A values were observed during Test 3 (the tribosystem consisting of DLC and Al_2O_3). The RandomForest method allows one to build the model of variability of sound levels as a function of sliding distance in a given tribological test.

When observing changes in the friction coefficient and linear wear, one can notice their correlation with sound emission. It is also possible to distinguish between material pairs on the basis of emitted sound. The observation of sound emission allows the monitoring the work of tribosystem and avoiding damages.

Future research will include the construction of classifiers for distinguishing between various material pairs, as well as classifiers for detecting the stage of wear.

References

- Kajdas Cz., Kulczycki A., Ozimina D.: A new concept of the mechanism of tribocatalytic reactions induced by mechanical forces. *Tribology International* 2017, 107, pp. 144–151.
- Rorrer R.A.L., Juneja V.: Friction-induced vibration and noise generation of instrument panel material pairs. *Tribology International*, 2002, 35, pp. 523–531.
- Ene N.M., Dimofte F.: Effect of fluid film wave bearings on attenuation of gear mesh noise and vibration. *Tribology International*, 2012, 53, pp. 108–114.
- Wang D.W., Mo J.L., Zhu Z.Y., Ouyang H., Zhu M.H., Zhou Z.R.: How do grooves on friction interface affect tribological and vibration and squeal noise performance. *Tribology International*, 2017, 109, pp. 192–205.
- Min D., Jeong S., Yoo H.H., Kang H., Park J.: Experimental investigation of vehicle wiper blade's squeal noise generation due to windscreen waviness. *Tribology International*, 2014, 80, pp. 191–197.
- Lu G., Shi X., Liu X., Zhou H., Chen Y.: Effects of functionally gradient structure of Ni_3Al metal matrix self-lubrication composites on friction-induced vibration and noise and wear behaviors. *Tribology International*, 2019, 135, pp. 75–88.
- SpectraPlus: *Acoustic and Vibration Spectrum Analyzer solutions*. [Online]. 2019. [Accessed 30 April 2019]. Available from: <http://www.spectraplus.com>
- International Electrotechnical Commission: *Audio and audiovisual equipment – Digital audio parts – Basic measurement methods of audio characteristics – Part 3: Professional use*. IEC 61606-3:2008. IEC, 2008.
- International Organization for Standardization: *Acoustics – Determination of occupational noise exposure – Engineering method*. ISO 9612:2009. IOS, 2009.
- Breiman L.: Random Forests. *Machine Learning*, 2001, 45(1), pp. 5–32.
- Frank E., Hall M.A., Witten I.H.: *The WEKA Workbench. Online Appendix for “Data Mining: Practical Machine Learning Tools and Techniques”*. Morgan Kaufmann, Fourth Edition, 2016.
- International Electrotechnical Commission: *Electroacoustics – Sound level meters – Part 1: Specifications*. IEC 61672-1:2003, IEC, 2003.
- Ozimina D., Madej M., Desaniuk T., Żółty M., Kulczycki A.: Effects of a graphene-enhanced lubricant on the performance of a tribosystem. *DEStech Transactions*, 2019, paper accepted.
- Piotrowska K., Baranowicz P., Wysokińska-Miszczuk J., Madej M., Skóra M.: The Tribological Properties of the Ti6Al4V Alloy with Nitrogen Ion Implantation. *Tribologia*, 2019, 1, pp. 37–47.
- Ozimina D., Madej M., Kowalczyk J.: Determining the tribological properties of diamond-like carbon coatings lubricated with biodegradable cutting fluids. *Archives of Metallurgy and Materials*. 2017, 62(4), pp. 2065–2072.

This article appeared in its printed version in Journal of Machine Construction and Maintenance. The electronic version is published in DEStech Publications, Inc., Lancaster, PA, 2019, Proceedings of FUTURE ENGINEERING CONFERENCE.

Krzysztof STANKIEWICZ*

Institute of Mining Technology KOMAG, Gliwice, Poland

* Corresponding author: kstankiewicz@komag.eu

SMART MINING COMMUNICATION SYSTEMS

© 2019 Krzysztof Stankiewicz

This is an open access article licensed under the Creative Commons Attribution International License (CC BY)

<https://creativecommons.org/licenses/by/4.0/>**Key words:** sensors, communication, network, data.

Abstract: Polish industry stands at the threshold of the 4th Industrial Revolution, whose core is data collected from manufacturing and exploitation processes. The number of the devices that are capable of communication increases exponentially. These facts imply a constant evolution of automated systems, intelligent data analysis, and methods for their reliable and efficient transmission. The current rapid development of communication technologies mainly focuses at the transmission of digital data. Digital data is most often sent within separated hardware segments of business management structures, for the control and monitoring of machines, devices, and processes. At the lowest levels, fieldbuses prevail, from which data is aggregated and transmitted, often by Ethernet protocols, to the level of enterprise branch servers. Then branches connect to the central structures using encrypted tunnels created within the Internet. The whole structure is exposed to a number of threats related to the presence of typical failures, disruptions, as well as actions leading to the data mismatch or transmission failures. A similar state of needs and threats in the field of acquisition and transmission of digital data occurs in Polish mining. The problem of the complexity of communication structures, including sensory networks and battery-powered wireless sensors, becomes a part of mining technology and the processing of raw materials. Development processes of sensory networks are mainly focused on its reliability, followed by performance. For this reason, as well as bearing in mind the reduction of the costs of building the communication infrastructure, networks with mesh topology develop, which are characterized by high transmission reliability due to its multi-redundant structure. This article describes the development of one of the latest communication protocols SSKIR, intended for use in mesh networks.

Inteligentne górnicze systemy komunikacyjne

Słowa kluczowe: sensory, sieć, komunikacja, dane.

Streszczenie: Polski przemysł stoi u progu 4 Rewolucji Przemysłowej, której trzon stanowią dane pochodzące z procesów wytwórczych i eksploatacyjnych. Liczba urządzeń zdolnych do komunikacji rośnie wykładniczo. Fakty te implikują stałą ewolucję systemów zautomatyzowanej, inteligentnej analizy danych i metod ich niezawodnej oraz wydajnej transmisji. Obecny, gwałtowny rozwój technik komunikacyjnych dotyczy przede wszystkim transmisji danych cyfrowych. Dane cyfrowe przesyłane są najczęściej w ramach wyraźnie wyróżnionych segmentów sprzętowych struktur kierowania przedsiębiorstwem, sterowania i monitorowania maszyn, urządzeń oraz procesów. Na najniższych poziomach dominują magistrale polowe, z których dane są agregowane i przesyłane, często protokołami ethernetowymi, na poziom serwerów oddziałów przedsiębiorstwa. Następnie oddziały łączą się ze strukturami centralnymi za pomocą szyfrowanych tuneli tworzonych w ramach sieci Internet. Struktura ta narażona jest na szereg zagrożeń związanych z obecnością typowych awarii, zakłóceń, jak i celowych działań prowadzących do zawłaszczenia danych lub unieruchomienia transmisji. Podobny stan potrzeb i zagrożeń w zakresie akwizycji i transmisji danych cyfrowych sygnalizuje polskie górnictwo. W ramach procesów wydobywczych i przerobczych surowców skalnych coraz częściej napotyka się na problem złożonych struktur komunikacyjnych, w tym sieci sensorycznych obejmujących czujniki bezprzewodowe zasilane bateryjnie. W ramach sieci sensorycznych główny nacisk kładziony jest na jej niezawodność, a w dalszej kolejności na wydajność. Z tego powodu, oraz mając na uwadze redukcję kosztów budowy infrastruktury komunikacyjnej, rozwija się sieci o topologii kratownicowej (ang. mesh), charakteryzujące się wysoką niezawodnością transmisji dzięki strukturze multiredundantnej. W niniejszym artykule opisano rozwój jednego z najnowszych protokołów komunikacyjnych SSKIR, przeznaczonego do zastosowań w sieciach kratownicowych.

Introduction

The most important way to increase the efficiency of coal mining, while maintaining the safety of crews, is to include Polish mining in the idea of Industry 4.0. Research into key sectors of the German and European economy has shown [3] that progress is possible through digital transformation, whose basic factors are digital data, automation, communications, and digital access of consumers.

The broadly understood Polish underground mining industry is beginning to transform itself within the idea of the Mining 4.0 programme, which means the development of such areas as the Internet of Things, mechatronics, telematics, and product distribution.

The first area, the Internet of Things (IoT), is aimed at including all devices into the network of intelligent management, both from the local manufacturer's level and from the external supplier/manufacturer/service provider of machines and devices. From the point of view of security and economy, it is important to combine production processes [11] with business processes [14] through appropriate software. On the basis of the collected data, their evaluation, inference, and suggestions of solutions are made. Thanks to the connection with economics, it is possible to obtain measurable information about the conducted production and business processes [16].

The second area, mechatronics, combines elements of mechanics, electronics, control and computer science, and it is used, among others, to design modern machines and equipment for automation and robotics. According to the definition adopted by the International Federation for the Theory of Machines and Mechanism, mechatronics is a "synergistic combination of precision mechanics, electronic control and system thinking in the design of products and production processes" [10]. It should be stated that this area has been developed for several years by scientists and manufacturers of products working for the mining industry. The fact that mechatronics in mining is already well established is also confirmed by that education in the field of mechatronics is one of the requirements for qualifications in the area of professional training of a person who is supervising underground activities of a mining plant with mechanical specialization in the field of underground machines and equipment.

Telematics is understood as [12] structural solutions, in which electronic information acquisition and processing are integral elements of the telecommunications system and technical solutions integrating universal telecommunications and IT systems. Telematics basically defines new telecommunication functions connected with the field of IT, which, in mining, means specialized ICT systems

integrating telecommunications with IT used in these systems [13].

The last of the areas, product distribution, is oriented towards the final customer, while the distribution itself is an element of logistic activities in the company [17]. The character of this area is best explained by one of many definitions, which states that the purpose of distribution is to provide customers with products in appropriate quality, in the appropriate time and place, in the most convenient forms and conditions of making purchases, as well as at the lowest possible costs of bringing them from production to intermediate and final customers [10].

1. State-of-the-art smart mining communication systems

The rock and coal, surrounding a coal mine roadway, act as relatively low-loss dielectric media in the frequencies of range 200–4,000 MHz and a dielectric constant of 5–10. Under these conditions, a reasonable hypothesis is that the transmission takes the form of wave propagation, since the wavelength of ultra-high-frequency (UHF) waves are smaller than the roadway dimensions. An electromagnetic wave traveling along a roadway in a dielectric medium can propagate in any one of a number of allowed waveguide modes. All of these modes are modes with losses, because any part of the wave that impinges on the roadway wall is partly refracted into the surrounding dielectric and partly reflected back into the waveguide. The reflected part propagates away from the waveguide and represents a power loss. The overall loss in the strength of the signal, in a straight roadway, is the sum of propagation loss and the insertion loss of the transmitting and receiving antennas. It has been found that the total loss is minimal in the range of 400–1000 MHz, depending on the desired communication distance. Hence, the UHF communication system is used in straight roadway for line-of-sight communication [1].

In the present market, there are many mining systems of wired and wireless communication, which must function under the harsh conditions described above. Most of them do not have smart features, understood as the ability to adapt and learn, which increases the resistance to failures and interference. Mining telecommunications networks are mainly used for analogue and digital voice communication, text communication, identification, positioning, and the aggregation of data coming from machinery and equipment during longwall and excavation operations. Mining communication networks are mostly created with the use of classical bus and star topologies as their assembly. The main communication routes are

commonly made with the use of a fibre optic medium. However, there are relatively many networks with copper medium in use, the core of which is inefficient serial communication based on the RS485 protocol.

As the hierarchy of communication becomes lower and lower, innovative solutions of fieldbus class networks, including networks intended for data acquisition from extensive sensory structures, are more and more frequently encountered. In this context, the solutions developed in recent years should be listed:

1. EH-PressCATER (Fig. 1) – a smart wireless network of pressure sensors with mesh topology produced by Elgór-Hansen Sp. z o.o., characterized by the following features:
 - anti-explosion structure according to the PN-EN 60079-25,
 - wireless control & communication – no troublesome wiring,

- robustness to damage of communication nodes due to adaptation and redundancy,
- pressure control inside pillars, props, and on inflow or outflow trunk lines,
- minimum one year work period on one battery,
- registration of the pressure course with the measurement frequency & result with a refreshing rate of 1 second,
- possible remote parameterization of the RPSI sensors adjustments from the computer,
- data/measurement archiving in the SQL database,
- open architecture,
- possible expansion of the wireless pressure sensor network,
- making data available to other visualization systems using standard transmission protocols & generation of reports.

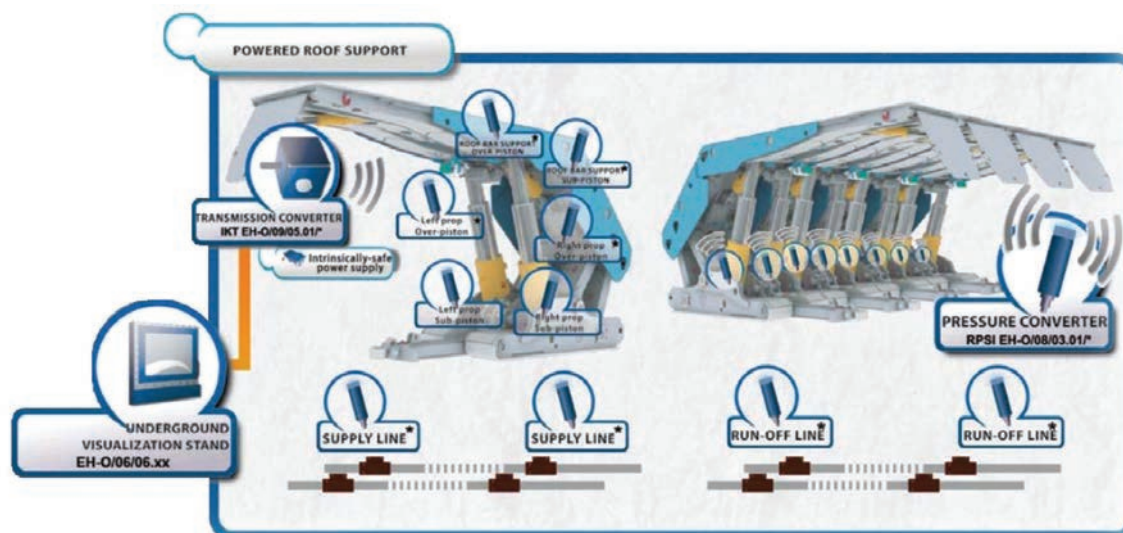


Fig. 1. EH-PressCATER wireless monitoring system [5]

2. DPS11 – mine smart telemonitoring system (Fig. 2) produced by ZAM-SERVICE s.r.o.. The DPS11 Mine Data Transfer System is a modular system for two-way transfer of data, visualization and control the mines technology and air monitoring in the SCADA standard. DPS11 use for the data transfer between the mine sections comprised of data concentrators fitted with terminal monitoring sensors or DKD11-ABV concentrators and the surface section comprised of modems and a server to process, store and visualise the data. The DPS11 provides communication and power supply to peripheries connected to the system. The system ensures the transfer of data with information referring to, for example, the methane concentrations measured, the levels of analogous signals, statuses of binary inputs, binary outputs, and voltage outputs.

The system also includes a state-of-the-art solution of communication cable RFK-01 which integrates WiFi access points and RFID readers in its structure (Fig. 3).

3. Since 2012, ITG KOMAG has been developing the concept of a protocol of self-organizing communication structure, named SSKIR [9], which is based on one of artificial intelligence technologies, “swarm intelligence,” which is a direct implementation of phenomena and behaviour observed in nature among organisms living in large groups. Their behaviour, to some extent, can be transferred to the operation of routing protocols. The system structures developed by humans (irrespectively to real implementation), using the swarm algorithm, have high possibilities for adaptation and high operational reliability. In 1987,

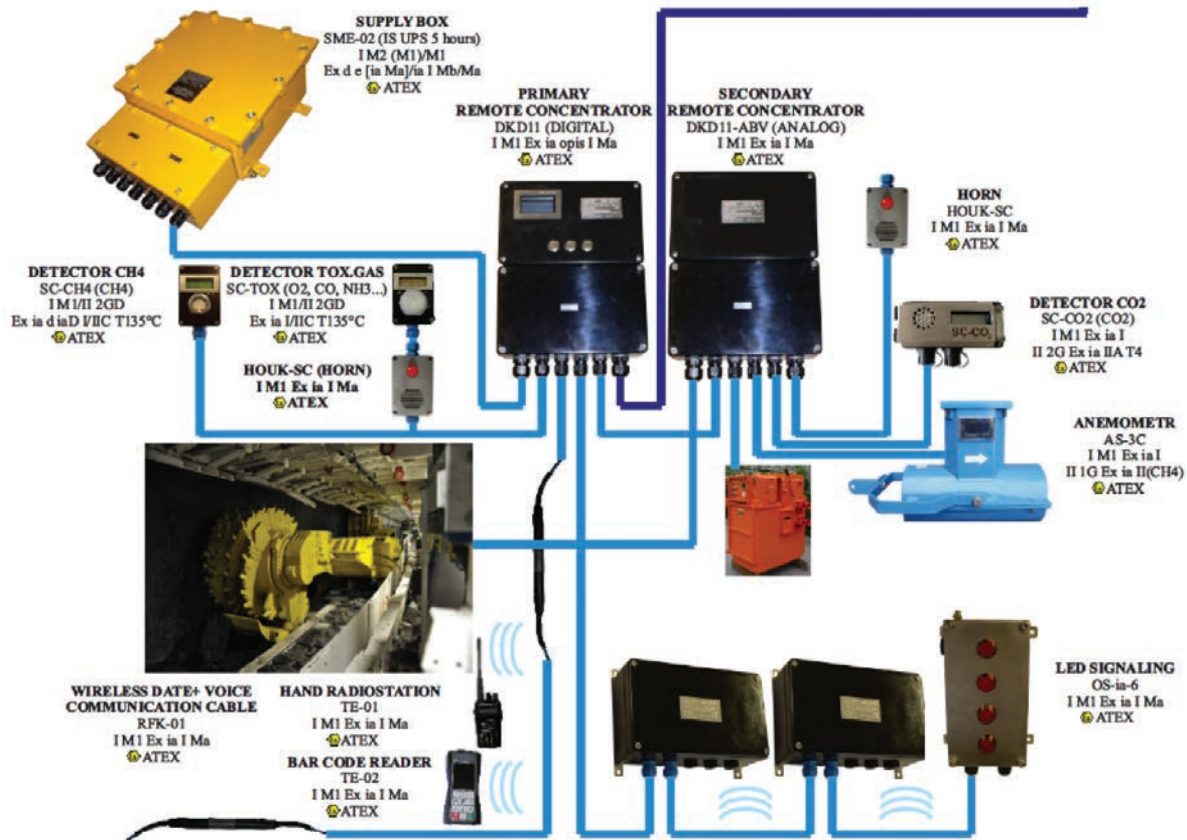


Fig. 2. DPS11 mine telemonitoring system diagram [15]



Fig. 3. RFK-01 communication cable

during the SIGGRAPH conference, a programmer, Craig Reynolds, in the paper entitled “Flocks, Herds, and Schools: A Distributed Behavioural Model,” suggested three basic rules of self-organization based on observed groups of animals, as follows [7]:

- Collision avoidance is control eliminating a local concentration of individuals. Collision avoidance eliminates accumulation of hardware and decision structures.
- Flock centring are actions towards the average behaviour of local groups of individuals.
- Velocity matching are actions towards the average objective of local groups of individuals. Velocity matching enables the individual to adapt its actions to other individuals from its local group.

Based on the above rules, the creation of a communication system made of a sensor network in which routing is based on a swarm algorithm was suggested [8]. Each data frame transferred by the Measure Transmission Unit (MTU) is marked by a quality coefficient W_p , specifying the transmission priority referring to the effectiveness of data transmission to the main transceiver stations. This coefficient can take a value that conforms to one of connections or path metrics [2, 4].

2. Smart mining wireless communication system based on the SSKIR protocol

The solution of sensory network proposed by ITG KOMAG is based on wireless network nodes working at the frequency of 2.4 GHz. The advantage of this solution is the short distance between the nodes (under 10m), and thus negligible problems with power loss and wave reflections in the mine roadways. The presented communication system will also be implanted in the SSMS longwall support geometry monitoring system [6].

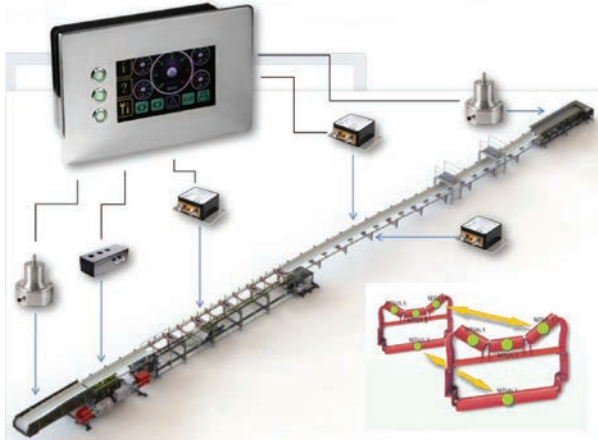


Fig. 4. Example of implementation of the SSKIR protocol in sensory network of belt conveyor rollers [8]

As mentioned above, the W_p coefficient can take a value that conforms to one of connections or path metrics; therefore, transmission speed and the number of hops of transmitted frames containing the following measurement data is based on data propagation times:

- Expected Transmission Count (ETX) is a metric that is widely used in mesh networks. ETX is the metric specifying the number of expected transmissions, which is indispensable when sending data to the next node without errors. The number varies from 1 to infinity. An ETX metric equal to 1 indicates a perfect data transmission path, and an ETX approaching infinity represents the connection that is not functioning.
- Expected Transmission Time (ETT) is an extension of ETX metrics, since it takes into consideration the difference in the speed of data transmission. The ETT of connection l is defined as an expected duration of the successful transmission of a data package in connection l . The importance of p path is defined as a sum of the ETT of all possible connections along the given path. The relationship between ETT and ETX can be expressed as follows:

$$ETT_l = ETX_l \frac{s}{b_l} \quad (1)$$

where b_l – is a speed of transmission of information in connection l , s – is a size of transmitted package.

- Hop count is the most often used routing metric in the existing routing protocols, such as DSR (Dynamic Source Routing), AODV (Ad Hoc On-Demand Distance Vector), or DSDV (Destination-Sequenced Distance Vector). Hop count is the routing measure used to measure a distance between transmitting and receiving stations counting the hops. The next hop can be a receiving station or device intermediating

in the exchange of information. The protocol using the Hop count metric determines the route with the lowest number of hops between transmitting and receiving stations.

- Weighted Cumulative ETT (WCETT) is a metric that includes both the quality of a connection (losses, throughput) and the number of hops. Thus, we can reach a compromise between delay and throughput.

$$WCETT(p) = 1 - \beta \cdot \sum_{l \in p} ETT_l + \beta \cdot \max_{1 \leq j \leq k} X_j \quad (2)$$

where β – is a set parameter from the range $0 \leq \beta \leq 1$. Higher values of β give priority to paths using many channels and its lower values give priority to shorter paths, $\max_{1 \leq j \leq k} X_j$ – counts the maximal time of appearance of the same channel in a given path.

- MIC is metric that improves the operation of WCETT by solving its isotonicity and inability of detecting the collisions. MIC metrics of p path can be defined as follows:

$$MIC(p) = \frac{1}{N \cdot \min(ETT)} \sum_{linkij \in p} IRU_{ij} \sum_{nodei \in p} CSC_i \quad (3)$$

where N – is a number of all nodes in the network, $\min(ETT)$ – is the lowest ETT in the network and it can be determined on the basis of the lowest speed of data transmission in radio charts.

Additionally, the following principles resulting from swarm phenomena are assigned to each data package so that the system can react to changes in a node structure (failures, nodes displacement):

1. The package matches its speed to the packages moving in paths of higher W_p coefficient.
2. The package uses the path parallel to the optimal route (of highest known W_p value), if its W_p decreases.
3. The package uses the optimal path (of higher known W_p value), if the W_p coefficient of the current route decreases.
4. The package avoids transmission through the nodes that are marked as damaged.
5. The package can leave the present path, if the main transceiver station is found.

Local data, which is indispensable for the realization of tasks resulting from the above principles, are calculated and stored in nodes. There is no need to create a master routing table. The use of these rules causes that the group of MTUs creating the transmission connection automatically develops the structure of reliable transmission routes while neglecting the damaged units. The data frame in the SSKIR protocol is defined by four additional values:

- Its own unique MTU identification number,
- X and Y coordinates defining the occupied position in the solution space of the communication path structure,
- The priority factor in the communication path of which the frame is an element,
- The baud rate for the X and Y dimensions, i.e. vX and vY .

The neighbours of frames with the number of a given MTU are called other frames that are in the MTU transmission range, i.e. those that are in a sufficiently short distance d and simultaneously in the field of view, defined by the value of virtual angle r . In order to check whether a given frame e of coordinates $e.X$ and $e.Y$ respectively, is a neighbour of MTU b of coordinates $b.X$ and $b.Y$, it is necessary to check first whether the element is in a sufficiently short distance.

$$\sqrt{(e.X - b.X)^2 + (e.Y - b.Y)^2} < d \quad (4)$$

If the inequality is not met, then the next rules are not checked, because a given frame from the MTU e is certainly not a neighbour of frames from the MTU b . If the inequality is met, it is checked if the frame is in the virtual viewing angle r by determining the angle r_1 under which the frame moves virtually:

$$r_1 = \arctan\left(\frac{b.vY}{b.vX}\right) \quad (5)$$

and the virtual angle r_2 of the segment connecting the MTU b frame with the MTU e frame:

$$r_2 = \arctan\left(\frac{e.Y - b.Y}{e.X - b.X}\right) \quad (6)$$

assuming that $b.vX \neq 0$ and $e.X - b.X \neq 0$. Then the absolute value of the angle difference is calculated and the inequality checked:

$$|r_1 - r_2| < r \quad (7)$$

If the unevenness is met, then the frames come from neighbouring MTU. Next, the first rule is applied, and each frame adjusts its path to frames from neighbouring MTU. One must calculate the average speed v_{avg} of all frames from the neighbouring MTU (separately for the vX and vY components) and then modify the frame transmission speed, taking into account the path priority factor, the current speed, and the calculated average, according to the following formulae:

$$\begin{aligned} b.vX &= b.vX + \left(W_p \cdot (vX_{avg} - b.vX)\right) \\ b.vY &= b.vY + \left(W_p \cdot (vY_{avg} - b.vY)\right) \end{aligned} \quad (8)$$

To apply the second rule, the average number of frame jumps in the d_{avg} transmission path should be calculated in relation to frames from neighbouring MTU, and then the frame transmission speed should be modified in relation to neighbouring MTU. Formulae (9) are the result of the triangular similarity claim. The frame's position in the transmission path, whose speed is modified b and the position of the neighbour e , is used:

$$\begin{aligned} d &= \sqrt{(e.X - b.X)^2 + (e.Y - b.Y)^2} \\ b.vX &= b.vX + \frac{(e.X - b.X) \cdot (d - d_{avg})}{d} \\ b.vY &= b.vY + \frac{(e.Y - b.Y) \cdot (d - d_{avg})}{d} \end{aligned} \quad (9)$$

The third rule shows that, when a frame in a path with a lower priority coefficient tries to carry out the transmission, competing with a frame with a higher priority, it should avoid it by modifying its speed. Formulae (10) also use the triangular similarity claim. Let b be a lower priority frame competing with a frame from the neighbouring MTU, with a higher priority e . In regard to the above rule, the following formulae should be applied:

$$\begin{aligned} d &= \sqrt{(e.X - b.X)^2 + (e.Y - b.Y)^2} \\ b.vX &= b.vX + \left(\frac{(e.X - b.X) \cdot d_{min}}{d} - (e.X - b.X)\right) \\ b.vY &= b.vY + \left(\frac{(e.Y - b.Y) \cdot d_{min}}{d} - (e.Y - b.Y)\right) \end{aligned} \quad (10)$$

where d_{min} is a preset minimum number of jumps in the transmission path, which should not be exceeded by the transmitted frame. The last two rules are introduced to the system by modifying the fourth rule based on the dependencies (10). It should be noted that each frame can move with a certain maximum speed imposed by the physical system. In simulations, this speed should be limited and the following entered:

- Limitations resulting from the presence of MTU in the emergency or start-up state (elements that frames should avoid creating transmission paths), and
- Attractors in the form of main receiving and transmitting stations.

Summary

Control and monitoring systems, capable of adaptation and learning, are used in industrial practice on a larger scale. The Internet of Things (IoT) techniques and direct communication M2M (Machine to Machine) have an impact on the structure and functionality of

control systems used in machines, shaping the idea of Industry 4.0.

Smart wireless communication systems based on the mesh topology are beginning to appear on the mining market. These systems are characterized by a high degree of reliability, scalability, and low energy consumption.

The method of the self-organization of the communication system based on a swarm algorithm enables an implementation of the state-of-the-art and effective routing technology in the networks of mesh topology, including those used in underground mines, especially in diagnostic and monitoring systems, as well as for the protection of machines. Sub-assemblies of the networks equipped with MTU nodes can be treated as components of a measuring swarm. It is particularly important for operational safety in underground mines due to the reliability of mesh networks.

References

1. Bandyopadhyay L.K., Chaulya S.K., Mishra P.K.: *Wireless Communication in Underground Mines: RFID-based Sensor Networking*. Springer, 2010.
2. Basagni S., Conti M., Giordano S., Stojmenovic I.: *Mobile Ad Hoc Networking*. New Jersey: IEEE Press, 2004.
3. Roland Berger Strategy Consultants, BDI: *The digital transformation of industry*. [Online]. 2015. [Accessed 30 April 2019]. Available from: https://www.rolandberger.com/publications/publication_pdf/roland_berger_digital_transformation_of_industry_20150315.pdf
4. Boukerchea A., Turgut B., Aydin N., Mohammad A.Z., Bölöni L., Turgut D.: Routing protocols in ad hoc networks: A survey. *Computer networks*, 2011, 55(13), pp. 3032–3080.
5. Elgór-Hansen: *Pressure monitoring system for roof supports*. [Online]. 2019. [Accessed 30 April 2019]. Available from: <https://elgorhansen.com/en/offer/pressure-monitoring-system-for-roof-supports>
6. PRASS III: *Main website*. [Online]. 2019. [Accessed 30 April 2019]. Available from: <http://prass3.komag.eu/>
7. Reynolds C.W.: Flocks, Herds, and Schools: A Distributed Behavioral Model. *Computer Graphics*, 1987, 21(4), pp. 25–34.
8. Stankiewicz K.: Mining control systems and distributed automation. *Journal of Machine Construction and Maintenance*, 2018, 2(109), pp. 117–122.
9. Stankiewicz K.: A self-organizing communication system based on the swarm algorithm. Presented at the *International Conference Mechatronics: Ideas for Industrial Applications*, Gdańsk (Poland), 11–13 May 2015.
10. Sztucki T.: *Marketing przedsiębiorcy i menedżera*. Warszawa: Agencja Wydawnicza Placet, 2000 [in Polish].
11. Trenczek S.: Kierunki rozwoju infrastruktury systemowej zasilania, informatyki technicznej i automatyki. *Mechanizacja i Automatykacja Górnicztwa*, 2009, 9, pp. 9–15 [in Polish].
12. Wydro K.B.: Telematyka – znaczenie i definicje terminu. *Telekomunikacja i techniki informacyjne*, 2005, 1–2, pp. 116–127.
13. Wojacek A.: Telematyka w podziemnych zakładach górniczych. *Mining – Informatics, Automation and Electrical*, 2017, 7, pp. 27–34 [in Polish].
14. Żeliński J.: *Co to jest proces biznesowy*. [Online]. 2012. [Accessed 30 April 2019]. Available from: <https://it-consulting.pl/autoinstalator/wordpress/2012/09/28/business-process-manifesto>
15. ZAM-SERVICE: *DPS II Mine Telemonitoring System*. [Online]. 2009. [Accessed 30 April 2019]. Available from: http://www.zam.cz/KATALOG_DULNI/EN/DPS-11_EN_V140116.pdf
16. Zawila-Niedźwiecki J.: *Zarządzanie ryzykiem operacyjnym w zapewnianiu ciągłości działania organizacji*. Kraków: Wyd. Edu-Libri, 2013 [in Polish].
17. Witkowski J.: *Rodzaje działań w zakresie strategii logistycznej przedsiębiorstwa*. Wrocław: AE we Wrocławiu, 1995 [in Polish].

This article appeared in its printed version in Journal of Machine Construction and Maintenance. The electronic version is published in DEStech Publications, Inc., Lancaster, PA, 2019, Proceedings of FUTURE ENGINEERING CONFERENCE.

Jacek DŁUGOPOLSKI^a, Maria RICHERT^{b,*}^a Faculty of Computer Science, Electronics and Telecommunications, AGH University of Science and Technology, Cracow, Poland^b Faculty of Management, AGH University of Science and Technology, Cracow, Poland

* Corresponding author: mrichert@agh.edu.pl

NATURALLY PARALLEL MEASURING SYSTEM BASED ON FPGA HARDWARE

© 2019 Jacek Długopolski, Maria Richert

This is an open access article licensed under the Creative Commons Attribution International License (CC BY)

<https://creativecommons.org/licenses/by/4.0/>**Key words:** FPGA, measurement, parallel, sensors, Air-conditioning.

Abstract: The FPGA (Field Programmable Gate Array) technology, usually a little unnoticeable, almost from the very beginning is developed simultaneously with the microprocessor technology. The possibility for the system designer or end user to influence the internal structure of the integrated circuit gives unattainable possibilities of building plastic and fully massively parallel systems that fit in almost one integrated circuit. This fact allows, among others for building fully parallel multi-point measuring systems. This manuscript presents the architecture proposal for such an FPGA-based exemplary multichannel measurement system and presents the results of its practical use to study the functioning of a tubular heat exchanger in automotive air-conditioning.

Naturalnie równoległy system pomiarowy oparty na technologii FPGA

Słowa kluczowe: FPGA, pomiary, równoległość, czujniki, klimatyzacja.

Streszczenie: Technologia programowalnych układów scalonych FPGA (Field Programmable Gate Array), zwykle trochę niezauważana, niemal od samego początku rozwija się równoległe z technologią mikroprocesorową. Możliwość wpływania przez projektanta systemów lub użytkownika końcowego na wewnętrzną strukturę układu scalonego daje nieosiągalne w przypadku zwykłych procesorów możliwości budowania plastycznych i w pełni masywnie równoległych systemów mieszczących się niemal w jednym układzie scalonym. Fakt ten pozwala m.in. na budowanie w pełni równoległych wielopunktowych systemów pomiarowych. W artykule tym pokazano właśnie propozycję architektury takiego bazującego na FPGA przykładowego wielokanałowego systemu pomiarowego oraz przedstawiono wyniki jego praktycznego wykorzystania do badania funkcjonowania rurowego wymiennika ciepła w klimatyzacji samochodowej.

Introduction

From the very beginning when we are dealing with new technologies and with various kinds of technical devices or we are trying to explore and understand complex systems occurring naturally in nature, then there is always a need to perform various measurements. Thanks to such measurements, we can, for example, determine the technical condition of the device or system, detect structural abnormalities or we can assess the effectiveness of its individual components [13]. A smaller problem is in the case, when we need to have measured a physical quantity only in a single point. Such a measurement, which of course takes a certain amount of time, will determine the value of the measured quantity

over a given time interval. It is worse when we have to make a multipoint measurement of some physical quantity, e.g. on the surface of a working mechanical or electronic device. Performing measurements one by one at specific points in the device is a solution, but produces a significant phase error in the time domain. Obtained in this way measurements of the measured quantity at different points of the device are slightly offset from one another in time, which in some cases may lead to erroneous analyzes and conclusions. Therefore, it seems advisable to build multi-point measuring systems that perform independent measurements at all tested points simultaneously (in parallel) without phase shifts in the time domain.

The motivation for adopting and commissioning the solution described here, i.e. a multi-point

measuring system that allows to perform many parallel measurements simultaneously at the same time (in this case temperature), was the need to examine the effectiveness of a proposed innovative tube-in-tube type of heat exchanger with torsion channels, intended for car air conditioning systems and implemented as part of the project INNOTECH – K3/IN3/2/225688/NCBR/14. Car air conditioners operate by using different types of coolant [8–9] in combination with various heat dissipation components. The project concerns a new solution applied in car air conditioners with CO₂ as a cooling medium. To build those air conditioners, aluminum alloys has been applied in the construction of their key components [4–7]. Assessment of the efficiency of such an exchanger requires determining the temperature on its surface at a given time simultaneously at many different points along its entire length. Performing individual measurements in a sequential manner one by one would not provide the right data for further analysis. The proposed measurement system is universal and could also be used in other diverse solutions of heat exchangers [10–18].

The eternal need for multi-point performance of various types of measurements has long been the cause of many previously proposed solutions. The simplest method of realizing this type of measurements is the use of already existing serial buses allowing communication between the controller (master) and multiple sensors (slaves). The most popular buses of this type are: 1-Wire, I2C, SPI or RS485. As a bus driver, a microprocessor or a single-chip controller is usually used. An example of such a solution is described in [19]. The authors presents there a flexible and multi-sensor temperature measurement system, consists of a control unit with a microcontroller ATmega 2560 and of only ten different 1-Wire temperature sensors DS18B20. The designed firmware has a pipeline architecture which of course increased the time of full measurement but it didn't solve the time phase problem between all channels, which do not appears in our approach here. Much better proposition is to drive each sensor independently in parallel way but then it required multiprocessor controller where we have to use dedicated processor for each sensor. As an alternative to this, we can also use a programmable logic chip FPGA (Field Programmable Gate Array). Such a chip allows parallel hardware implementation of an independent controller for each sensor. Our paper describes exactly this method of multipoint measurement of physical quantities. Similar approach was presented in [20]. The author proposes a system that utilizes parallel multi-channel temperature measurements with digital temperature sensors operating on separate serial 1-Wire buses but the system allows only six digital temperature sensor and uses wireless Bluetooth module to communicate. In our approach, number of sensors depends only on the logical capacity of the FPGA chip and we uses 100 Mb/s Ethernet

module for fast and reliable data acquisition. The use of FPGAs is also justified by the fact that they are used in CERN in collision detectors that require extreme detection speed [21, 22]. It also means that in the future it will be very easy to use the concept of the FPGA based measuring device presented here to build very fast multichannel measuring systems. An interesting review of the use of FPGA chips for the construction of sensor systems has been presented in [23]. In this article, however, the authors focused more on the construction and optimization of the sensors themselves than on the creation of multi-channel parallel measurement systems. For parallel multi-point temperature measurement, sometimes methods based on infrared radiation are also used. In the article [24], an interesting exemplary system for multipoint temperature measurement of the human body surface is shown. Unfortunately, these types of solutions require direct visibility of the tested object and the measured elements must be protected against reflecting external heat. Therefore, this approach is not appropriate for the applications described in this article.

1. The conception of the measuring system

The details of dynamic processes in industry resulting from the operation of various types of technological solutions, or the essential details of similar dynamic processes occurring during scientific research, often elude researchers or operators of various types of devices and machines. The need for control and monitoring of physical quantities in processes of this type, such as temperature, humidity, pressure, radiation level and other, at many points of the device simultaneously, i.e. without any phase shifts in time – is often a big challenge for constructors and engineers. Especially if the state of the object or process is to be known in a given very short time.

The standard approach to multi-point measurements of physical quantities based on microprocessors is incorrect when we really want parallel measurements at the same time. When using a single-thread processor, sequential measurements using subsequent sensors causes time phase shifts, which are all the more important the faster and more dynamically the value of the measured quantity changes. In the case of measurements for very slowly changing physical quantities, the error caused by time phase shift can of course be irrelevant in some applications and omitted.

In order for the designed measuring system to be universal and, depending on the needs, easy to adapt, it was decided to build it based on a programmable FPGA chip. The FPGA technology allows an individual end user to configure such a digital circuitry in accordance with its current needs. The FPGA technology allows an

individual end user to configure such a digital chip in accordance with its current needs. Additionally, when the need arises, the configuration of the system can be changed any number of times. In other words, the end user influences the current internal logic structure of the integrated circuit. The FPGA chip, depending on the capacity, can consist of tens or hundreds of thousands of individual independent logical blocks, which can be configured and combined into more complex digital structures depending on the needs. This allows to create your own hardware integrated circuit architecture. The internal structure of the FPGA chip can be designed either by means of an electronic scheme or by means of one of the hardware description languages, e.g. VHDL or SystemVerilog. FPGA technology allows for fully hardware, multi-threaded and massively parallel implementation of control algorithms, communication and all other kinds of information processing algorithms. The problem of one computational thread in popular processors and one-chip controllers is only first of the problems. The second important drawback of using processors is the relatively small number of external communication pins they have. This forces the use of a single serial bus that supports multiple sensors by means of their individual addressing. Unfortunately, it additionally increases delays in obtaining data and increases the time phase shifts between the indications of individual sensors. Compared to microprocessors, FPGA chips are characterized by a very large number of useful communication input-output pins which can be used for independent and parallel control of many additional modules and measuring sensors. The advantage of a solution using an FPGA chip with respect to a microprocessor based solution is depicted schematically in Fig. 1.

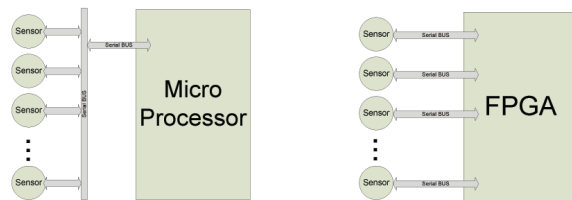


Fig. 1. Comparison of FPGA and microprocessor usage

On the left, a standard way of connecting multiple sensors to a single microprocessor is shown. A single digital serial bus (eg I2C, SPI, 1-Wire, etc.) is used, to which all subsequent sensors are connected. The microprocessor must in some way address the specific sensor from which it currently intends to read the data. At any given time, the processor can communicate with only one sensor. On the right side, the method used in the solution proposed in this article is shown. Instead of the microprocessor, a reconfigurable integrated circuit FPGA was used. Each sensor is connected to

other chip pins and thanks to this can use a separate and independent serial bus. In addition, each such sensor is operated by a separate independent part of the FPGA logic. Therefore, the FPGA chip acquires data from all sensors at the same time. Thanks to this, it is possible (within one system) to implement many parallel, simultaneous and independent measurement processes. The hardware (not software) solution proposed here, based on a programmable FPGA integrated circuit allows simultaneous (in the full sense of the word) reading data from all used sensors and making those data available through the network transceiver to outside computers in the form of measurement vectors. Thanks to this, the data can then be stored safely and securely or it can be analyzed in real time by any computer connected to the network. Fig. 2 shows the concepts of the presented solution.

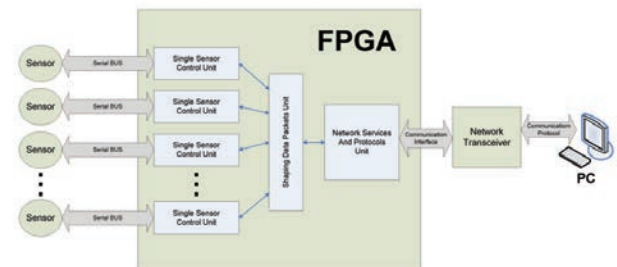


Fig. 2. The concepts of the FGA configuration

Data from multiple sensors are taken simultaneously by the independent modules of “Single Sensor Control Unit” (depicted on the left) and then, by means of the “Shaping Data Packets Unit”, they are formed into a multi-point vector of the measured state. The vector formed in this way is sent to the “Network Services and Protocols Unit” where the network packet is created and sent through the Transceiver module via network to PC computers. All the above-mentioned blocks, implemented in the FPGA chip using the VHDL hardware description language, work independently and in parallel, and are synchronized only by the logic of data flow. On a PC, any application that supports the used network protocol can download data from the measurement system and process them, also in real time. Moreover, not only one but many independent PCs (or other computers) can perform calculations on the provided data at the same time, which allows multithreaded simultaneous analysis of the same data with different algorithms.

2. Practical implementation of the proposed measuring system

As an example of the application of the concept discussed above, a test stand was designed and implemented to compare the efficiency of tubular heat exchangers (type: pipe-in-pipe) for automotive air

conditioning systems. The exchanger to be tested is shown schematically in Fig. 3. A counter-current variant is used here, in which the cold coolant flows through the central exchanger tube and the hot coolant flows through the outer tube.

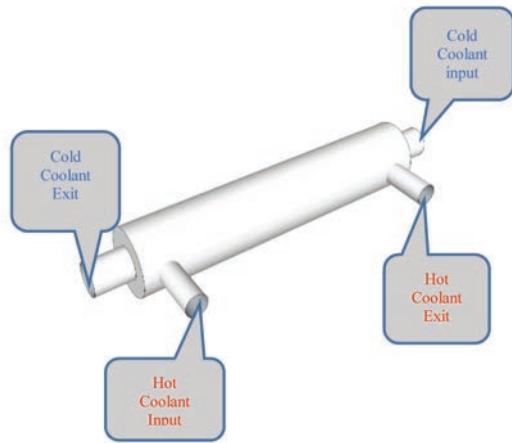


Fig. 3. Heat exchanger scheme of coolants flow

One of the research methods during the design of this type of systems was to measure the dynamics of the temperature distribution on the surface of the heat exchanger in order to check its effectiveness and throughput during operation. In order for such measurements to be possible, the model of the proposed solution was further elaborated by deciding on the types of individual components. This is shown in Fig. 4.

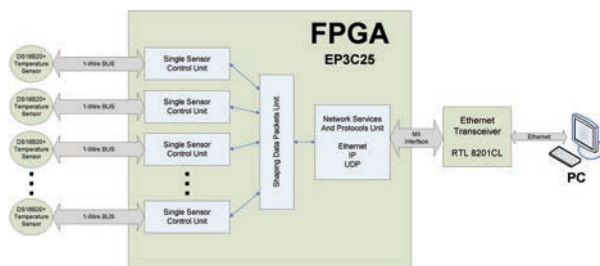


Fig. 4. FPGA based system detailed construction

To ensure simultaneous temperature measurement in many places of the exchanger, it was decided to use: digital temperature sensors DS18B20 + from MAXIM-DALLAS with temperature measurement range from -55°C to 125°C and the accuracy of 0.5% declared by the manufacturer. In many cases, a better solution is to use digital than analog sensors because of their initial calibration by the manufacturer. Of course, after proper adaptation, analog sensors can still be used in digital systems [25]. In our solution, the temperature sensors were connected via the 1-Wire buses to the programmable FPGA EP3C25 Cyclone III logic chip from INTEL to enable their independent and parallel operation. In

addition, the Realtek RTL8201CL Ethernet network module has been connected to the FPGA through the MII interface to enable constant and safe transmission of measured temperature values to an external computers. The UDP/IP protocols and broadcast packets were chosen to use.

The use of a programmable FPGA chip in place of a processor allowed for easy handling of a large number of sensors. An additional advantage of this solution is the parallel operation of all twenty-two measuring lines, and therefore all measurements take place at the same time. The undoubted disadvantage of this solution is a rather complicated and long-lasting process of creating a configuration description for the FPGA chip. This process is in fact based on developing a logical structure for a dedicated integrated circuit, using the chosen hardware description language, in this case it was the VHDL language. For example, separate hardware components for temperature sensors were created as well as a hardware MII (Medium Independent Interface) protocol component for communication with the RTL8201CL chip. The headings and data types for these components are shown in Fig. 5 and Fig. 6.

```

type ds18b20_type is
record
  event:          std_logic;
  temperature_Xdot0: integer range 0 to 255; --czesc calkowita
  temperature_OdotX: integer range 0 to 15; --czesc ułamkowa
  temperature_string: string(1 to 7);
end record;

component ds18b20_entity is
  port(
    i_clk:          in std_logic;
    i_ds18b20_bit: inout std_logic; -- 1-Wire
    i_data:         inout ds18b20_type
  );
end component;

```

Fig. 5. VHDL temperature sensor component interface code

```

type ethernet_type is
record
  port_in:          std_logic_vector(2 * 8-1 downto 0); --
  x"2ee0";
  port_in_string:  string(1 to 5);
  port_out:         std_logic_vector(2 * 8-1 downto 0); --
  x"32c8";
  port_out_string: string(1 to 5);
  trigger_send:    std_logic;
  packet_r:        std_logic_vector( (80+42) * 8-1 downto 0);
  packet_s:        std_logic_vector( (ethernet_LEN+42) * 8-1 downto 0);
  packet_port_to:  std_logic_vector(2 * 8-1 downto 0);
  receive_start:   std_logic;
  parser_reset:    std_logic;
  parser_byte:     std_logic_vector(7 downto 0);
  parser_clk:      std_logic;
  crc_error:       std_logic;
  do_send:         std_logic;
  event:           std_logic;
end record;

component ethernet_entity is
  port(
    txd:          out std_logic_vector(3 downto 0);
    txc:          in std_logic;
    txen:         inout std_logic;
    rxd:          in std_logic_vector(3 downto 0);
    rxce:         in std_logic;
    rxdv:         in std_logic;
    data:         inout ethernet_type
  );
end component;

```

Fig. 6. VHDL Ethernet sensor component interface code

The final effect of the built and commissioned controller for the measuring system is shown in Fig. 7.

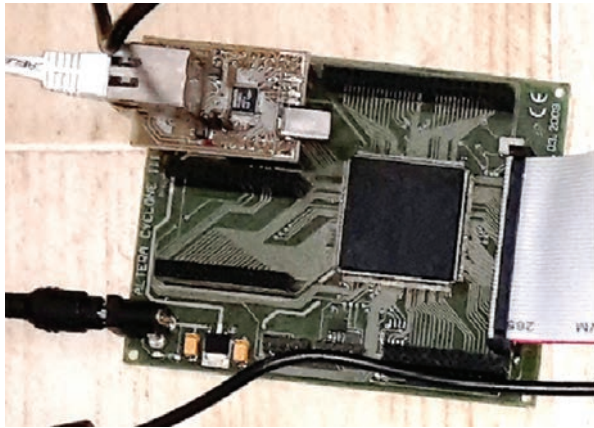


Fig. 7. The FPGA controller

As already mentioned, the DS18B20 + temperature sensors are connected to a controller based on a programmable FPGA Cyclone III system using a 1-Wire digital bus, while the RTL8201CL Ethernet system using a MII bus. In order to achieve the intended functionality of the system, a dedicated internal configuration for FPGA chip was developed using VHDL hardware description language, including implementation of:

- hardware 1-Wire communication algorithm for twenty two temperature sensors
- hardware algorithm for reading and processing data from sensors.
- communication algorithm with the Ethernet network module via the MII interface
- hardware version of the UDP/IP network protocol stack to the extent necessary to obtain communication between the measuring device and PCs collecting data.

The final effect of the constructed device is shown below in Fig. 8.

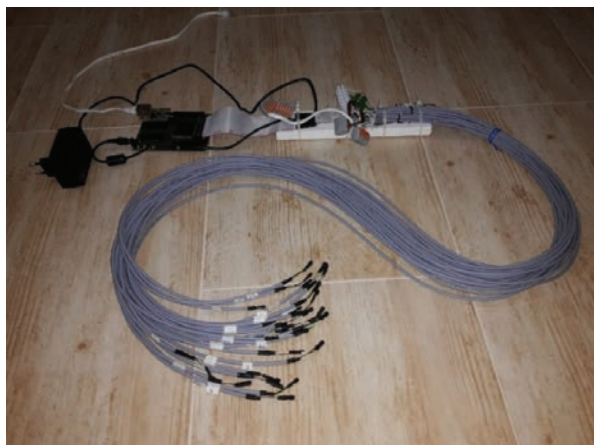


Fig. 8. The complete FPGA based device for multipoint temperature measurement

Fig. 9 shows (from the left side) the power supply, then the controller based on FPGA chip, which is connected with a special tape with temperature sensors placed on the ends of one and a half meters wires. In order to enable the automatic collection of data during experiments, a dedicated computer application was developed in the C # programming language. An exemplary screen of a running application is shown in Fig. 9.



Fig. 9. An exemplary screen of a running application

The application allows a real time observation of all measurements being performed, as well as to regularly save them to a text file in CSV format for later processing and analysis. In addition to the above, the application allows the occasional additional correction of temperature sensors indications and let user entering the name of the data file. Adding current measurements to the file can be done manually by pressing the SAVE button at any time, or you can also do it automatically by setting up the “Auto save” option and entering time after which the recording of current measurements will take place automatically. Each measurement vector is saved in a separate line of the text file. The line begins with the date and time of measurement, followed by twenty-two numbers representing measurements from subsequent sensors. The position of the measured value corresponds to the number placed on the temperature sensor from which this value originates. The running measuring station used for the experiments is depicted in Fig. 10.

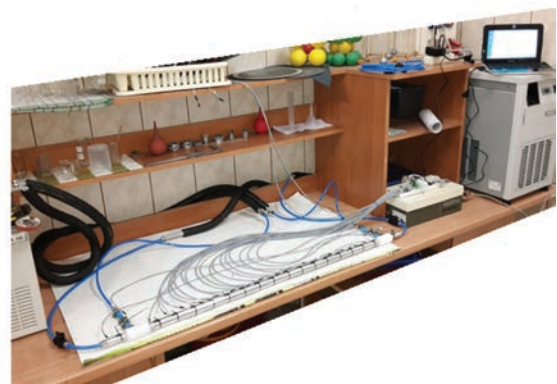


Fig. 10. The complete measuring station

The figure shows the running heat exchanger under test, to which probes with temperature sensors of the constructed measuring device were attached. On the surface of the external exchanger tube, the sensors were placed at a distance of 5.88 cm from each other. Constant input temperatures of hot and cold coolants are provided by the Lauda A100 and Lauda WKL 1000 aggregates. Fig. 11 shows one of the average temperature distributions measured by the constructed device on the surface of the tested heat exchanger. The chart was generated using the WolframAlpha.

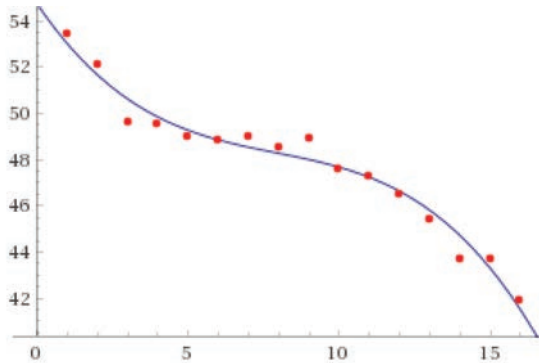


Fig. 11. The average temperature distributions chart

The temperature is marked on the OY axis and the distance from the hot coolant inlet is on the OX axis. Red points show average temperatures from dozens of measurements, and the blue continuous curve is an approximation of the obtained points using the polynomial of degree three model. As you can see the graph shows lower cooling efficiency of the central part of the tested exchanger.

Summary

The concept of a multi-point measuring system presented in this article showed in practice the effectiveness and usefulness of FPGA technology for building fully parallel data processing systems. Deprived of phase shifts in the time domain measurements of the surface temperature of the heat exchanger made it possible to visualize its true and accurate heat dissipation characteristics. The presented device can be easily used for continuous monitoring of operating parameters of air conditioning systems in real time, allowing for example detection of sudden partial obstructions in the heat exchanger pipes. Such obstructions are very difficult to detect with other methods.

The modular design of the hardware configuration for the FPGA chip, written in VHDL, allows for very easy adaptation of the device for measuring other physical quantities than temperature, e.g. pressure, humidity, light, radiation, etc. In this case, it is enough to connect other digital sensors to the device and replace in the

configuration of the FPGA chip the modules responsible for reading the measurements. FPGAs can meet the most demanding operating parameters, as evidenced, for example, by their intense use in CERN collision detectors. On the basis of the presented solution, it would be relatively simple to build a system that performs simultaneous and independent measurements of many different physical quantities, which would enable the detection of complex relationships between various parameters of a particular environment or device.

Acknowledgement

The work was supported by project: INNOTECH-K3/IN3/2/225688/NCBR/14.

References

1. Mohammed I., Abu Talib A.R., Sultan M.T.H., Saadon S.: Temperature and heat flux measurement techniques for aeroengine fire test: a review. *IOP Conference Series: Materials Science and Engineering*, 2016, 152(1), pp. 1–11.
2. Abram Ch., Fond B., Beyrau F.: Temperature measurement techniques for gas and liquid flows using thermographic phosphor tracer particles. *Progress in Energy and Combustion Science*, 2018, 64, pp. 93–156.
3. Duff M., Towey J.: Two Ways to Measure Temperature Using Thermocouples Feature Simplicity, Accuracy, and Flexibility. *Analog Dialogue*, 2010, 44–10, pp 1–6.
4. Miller W.S., Zhuang L., Bottema J., Wittebrood A.J., De Smet P., Haszler A., Vieregge A.: Recent development in aluminium alloys for the automotive industry. *Materials Science and Engineering: A*, 2000, 280(1), pp. 37–49.
5. Sakurai T.: The Latest Trends in Aluminum Alloy Sheets for Automotive Body Panels. *Kobelco Technology Review*, 2008, 28, pp. 22–28.
6. Hirsch J.R.: Recent development in aluminium for automotive applications. *Transactions of Nonferrous Metals Society of China*, 2014, 24(7), pp. 1995–2002, DOI: 10.1016/S1003-6326(14)63305-7.
7. Leszczyńska-Madej B., Richert M., Wąsik A., Szafron A.: Analysis of the Microstructure and Selected Properties of the Aluminium Alloys Used in Automotive Air-Conditioning Systems. *Metals*, 2018, 8(1), 10, pp. 1–15, DOI: 10.3390/met8010010.
8. Hall-Geisler K.: *How Automotive Air Conditioning Works*. Online. 2019. Accessed 30 April 2019.

- Available from: <https://auto.howstuffworks.com/automotive-air-conditioning.htm>.
9. Kuczek Ł., Mroczkowski M., Richert M.: CAD supportive in design of multichannel pipe for automotive application. *Journal of Machine Construction and Maintenance. Problemy Eksploatacji*, 2017, 4, pp. 71–80.
 10. Magadam A., Pawar A., Patil R., Phadtare R.: Review of Experimental Analysis of Parallel and Counter Flow Heat Exchanger. *International Journal of Engineering Research & Technology (IJERT)*, 2016, 5(2), pp. 295–397.
 11. Maheshwari D.A., Trivedi K.M.: A Review on Experimental Investigation of U-Tube Heat Exchanger using Plain Tube and Corrugated Tube. *International Journal of Engineering Development and Research*, 2015, 3(4), pp. 255–259.
 12. Osueke Ch.O., Onokwai A.O., Adeoye A.O.: Experimental Investigation on the Effect of Fluid Flow Rate on the Performance of a Parallel Flow Heat Exchanger. *International Journal of Innovative Research in Advanced Engineering (IJIRAE)*, 2015, 2(6), pp. 2349–2163.
 13. Tapre R.W., Jayant Dr., Kaware P.: Review on Heat Transfer in Spiral Heat Exchanger. *International Journal of Scientific and Research Publications*, 2015, 5(6), pp. 1–5.
 14. Ahire S., Shelke P., Shinde B., Totala N.: Fabrication and Analysis of Counter Flow Helical Coil Heat Exchanger. *International Journal of Engineering Trends and Technology (IJETT)*, 2014, 15(5), pp. 2231–5381.
 15. Mukeshkumar P.C., Kuma J., Suresh S., Praveen K.: Experimental study on parallel and counter flow configuration of a shell and helically coiled tube heat exchanger using Al₂O₃ / water nanofluid. *Journal of Materials and Environmental Science*, 2012, 3(4), pp. 766–775.
 16. Hasan M.I., Muhsin A., Rageb A., Yaghoubi M.: Investigation of a Counter Flow Micro-channel Heat Exchanger Performance with Using Nanofluid as a Coolant. *Journal of Electronics Cooling and Thermal Control*, 2012, 2, pp. 35–43.
 17. Kragh J., Rose J., Nielsen T.R., Svendsen S.: New counter flow heat exchanger designed for ventilation systems in cold climates. *Energy and Buildings*, 2007, 39, pp. 1151–1158.
 18. Gupta P., Atrey M.D.: Performance evaluation of counter flow heat exchangers considering the effect of heat in leak and longitudinal conduction for low-temperature applications. *Cryogenics*, 2000, 40(7), pp. 469–474.
 19. Pantoli L., Muttillio M., de Rubeis T., Nardi I., Stornelli V., Ferri G.: Digital Multi-Probe Temperature Monitoring System for Long-Term on Field Measurements. In: *EuroSensors Conference, Paris (France), 3–6 September 2017*. Proceedings, 2017, 1(4), 596, DOI: 10.3390/proceedings1040596.
 20. Wojtkowski W.: Power semiconductor devices temperature monitoring system. *Zeszyty Naukowe Wydziału Elektrotechniki i Automatyki Politechniki Gdańskiej*, 2017, 54, pp. 232–236.
 21. L. Musa: FPGAs in high energy physics experiments at CERN. In: *International Conference on Field Programmable Logic and Applications, Heidelberg (Germany), 8–10 September 2008*. IEEE, 2008, DOI: 10.1109/FPL.2008.4629896.
 22. Pernegger H.: The Pixel Detector of the ATLAS experiment for LHC Run-2. *Journal of Instrumentation*, 2015, 10(15), C06012.
 23. de la Piedra A., Braeken A., Touhafi A.: Sensor Based on FPGAs and Their Applications: A Survey. *Sensors*, 2012, 12(9), pp. 12235–12264.
 24. Chen J., Wang J.-P., Shen T.-Y., Xiong D.-X., Guo L.-Q.: High Precision Infrared Temperature Measurement System Based on Distance Compensation. *ITM Web of Conferences*, 2017, 12, 03021, DOI: 10.1051/itmconf/20171203021.
 25. Moghavvemi M., K.E. Ng; C.Y. Soo; S.Y. Tan, A reliable and economically feasible remote sensing system for temperature and relative humidity measurement. *Sensors and Actuators A: Physical*, 2005, 117, pp. 181–185.
- This article appeared in its printed version in Journal of Machine Construction and Maintenance. The electronic version is published in DEStech Publications, Inc., Lancaster, PA, 2019, Proceedings of FUTURE ENGINEERING CONFERENCE.

Mirosław NESKA*

Łukasiewicz Research Network – Institute for Sustainable Technologies, Radom, Poland

* Corresponding author: miroslaw.neska@itee.radom.pl

REFRIGERATION SYSTEMS WITH ONE ADSORPTION BED

© 2019 Mirosław Neska

This is an open access article licensed under the Creative Commons Attribution International License (CC BY)

<https://creativecommons.org/licenses/by/4.0/>**Key words:** adsorption, desorption, adsorbent, adsorbate.

Abstract: In the article, solutions of devices, using the process described by the Clapeyron diagram are analysed. The diagram characterizes the individual operation phases of a single adsorption bed. Those types of the device solutions are used, among others, for heat receiving. The basic principles describing thermal energy transfer in the single bed adsorption refrigeration system are presented. Multiple adsorption refrigeration solutions with a single adsorption bed are discussed. The solutions use different pairs, e.g., an adsorbent-adsorbate pair. The presented case study includes devices using the cyclical heat exchange during the adsorption and desorption process which are applied in the following: adsorption ice maker, adsorption air conditioning and energy storage systems, as well as solutions for heat receiving and adsorption air-heating systems. Moreover, advantages and disadvantages of the adsorption systems mentioned above are reported. Our own solution of a system with a single adsorption bed is presented. The author's system is characterized by the possibility of using adsorption systems for both air conditioning and adsorption ice makers. The directions and tendencies of further development of the adsorption solutions for refrigeration systems are discussed.

Układy chłodnicze z pojedynczym złożem adsorpcyjnym**Słowa kluczowe:** adsorpcja, desorpcja, adsorbent, adsorbat.

Streszczenie: W artykule dokonano analizy rozwiązań urządzeń wykorzystujących proces opisany wykresem Clapeyrona, który charakteryzuje poszczególne fazy pracy pojedynczego złoża adsorpcyjnego. Rozwiązania tego typu są wykorzystywane między innymi do odbierania ciepła. Przedstawiono podstawowe zależności charakteryzujące przepływ energii cieplnej w jednozłożowym adsorpcyjnym układzie chłodniczym. Omówiono szereg rozwiązań adsorpcyjnych układów chłodniczych z pojedynczym złożem adsorpcyjnym, wykorzystujących różne pary jako adsorbent-adsorbat. Prezentowane studium przypadku obejmuje rozwiązania, które wykorzystują adsorpcyjny obieg wymiany ciepła w następujących urządzeniach: wytwornicach lodu, układach klimatyzacji i magazynowania energii oraz rozwiązaniach odbierania ciepła i podgrzewania powietrza. Przedyskutowano wady i zalety przytoczonych przykładowych układów adsorpcyjnych. Przedstawiono własne rozwiązanie układu z pojedynczym złożem adsorpcyjnym, które charakteryzuje się możliwością zastosowania zarówno w układach klimatyzacji, jak i w wytwornicach lodu. Omówiono kierunki i tendencje dalszego rozwoju adsorpcyjnych układów chłodniczych.

Introduction

The development of techniques and technology and the increased demand for electricity prompts search for new methods of reducing the electricity consumption in devices and technical objects. Currently, heating and cooling processes absorb approximately 50% of the primary energy consumed [1]. A substitute for electricity could be solar energy or thermal energy from low temperature sources [2], including the following: waste heat from operating fluids, heat of exhaust gases

from industrial processes [3], together with heat of drain water from the heating plants or geothermal waters heat. As an example of a device which does not use any electricity or requires a minimum electric power supply for refrigeration process is an adsorptive refrigeration system [4]. However, this system needs low temperature thermal energy for its work. This solution for heat receiving process involves an adhesion phenomenon of adsorbate to a surface (adsorption). In order to perform the regeneration of an adsorption bed, external thermal energy needs to be supplied, causing the

process of removing adsorbed particles from a surface of the adsorbent (desorption). This type of refrigeration devices utilize sorption processes and require external thermal energy to accomplish the refrigeration cycle. Moreover, in these systems, the refrigerant undergoes phase conversions. The main elements of the adsorption refrigeration systems are the adsorbent and the adsorbate, which are a pair of cooperating substances. The adsorbent-adsorbate pair consists of different substances that can form various combinations of substances within the pair. Generally, adsorbents are divided into physical, chemical, and composite, depending on the abilities of adsorption interactions [5]. Examples of adsorbents could be activated carbon, zeolites, silica gel, or metal chlorides. Examples of adsorbates are water, methanol, ethanol, or ammonia [6–8].

The article presents systems with a single adsorbent bed, using sorption processes as well as varied substances as an adsorbent-adsorbate pair. The number of adsorption refrigeration systems for the heat transfer which include devices of various constructions and applications are described. Furthermore, the author's solution of an adsorption system is briefly discussed.

1. The cycle of work of a single bed

The typical structure of the adsorptive refrigeration system with a single bed consists of the following elements: an evaporator, one adsorber bed, a condenser, and a throttling valve (Fig. 1). This kind of system is powered by thermal energy which generates the cyclical heat receiving process in the evaporator. The work cycle of this type of refrigeration system is comprised of four phases: the adsorbent bed heating phase, the bed regeneration (desorption), the adsorbent bed cooling phase, and the adsorbate adsorption. Furthermore, the periodic run of individual phases in the *Clapeyron* diagram is shown (Fig. 2). During the first phase (1-2), the adsorbent bed is heated in the isochoric process causing the pressure and temperature to increase simultaneously. When the pressure reaches the value p_s at the Point 2, then the desorption process takes place. During the second phase (2-3), there is further heating of the bed over the isobaric process and desorption is carried out at that time. The end of this phase occurs after reaching Point 3, when the adsorbent bed is completely regenerated. The next stage of the process is the 3-4 phase, when heat is given back.

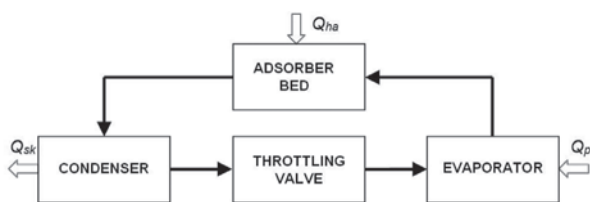


Fig. 1. Block diagram of a single bed adsorption refrigeration system

During this phase, which is the isochoric cooling of a single bed, a decrease in temperature and pressure occurs. At the moment of the p_p pressure of adsorbate evaporation, when Point 4 is reached, the adsorption process starts on the surface of the adsorbent bed. This process is performed during the 4-1 phase while heat is received from the system. At Point 2, when the desorption process in a single adsorber bed is started in parallel, evaporated refrigerant flows from the adsorber bed to the condenser (Point 3'). Under the 3'-4' step, condensation of the refrigerant in the condenser happens.

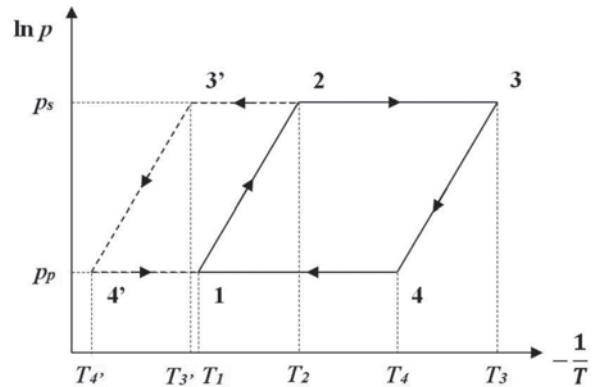


Fig. 2. Diagram of the ideal adsorption cycle running in a single bed of an adsorption refrigeration device [9, 10]

In a further stage, the liquid phase of the adsorbate via the throttling valve into the evaporator space is dosed (Point 4'). In the evaporator space, the evaporation of the refrigerant takes place whose steam goes to the adsorber bed, where it is re-adsorbed. Moreover, evaporation of the adsorbate in the evaporator causes a decrease of the temperature in the evaporator space under the influence of receiving heat. As a result, a cooling effect in the adsorption refrigeration system is created.

2. The basic principles of energy transfer in a single bed

The above adsorption refrigeration device is powered by thermal energy, which is supplied to the system. Furthermore, the total thermal energy, Q_{ha} , provided to the system comes into a single bed of the adsorber for its heating (Fig. 1). The presented graph (Fig. 2) of the ideal cycle of the adsorption heat exchange shows that the total thermal energy Q_{ha} supplied to the system is equal to the sum of energy Q_{1-2} and energy Q_{2-3} [11, 12]. Whereas, the Q_{1-2} is the energy required to increase the adsorbent temperature of a single bed and the adsorbate (from Point 1 to Point 2). On the other hand, the Q_{2-3} is the energy needed to continue the heating and desorption process of the adsorbate (from

Points 2 to 3). The energies can be calculated using the following relations:

$$Q_{ha} = Q_{1-2} + Q_{2-3} \quad (1)$$

$$Q_{1-2} = (m_s C_{p_s} + m_{w1} C_{p_w})(T_2 - T_1) \quad (2)$$

$$Q_{2-3} = (m_s C_{p_s} + C_{p_w}[(m_{w1} + m_{w3})/2]) \quad (3)$$

$$(T_3 - T_2) + (m_{w1} - m_{w3})H_{aw}$$

where: m_s – mass of a single bed of the adsorbent, kg; m_{w1} , m_{w3} – adsorbate mass, kg, (1,3 – the points on the Clapeyron diagram (Fig. 2)); T_1 , T_2 , T_3 – temperature, K, (1,2,3 – the points on the Clapeyron diagram (Fig. 2)); C_{p_s} – specific heat of the adsorbent, kJ/kgK; C_{p_w} – specific heat of the adsorbate, kJ/kgK; H_{aw} – heat adsorption of the adsorbate, kJ/kg; Q – thermal energy, kJ.

A calculation of the entire evaporative energy of the adsorbate (Q_p) generated in the heat receiving process in the evaporator is shown below:

$$Q_p = (m_{w1} - m_{w3})H_{pw} \quad (4)$$

where: H_{pw} is the heat of the evaporation of the adsorbate, kJ/kg.

The total Q_{sk} energy dissipated as a result of the refrigerant condensation in the condenser is represented as follows:

$$Q_{sk} = (m_{w1} - m_{w3})C_{p_w}(T_{3'} - T_{4'}) \quad (5)$$

where: $T_{3'}$, $T_{4'}$ – temperature, K, (3',4' – the points on the Clapeyron diagram (Fig. 2)).

Performance of an adsorption refrigeration cycle for an adsorber with a single bed, defined as the Coefficient of the Performance (COP), is calculated by the following equation:

$$COP = \frac{Q_p}{Q_{ha}} \quad (6)$$

3. Case study of adsorption systems with a single bed

3.1. Adsorptive Ice Makers with a Cylindrical Adsorber

A series of adsorption refrigeration systems are devices powered by solar thermal energy. One of these solutions is a system used to produce ice [13] in which a single adsorber bed consists of a set of parallel tubes (Fig. 3). The basic elements of the system construction are a solar collector-adsorber, a condenser, a condensate tank, a valve, a cold cabinet with evaporator, and ice storage. The solar collector-adsorber in the device is one element. However, they play different roles. On the one hand, the solar collector collects energy from the sun using its thermal exchange area (2 m²). Whereas, sorption processes take place in the adsorber. The adsorber is built

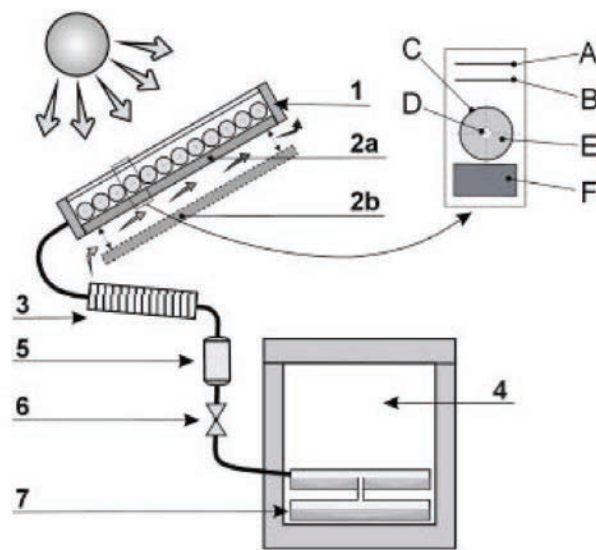


Fig. 3. View and draft of adsorptive solar refrigerator: 1 – solar collector-adsorber with detail: A – glass cover, B – Teflon film, C – tube covered with selective surface and internally layered with Papyex, D – central tube for vapour transport, E – silicagel bed, F – thermal insulation around the collector; 2 – ventilation dampers: 2a – closed and 2b – open, 3 – condenser, 4 – cold cabinet, 5 – graduated tank, 6 – check valve, 7 – evaporator and ice storage [13]

of twelve parallel cylindrical tubes with a diameter of 72.5 mm . A tube with a smaller diameter (15 mm) runs inside each of the pipes. The central pipes are made of a grid with a mesh of 1 mm (wire 0.45 mm). A single adsorber bed contains the adsorbent, which is silicagel (78.8 kg), and water is used as an adsorbate in the system. The solar collector-adsorber works in such a way that it is heated by solar radiation during the day and cooled at night by natural convection. The next element of the system is the condenser. It is constructed by eight parallel finned tubes, which are air-cooled as well as through natural convection. Moreover, the total heat transfer surface of the finned condenser is 6.9 m^2 . The next component of the system is the evaporator, which is made from square pipe in the form of three rings. Furthermore, the entire area of heat exchange in it is 3.4 m^2 . The evaporator is placed in an insulated chamber with a volume of 320 l , and the evaporator contains 40 litres of water, which is converted into ice.

In the presented system, after performing numerous verification tests and improvements, a COP from 0.10 to 0.25 was obtained. The distinguishing features of the presented solution are the following: simple construction, the possibility of using solar thermal energy, utilizing ecological substances as the adsorbent-adsorbate pair, and dispensing refrigerant from the graduated tank. The challenges of the system are cyclical operation and the low value of the coefficient of the performance.

Another analysed adsorption refrigeration system is a device for ice production in which the adsorber is designed in a shape of a flat cylindrical container (Fig. 4). In this solution, as in the previous one, solar energy is used as a supply source of the thermal energy. Charcoal with small pieces of blackened steel and methanol are utilized as an adsorbent-adsorbate pair. The charcoal is in the form of granules with a diameter of 5 to 7 mm . The analysed system is built of an adsorbent bed located in the adsorber, condenser, and evaporator. The adsorbent bed is placed in a flat glass circular container with a diameter of 20 cm and a thickness of 5 cm . The thickness of the cylindrical glass of the bed is 3 mm . The amount of charcoal grains found in the deposit is 0.6 kg , and the weight of the small pieces of steel is 0.2 kg . The next element of the system, the condenser, is constructed of a glass tube with a 15 mm diameter and a 50 cm length. Another component of the device is the evaporator, which is designed in a shape of a cylinder with a 5 cm diameter and is also made of glass, and it contains 0.2 kg of methanol. The operation of the presented solution consists of adsorption and desorption of methanol by the adsorbent bed. During the day, the adsorbent bed is heated by the solar radiation, and the evaporated adsorbate flows to the condenser. In order to condense the evaporated refrigerant in the condenser, the refrigerant in the liquid phase then runs to the evaporator where it is stored. During the night, since there is no supply by the solar energy, the adsorbent bed is cooled through natural convection of the ambient air.

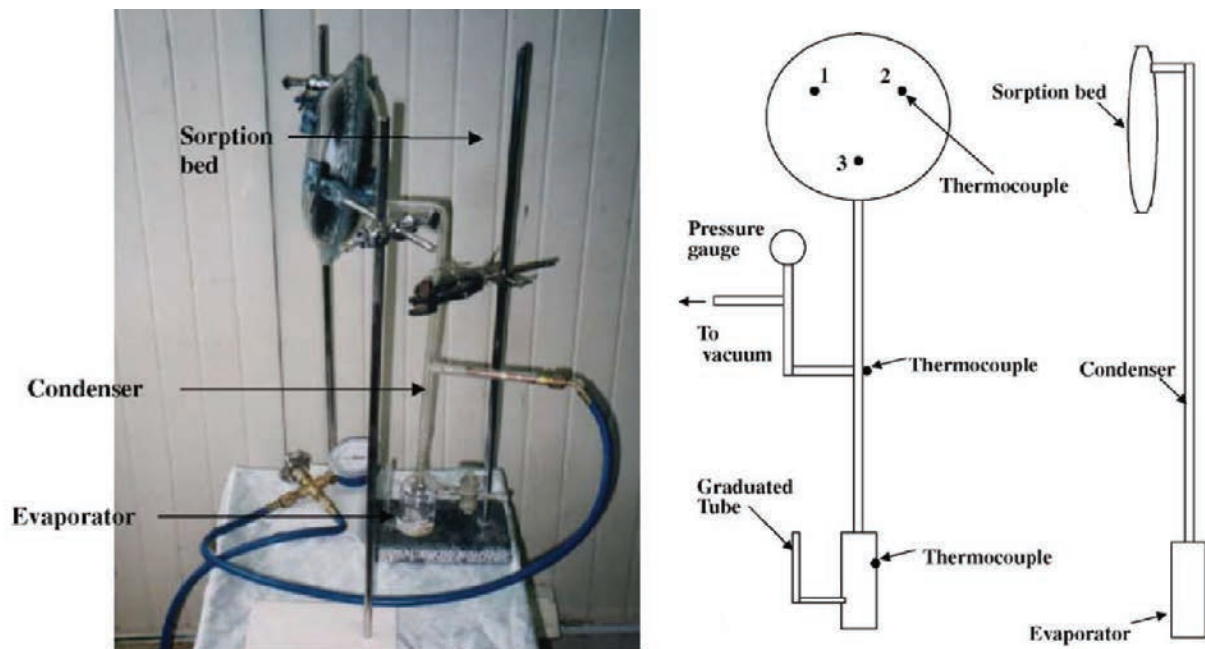


Fig. 4. Photograph and scheme of the adsorption refrigeration system with adsorber in a form of flat cylindrical container [12]

Afterwards, the methanol stored in the evaporator evaporates, resulting in a heat receiving process and ice production. Then, the vapour of the refrigerant is adsorbed by the adsorbent bed during the adsorption process. Operation parameters of the system are as follows: the lowest temperature in the evaporator is -1°C by 4 mbar pressure; 24 to 33°C is average temperature in the condenser by 125 to 220 mbar pressure; 114 to 130°C is maximum temperature of the adsorbent bed; 120 to 162 g is amount of methanol obtained in the desorption process; and, the gained value of the coefficient of the performance is from 0.136 to 0.159 . The presented solution is characterized by the possibility of utilizing solar energy, simple construction, and the use of ecological substances as the working pair. An unfavourable aspect of the system is storing the liquid

refrigerant directly in the evaporator, since it can evaporate in an uncontrolled way. Other unfavourable aspects include the low value of the coefficient of the performance and the periodical work of the device.

3.2. Adsorption Refrigeration System for Air Conditioning with Energy Storage

A different solution using the adsorption refrigeration system with a single bed is a device for the storage of thermal energy in the adsorbent bed. This device is utilized for the heat receiving in the evaporator (generating cold), in this way, air cooling is realized in a connected room. Moreover, the received thermal energy can be directly transferred to this room as well (Fig. 5). The system is dedicated to the cyclical storage

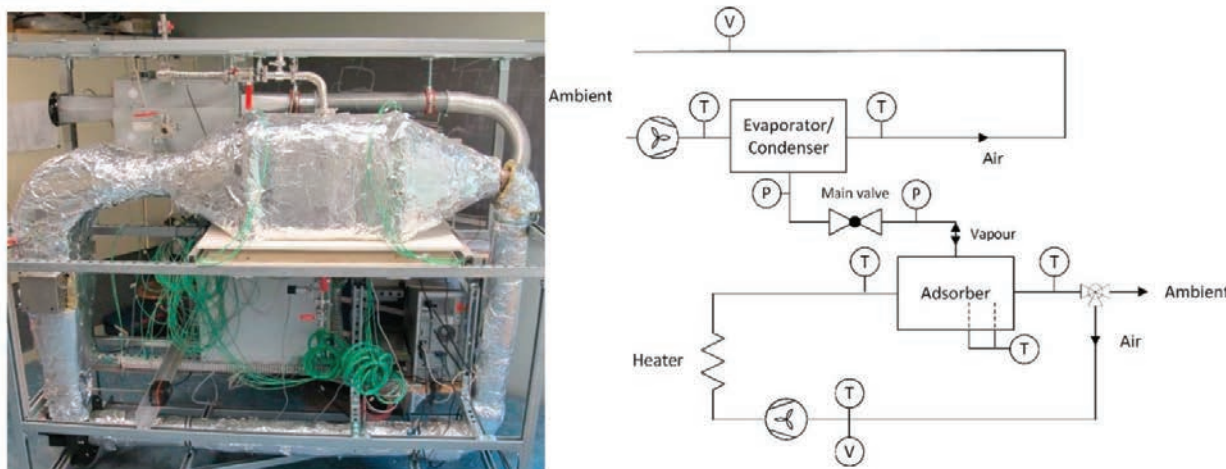


Fig. 5. View and diagram of the adsorption refrigeration setup for air conditioning with energy storage [14]

of thermal energy from hot exhaust gas of a combustion engine during the daytime and cold generation from the stored heat during the night. The presented solution consists of the two main components: the adsorber and the evaporator/condenser as one element. Furthermore, in this system, 13XBF zeolite and water is exploited as an adsorbent-adsorbate pair. A single bed is placed inside a finned copper adsorber, which consists of an inner and outer layer, and it is in the shape of a rectangle. The construction of the finned copper adsorber has its benefits, i.e. better heat transfer to the bed. However, this effect is a weak spot of the solution, because it prevents maintaining a low temperature in the bed. Moreover, the internal volume of the adsorber in which the bed is located is 35 l . The second main component of the system is the evaporator/condenser as one unit, which contains a vessel for a refrigerant.

This element plays the role of the condenser and a refrigerant storage place in the liquid phase during the

desorption process. When hot exhaust gas flows by the adsorber, heat transfer to the bed occurs. During this time, the desorption process takes place and thermal energy storage in the adsorbent bed happens. When the desorption process stops and the adsorption starts, the component of the system changes its function from the condenser to the evaporator. Afterwards, the refrigerant stored in the liquid phase evaporates and generates cooling in the evaporator space. During the adsorption process, ambient air flows through the evaporator where is cooled down and flows into the room to be cooled. An additional component of the system is the main valve connecting the adsorber and the unit of the evaporator/condenser. It works periodically by its cyclic opening and closing. Values of the main parameters of the work of the system are as follows:

- The minimum pressure in the adsorber is $0.1\text{--}10\text{ Pa}$.
- The maximum temperature of exhaust gas that flows throughout the adsorber is under 300°C .

- $12\text{--}20^\circ\text{C}$ is the air temperature in a cooled room.
- The entire amount of stored energy for several hours of cooling is 3 kWh .
- $20\text{--}100\text{ mbar}$ is the range of pressure change during the desorption process in the adsorber and the condenser.
- $24\text{--}40^\circ\text{C}$ is the temperature in the condenser.
- The pressure change during the adsorption process in the evaporator is $10\text{--}24\text{ mbar}$ when the temperature in the evaporator is below 20°C .

The interesting features of this system are the possibility of utilizing energy from the heat of exhaust waste gas, using the adsorbent bed as an innovative thermal energy store and applying ecological substances as the adsorbent-adsorbate pair. Furthermore, in the solution, there are some aspects to take into consideration, such as the following: using medium-temperature sources as heat sources, a complicated construction of the device, cyclical operation of the system, and the lack of possibility of long-term maintenance of the low temperature in the adsorbent bed.

3.3. Adsorption System for Heat Receiving and Ambient Air Warming

Another analysed system using the adsorption process is a solution in which the device is utilized to increase the ambient air temperature (Fig. 6). A characteristic feature of this solution is the low temperature of $2\text{--}25^\circ\text{C}$ applied as a heat source. The main components of the presented prototype are the adsorber and the evaporator/condenser as one element. The adsorber is made of two commercial heat exchangers, which are constructed in the form of finned flat tubes. The heat exchange surface of each is 1.24 m^2 . Moreover, the volume of the adsorber is 110 ml , and it is filled with the adsorbent in the form of a CaClBr/SiO_2 composite (a grain size of $0.2\text{--}0.5\text{ mm}$ and a mass of 700 g). The next component of the system is the evaporator/condenser, which is built as a single exchanger, which is the same as mentioned above. In this unit, the refrigerant is stored in the liquid phase.

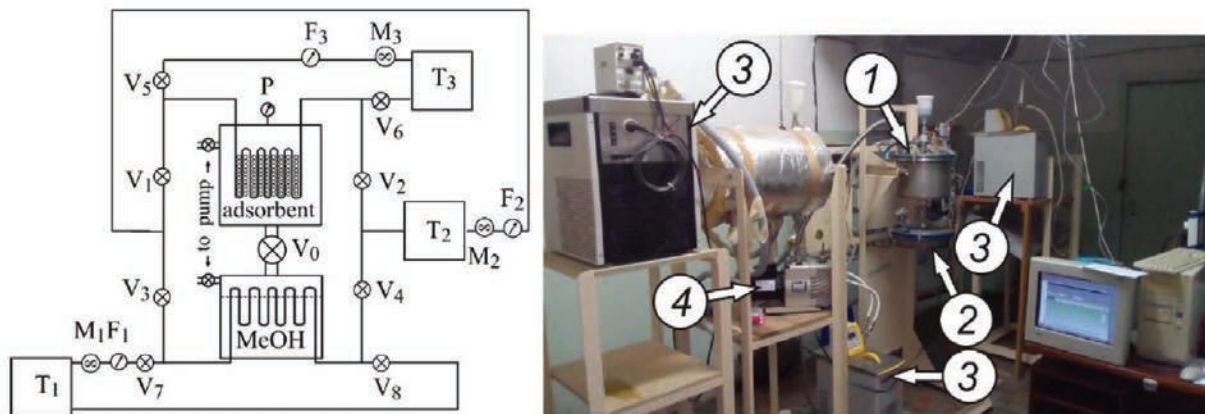


Fig. 6. Photography and diagram of the adsorption system for air heating; 1 – adsorber; 2 – condenser/evaporator; 3 – thermocryostats; 4 – vacuum pump; F1-F3 – flowmeters; V0 – vacuum valve; V1-V8 – valves; P – pressure gauge [15]

The composite and methanol are used as the adsorbent-adsorbate pair. In this device, the methanol is adsorbed at the level of 0.48 g/g . The subsequent components of the system are the following: the vacuum valve, the vacuum pump, the flow meters, and the pressure and temperature sensors. The system operation depends on the heat received in the evaporator during the adsorption process. In this case, a fluid of the low temperature heat source with a temperature of $2\text{ to }30^\circ\text{C}$ runs through the evaporator. This kind of energy source can be the waste heat of the domestic sector or the heat of natural water basins. Then, the received heat from the evaporator is transferred to the single adsorbent bed from where the heat is transmitted outside the system as useful heat. The temperature of the thermal energy generated in this way is in the range of $32\text{--}49^\circ\text{C}$. Thus,

the energy at this temperature can be utilized, for example, for warm floor systems. During the desorption process, the external circulation in the adsorber is replaced from a higher temperature circuit to the lower temperature cycle at the range of $2\text{--}30^\circ\text{C}$. The evaporator switches into the condenser function by changing the outer circulation of the fluid. The circulation is changed from the lower temperature circuit ($2\text{--}30^\circ\text{C}$) to the very low temperature cycle, which is in the range of $-10\text{ to }-60^\circ\text{C}$. Therefore, this very low temperature energy source can be, for instance, natural ambient air in cold regions. The desorption process runs in the adsorber at a stable temperature of the low-temperature source, after achieving in the condenser of low pressure in the range of $10\text{--}100\text{ mbar}$. The presented solution allows the generation of the maximum heating power at the

level of $1.0\text{--}2.5\text{ kW}$ with the temperature of the released heat in the range of $32\text{ to }49^\circ\text{C}$. A fascinating property of this solution is the innovative application of the adsorption system for the generation of thermal energy using low and very low-temperature heat sources with extreme temperatures from -60°C to 30°C . Furthermore, the challenges of the prototype can be cyclic work, the complexity of the structure, the necessity of mechanical switching of the individual circulations to trigger another sorption process, and no refrigerant container.

3.4. The Author Adsorption Refrigeration System

The major components of the developed proprietary adsorption refrigeration system are the following: adsorber, condenser, throttling valve, and evaporator (Fig. 7). In the prototype, there is a single adsorbent bed which is placed in the adsorber, where the adsorption and desorption process alternate runs. In the device, silica gel and water is exploited as the adsorbent-adsorbate pair, and the amount of silica gel loaded is 4.85 kg . The adsorber is made of copper in the shape of a cylinder. The condenser is built of copper tubes connected with single flat elements performed with a copper sheet. The adsorber is made of copper in the shape of a cylinder.

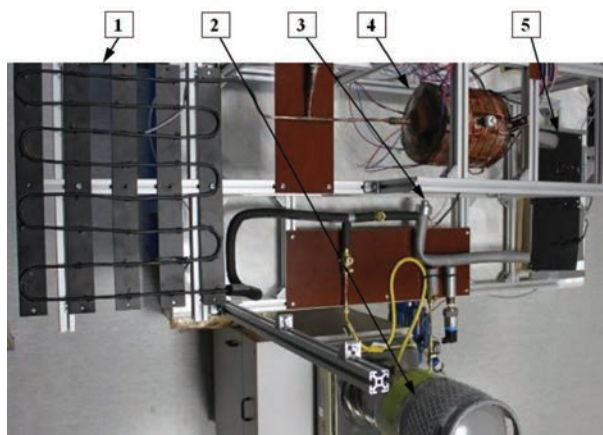


Fig. 7. View of the model adsorption refrigeration system; 1 – condenser; 2 – refrigerant tank; 3 – expansion valve; 4 – adsorber; 5 – evaporator

The condenser is built of copper tubes connected with single flat elements formed from copper sheets. A commercial electronic expansion valve (*LNE* type, *Saginomiya Seisakusho INC*) is used. Another component of the system is the evaporator which is made in the form of a copper plate with copper tubes attached. The system works by forcing the desorption process on the adsorbent bed, and heating the adsorber to a temperature of $70\text{--}100^\circ\text{C}$. As a result, the evaporated adsorbate passes to the condenser, where the condensation of it takes place. Afterwards, the refrigerant is storage in its tank. From the reservoir, the refrigerant is dosed into the

evaporator space via the expansion valve. Evaporated refrigerant in the evaporator flows to the single bed of the adsorbent where it is adsorbed. The evaporation process of the refrigerant in the evaporator causes heat receiving, which results in many hours of temperature drop in the evaporator. The decrease is to the average minimum temperature of 11°C [16]. As an effect of the multi-day investigations of the device, the average value of the coefficient of the performance is 0.44 .

Conclusions

The analysis shows that the great benefit of the adsorption refrigeration systems is the prospect of their utilization for various applications. In the article, solutions used for ice production, the storage of thermal energy and its use in air-conditioning systems and useful thermal energy generation are presented. The author's solution that can be applied in both air-conditioning systems and ice-maker devices is also described. Other examples of applications of the adsorption refrigeration systems are the following: adsorption chillers [17], sorption heat pumps [18], trigeneration systems [19], and desalination systems [20].

The constructions of the adsorption refrigeration systems are being widely develop due to their advantages, particularly their ecological aspects. This type of solutions have plenty of strengths, e.g., the following [10, 21]: simplicity of construction, low costs of exploitation, noiseless work, immunity to thermal shocks, the possibility of using low-temperature heat sources, corrosion resistance, environmental friendliness (among others due to implementing of environmentally friendly refrigerants), low electricity consumption, no vibration generated during working, and vibration tolerance and insensitivity to deviations and rotation of the system. However, the principal direction of the amelioration of such solutions is the eliminating their drawbacks. Therefore, the challenges include the following [5, 11]: low adsorption ability, weak efficiency, discontinuity in operation (cyclic work), insufficient identification of the adsorption and desorption process, low heat transfer coefficients between the adsorber wall and the adsorbent layer, relatively large dimensions and weight in relation to traditional systems, and economic competitiveness in relation to the compressor driven systems. Thus, adsorption refrigeration systems are expected to be widely developed due to their advantages, which will lead to the mitigation or elimination of their disadvantages. The general conclusions resulting from the performed analysis lead to statements about the necessity of the further development of the adsorption systems. This action can be carry on through the following: the development of substances used for the adsorbent-adsorbate pair; improvement of the adsorber construction (as cylindrical, flat or with a complex

shape); ameliorating and lengthening the time of refrigerant dosing to the evaporator working space; the development of the construction and operation of the condenser; and, the improvement of other components of this type of systems, e.g., shut-off valves, expansion valves, reservoirs, and an appropriate location of these subsystems in the installation.

The tendency of investigations of the adsorption refrigeration systems is currently focused on the following issues: increasing the coefficient of the performance, the constructing of systems with a minor cubature, and improving reliability. Furthermore, there should be design solutions that guarantee more effective cooling and heating of the adsorbent, which can be supported by applying modern technologies, such as infrared thermography [22] or innovative coatings of heat exchange elements [23, 24].

References

1. European Commission: *Communication from the commission to the European parliament, the council, the European economic and social committee and the committee of the regions. An EU Strategy on Heating and Cooling, Brussels, 2016*. [Online]. 2016. [Accessed 15 April 2019]. Available from: https://ec.europa.eu/energy/sites/ener/files/documents/1_EN_ACT_part1_v14.pdf
2. Alam K.C.A., Akahira A., Hamamoto Y., Akisawa A., Kashiwagi T.: A four-bed mass recovery adsorption refrigeration cycle driven by low temperature waste/renewable heat source. *Renewable Energy*, 2014, 29, pp. 1461–1475.
3. Zarzycki R.: Wykorzystanie ciepła odpadowego z układu sprężania CO₂ do produkcji wody lodowej. *Zeszyty Naukowe Instytutu Gospodarki Surowcami Mineralnymi i Energią Polskiej Akademii Nauk*, 2016, 95, pp. 169–180 [in Polish].
4. Oliveira R.G.: *Solar powered sorption refrigeration and air conditioning. Refrigeration: Theory, Technology and Applications*. Nova Science Publishers, Inc., chapter 4, 2011, pp. 205–238.
5. Wang L.W., Wang R.Z., Oliveira R.G.: A review on adsorption working pairs for refrigeration. *Renewable and Sustainable Energy Reviews*, 2009, 13(3), pp. 518–534.
6. Mohammed R.H., Mesalhy O., Elsayed M.L., Chow E.M.L.: Assessment of numerical models in the evaluation of adsorption cooling system performance. *International Journal of Refrigeration*, 2019, 99, pp. 166–175.
7. Ramji H.R., Leo S.L., Tan I.A.W., Abdullah M.O.: Comparative study of three different adsorbent-adsorbate working pairs for a waste heat driven adsorption air conditioning system based on simulation. *IJRRAS*, 2014, 18(2), pp. 109–121.
8. Hamed A.M., Abd El Rahman W.R., El-Emam S.H.: Experimental study of the transient adsorption/desorption characteristics of silica gel particles in fluidized bed. *Energy*, 2010, 35(6), pp. 2468–2483.
9. Wu W.-D., Zhang H., Sun D.-W.: Mathematical simulation and experimental study of a modified zeolite 13X–water adsorption refrigeration module. *Applied Thermal Engineering*, 2009, 29, pp. 645–651.
10. Sumathy K., Yeung K.H., Yong L.: Technology development in the solar adsorption refrigeration systems. *Progress in Energy and Combustion Science*, 2003, 29(4), pp. 301–327.
11. Ambarita H., Kawai H.: Experimental study on solar-powered adsorption refrigeration cycle with activated alumina and activated carbon as adsorbent. *Case Studies in Thermal Engineering*, 2016, 7, pp. 36–46.
12. Khattab N.M.: A novel solar-powered adsorption refrigeration module. *Applied Thermal Engineering*, 2004, 24, pp. 2747–2760.
13. Hildbrand C., Dind P., Pons M., Buchter F.: A new solar powered adsorption refrigerator with high performance. 2004, *Solar Energy*, 77, pp. 311–318.
14. Semprini S., Asenbeck S., Kerskes H., Druck H.: Experimental and numerical investigations of an adsorption water zeolite heat storage for refrigeration applications. *Energy Procedia*, 2017, 135, pp. 513–521.
15. Tokarev M.M., Gordeeva L.G., Grekova A.D., Aristov Y.I.: Adsorption cycle “heat from cold” for upgrading the ambient heat: The testing a lab-scale prototype with the composite sorbent CaClBr/silica. *Applied Energy*, 2018, 211, pp. 136–145.
16. Neska M., Majcher A.: *Koncepcja sterowania adsorpcyjnego układu chłodniczego małej mocy*. In: Całus D., Ożga K., Popławski T., Michalski A., Szczepański K. (eds): *Możliwości i horyzonty ekoinnowacyjności. Zielona Energia*. Częstochowa: Wyd. Politechniki Częstochowskiej, 2018, pp. 141–153.
17. Szyk M., Nowak W.: Operation of an adsorption chiller in different cycle time conditions. *Chemical and Process Engineering*, 2014, 35(1), pp. 109–119.
18. Miles D.J., Shelton S.V.: Design and testing of a solid-sorption heat-pump system. *Applied Thermal Engineering*, 1996, 16(5), pp. 389–394.
19. Gazda W., Stanek W.: Energy and environmental assessment of integrated biogas trigeneration and photovoltaic plant as more sustainable industrial system. *Applied Energy*, 2016, 169, pp. 138–149.
20. Mitra S., Thu K., Saha B.B., Dutta P.: Performance evaluation and determination of minimum desorption temperature of a two-stage air cooled silica gel/water adsorption system. *Applied Energy*, 2017, 206, pp. 507–518.

21. Gwadera M., Kupiec K.: Adsorpcyjne układy chłodnicze”, *Inżynieria i Aparatura Chemiczna*, 2011, 50(5), pp. 38–39.
22. Dudzik S.: Investigations of a heat exchanger using infrared thermography and artificial neural networks. *Sensors and Actuators A: Physical*, 2011, 166, pp. 149–156.
23. Kucharczyk W., Przybyłek P., Opara T.A.: Investigation of the thermal protection ablative properties of thermosetting composites with powder fillers: the corundum Al₂O₃ and the Carbon Powder C. *Polish Journal of Chemical Technology*, 2013, 15(4), pp. 49–53.
24. Przybylski J., Majcher A.: The structure and application of a test stand for a PVD technology research control system. *Problemy Eksploatacji*, 2014, 2, pp. 73–82.

This article appeared in its printed version in *Journal of Machine Construction and Maintenance*. The electronic version is published in *DEStech Publications, Inc.*, Lancaster, PA, 2019, *Proceedings of FUTURE ENGINEERING CONFERENCE*.